

## **Simulating contrail formation within cirrus in the high-resolution ICON-LEM model**

Pooja Verma

Deutsches Zentrum für Luft- und Raumfahrt  
Institut für Physik der Atmosphäre  
Oberpfaffenhofen

Dissertation  
an der Fakultät für Physik  
der Ludwig-Maximilians-Universität  
München



DLR

Deutsches Zentrum  
für Luft- und Raumfahrt

# **Forschungsbericht 2022-23**

## **Simulating contrail formation within cirrus in the high-resolution ICON-LEM model**

Pooja Verma

Deutsches Zentrum für Luft- und Raumfahrt  
Institut für Physik der Atmosphäre  
Oberpfaffenhofen

Dissertation  
an der Fakultät für Physik der  
der Ludwig-Maximilians-Universität  
München

151 Seiten  
47 Bilder  
3 Tabellen  
171 Literaturstellen



*Herausgeber:*

Deutsches Zentrum  
für Luft- und Raumfahrt e. V.  
Wissenschaftliche Information  
Linder Höhe  
D-51147 Köln

ISSN 1434-8454  
ISRN DLR-FB-2022-23  
Erscheinungsjahr 2022

DOI: [10.57676/w2f9-kd47](https://doi.org/10.57676/w2f9-kd47)

**Erklärung des Herausgebers:**

Als Manuskript gedruckt.  
Abdruck oder sonstige Verwendung nur nach Absprache mit dem DLR gestattet.

*Large Eddy Simulation mit dem ICON Modell, Kondensstreifen, Modellierung von Kondensstreifen, Bildung von Kondensstreifen in Zirruswolken, Zirruswolken, optische Dicke*

Pooja Verma

DLR, Institut für Physik der Atmosphäre des DLR, Oberpfaffenhofen

***Modellierung der Bildung von Kondensstreifen in Zirruswolken mit dem hoch-aufgelösten ICON-LEM Modell***

*Dissertation, Ludwig-Maximilians-Universität München*

Die Bildung von Kondensstreifen in eis-übersättigten Regionen und deren Klimawirkung wird häufig untersucht. Allerdings wird die Bildung von Kondensstreifen in schon bestehenden Zirruswolken und deren Wirkung auf die Wolkeneigenschaften dieser Zirren nicht beachtet. Deshalb ist die Klimawirkung dieser Effekte nicht bekannt. Die Bildung von Kondensstreifen in natürlichen Zirren kann eine große Störung in der Anzahl der Eispartikel verursachen. Dabei werden die mikrophysikalischen und die optischen Eigenschaften der natürlichen Zirren verändert. Aus diesem Grund wird in dieser Arbeit der Einfluss der Kondensstreifenbildung auf die Eigenschaften umliegender, schon bestehender Zirren untersucht.

Um Kondensstreifenbildung in schon bestehenden Zirren zu untersuchen wird das hoch-aufgelöste ICON-LEM (ICOsahedral Non-hydrostatic- Large eddy simulation model) mit einer horizontalen Auflösung von 625m genutzt. Eine Parametrisierung für Kondensstreifenbildung in Zirren wurde implementiert und so angepasst, dass der Einfluss der schon bestehenden Zirren bei der Kondensstreifenbildung berücksichtigt wird.

Die vorliegende Arbeit gibt Aufschluss über den Effekt schon bestehender Zirren auf die Bildung von Kondensstreifen, sowie den Einfluss der Kondensstreifenbildung auf die mikrophysikalischen und optischen Eigenschaften der umliegenden Zirren.

*Large Eddy simulation ICON model, Contrails, contrail modelling, contrail ice formation within cirrus, cirrus clouds, optical depth*

*(Published in english)*

Pooja Verma

German Aerospace Center (DLR), Institut für Physik der Atmosphäre, Oberpfaffenhofen

***Simulating contrail formation within cirrus in the high-resolution ICON-LEM model***

*Doctoral Thesis, Ludwig-Maximilians-Universität München*

Contrail ice formation in ice supersaturated region and their impact on climate is often studied. However, contrail ice formation within cirrus and their impact on cirrus cloud properties are overlooked therefore, their climate impact is unknown. Contrail formation within natural cirrus can introduce a large perturbation in ice crystal numbers modifying the microphysical and optical properties of the natural cirrus. Therefore, in this thesis work, the impact of contrail ice formation within cirrus on cirrus properties is analysed.

In order to study contrail formation within cirrus a high-resolution ICON-LEM (ICOsahedral Non-hydrostatic- Large eddy simulation model) at a horizontal resolution of 625m is used. A parameterization for contrail formation within cirrus is implemented and modified to include the impact of pre-existing cirrus on contrail ice formation.

The presented work provides insights into the effect of pre-existing cirrus on contrail ice formation within cirrus and the effect of contrail formation within cirrus on cirrus microphysical and optical properties.



---

# Simulating contrail formation within cirrus in the high-resolution ICON-LEM model

Pooja Verma

---



München 2023



---

# **Simulating contrail formation within cirrus in the high-resolution ICON-LEM model**

**Pooja Verma**

---

Dissertation  
an der Fakultät für Physik  
der Ludwig-Maximilians-Universität  
München

vorgelegt von  
Pooja Verma  
aus Kanpur (Indien)

München, den 08. June 2022

Erstgutachter/in: Prof. Dr. Markus Rapp

Zweitgutachter/in: Prof. Dr. George Craig

Tag der mündlichen Prüfung: 13. Oktober 2022

# Kurzfassung

Zirruswolken treten häufig in der oberen Troposphäre auf und tragen zur Energiebilanz der Erde bei. Der Strahlungsantrieb von Zirren hängt von deren makrophysikalischen, mikrophysikalischen und optischen Eigenschaften ab. Deshalb führt eine Änderung der Zirruswolkeigenschaften zu einer Änderung ihrer Strahlungswirkung. Eine kürzlich erschienene Studie analysierte Satellitenfernerkundungsdaten und lieferte den Hinweis, dass Kondensstreifeneisbildung in Zirren deren optische Dicke beeinflusst. Bis jetzt existieren keine detaillierten Studien, die den Einfluss von Kondensstreifeneisbildung in Zirren auf deren mikrophysikalische und optische Eigenschaften quantifizieren. Daher ist es das Ziel dieser Arbeit, das Verständnis zu Kondensstreifeneisbildung in Zirren und zum Einfluss von Kondensstreifen auf die Zirrusbewölkung zu verbessern.

Das hochauflösende Modell ICON-LEM (ICOsahedral Non-hydrostatic- Large-Eddy Modelling) wird verwendet und im Wetterprognose-Modus mit einer horizontalen Auflösung von 625 Metern betrieben. Um Kondensstreifenbildung in Zirren zu untersuchen wird eine Parametrisierung für Kondensstreifenbildung in Zirren implementiert, welche Kondensstreifeneisbildung und den Eiskristallverlust in der Vortex-Phase beschreibt. Diese Parametrisierung wird modifiziert, um den Einfluss präexistierender Zirruswolken auf die Kondensstreifeneisbildung einzubeziehen. Zwei sehr unterschiedliche synoptische Situationen und entsprechende Zirruswolkenfelder werden beprobt, um eine große Spannweite verschiedener Zirruseigenschaften abzudecken. Zum einen eine sehr dünne Zirruswolke verbunden mit einem Hochdruckgebiet, zum anderen eine in-situ und konvektiv geformte Zirruswolke mittlerer Dicke verbunden mit einem Frontsystem. Die Sublimation von Zirruseiskristallen im Flugzeugtriebwerk und die Sublimation von / Deposition auf die Zirruseiskristalle gemischt in der Abgasfahne bewirkt eine Änderung des Wasserdampfmischungsverhältnisses in der Abgasfahne. Diese Änderung ist meist positiv und trägt zu maximal 20% des vom Flugzeug durch Verbrennung konventioneller Treibstoffe emittierten Wasserdampfes bei. Diese Änderung des Wasserdampfmischungsverhältnisses der Abgasfahne führt zu einer Änderung des Temperaturschwellwertes der Bildung von Kondensstreifen und der Kondensstreifeneisbildung, während das Überleben der Eiskristalle in der Vortexphase weitgehend unverändert bleibt. In Gebieten mit hohem Zirruseiswassergehalt reicht diese Änderung der Temperaturschwelle der Kondensstreifenbildung bis zu 2K. Damit verbundene Änderungen der Nukleationsrate von Zirruseiskristallen führen zu Änderungen der Eiskristallanzahlkonzentration von maximal  $10^7 \text{ m}^{-3}$ . Diese Größenordnung ist vergleichbar mit dem Effekt einer Vernachlässigung des Einflusses von Zirruseiskristallen. Obwohl Zirruseiskristalle in den absinkenden Vortices sublimieren und damit die relative Feuchte erhöhen, was eine verringerte Sublimation des Zirruseises bewirkt, führt das schnellere Anwachsen der Eiskristalle in der vorangegangenen Wachstumsphase, oft auf Kosten der Zirruseiskristallbildung, zu kleineren Eiskristallen in Kondensstreifenzirren. Diese beiden Effekte kompensieren sich gegenseitig, so dass die Überlebensrate der Eiskristalle kaum verändert wird.

Die Bildung von Kondensstreifeneiskristallen in Zirruswolken bewirkt eine beträchtliche Störung der Kristallzahlen, was zu einer Erhöhung der Eiskristallanzahlkonzentration von zwei bis vier Größenordnungen führt. Der Eiswassergehalt in der Zirruswolke verändert sich ebenfalls, jedoch sind diese Änderungen geringer als im Fall der Eiskristallanzahlkonzentrationen. Diese Störungen können langlebig sein, so dass Änderungen auch nach sechs Stunden sichtbar sind. Während der Lebensdauer der Störungen verteilen diese sich und beeinflussen große Teile der Zirruswolken in Flughöhe und darunter. Kondensstreifeneisbildung kann die Auflösung von Zirren beschleunigen, da statt weniger großer Zirruseiskristalle, eine große Zahl kleiner Kondensstreifeneiskristalle

entstehen. Die Veränderung der Zirrusseigenschaften bewirkt eine Änderung der optischen Dicker der Zirren. Maximalwerte für Zu- und Abnahme der optischen Dicker der Zirren betragen bis zu 4 in dichten Zirruswolken. Jedoch ist die Wahrscheinlichkeit einer Abnahme der optischen Dicker durch Kondensstreifenbildung in Zirren deutlich geringer als die Wahrscheinlichkeit einer Zunahme. Die Simulationen zeigen deutliche Anzeichen für Anpassungen der Wolkeneigenschaften von Zirren in Windrichtung von Zirruswolken, die direkt durch Kondensstreifenbildung modifiziert wurden. Der Eiswassergehalt, die Eiskristallanzahlkonzentrationen und die optische Dicke jener in Windrichtung gelegener Zirren scheinen verringert zu sein. Dieser Effekt sollte in Zukunft bei der Abschätzung des Klimaeffektes der Kondensstreifenbildung in Zirren berücksichtigt werden.

# Abstract

Cirrus clouds are common in the upper troposphere and contribute to the earth's radiation budget. The radiative forcing caused by cirrus is dependent on their macro-, microphysical and optical properties; therefore, a change in the cirrus properties leads to a change in their radiative impacts. Recently a study showed evidence of changes in cirrus optical depth due to contrail ice formation within cirrus in satellite remote sensing data. So far, no detailed studies are available that can quantify the impact of contrail ice formation within cirrus on cirrus microphysical and optical properties. Therefore, the aim of the presented work is to improve our understanding of contrail formation within cirrus and their impact on cirrus cloudiness.

A high-resolution ICON-LEM (ICOsahedral Non-hydrostatic- Large-Eddy Modelling) in weather forecasting mode at a horizontal resolution of 625 meters is used. In order to study contrail formation within cirrus, a parameterization for contrail formation within cirrus, consisting of contrail ice nucleation and ice crystal loss in the vortex phase, is implemented and modified to include the impact of pre-existing cirrus on contrail ice formation. Two very different synoptic situations and associated cirrus cloud fields are sampled to cover a large range of cirrus properties, which represent a very thin cirrus connected with a high-pressure system and an average thick in-situ formed and liquid origin cirrus connected with a frontal system. The sublimation of cirrus ice crystals in the engine and sublimation of/ deposition on the cirrus ice crystals mixed in the exhaust plume causes a change in the plume's water vapor mixing ratio. This change is mostly positive and contributes maximally 20% of the water vapor emitted from aircraft due to the combustion of conventional fuels. This change in the plume's water vapor mixing ratio leads to a change in the contrail formation threshold temperature and contrail ice nucleation while ice crystal survival within the vortex phase appears to be nearly unchanged. In areas where the cirrus ice water content is large, the change in the contrail formation threshold temperature reaches values of up to 2K, and associated changes in the nucleation rate of contrail ice crystals lead to changes in ice crystal number concentrations of maximally  $10^7 \text{ m}^{-3}$ , the similar order of magnitude that would result from disregarding the impact of cirrus ice crystals. Even though cirrus ice crystals sublimate within the descending vortices and may act to increase relative humidity leading to a decrease in contrail ice sublimation, the preceding growth phase, in which cirrus ice crystals can grow faster, often even at the expense of contrail ice crystals, leads to smaller contrail ice crystals. Both effects together compensate, leaving ice crystal survival rates approximately unchanged.

The formation of contrail ice crystals within cirrus introduces large perturbations in ice crystal numbers, increasing ice number concentrations by 2 to 4 orders of magnitude. The ice water content in the cirrus also changes, but the changes are smaller than for ice crystal number concentrations. Perturbations can be long-lived, with changes discernible even after 6 hours. During their lifetime, perturbations spread and affect large parts of the cirrus clouds at flight level and below. Contrail ice formation can accelerate the dissolution of cirrus due to the replacement of a few large cirrus ice crystals by many small contrail ice crystals. The change in the cirrus properties causes a change in the optical depth of the cirrus. Maximum increase and decrease in cirrus optical depth reach values of 4 in thick cirrus. However, probability of decrease in optical depth is significantly lower than the probability of increase in optical depth due to contrail formation within cirrus. The simulations show clear signs of adjustments of cloud properties of cirrus downwind of cirrus that was directly modified by contrail formation. The ice water content, ice number concentrations, and optical depth of those cirrus further downwind appear to be decreased, which needs to be considered when estimating the climate impact of contrail formation within cirrus in the future.



---

## **Publication**

*Some parts of Chapter 3 and complete Chapter 4 are published in the below article.*

Verma, P. and Burkhardt, U.: Contrail formation within cirrus: high-resolution simulations using ICON-LEM, Atmos. Chem. Phys. Discuss. [preprint], URL: <https://doi.org/10.5194/acp-2021-497>, in review, 2021

---



# *Table of contents*

<b>1</b>	<b>Introduction .....</b>	<b>1</b>
1.1	Motivation.....	1
1.2	Objective.....	5
1.3	Thesis structure.....	5
<b>2</b>	<b>Ice cloud physics and aviation induced perturbations .....</b>	<b>7</b>
2.1	Ice supersaturation .....	7
2.2	Ice crystal nucleation .....	9
2.2.1	Homogeneous nucleation .....	10
2.2.2	Heterogeneous nucleation .....	10
2.3	Cirrus clouds properties .....	11
2.4	Contrail physics .....	14
2.4.1	Aircraft engine emission and aerosol particles in the exhaust plume.....	14
2.4.2	Aircraft wake evolution.....	16
2.5	Contrail observation.....	18
2.5.1	In-situ observation .....	18
2.5.2	Remote sensing observation .....	20
2.6	Simulations of contrails at different resolutions .....	23
2.6.1	Large-eddy Simulations.....	23
2.6.2	Global climate model simulation.....	24
2.6.3	Contrails in NWP model .....	25
2.7	Summary.....	25
<b>3</b>	<b>Simulating contrails within ICON-LEM and definition of case studies.....</b>	<b>27</b>
3.1	ICOsahedral Non-hydrostatic model (ICON-LEM): .....	28
3.1.1	Two moment cloud microphysics.....	28
3.1.2	Tracer advection .....	30
3.2	Contrail formation parameterization for ICON-LEM.....	31
3.2.1	Contrail ice crystal nucleation .....	32
3.2.2	Parameterization for the ice crystal loss during vortex descent .....	42
3.3	Data.....	46
3.3.1	Initial and boundary data .....	46
3.3.2	Flight inventory .....	46
3.4	Model setup .....	48
3.5	Synoptic conditions for the case studies .....	48
3.6	Cloud frequency altitude diagram for control experiments .....	50
3.7	Apparent ice emission index of contrail ice crystal .....	51
3.8	Diffusional growth equation to calculate sublimation and deposition rate of an ice crystal 52	
3.9	Optical depth calculation of the contrail perturbed cirrus .....	53

<b>4</b>	<b>Impact of the background cirrus on contrail formation.....</b>	<b>57</b>
4.1	Effect of pre-existing cirrus ice crystals on contrail ice nucleation .....	58
4.1.1	Effect of pre-existing cirrus on contrail formation threshold temperature.....	58
4.1.2	Effect of pre-existing cirrus on number of nucleated contrail ice crystals.....	60
4.2	Impact of pre-existing cirrus on contrail ice crystals loss during vortex descent.....	67
4.2.1	Far away from contrail formation threshold condition .....	68
4.2.2	Close to contrail formation threshold condition.....	72
4.3	Impact of contrail formation on ice crystal number concentrations.....	75
4.4	Conclusion.....	76
<b>5</b>	<b>Impact of contrail formation within pre-existing cirrus on cirrus properties....</b>	<b>79</b>
5.1	Perturbation of cirrus cloud properties .....	79
5.2	Spatial distribution of the cirrus and its contrail induced perturbations.....	83
5.2.1	24 <sup>th</sup> April 2013 case .....	83
5.2.2	26 <sup>th</sup> April 2013 case .....	85
5.3	Vertical distribution of the cirrus and its contrail induced perturbations .....	88
5.3.1	24 <sup>th</sup> April 2013 case .....	88
5.3.2	26 <sup>th</sup> April 2013 case .....	91
5.3.3	Change in ice water content .....	94
5.4	Optical depth of the contrail perturbed cirrus .....	96
5.4.1	Optical depth of the contrail perturbed cirrus along with the vertical cut.....	96
5.4.2	Optical depth of the whole cloud .....	99
5.4.3	Horizontal variability of the optical depth in the contrail modified cirrus.....	101
5.5	Life cycle of the contrail induced cirrus perturbation and impact on the ice number concentration and ice crystal sizes .....	107
5.5.1	Ice crystal number size distributions in contrail perturbed cirrus .....	108
5.5.2	Comparison with the observation.....	109
5.6	Conclusion.....	111
<b>6</b>	<b>Conclusion and outlook.....</b>	<b>113</b>
6.1	Conclusion.....	113
6.2	Outlook.....	117
	<b>List of Figures.....</b>	<b>119</b>
	<b>List of Tables .....</b>	<b>125</b>
	<b>References.....</b>	<b>127</b>

# Chapter 1

## Introduction

### 1.1 Motivation

Aviation modifies the upper tropospheric cloudiness and aerosol concentration, specifically in heavy air traffic routes in mid-latitudes. The aircraft exhaust emission consists of CO<sub>2</sub>, aerosols, water vapor, nitrogen oxides, and other gases that change the atmosphere's chemical composition and cloudiness, specifically at main air traffic altitudes. Those changes influence the earth's radiative budget. The aviation-induced perturbation in the upper troposphere and lower stratosphere contributes around 3.5%-5% of the anthropogenic radiative forcing (Lee et al., 2021). Contrail cirrus is the largest known contributor among all radiative forcing components associated with air traffic (Lee et al., 2021), even larger than the climate forcing contribution from accumulated CO<sub>2</sub> induced by aviation (Burkhardt and Kärcher, 2011). However, in the assessments of aviation-related climate change (Lee et al., 2021), contrail cirrus, and particularly the indirect aerosol effects involving aviation aerosol emissions, are the most difficult to estimate and thus very uncertain (e.g., Righi et al., 2013, Kapadia et al., 2016, Lee et al., 2021). The study published by ICAO (2013) has shown that the annual increase in air passenger kilometer by 5% till the year 2030 can lead to a rise in the aircraft emitted CO<sub>2</sub> by a factor of 3 to 4 from the year 2010 to 2040. An increase in aviation emissions by a factor of 4 is expected to increase contrail cirrus radiative forcing approximately by a factor of 3 (Bock and Burkhardt, 2019).

Air traffic causes change in cloudiness through different ways, e.g., distrails and hole punch clouds, indirectly through aerosol-cloud interaction, and contrail formation in cloud-free ice supersaturated regions and contrail formation within cirrus. Distrails (dissipation trail) and hole punch clouds cause a decrease in cloud cover and are observed primarily on mid-level supercooled clouds (e.g., altocumulus clouds) (Corfidi and Brandli 1986; Duda and Minnis 2002) when aircraft's takeoff or descend. Therefore, their impact on cloudiness and radiation is expected to be very low, significantly lower than the contrails. Air traffic affects cloudiness indirectly due to aviation aerosol-cloud interaction. The presence of aircraft emitted aerosol particles, mainly soot, sulfate, and organic compounds (Kärcher et al., 2000) in cloud formation regions, influence the cloud properties by affecting the formation of cloud droplets and ice crystals (Lee et al., 2021). The aviation sulfate aerosols are efficient cloud condensation nuclei (CCN) and mainly affect liquid clouds. Whereas, the effect of the aircraft-induced soot particles on background cloudiness is highly uncertain. The uncertainties are caused mainly due to incomplete knowledge about the number and ice nucleating properties of emitted and subsequently aging aviation soot particles (Zhou and Penner 2014; Penner et al., 2018; DeMott et al., 1999; Mohler et al., 2005; Hoose and Möhler 2012).

Furthermore, the formation of contrails in the upper troposphere has a certain importance for the radiative budget as these altitudes often have favorable formation conditions for natural cirrus and therefore, may have an impact on the occurrence of natural cirrus and their micro and macrophysical properties. Contrails form at low ambient temperatures (below -40 °C) when the hot and moist (but subsaturated) exhaust plume mixes with the surrounding cold ambient air, and during the mixing, saturation with respect to liquid water is surpassed within the plume (Schmidt-Appleman criterion,

Schmidt, 1941; Appleman, 1953; Schumann 1996). At contrail formation, water droplets form predominantly on soot particles but also on entrained ambient aerosols and subsequently freeze (Kärcher et al., 2015). Contrails formed in ice supersaturated regions can persist for many hours. They can spread over large areas, and their ice water increases due to deposition on contrail ice crystals. Eventually, they lose their initial linear shape and transform into thin cirrus-like structures (often called contrail cirrus). Contrail cirrus can be difficult to distinguish from thin natural cirrus, although their formation pathway is different. The linear-shaped young contrails and contrail cirrus cause an increase in the upper tropospheric cloudiness (Boucher 1999; Boucher 2013), cause a decrease in the natural cirrus cloudiness, and have shown significant effect on radiation budget (e.g., Burkhardt and Kärcher, 2011; Meerkötter et al. 1999; Myhre et al., 2009; Schumann and Graf, 2013; Bock and Burkhardt, 2016b). Various modeling studies have shown that the line-shaped contrail induced radiative forcing varies between 3.5 to 17  $\text{mWm}^{-2}$  (Minnis et al., 1999; Myrhe and Stordal, 2001; Ponater et al., 2002; Marquart et al., 2003; Fichter et al., 2005; Rap et al., 2010). However, the impact can be larger, between 12 to 111.4  $\text{mWm}^{-2}$  if aged contrails are considered in the estimation (Burkhardt and Kärcher, 2011; Chen et al., 2012; Schumann, 2012; Lee et al., 2020).

Moreover, contrail formation within cirrus can impact the upper tropospheric cloudiness. The formation of contrail ice within cirrus is similar to that in cloud-free air, except that the background cirrus field may have an impact on contrail ice formation. The impact of contrail ice formation within cirrus had been thought negligible and, therefore, have not been considered in the assessment report of Lee et al., 2021. However, a recent study published by Tesche et al., (2016) shows that contrail formation within cirrus can alter the cloud microphysical and optical properties. The increase in optical depth of the natural cirrus has been observed from Cloud-Aerosol Lidar and Infrared Pathfinder Satellite Observations (CALIPSO) 30 minutes after passing the aircraft. The observed optical depth of the cirrus was 22% larger behind the aircraft track compared to the optical depth at the side and front of the aircraft path. Since those contrail-induced cloud modifications have been shown to be detectable in satellite remote sensing data, they may turn out to be a non-negligible component of the climate impact of aviation. Therefore, this thesis work focuses on the contrail formation processes within cirrus and their impact on the microphysical properties.

Contrail formation in ice supersaturated but cloud-free air has been widely studied for many years. Different observation and modeling methods have been used to study contrail formation and its evolution in cloud-free air. Many studies, detecting and tracking contrails in satellite images, have been performed. In the first instance, the detection of contrails was limited to line-shaped contrails (Baken et al., 1994, Joseph et al., 1975, Mannstein et al., 1999). Later, with improved detection techniques, the identification of aged contrails that were tracked over their life cycle became possible (Vázquez-Navarro et al., 2010, Vázquez-Navarro et al., 2015). Contrail properties, e.g., ice crystal number concentration and ice crystal sizes, were probed during different flight campaigns (Schumann et al., 1996, Petzold et al., 1997, Schröder et al., 1999, Febvre et al., 2009, Heymsfield et al., 1998, Voigt et al., 2017, Schumann et al., 2017). Collected in-situ data show that contrail properties are quite different from the natural cirrus in terms of the number and size of ice crystals. Contrail consists of a very high number concentration of very small ice crystals, whereas the properties of natural cirrus depend on their nucleation pathway and background atmospheric variability.

Modeling the life cycle of contrails involves processes on a large range of scales, comprising microphysical processes as well as large-scale dynamics that need to be covered. Large Eddy Simulation (LES) models are a suitable tool for studying contrail formation processes due to their

high resolution and detailed microphysical treatment. The early development of contrails, starting immediately after aircraft emission to the first few minutes or the evolution of the whole contrail life cycle, can be studied in LES (e.g., Lewellen et al., 2014, Unterstrasser, 2014, Paoli and Shariff, 2016). LES is important since Initial evolution in contrail potentially affects the microphysical and optical properties of the evolving contrail-cirrus (Bier et al., 2017; Burkhardt et al., 2018). The obvious drawback of this modeling approach is that LES does not capture the impact of the background atmospheric variability on the evolution of the contrails, and studies are limited to a relatively small set of atmospheric and aircraft parameters due to high computational requirements. Therefore, this method is not suited to simulating a cluster of contrails that may arise from real air traffic movements and their interaction with the background atmosphere and their impact on climate. Global circulation models (GCM) and Numerical Weather Prediction (NWP) models are useful for simulating contrail evolution, which is controlled by the large-scale atmospheric variability, contrail properties, and the climate impact of a large number of contrails in low resolution. To study contrails' life cycle and their radiative forcing, the GCM is extended by a contrail parameterization that simulates line-shaped and aged contrails (Burkhardt and Kärcher, 2011; Bock and Burkhardt, 2016a, 2016b, 2019; Bier et al., 2017; Schumann et al., 2015). However, the contrail schemes in GCMs are significantly simplified relative to LES, with parameterizations of contrail processes based on the large-scale mean atmospheric variables unable to capture cloud-scale dynamics and atmospheric variability. For this reason, an approach using a high-resolution weather forecasting model, such as the one chosen in this thesis, can introduce significant improvements and enable studying contrail processes and the interaction between background atmosphere and contrail in more detail.

Despite having a large number of studies about contrail cirrus, the uncertainty remains significant in the estimation of contrail-induced radiative impact due to uncertainty in data and lack of understanding. Many of those uncertainties will also affect simulations of contrail formation within cirrus clouds, for example, the lack of understanding of the upper tropospheric water budget, including aerosol concentrations and their properties, the importance of different ice nucleation pathways (Hoose and Möhler, 2012), and the frequency of ice supersaturated conditions in the upper troposphere (Lamquin et al., 2012). Consequently, models display a large variability in upper tropospheric cloud and ice supersaturation fields (Waliser et al., 2009; Jiang et al., 2012). The connected uncertainty leads to uncertainty in the estimation of contrail properties. Uncertainty connected with soot number emissions and contrail ice nucleation adds uncertainty in the estimation of contrail properties. Inability to predict the ice crystal habits, habit mix, and their growth evolution in contrails and cirrus, and therefore, the inability to parameterize them properly in the model adds to the uncertainty. The interaction between contrails and natural clouds and generally the upper tropospheric water budget is not well known, and associated estimates of cloud changes due to contrail formation vary widely (Burkhardt and Kärcher, 2011; Schumann et al., 2015, Bickel et al., 2020).

It is known that contrail formation within cirrus can lead to an increase in cloud optical depth (Tesche et al., 2016). Therefore, we hypothesize that this increase in optical depth is caused by an increase in ice crystal numbers and possibly ice water content. The change in the ice crystal size spectrum may cause a change in the microphysical processes, i.e., diffusional growth of the cirrus ice crystals and consequently sedimentation rate, aggregation of ice crystals, and nucleation pathway of natural cirrus ice crystals. The many small ice crystals within a cirrus perturbed by contrail formation will experience slower sedimentation rates and, therefore, cloud top height may remain higher (Rybka et al., 2021) than in the case of cirrus that is not perturbed by contrail

formation. If the contrail does not form at the cloud top then the aggregation rate in the perturbed cirrus may increase since the larger cirrus ice crystals can sediment into the perturbed area reducing ice crystal concentrations. The presence of contrail ice crystals may also affect the nucleation pathway by affecting in-cloud ice supersaturation. The life cycle of contrail perturbed cirrus is unclear since increases in ice crystal number concentrations may affect cirrus differently depending on the atmospheric variability.

So far, there is no detailed study available which quantifies the above-mentioned impacts due to contrail formation within cirrus. This thesis is the first step toward studying contrail formation within cirrus and evaluating the impact on cirrus properties. Continuous air traffic may completely change the natural cirrus properties by forming contrail ice crystals. The effects may not be easily visible in satellite images or maybe only detectable in certain areas since associated changes in optical depth, the primary quantity observed in passive remote sensing, changes only slightly, and making them hard to distinguish from the unperturbed cirrus. Therefore, the motivation of this work is to estimate how far seemingly natural cirrus may be modified by contrail formation within cirrus.

Before studying changes in microphysical processes, we need to study contrail formation within cirrus, including the ice nucleation in the contrail's jet phase and contrail ice crystals loss in the contrail's vortex phase. Both may be modified by the presence of cirrus ice crystals. Gierens (2012) found that when assuming typical cloud properties, the cirrus ice crystals that are sucked into the engine sublimate during combustion cause a slight increase in the water vapor concentration in the exhaust plume. Furthermore, he finds that any deposition of water vapor on cirrus ice crystals that may be mixed into the plume is a negligible effect compared to the large changes in plume relative humidity due to mixing within environmental air. Gierens (2012) concludes that both effects would not cause a change in contrail ice nucleation. Kärcher et al. (1998), on the other hand, study the formation of a contrail at atmospheric conditions that should not have allowed contrail formation. They conclude that the surrounding pre-existing cirrus ice crystals that were mixed into the plume cause a further increase in the water vapor mixing ratio due to sublimation of the cirrus ice crystals so that contrail formation could occur (Kärcher et al., 1998). Furthermore, Gierens (2012) estimates that the contrail ice crystal loss in the contrail's vortex phase is not modified by the presence of cirrus ice crystals when assuming typical cloud properties.

This thesis aims to expand this work considering the impact of the cirrus ice crystals that are mixed into the plume on the evolution of relative humidity and, therefore, on ice nucleation. Furthermore, the growth of contrail and cirrus ice crystals after nucleation is estimated. After that, the impact of the cirrus ice crystals on the evolution of relative humidity within the sinking vortices and, therefore, the contrail ice crystal loss is estimated. Instead of assuming some fixed cloud properties and fixed atmospheric background state, contrail formation has been calculated in a large number of different situations in this work. The effect of the background cirrus on the contrail ice formation will vary for different natural cirrus properties. Therefore, in this thesis work, microphysical properties of two very different synoptic situations from a thin cirrus field in a high-pressure system to medium thick cirrus connected with a frontal system over Germany have been analyzed. A numerical weather prediction (an approach between LES and GCM) model with a resolution of a few hundred meters has been established for this study. The high-resolution model, including a two-moment-cloud microphysical scheme, has been shown to resolve cloud fields and provide a realistic representation of clouds in terms of shape, structure, and distribution of the cloud (Stevens et al., 2020, Heinze et al., 2017). The vast variability of the simulated cloud properties provides a good opportunity to study contrail formation within cirrus.

## 1.2 Objective

The overall aim of this thesis work is to study cirrus perturbations caused by contrail formation within cirrus and to estimate the impact of contrail formation on the optical depth of the cirrus. In order to do that, the first step is to investigate the impact of the background cirrus on contrail formation, which includes studying contrail ice nucleation and the survival of ice crystals when contrails form within cirrus. After that the second step is to understand the life cycle of contrail induced perturbations and their impact on cirrus microphysical and optical properties. To investigate these impacts, this thesis work seeks to answer the following questions divided into the following objectives:

1. Which contrail formation processes are affected due to the presence of background cirrus ice crystals? How large is the impact of background cirrus ice crystals? What kind of background cirrus and ambient properties can impact contrail formation significantly?
2. How large is the perturbation of cirrus due to contrail formation within cirrus? Are cirrus microphysical properties affected, and how large is the impact on the cirrus microphysical properties, e.g. ice number concentration, ice water content, and volume mean radius of ice crystals and optical depth?
3. How long can the impact of contrail formation be seen in the perturbed cirrus microphysical properties?

The answer to these questions can provide the basis for a new generation of climate projection that will more accurately assess the impact of aviation on climate.

## 1.3 Thesis structure

In chapter 2, some background knowledge about natural cirrus clouds and contrails is given. Chapter 2 introduces information about ice supersaturation, the prerequisite for the persistence of cirrus clouds and contrails, and describes different pathways of ice nucleation in cirrus. This chapter also describes important findings from observations and modeling regarding aviation and clouds. To study contrail formation within cirrus, the parameterization for contrail ice nucleation (Kärcher et al., 2015) and ice crystals loss in the vortex phase (Unterstrasser 2016) need to be extended in the model. Therefore, chapter 3 provides firstly general descriptions of ICON-LEM (ICOsahedral Non-hydrostatic- Large-Eddy Modelling) and the two-moment cloud microphysical scheme of the model, including important processes. After that, contrail scheme including contrail ice nucleation (Kärcher et al., 2015) (section 3.2.1) and survival fraction of ice crystals in vortex phase (Unterstrasser 2016) (section 3.2.2) are described.

The initial and boundary data including flight inventory used for simulations, are given in section 3.3. The waypoint data of AEDT (Aviation Environmental Design Tool) flight inventory (Wilkerson et al., 2010) were interpolated to icosahedral grid box; are described in section 3.3. To simulate contrails within natural cirrus, the model domain with 625 meters horizontal resolution has been set up over Germany (section 3.4). The two different synoptic conditions and associated cirrus cloud properties (Heinze et al., 2017) that have been used in this thesis work are explained in section 3.5 and cloud properties connected with above synoptic conditions, i.e., ice number concentration, ice water content, and volume mean diameter are described in section 3.6. The diffusional growth equation to calculate deposition and sublimation of the ice crystals used during

different processes is described in section 3.8. In order to calculate the change in optical depth, the importance of size distribution and ice crystal habits are shown in section 3.9.

Chapter 4 contains the results for objective one of this thesis regarding the impact of pre-existing cirrus on the contrail formation processes. In the first part, the change in contrail ice nucleation consisting of a change in contrail formation threshold temperature (section 4.1.1) and the change in the number of nucleated ice crystals (section 4.1.2) depending on the cirrus cloud properties are explained. After that, in the second part of this chapter, the change in survival of the contrail ice crystals due to the presence of cirrus ice crystals in the plume is explained (section 4.2).

Chapter 5 explains the effect of contrail formation within cirrus on cirrus properties. The first section discusses the effect of air traffic on cirrus properties (section 5.1). After that, the horizontal and vertical variability of the cirrus after contrail formation is shown to understand how large the perturbation of cirrus is (sections 5.2 and 5.3). Changes in the microphysical properties of cirrus may lead to a change in the optical depth; therefore, the optical depth of the cloud, after a contrail-induced perturbation, has been estimated in section 5.4. The above mentioned all four sections in this chapter all together discuss the objective two of this thesis regarding ‘how large is the perturbation of cirrus due to contrail formation within cirrus and how large is the impact of contrail ice formation on the cirrus microphysical properties?’. The last section of this chapter addresses the third objective of this thesis regarding how long can the impact of contrail formation be seen in the cirrus microphysical properties. For that, the life cycle of the cirrus perturbation due to 10 minutes of air traffic is discussed (section 5.5). Chapter 6 comprises the conclusion of this thesis and important findings with future outlooks regarding this work.

## Chapter 2

# Ice cloud physics and aviation induced perturbations

Aviation leads to the formation of thermodynamic jet engine exhaust contrails (Schumann, 1996; Kärcher et al., 1996) and aerodynamic contrails (Gierens et al., 2009; Kärcher et al., 2009). While the impact of aerodynamic contrails is thought to be very low, thermodynamic contrails significantly impact the upper tropospheric cloudiness. Therefore, this thesis uses the term ‘contrails’ for thermodynamic contrails. Contrails form exclusively in the upper troposphere in the pure ice cloud regime at temperatures below  $-40^{\circ}\text{C}$ . In order to understand the impact of aviation on natural clouds, it is necessary to comprehend contrail and cirrus clouds and the processes that lead to aviation-induced modifications in cirrus clouds.

Initially, ice supersaturation and its frequency of occurrence is explained (section 2.1) because ice supersaturation is a prerequisite for both formations of natural cirrus as well as for persistence of natural cirrus and contrails. Since this thesis aims to study cirrus modifications that are induced by contrail formation within cirrus, therefore, first the nucleation of cirrus ice crystals via two main nucleation pathways, homogeneous and heterogeneous is explained in section 2.2. The processes and properties of natural cirrus dependent on their nucleation pathway are then discussed in section 2.3. After that, contrail physics, including the different regimes in contrail during their life cycle, are explained (section 2.3). The current research observing and simulating contrails is described in sections 2.4 and section 2.5, respectively.

### 2.1 Ice supersaturation

Ice supersaturation is an important atmospheric condition for the formation of cirrus clouds and the persistence of cirrus and contrail ice crystals (Burkhardt and Kärcher, 2011; Gierens, 2012; Lamquin et al., 2012). Therefore, it is essential to understand ice supersaturation conditions and their probability of occurrence in high altitudes. Ice supersaturated (or water supersaturated) regions are formed when water vapor exceeds its saturation vapor pressure value. Saturation vapor pressure is the thermodynamic equilibrium state between water vapor and liquid water (also called saturation vapor pressure with respect to water or water saturation pressure) or between water vapor and ice (also called saturation vapor pressure with respect to ice or ice saturation pressure) (Pruppacher and Klett, 1996). The saturation vapor pressure over water (ice) increases nonlinearly with increasing temperature (Clausius-Clapeyron equation). However, atmosphere is not always in thermodynamic equilibrium state, the concentration of the water vapor can exceed from their saturation vapor pressure and that is called supersaturation with respect to ice (water). Often, it is seen that upper tropospheric air is supersaturated with respect to ice and subsaturated with respect to water because the saturation vapor pressure over ice is smaller than the saturation vapor pressure over water. The ice saturation ratio can define as:

$$S = \frac{P_{H_2O}}{P^*_{H_2O}}$$

Where  $P_{\text{H}_2\text{O}}$  is the partial vapor pressure of water vapor with respect to ice and the  $P_{\text{H}_2\text{O}}^*$  is the saturation vapor pressure. The ice supersaturation 's' is defined as  $(S-1)$ . The upper tropospheric air can stay ice supersaturated for a long period of time in the absence of ice crystals or ice nuclei; otherwise, processes, i.e. ice nucleation in the presence of suitable ice nuclei and deposition of available water vapor on already existing ice crystals, take place to bring back the air to the equilibrium state of saturation. However, nucleation of ice crystals is a complicated process that does not start immediately once saturation with respect to ice surpasses because nucleation of ice crystals needs significantly high ice supersaturation depending on the nucleation pathway. For example, heterogeneous ice nucleation requires suitable ice nuclei and ice supersaturation that may be as low as 1.2 or even below 1.5 depending on the ice nucleation efficiency of the aerosol (Hoose and Möhler, 2012). Homogeneous freezing of aqueous solution requires ice supersaturation of around 1.5 (Koop et al., 2000). Therefore, the ice supersaturation condition is called a metastable state in contrast to the unstable state. In an unstable state, processes, e.g. condensation, evaporation and sublimation, start immediately to revert back to the equilibrium state (Koop, 2004). For example, supersaturation with respect to water is an unstable state because the condensation on suitable condensation nuclei begins almost immediately at water saturation and forms a water cloud because a sufficiently large number of condensation nuclei (a certain fraction of aerosols) are available in the atmosphere providing a surface for water molecules to condense on and form water droplets. In-cloud subsaturation, where the partial vapor pressure is smaller than the saturation vapor pressure, it is also unstable because this state induces the evaporation of water droplets or sublimation of ice crystals immediately.

Large scale ice supersaturated regions often form when water vapor is carried to upper altitudes through a large-scale rising motion of the air and the accompanying adiabatic cooling; this increases the saturation ratio with respect to ice (Gierens and Brinkop, 2012). Ice supersaturated regions can form in cloud-free air as well as within cirrus clouds. High ice supersaturation, below the homogeneous freezing threshold, can exist in the cirrus if the ice crystal's number concentration is low. Ice supersaturation within cirrus decreases with an increase in the product of the number concentration of the ice crystals and radius of the ice crystal (Korolev and Mazin, 2003). The cirrus with low ice number concentration consumes available water vapor slowly. Therefore, high ice supersaturation can exist for an extended period of time, specifically in cold cirrus below a temperature of 205 K, since at this temperature, diffusion of water vapor is relatively slow (Krämer et al., 2009). The possible reason for a low number of ice crystals in the cirrus cloud could be due to (a) heterogeneous nucleation in the presence of few ice nuclei or (b) homogeneous nucleation of ice crystals connected with very low updraft speeds (Krämer et al., 2009).

The regular in-situ measurement of water vapor started in late 1990 in Europe under the MOZAIC program (Measurement of Ozone and Water Vapor by Airbus In-Service Aircraft), in which atmospheric water vapor was regularly measured from research quality hygrometers installed on commercial aircraft. The MOZAIC database showed that ice supersaturated regions often occur in the upper troposphere and lower stratosphere (Gierens et al., 1999, 2000). Ice supersaturated regions were observed in different ways, including Radiosonde, airborne measurement campaign and satellite data, showing the existence of ice supersaturated regions. The global distribution of ice supersaturated regions can be obtained from satellite data. Lamquin et al. (2012) (see figure 2.1) provided a complete picture of the distribution of the ice supersaturated regions globally and in the vertical dimension. For the analysis, the water vapor has been observed from the Atmospheric Infrared sounder (AIRS) on the NASA AQUA satellite and calibrated using MOZAIC data. The measurements reveal that a high frequency of ice supersaturated regions occurs in the tropics at

around 150 hPa pressure level within the tropical tropopause layer (TTL). Ice supersaturation occurs at lower altitudes (increase in pressure) in the extratropics. Ice supersaturation frequency is most significant in the upper troposphere and decreases strongly in the stratosphere. Since the tropopause slopes downwards when moving towards the poles, high frequencies of ice supersaturation above 200 hPa are confined to the tropics. Ice supersaturated regions in the atmospheric pressure layer between 200 hPa to 250 hPa are found along the storm tracks in the mid-latitudes, and below 250 hPa, ice supersaturated regions are located in the polar regions.

Water is transported into the upper troposphere mainly through high reaching convective events in the tropics. Gravity waves connected with convection and the slowly rising air in the TTL are responsible for the formation of ice supersaturated regions in high altitudes. In the extratropics, water vapor reaches the upper troposphere often through vertical transport connected with the synoptic-scale baroclinic instability where optically thick natural cirrus are often observed (Carlson, 1991). These ice supersaturated regions are suitable for persistent contrails. Contrail outbreaks (a large field of persistent contrails) are often seen in these regions when air-traffic density is high (Carleton et al., 2008; Schumann, 2005, Bier et al., 2017).

Ice supersaturated regions are found along the storm track zones where extratropical cyclones form in mid-latitudes. Also, ice-saturated regions are formed in anti-cyclonic flow patterns where hot and warm air from the south is lifted upward by the cold and dry air of the north. The vertical thickness of ice supersaturated layers is on average shallower than 500 meters, but in a very rare situation, the ice supersaturated layers can be thicker, up to 3000 meters (Dickson et al., 2010). The horizontal extension of the ice supersaturated region is difficult to estimate. However, Gierens and Spichtinger (2000) estimated the mean path length of the ice supersaturated layer to be 150 km long with a standard deviation of 250 km.

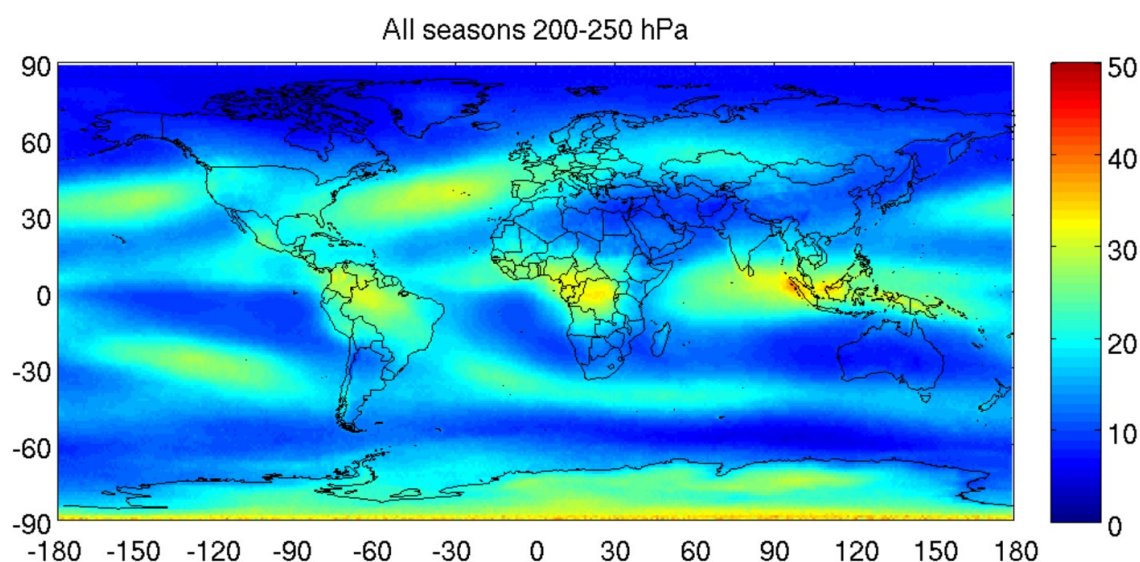


Figure 2.1: Frequency of occurrence of ice supersaturation globally for pressure layer 200 to 250 hPa. This shows statistics of 7 years' data from the years 2003 to 2009 taken from Atmospheric Infrared sounder (AIRS). Source: (Lamquin et al., 2012)

## 2.2 Ice crystal nucleation

Before discussing cirrus cloud properties, it is essential to know the nucleation pathway of the ice crystal in the cirrus because cirrus characteristics are dependent on this pathway. High altitude

clouds at a temperature below  $-38\text{ }^{\circ}\text{C}$  are completely composed of ice crystals and formed via two primary nucleation pathways, homogeneous and heterogeneous nucleation. The homogeneous and heterogeneous ice nucleation processes are described below; following this, diffusional growth of ice crystals is explained.

### 2.2.1 Homogeneous nucleation

The homogeneous nucleation process is an ice formation mechanism in in-situ formed cirrus. In this nucleation process, the ice crystals form predominantly due to the freezing of supercooled liquid aerosols at a temperature below  $-38\text{ }^{\circ}\text{C}$  in highly ice supersaturated air ( $>150\%$ ) (Koop et al., 2000; Koop, 2004). A small liquid droplet of micrometer size can remain supercooled at temperatures up to  $-38\text{ }^{\circ}\text{C}$  and below that temperature, homogeneous freezing of the liquid droplets occurs (Heymsfield and Sabin, 1989). The exact temperature at which spontaneous freezing of the liquid droplets occurs depends on the size of the droplet, purity of the water and other factors (Koop, 2004). In the upper troposphere, the number concentration of suitable ice nuclei is small but sufficient liquid aerosols are available; therefore, liquid aerosols significantly affect the cirrus ice formation process. The most common chemical (solute) present in aqueous solutions is sulfuric acid ( $\text{H}_2\text{SO}_4$ ), although organic species are also mixed in these aqueous solutions. Due to the hygroscopic properties of these liquid aerosol particles, aerosol particles absorb water vapor; with the increase in relative humidity, the adsorption of the water vapor molecules increases. Therefore, the size of the solution droplets increases and weakens the solution effect, which is necessary for freezing. Therefore, high ice supersaturation is required for the freezing of the aqueous solutions. The critical supersaturation threshold for ice nucleation depends on temperature and water activity needed for the homogeneous freezing of aqueous solutions, as derived by Koop et al. (2000). It has been measured that homogeneous freezing of fully liquid aqueous solution droplets formed from a wide range of solutes occurs below temperatures of  $-40\text{ }^{\circ}\text{C}$  and that the exact freezing temperature depends on the radius of the solution droplet (Koop, 2004). The freezing rate of droplets increases with the increasing droplet volume.

### 2.2.2 Heterogeneous nucleation

Heterogeneous ice nucleation can occur at much warmer temperatures than homogeneous nucleation. The ice crystals form in the presence of the ice nuclei (IN); this provides a solid surface upon which the nucleation process starts and reduces the energy barrier to transform from the liquid phase to solid phase. In the presence of IN, heterogeneous nucleation can occur at lower ice supersaturation than the ice supersaturation required for homogeneous freezing of liquid aerosols. Heterogeneous ice nucleation is dependent on the atmospheric temperature and different pathways of heterogeneous nucleation. The supercooled liquid droplets don't freeze quickly; therefore, in the mixed-phase temperature regime, the presence of IN is necessary to convert water droplets to ice ('glaciation'). The number concentration of the suitable IN from the available aerosols in the upper troposphere is very low, between  $0.01$  and  $100\text{ dm}^{-3}$  (Hoose et al., 2010); therefore, the number of heterogeneously nucleated ice is smaller than the number of ice crystals that usually form through the homogeneous nucleation process when connected with a fast updraft speed. The main characteristics of the suitable ice nuclei are that they are highly water-insoluble, have a size larger than  $0.1\text{ }\mu\text{m}$  and have a lattice structure like crystalline ice, allowing the water molecules to attach and cluster into an ice-like molecular arrangement (Pruppacher and Klett, 1996). Dust, organic substance and volcanic ash can be suitable IN and are commonly available in the atmosphere. The

activation of these INs and related heterogeneous nucleation events is strongly dependent on temperature and ice supersaturation.

There are four types of heterogeneous nucleation modes i.e. - deposition, immersion, condensation and contact freezing (Hoose and Möhler, 2012). A schematic diagram for different nucleation modes is shown in figure 2.2. In deposition freezing, water vapor deposits onto the suitable IN surface and forms the crystalline structure. In immersion freezing, nucleation starts from the nuclei that reside in the droplets and freeze the droplet. Condensation freezing occurs when water vapor condenses on the nucleus and subsequently freezes. Contact freezing involves the collision of the IN and water droplets. Nucleation starts when IN and water droplets come into contact in this freezing mode due to the collision. This nucleation mode is efficiently active in the presence of the cloud droplets, e.g. mixed-phase clouds, because cloud droplets have a large contact area for contact freezing compared to liquid aerosols. Immersion freezing is the most efficient freezing mode in cirrus clouds, although immersion freezing and condensation freezing modes are difficult to distinguish in measurements (Gierens, 2003; Kärcher and Lohmann, 2003). Activation of these different heterogeneous nucleation modes depends on the set of ice supersaturation and temperature, even if IN type remains the same.

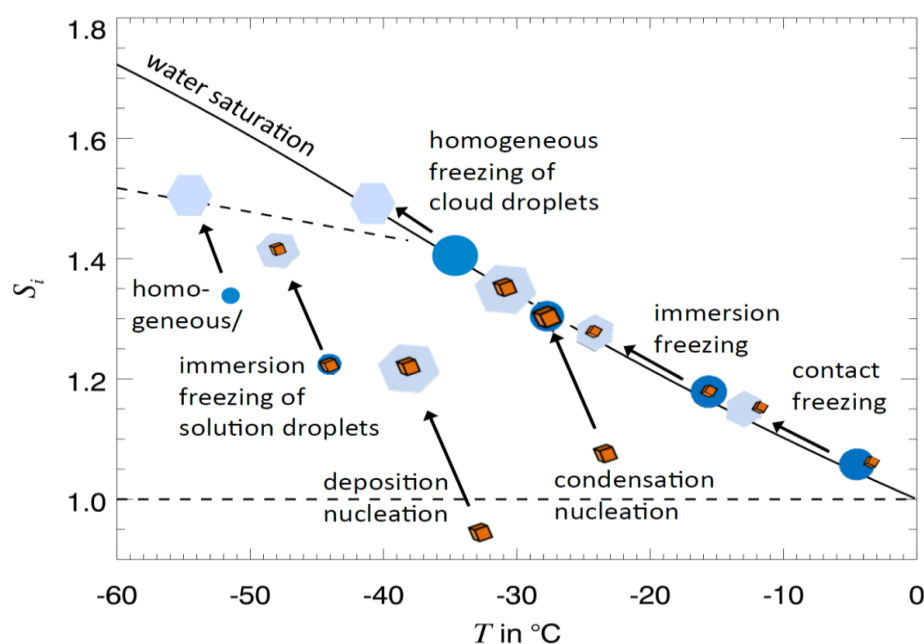


Figure 2.2: Schematic diagram for different ice nucleation modes. Source: (Hoose and Möhler 2012)

## 2.3 Cirrus clouds properties

Cirrus clouds are entirely composed of ice crystals in the upper troposphere at a temperature below  $-38^{\circ}\text{C}$ , where contrail cirrus also exist. Cirrus clouds are visible as white fibrous structures at high altitudes ( $\sim 10$  km).

Cirrus clouds are widespread globally; they contribute to atmospheric dynamics, thermodynamics and influence the radiation budget (Gu and Liou, 2000). The occurrence of the cirrus has been estimated around 16.7% through global satellite observation using data from the multispectral High-Resolution Infrared Radiation Sounder (HIRS) (Sassen et al., 2008). However, estimates of cirrus cover are very much dependent on the sensitivities of applied measurement techniques. Some

instruments can detect only optically thick clouds while others can also detect much thinner clouds. The highest occurrence of cirrus clouds is found in the tropics due to the existence of anvil and sub-visible cirrus. In the mid-latitudes, cirrus clouds form through the substantial uplift of air which carries water vapor to the upper troposphere in specific synoptic conditions, e.g. storm track areas and associated frontal systems. Low-pressure systems form ice supersaturated regions in high altitudes and nucleate ice crystals, predominately by the homogeneous nucleation process, (Sassen and Campbell, 2001) in high ice supersaturation conditions ( $>1.5$ ) (DeMott et al., 2003; Koop, 2004). However, one study indicates that heterogeneous nucleation may be the dominating nucleation process in the cirrus cloud (Cziczo et al., 2013). Apart from that, wave cirrus forms via the orography effect due to local uplifting of air following the terrain at a mountain and due to gravity waves caused by the flow over orography (Field et al., 2001). Finally, the aviation-induced contrail cirrus is an anthropogenic cirrus cloud that forms in the upper troposphere due to aircraft emissions, mainly water vapor and soot particles emission (Schumann, 2002).

The optical properties of cirrus cloud vary widely and depend on the dynamical origin. For example, cirrus clouds that are connected the convective and frontal systems, e.g. anvil cirrus and frontal system originated cirrus, are optically thick, while some in-situ cirrus is optically very thin with low ice water content. Cirrus with optical depths below 0.02 is not visible to the human eye. These optically thin cirrus are called sub-visible cirrus and are easily detectable from lidar measurement (Immler and Schrems, 2002; Sassen et al., 2008) but not from passive remote sensing instruments.

The cirrus cloud and its microphysical and optical properties can be classified based on their formation mechanism. Krämer et al. (2016) and (2020) analyzed the observational data taken from 150 flights from 24 campaigns and classified the cirrus and their microphysical properties based on their formation mechanism. Cirrus types and their formation mechanisms depend on the atmospheric temperature and updraft speed. The cirrus of different origins can be differentiated by the ice water content, number and size of ice crystals in the cirrus. Cirrus clouds are classified into two groups; the first is in-situ origin cirrus and the second is liquid origin cirrus. These two groups are further divided into two subgroups based on slow and fast updraft speed. The in-situ origin cirrus is usually optically thin and has low to medium ice water content and number concentration; it can have high number concentration when the updraft speed is high. In-situ origin cirrus consists of ice crystals that are formed directly from the gas phase via homogeneous and heterogeneous nucleation at a temperature below  $-38$  °C. The sizes of the ice crystals are initially small. In-situ origin cirrus is connected with slow updraft speed ( $>10$  cm $s^{-1}$ ) in large-scale synoptic systems e.g. low-pressure systems where the air is ascending slowly form long-lived thin cirrus with large coverage areas. The cirrus formed in slow updraft has low ice water content and few large ice crystals (table 2.1). Ice formation can start in the presence of efficient ice nuclei with a heterogeneous nucleation event that can be followed up by a second nucleation event through homogeneous freezing. With rising motion and decreasing temperature, ice supersaturation increases and firstly reaches the heterogeneous nucleation threshold, forming ice crystals in the presence of suitable ice nuclei. At this point, cirrus appears with low ice crystal number and low ice water content. The formed ice crystals grow by uptake of available water vapor, thus reducing the ice supersaturation. Ice supersaturation may not reach the homogeneous nucleation threshold at all if many ice crystals are formed from heterogeneous nucleation and reduce the ice supersaturation. In the absence of a sufficiently large number of ice crystals and any further ice nuclei (e.g. low number of ice crystals formed from heterogeneous nucleation or reduction in the number of ice crystals due to sedimentation), ice supersaturation may pass the homogeneous formation threshold and a second nucleation event starts. The second nucleation event in slow

updraft speed is controlled by the increase in the ice saturation ratio, which also depends on the cirrus ice crystal number concentration.

In-situ origin cirrus connected with fast updraft speed, e.g. in gravity waves and close to orography, are thick and have high ice crystal numbers (Krämer et al., 2020). In principle, they are often short-lived (less than an hour) and occur on a small scale. They can be seen for a longer period of time if they form continuously in the standing wave e.g. mountain wave cirrus. These cirrus clouds are dominated by homogeneous nucleation because ice supersaturation quickly reaches the homogeneous nucleation threshold and forms many ice crystals via homogeneous freezing. The number of nucleated ice crystals increases with the increase in updraft speed. Although ice water content is high in these clouds, the size of the ice crystals remains small since available water vapor is distributed equally on many ice crystals.

Liquid origin cirrus is formed mainly via heterogeneous freezing of liquid droplets in the mixed-phase regime at temperatures higher than  $-38\text{ }^{\circ}\text{C}$  that are subsequently lifted to higher altitudes. Additionally, ice crystals may form via homogeneous freezing of liquid droplets at temperatures below  $-38\text{ }^{\circ}\text{C}$  if supercooled liquid droplets are lifted to the low-temperature atmospheric layer. Liquid-origin cirrus usually has high ice water content and a high number concentration of large ice crystals (Krämer et al., 2020; table 2.1). The high ice water content in liquid-origin cirrus is because of their formation through the freezing of water droplets. The in-situ nucleation mechanism cannot directly produce a similarly high ice water content from the gas phase. The high number concentration of ice crystals is mainly because of the freezing of a large number of liquid droplets. However, a high ice crystal number can also be produced from the secondary nucleation event in the presence of pre-existing cirrus, but only if the ice number concentration is not too high and updraft speed is fast enough. The second nucleation event is more likely to be homogeneous nucleation since all the ice nuclei are already consumed. The liquid-origin cirrus often forms in convective systems and warm conveyor belts. The cirrus connected with a convective system is known as anvil cirrus. Anvil cirrus is the outflow of an updraft in a deep convective system. In the main convective system, firstly, water droplets form and subsequently freeze into ice either via homogeneous freezing of water droplets in the cold temperature around  $-40\text{ }^{\circ}\text{C}$  or via heterogeneous freezing when coming into contact with ice crystals or ice nuclei (IN) at a temperature above  $-40\text{ }^{\circ}\text{C}$ . Anvil cirrus stays for an extended period of time in the upper troposphere (sometimes for a day) (Luo and Rossow, 2004).

The in-situ origin cirrus, which forms at low updraft speeds, is optically thin; this produces, on average, a warming effect (Krämer et al., 2020). The associated cirrus optical depth ranges typically between 0.001 to 0.05, with the depth of the in-situ cirrus that forms at fast updraft speed at a range between 0.05 to 1. The liquid origin cirrus is often optically thick and has large ice water content and a high number concentration of large size ice crystals. The optical thickness of liquid origin clouds is in the range 1 to 12, therefore, having a cooling effect (Krämer et al., 2020). Observed ice water contents, number concentrations of ice crystal, and mean diameters of the ice crystals for different cirrus types are summarized in Krämer et al. (2020) (see table 2.1).

**Table 2.1: Observed cirrus cloud properties for different cirrus types (Krämer et al., 2020)**

<b>Cirrus origin</b>	<b>Cloud altitudes (km)</b>	<b>Ice crystal number concentration (m<sup>-3</sup>)</b>	<b>Ice water content (gm<sup>-3</sup>)</b>	<b>Mean radius (μm)</b>
<b>In-situ (slow)</b>	10-12	10 <sup>3</sup> – 2x10 <sup>4</sup>	10 <sup>-5</sup> – 5x10 <sup>-4</sup>	15-25
<b>In-situ (fast)</b>	9-12	10 <sup>5</sup> – 5x10 <sup>6</sup>	10 <sup>-4</sup> – 7.5x10 <sup>-3</sup>	5-15
<b>Liquid</b>	7-10	5x10 <sup>5</sup> – 2x10 <sup>6</sup>	0.03 – 0.375	50-70

The optical depth of the cloud determines its effect on the radiative budget. The cloud's optical depth depends on the mean effective radius of the ice crystals and ice water content over the cloud depth (ice water path IWP). A detailed explanation for calculating optical depth and their dependency on assuming different ice habits and particle size distribution is given in chapter 3, section 3.9. The smaller effective radius reflects shortwave radiation to a greater degree compared to the large effective radius for the same ice water content, meaning that the cloud's albedo increases with decreasing effective radius and, as a consequence, there is a warming effect and cooling at the earth's surface (Zhang et al., 1999). For example, young contrails have a high number concentration of small ice crystals, making them different from natural cirrus (Bock and Burkhardt, 2016a, b; Schumann et al., 2015; Voigt et al., 2015), and therefore contrail ice crystals can reflect more shortwave radiation than cirrus ice crystals for the same ice water content.

## 2.4 Contrail physics

Persistent contrails are formed in the upper troposphere where most of the natural cirrus clouds are formed; therefore, contrail formation introduces modification in the upper tropospheric cloudiness and natural cirrus occurrence (Burkhardt and Kärcher, 2011). In these upper tropospheric altitudes, the temperature is usually very cold, below -40 °C; therefore, a small amount of water vapor is sufficient to provide ice supersaturation in those altitudes. Contrail ice crystals can persist where the air is slightly supersaturated with respect to ice and grow further in size, quickly reducing the ice supersaturation. However, cirrus ice nucleation needs a very high supersaturation with respect to ice (section 2.2). It has been observed that persistent contrails have occurred in those areas where moist air masses are vertically advected to the high altitudes through convection, Rossby waves and frontal system (Bier et al., 2017).

In the following, the role of the aircraft engine emitted aerosol particles on the formation of contrail ice crystals is explained; the different regimes in the contrail life cycle are then discussed.

### 2.4.1 Aircraft engine emission and aerosol particles in the exhaust plume

Aircraft jet fuel mainly consists of hydrocarbon and during combustion, produces different aerosol particles, gases and water vapor. The exhaust plume volume consists of 91.5% natural air components, namely nitrogen (75.2%) and oxygen (16.2%); the rest is made up of 72% carbon dioxide, 27.6% water vapor and 0.4% pollutants depending on fuel and engine properties (IPCC, 1999). The emitted pollutants mainly consist of nitrogen oxide 84%, carbon monoxide 12% and a very small amount of sulfur dioxide. Additionally, soot and ultrafine volatile particles are emitted due to the fuel burn. The ultrafine volatile particles are of nano-meter size and form from the gas phase in the plume before relative humidity with respect to water is reached within the

plume (Kärcher, 1998a). The nonvolatile particles are those that leave residuals when heated at a temperature around 500K. On the other hand, volatile particles evaporate when heated at such a high temperature (Kärcher et al., 2015).

Much observational data has been collected to explain the formation of contrail ice crystals and the role of exhaust aerosol particles in the formation of ice crystals in a contrail. This data has shown that exhaust soot particles are involved in the formation of ice crystals in contrails (Petzold et al., 1998; Schröder et al., 1999). Different sources show that soot particles are not efficient heterogeneous ice nuclei at colder temperatures e.g. upper troposphere temperature (Kärcher et al., 2007; Bond et al., 2013). Therefore, to form ice in contrail, soot particles should first activate into water droplets and subsequently homogeneously freeze and form ice particles. Laboratory measurements have shown that an increase in sulfur content in the fuel increases the hygroscopic properties of the aircraft emitted soot particles, meaning that aircraft soot particles may easily wet depending on the fuel composition (Popovicheva et al., 2004; Petzold et al., 2005; Koehler et al., 2009).

The number of exhaust soot particles plays a crucial role in the formation of ice crystals in contrail in the distinct regimes (soot-rich and soot-poor) of these emitted particles (Kärcher and Yu, 2009; Wong et al., 2013). The soot-rich regime is defined by the soot particle number emission indices (EIs) larger than  $\sim 1.0 \times 10^{14} \text{ (kg-fuel)}^{-1}$ . Ice particles nucleate mainly on the soot particles in the soot-rich regime; the number of nucleating ice crystals in contrail increases with an increasing soot particle number emission index. In the case of soot particle number emission indices ranging between EIs  $\sim 10^{13} - 10^{14} \text{ (kg-fuel)}^{-1}$  (transition regime), the number of nucleated ice crystals in a contrail is significantly affected by the entrained ambient aerosols. In the case of a soot-poor regime, where soot particle number emission indices are below EIs  $\sim 10^{13} \text{ (kg-fuel)}^{-1}$ , the ultrafine volatile particles can be activated and contribute to the number of nucleated ice crystals in contrail if atmospheric temperature is sufficiently low; this leads to a high supersaturation with respect to ice. In this thesis, soot rich emissions are assumed as they are typically found in current aircraft engines using current fuels.

Apart from plume particles, ambient aerosol particles entrain into the plume during the mixing; these mainly contain liquid (soluble and volatile) aerosol particles, with very few heterogeneous ice nuclei present. The entrained aerosol particles themselves can't form visible contrail since their number concentration is not as high as the number of ice crystals observed in a visible contrail (Kärcher et al., 1996). Past studies have shown that most contrail ice crystals are formed on entrained ambient aerosol particles only if the number of soot particles emitted from aircraft engines is very low (Jensen et al., 1998; Kärcher and Yu, 2009; Rojo et al., 2015). The ambient aerosols are likely to contribute to ice crystal formation in the contrail if they are big. The chemical and physical properties of the upper-tropospheric aerosol particles are highly variable, as most of them are formed from supercooled liquid chemical solution, mainly containing water-soluble substances e.g. organic, sulfate, nitrate and ammonium (Murphy et al., 1998). The observation data showed that the upper-tropospheric aerosols' dry particle sizes (without including the water fraction) are around 10 nm; the aerosol number concentration can be in the range between 100 to 2500  $\text{cm}^{-3}$  depending on the location and season (Schröder et al., 2002).

## 2.4.2 Aircraft wake evolution

Aircraft wake evolution is classified into four different regimes namely, the jet, vortex, dissipation and diffusion regimes (Gerz et al., 1998). The schematic diagram of these four regimes is shown in figure 2.3 and explained in the following sections.

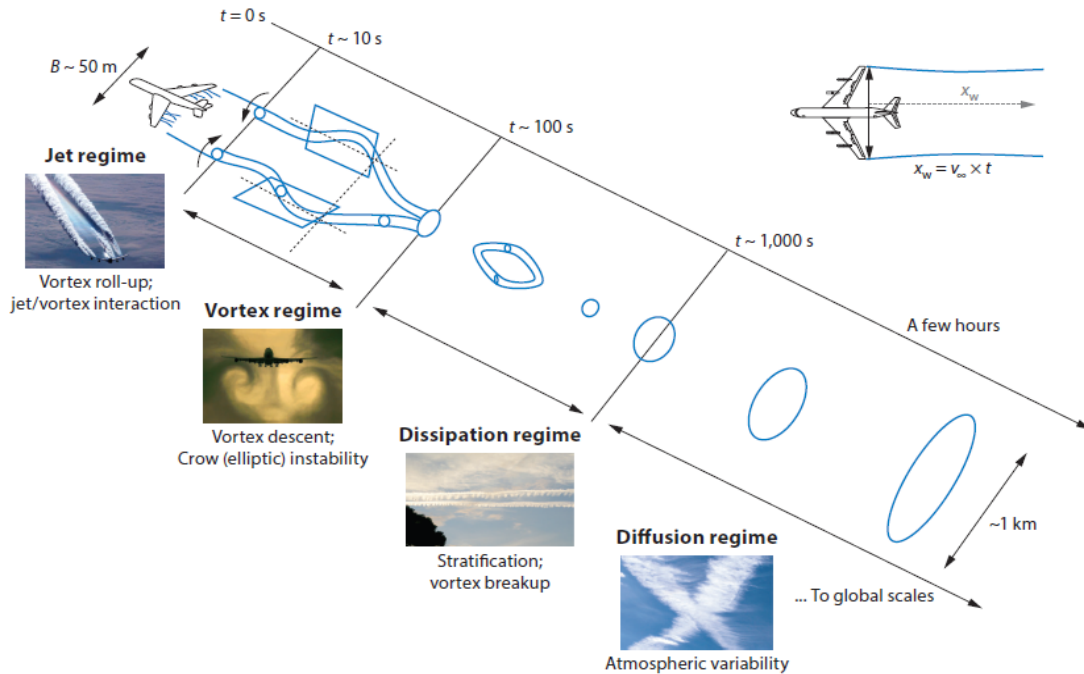


Figure 2.3: Schematic diagram of aircraft wake evolution into four regimes - jet, vortex, dissipation and diffusion. Source: (Paoli and Shariff, 2016)

**Jet regime** After aircraft emission, the first few seconds are jet regime in the aircraft wake evolution. In this regime, the contrail ice crystals nucleate within a second and simultaneously, the vortex sheet is rolled up at the aircraft's wings tip due to the pressure difference and forms the counter-rotating vortices that trap the freshly nucleated ice crystals in the core of the vortices. Ice crystals nucleate in contrail when the aircraft emitted hot and sub-saturated air mixes with the ambient cold air and during the mixing if supersaturation with respect to the water is reached locally (contrail formation Schmidt-Appleman criterion (Schmidt, 1941; Appleman, 1953, Schumann 1996)) (chapter 3 and section 3.2.1.1). Then water droplets form by condensation of water vapor on emitted soot particles and entrained ambient aerosols and subsequently freeze (Kärcher et al., 2015). The immediate freezing of the water droplets is essential to form persistent contrails because the upper troposphere is not supersaturated with respect to water but supersaturated with respect to ice which can allow ice crystals but not water droplets to persist. The number of nucleated ice crystals in a contrail is subject to the atmospheric state as well as aircraft and fuel parameters, particularly the number of aerosol particles released by the engine (Kärcher et al., 2015). At cruise altitude in the mid-latitudes, the atmospheric state is such that the number of emitted aerosol particles constrains the number of ice crystals forming within the contrail's jet phase (Bier and Burkhardt, 2019). This is not necessarily the case at lower altitudes and in warmer atmospheric temperatures; here, the ambient atmosphere's thermodynamic state responsible for the evolution of relative humidity in the plume limits ice nucleation within contrails. In the case of contrail formation

within cirrus (which is the main objective of this thesis), the ice nucleation process may become affected by the pre-existing cirrus cloud properties i.e., ice water content and ice crystal number. The surrounding ice crystals get sucked into the combustion chamber and sublimate. Furthermore, after emission, cirrus ice crystals mix with the exhaust plume and sublimate as long as the plume is subsaturated. Later in the plume development, water vapor can be deposited on the cirrus ice crystals. Both the ice crystals sucked into the engine and those mixed into the plume affect the plume properties and, therefore, the nucleation process (Chapter 3).

**Vortex-dissipation regime** Following the jet regime, the vortex regime starts, where the counter-rotating vortices propagate downward depending on atmospheric stability and aircraft properties, such as weight, wingspan and speed (Gerz et al., 1998; Paoli and Shariff, 2016). The density contrast between the air in the vortex that descends through a stably stratified atmosphere and the surrounding air creates vorticity that is shed upwards (secondary wake); part of the exhaust, between 10% to 30% (Gerz et al., 1998) is detrained into the secondary wake. The secondary wake stays close to the flight level. The primary wake often descends a few hundred meters. Many ice crystals within the primary wake sublimate due to adiabatic heating and the associated decrease in relative humidity, while the ice crystals in the secondary wake are more likely to survive (Schumann and Gierens, 1999; Lewellen and Lewellen, 2001; Unterstrasser, 2016).

Survival of the ice crystals in the vortex regime depends on atmospheric temperature, humidity, number of nucleated ice crystals and the maximum vertical displacement of the vortices (chapter 3, section 3.2.2). After the vortex descent, most of the air that was forced downwards rises again, creating a vertically extended contrail. The contrail ice crystal loss during vortex descent may be affected by the pre-existing cirrus in the case of contrail formation within cirrus. The surrounding cirrus ice crystals, which were entrained into the plume during mixing, are carried down by the vortices together with the contrail ice crystals. The adiabatic heating in the downward moving vortices will cause sublimation of cirrus and contrail ice crystals. The sublimation of cirrus ice crystals leads to a slight increase in the plume's relative humidity and therefore an increase in the survival fraction of the ice crystals. Within this thesis, the sublimation of pre-existing cirrus during vortex descent has been included in the contrail formation parameterization, as explained in chapter 3.

In the dissipation regime, vortices disintegrate and release the ice crystals. The surviving ice crystals grow in the presence of the available water vapor, causing an increase in the ice water content. The growth and the sizes of the ice crystals are dependent on the ambient relative humidity with respect to ice. In the case of contrail formation within cirrus, the growth of contrail ice crystals is very much dependent on the in-cloud ice supersaturation and the relative sizes of the ice crystals in cirrus and contrail. Cirrus ice crystals and contrail ice crystals compete for the available water vapor.

**Diffusion regime:** In this regime, the aircraft dynamics no longer controls the aircraft wake evolution; atmospheric variability controls the further mixing and diffusion of the contrail plume. The diffusion regime may last for a few hours (Paoli and Shariff, 2016). Atmospheric turbulence plays an important role in the mixing, spreading and diffusion of the contrail plume. The vertical wind shear causes an increase in the further spreading of the contrail (Schumann et al., 1998; Burkhardt and Kärcher, 2009; Bock and Burkhardt, 2016a; Gierens and Jensen, 1998; Jensen et al., 1998a). The spreading makes contrail geometrically and optically thin. In saturated or sub-saturated air, the contrail cover and optical depth will decrease. Spreading in the highly supersaturated air will cause the growth of contrail ice crystals and an increase in contrail cover.

During this regime, the relative humidity also plays a vital role in developing young contrails. The contrail ice particles may sublime or grow dependent on the atmospheric conditions, mainly ice supersaturation (Bier et al., 2017). For example, contrail ice crystals will persist and grow further if they spread in the ice supersaturated air and sublime if the air becomes subsaturated or ice crystals sediment into the sub-saturated air (Paoli and Shariff, 2016). However, in the presence of cirrus ice crystals (contrail formation within cirrus or contrail embedded cirrus), the development of the contrail will be affected because ice crystals of contrail may not grow as large as they can grow in the absence of cirrus ice crystals since contrail and cirrus ice crystals compete for available water vapor. On the other hand, the development of cirrus is also affected due to the presence of contrail ice crystals which will lead to a change in sedimentation rate and ice water distribution in the cirrus. These effects and the life cycle of the contrail perturbed cirrus have been analyzed in chapter 5.

## 2.5 Contrail observation

In-situ and satellite observations are necessary to determine contrail properties and to evaluate model studies. The following section summarizes in-situ and satellite observations of contrails.

### 2.5.1 In-situ observation

An early in-situ observation of contrails is described by Knollenberg (1972) when the first-time ice particle size spectra in an aged contrail were probed. Later, in-situ observations of young contrails have been carried out during different campaigns like SULFUR and PAZI (Partikel und Zirren) (Schumann et al., 1996; Petzold et al., 1997; Schröder et al., 2000; Febvre et al., 2009). The evolution of the contrail's ice crystal size spectra and the number concentration have been measured during different campaigns. Micrometer-sized ice crystals with high ice number concentration, around  $1000 \text{ cm}^{-3}$ , have been detected in 10 seconds old contrails (Petzold et al., 1997; Heymsfield et al., 1998; Schröder et al., 2000); a lower ice number concentration, around  $100 \text{ cm}^{-3}$ , has been found in few minutes old contrails since ice number concentration decreases due to dilution of contrail (Poellot et al., 1999; Febvre et al., 2009). Mean effective radii of ice crystals derived from observations of fresh contrails are below 2 micrometers (Heymsfield et al., 1998; Baumgardner and Gandrud 1998); these increase due to depositional growth, reaching around 1 to 3 micrometers in less than 30 minutes of contrail lifetime (Schröder et al., 1999; Voigt et al., 2010).

A compilation of the size spectrum of contrail ice crystals for different contrail ages has been compiled by Schröder et al., 1999 (figure 2.4). The data was collected over central Europe during several campaigns (e.g. AEROCONTRAIL) from 1996 to 1997. Mean diameter sizes of the freshly nucleated ice crystals in the jet phase (a few seconds old) are about 1 micrometer. Because of the small plume volume, the number concentration of ice crystals is very high, up to  $1.0 \times 10^4$  per  $\text{cm}^3$  during this phase. In 3 to 5 minutes old contrails, the number concentration of the ice crystals is comparably low, reaching only up to  $\sim 2 \times 10^2 \text{ cm}^{-3}$ . The number concentration of the ice crystals reached around  $\sim 30$  per  $\text{cm}^3$ , with mean diameter sizes below 10 micrometers in the 30 minutes old contrail.

After the vortex phase, aircraft dynamics no longer control the further evolution of the contrail; atmospheric variability does. In persistent contrails, contrail to cirrus transition during the dispersion phase and evolution of ice crystals sizes and ice number concentration, is mainly dependent on atmospheric parameters, i.e., wind shear, ice supersaturation, ambient temperature, vertical wind and turbulence (Heymsfield et al., 2010). The number concentration of ice crystals

decreases around 100 times from its initial value due to the dilution of the plume. In one-hour-old contrails, ice number concentration has been found below  $10 \text{ cm}^{-3}$  and mean effective radius larger than 5 micrometers (Heymsfield et al., 1998; Schröder et al., 2000; Febvre et al., 2009).

In the past few years, various other measurement campaigns have been introduced to study differences between natural cirrus and contrail cirrus microphysical properties e.g. CONCERT 2008 (Voigt et al., 2010), ICE 89 (Gayet et al., 1995) and ML-Cirrus 2014 (Voigt et al., 2016). These campaigns investigated the difference between the few minutes old contrails and the surrounding cirrus cloud. The number concentration of the ice crystals in the few minutes old contrails is comparably higher than the number concentration of the ice crystals (2 to 3 orders of magnitude higher) in the surrounding cirrus cloud because of the different ice nucleation mechanisms in the contrail and cirrus clouds (Voigt et al., 2010). The high soot emission from conventional kerosene fuel causes a high number concentration of ice crystals in the young contrails. The mean diameters of ice crystals in the few minutes old contrails are measured below 10 micrometers; on the other hand, the mean diameter of the aged natural cirrus ice crystals is comparably bigger ( $\sim 100$  micrometers) (Schröder et al., 2002). Aged contrail cirrus can be difficult to distinguish from the natural cirrus in terms of the number, concentration as well as size of the ice crystals, even though their nucleation mechanism is different. Therefore, it is necessary to have combined knowledge from the in-situ measurement, satellite observation and model studies to understand the contrail cirrus better and to identify the differences between natural cirrus and contrail cirrus.

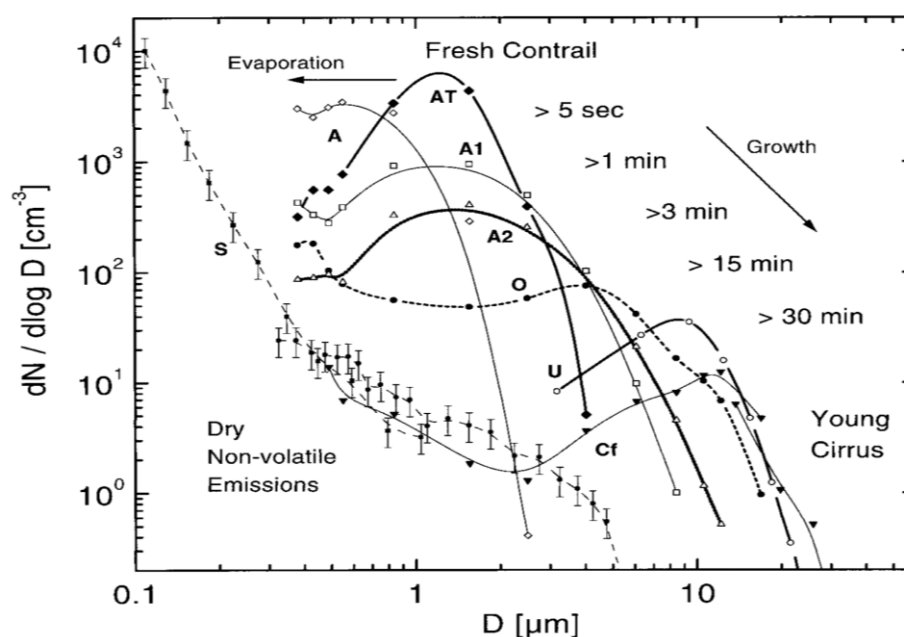


Figure 2.4: Number concentration and mean diameter of the ice crystals for different contrail ages and cirrus clouds. The data has been collected from various measurements campaign, e.g. AEROCOTRIL, from the year 1996 to 1997. Source: (Schröder et al., 1999).

Apart from the studies mentioned above for contrails, the indirect effect of the aviation-induced aerosols on natural cirrus, e.g. aerosol loading in the cirrus formation region and their number and ice nucleating properties, plus contrail formation within cirrus, is less known. Past studies show that aircraft exhaust emitted particles can be efficient ice nuclei for heterogeneous freezing in polluted areas (Jensen and Toon, 1997) if sufficiently large ice supersaturation is available. A high

number density of ice crystals has been found inside the cirrus together with the presence of elevated black carbon concentration in in-situ measurements (Ström and Ohlsson, 1998; Kristensson et al., 2000). A recent study by Urbanek et al. (2018) has shown a high depolarization ratio in some cirrus clouds where ice supersaturation is low. For this study, airborne high-spectral-resolution lidar data collected during the ML-Cirrus campaign in 2014 over Europe has been used to measure the cirrus particle linear depolarization ratios (PLDRs). A trajectory analysis has shown that high aviation emission regions over North Atlantic and the European mainland are the formation regions of the affected cirrus cloud. The depolarization ratio is related to the shape and number of particles and is high for irregular shaped particles like aggregated ice crystals. These high depolarization ratios in cirrus come with a low ice supersaturation ratio which indicates more frequently heterogeneous freezing in those areas in the presence of ice nuclei. This might be the explanation that the indirect aerosol effect is caused by the presence of aviation particles in altitudes where heterogeneous freezing may occur. However, the study did not clarify that the high number concentration of ice crystals was caused by the heterogeneous nucleation on the aviation particles or caused by the contrail formation within cirrus. Some modeling studies have also been performed to estimate radiative impact due to the indirect effect of aviation aerosols (Hendricks et al., 2005; Gettelman and Chen, 2013; Zhou and Penner, 2014). These studies indicate that the indirect effects of aviation can produce a significant uncertainty in the estimation of radiative forcing caused by aviation (Lee et al., 2021). Therefore, further investigations are needed to understand the indirect effect of the aviation aerosols; these should include the contrail formation within cirrus, aerosol loading in the cirrus formation region and their characteristics, aviation emission pattern, measurements and model study of the microphysical as well as optical properties of the aviation aerosols perturbed cloud.

### 2.5.2 Remote sensing observation

In-situ measurements are limited to the time, space and number of contrails sampled at given atmospheric conditions. On the other hand, remote sensing provides large coverage in terms of space and time and is helpful for the estimation of spatial coverage by contrails. The detection of contrails from a satellite is limited to high contrast in brightness temperature of contrail and background environment. This means overlapped contrails, contrail embedded cirrus, contrails underneath the cirrus and optically thin contrails (optical depth below 0.5 for wavelength 550 nm) are difficult to detect from the satellite.

Several single contrails over the Mediterranean, south of Cyprus, were identified in two satellite images in the year 1973. Optical depth, number concentration of ice and the spreading rate of the contrails were also derived from the satellite data, captured by the satellite 'Landsat 1' with a pixel resolution of 90 meters (Joseph et al., 1975). Several studies on the coverage due to line-shaped contrails over varying areas and for different years have been performed (Meyer et al., 2002; Palikonda et al., 2005; Minnis et al., 2005). One of the earliest studies determined cloudiness over Europe and the eastern part of the North Atlantic Ocean due to the line-shaped contrails for the two time periods September 1979-December 1981 and September 1989-August 1992 using visual inspection of the photographic prints of National Oceanic and Atmospheric Administration/Advanced Very High-Resolution Radiometer (NOAA/AVHRR) thermal infrared images (Bakan et al., 1994). The contrail coverage over western Europe was found to be on average 0.5%, while along the transatlantic flight corridor, the contrail coverage was around 2%. This study had been used for many years and was the basis for estimating the climate impact of linear-shaped contrails (Ponater et al., 2002; Marquart et al., 2003; Fichter et al., 2005; Rap et al., 2010). However,

the visual analysis of satellite images is highly subjective because the pixel-based distinction between the contrail and surrounding area is very difficult. The contrail detection and contrail radiative forcing were only limited to the line-shaped contrail. The detection of those contrails that already have lost their linear shape and look similar to the natural cirrus was almost impossible. Therefore, estimation of contrail coverage and their radiative impact may involve considerable uncertainty. Later on, with the development of advanced digital image processing systems, brightness temperature difference techniques through different channels (i.e., 11 and 12-micrometer channels) have become available. The brightness temperature difference technique increased the possibility of contrail detection and all cirrus clouds which are optically thin (larger than 0.05). The brightness temperature difference is dependent on the optical thickness, horizontal spreading of the contrails and the presence of the cirrus cloud.

A 'Cloud Detection Algorithm (CDA)' was developed to detect line-shaped young contrails and distinguish them from natural cirrus (Mannstein et al., 1999). The algorithm uses spectral and morphological information for contrail detection. A thermal infrared channel has been used to enable both daytime and nighttime observations. Firstly, data is converted equivalent to the blackbody temperature and then the brightness temperature difference for the ice clouds is calculated. The brightness temperature difference increases with increasing optical depth. The CDA has been used to detect contrails in data from many satellite instruments i.e., Moderate Resolution Spectral Imaging Radiometer (MODIS) on the Terra and Aqua satellites, the Spinning Enhanced Visible and Infrared Imager (SEVIRI) instrument on the geostationary satellites Meteosat -8 and -9 and Advanced Along-Track Scanning Radiometer (AATSR) on ENVISAT. The algorithm was modified to adapt and apply to different instruments and sensors. The modification in CDA didn't change the basic structure of the algorithm but made it possible to adapt input data and parameters of the new sensor. Once contrails are many hours old and have lost their line-shaped structure, then CDA couldn't detect those aged contrails.

To enable the detection of those aged contrails, an Advanced Contrail Tracking Algorithm (ACTA) was developed by Vázquez-Navarro et al. (2010). Later, this algorithm was applied to the SEVIRI data from the Meteosat geostationary satellite (Vázquez-Navarro et al., 2015). ACTA combines the higher spatial resolution observational data from the MODIS instrument mounted on polar-orbiting satellites, e.g. Terra and Aqua, with the high temporal resolution observational data from SEVIRI on the geostationary satellite Meteosat. The ACTA could track the aged contrails if the observation began when the contrails were still line-shaped. Combining data from a polar-orbiting satellite and a geostationary satellite made it possible to track the contrails' properties and life cycle. The detection of contrails starts by using the result from CDA on high spatial resolution observational data from polar-orbiting sensor MODIS. It then tracks those identified contrails and their life cycles in the 5 minutes temporal resolution rapid scan images from the Meteosat-SEVIRI sensor. The large coverage from SEVIRI made it possible to estimate the radiative forcing from the detected contrail coverage. The ACTA detected that aged contrail's (3 to 4 hours old contrails) optical depth had been observed higher than the optical depth of the 30 minutes old cloud. On the other hand, other studies estimated that the optical depth of the contrail is highest at the beginning of the contrail's life cycle due to the high number concentration of the ice crystals in contrail and decreases with the age of the contrail (Unterstrasser and Gierens, 2010a). The possible explanation for the high optical depth in the old contrail is that the detected contrails by ACTA are often observed in the synoptic situation where high humidity leads to a significant increase in contrail ice water content.

Remote sensing studies were mainly carried out for the northern hemisphere, where 93% of air traffic takes place; in observation, they appear to show that the largest global air-traffic coverage is

over the north Atlantic corridor (Bedka et al., 2013; Duda et al., 2013). Global simulation results show the maximum cloudiness due to young contrails is over the southeastern United States and Europe (Burkhardt and Kärcher, 2011), while remote sensing often shows peaks in contrail cirrus coverage over the ocean. The reason is that these areas have very high air-traffic density and lined shape contrails commonly overlap vertically with each other (Minnis et al., 2013). Consequently, satellite data tends to underestimate the coverage over Europe and the United States. Furthermore, higher detection efficiencies due to larger contrasts of a contrail over a homogeneous ocean may be the cause for the higher line-shaped contrail coverage over the ocean in observational data.

In order to evaluate model simulated contrail with satellite observation, an optical depth threshold for contrail detection of a minimum of 0.05 had been derived from the comparison of theoretical calculated optical depth with the satellite observation over the United States (Kärcher et al., 2009). That means when evaluating model simulations of contrails with satellite observations, only contrails with an optical depth larger than 0.05 should be considered. This often excludes several hours old aged contrails whose optical depth has decreased significantly and which are usually found in a large proportion in the atmosphere (Bock and Burkhardt, 2016a).

The studies mentioned above focus only on the visible contrails formed in ice supersaturated clear sky. Recently, for the first-time, contrail formation within cirrus has been studied through Lidar observation from satellite (figure 2.5) (Tesche et al., 2016). The study has shown that the optical depth of the natural cirrus increases due to the formation of the contrail within pre-existing cirrus. The analysis has been performed for the year 2010 to 2011 by selecting the air traffic between the western coast of the United States and Hawaii. A cloud aerosol lidar with orthogonal polarization (CALIOP) has been used for the study. CALIOP is a space-borne lidar observation instrument on the polar-orbiting cloud-aerosol lidar and infrared pathfinder satellite observations (CALIPSO) satellite with a return cycle of 16 days. The observation data has been selected for those individual aircraft whose arrival time is up to 30 minutes ahead or after the CALIPSO overpass. The optical depth of the cirrus cloud along the flight track has been observed and compared with the surrounding cirrus optical depth. 30 minutes after the passing of the aircraft, the cirrus optical depth

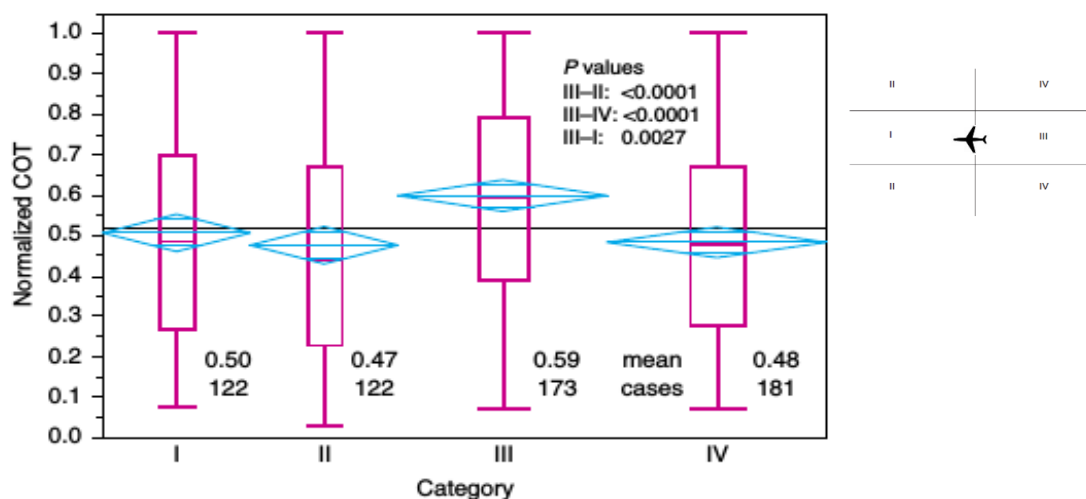


Figure 2.5: The normalized optical thickness of the cloud with a geometrical depth of 5 km for four categories (I) inside the flight track ahead of the aircraft, (II) outside the flight track, (III) inside the flight track behind the aircraft and (IV) outside the flight track behind the aircraft. Diamond (Cyan color) indicates a mean value of normalized optical thickness for all four categories. Mean optical thickness is highest for category III inside the flight track and behind the aircraft. Source: (Tesche et al., 2016).

had been increased by on an average of 22% relative to the optical depth of the cirrus in front and at the side of the aircraft track.

## 2.6 Simulations of contrails at different resolutions

In the mid-1990s, first attempts to study contrail evolution, properties and climate impact within LES and GCMs were made. Since then, contrail schemes have been implemented in models describing contrail formation and evolution in varying degrees of detail. Contrail representation in the model made it possible to understand contrail development, microphysical processes and their life cycle. Both GCM and LES model studies have their advantages and restrictions. On the one hand, LES simulations allow the study of individual contrails in a more refined grid structure and with detailed microphysical schemes. However, contrails are simulated with idealized atmospheric conditions. On the other hand, the GCM study provides global coverage of the contrail field and its effect on climate radiative forcing. Due to the coarser resolution of the GCM model, most contrail parameterizations are not for individual contrails but for a cluster of several contrails within a grid box; this can be suitable to study the lifecycle of the contrail cluster in different synoptic conditions. The actual life cycle of individual contrails is difficult to estimate since some contrails may be short-lived while others can be long-lived. Recently, contrails have been simulated in an NWP model with realistic background atmospheric variability. Studies of contrails in the GCM, LES and NWP models are explained in the following sub-sections.

### 2.6.1 Large-eddy Simulations

Large-eddy simulation (LES) studies have enabled us to understand processes involved in the formation and development of individual contrail like the formation of ice crystals in contrails (Garnier et al., 1997; Kärcher et al., 1996; Paoli et al., 2003; Paoli et al., 2004) and the loss of ice crystals during vortex descent (Lewellen and Lewellen, 2001; Huebsch and Lewellen, 2006; Unterstrasser et al., 2008; Unterstrasser and Sölch, 2010) that potentially affect the life cycle and the optical properties of the evolving contrail-cirrus.

The contrail vortex phase has been studied in detail using 3-D LES models, providing a realistic representation of the vortex phase in high temporal resolution (Lewellen and Lewellen, 2001; Huebsch and Lewellen, 2006). Due to the high computational requirements, these simulations are limited to a small set of atmospheric and aircraft parameters. On the other hand, 2-D LES simulations (Unterstrasser et al., 2008; Unterstrasser and Sölch, 2010) extend the use through a larger set of atmospheric and aircraft parameters. However, 2-D LES simulations are restricted to less detailed vortex dynamics because vortex dynamic (crow instability) is a 3-D phenomenon and therefore cannot be fully resolved in 2-D LES (Unterstrasser et al., 2008; Unterstrasser and Sölch, 2010). LES studies have shown that the number of surviving ice crystals after the vortex phase is highly variable and sensitive to atmospheric and aircraft parameters i.e., ice saturation ratio, ambient temperature, atmospheric stability, aircraft weight, fuel burn and soot emission index. The effect of those parameters on the survival fraction of contrail ice crystals is explained in detail in Section 3.2.2. The LES study of individual contrails allows understanding of the sensitivity of individual parameters on the evolution of contrails. For instance, if ice supersaturation is higher than 130%, then more than half of the total number of formed ice crystals will survive in the vortex phase (figure 2.6) (Unterstrasser, 2014; Unterstrasser, 2016). This further affects the ice water mass, optical depth and thus the radiative forcing. The loss of contrail ice crystals in the vortex phase is also significantly affected by the initial number of nucleated ice crystals in a contrail. The higher

the number of initially nucleated ice crystals, the smaller the mean mass and the mean radius of the ice crystals, leading to the sublimation of a large fraction of the total number of nucleated ice crystals. All the parameters mentioned above affect the dimension and properties of the contrail. Therefore, microphysical properties and the dimension of the contrail after the vortex phase are different for different contrails and govern the further spreading, and thus evolution of the contrail-cirrus. One of the drawbacks of the LES study of contrails is that contrails cannot be studied with evolving background meteorological conditions. Therefore, LES cannot study the interaction between contrail formation and the evolving state of the atmosphere.

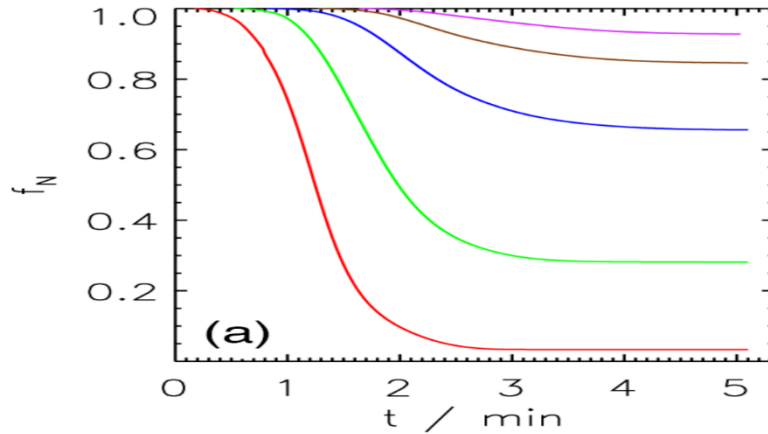


Figure 2.6: Temporal evolution of the normalized ice crystal number is shown for the first 5 minutes after contrail formation. Relative humidity over ice (red-100%, green-110%, blue-120%, brown-130%, and purple- 140%) at a fixed temperature of 217K has been taken to simulate contrail for a B777 aircraft type (Unterstrasser, 2016).  $f_N$  is a surviving ice crystal number fraction. Value 1 means all ice crystals survived, value 0 means all ice crystals sublimated. Source: (Unterstrasser 2016).

## 2.6.2 Global climate model simulation

After the vortex phase, further development of the contrails and their life cycle is mainly controlled by atmospheric variability. GCMs and numerical weather prediction models are suited to simulating the life cycle of the contrails within realistic atmospheric variability and the interaction between atmospheric variability and contrail development. GCM models allow the study of contrail properties, contrail coverage globally, their radiative forcing and the importance of microphysical processes in different synoptic conditions (Bier et al., 2017).

Initially, model-based studies considered only the line-shaped contrails, examining their radiative impact (Sausen et al., 1998; Ponater et al., 2002; Frömming et al., 2011) using satellite estimates of line-shaped contrail cover (Burkhardt et al., 2010). Further, process-based model studies have been conducted by including the evolution of the whole life cycle of the contrail, transition from contrail to cirrus and competition between a contrail and natural cirrus for available water vapor (Burkhardt and Kärcher, 2009). They estimated contrail-cirrus coverage and their radiative forcing (Burkhardt and Kärcher, 2011; Bock and Burkhardt, 2016b), exploring the variability resulting from synoptic variability (Bier et al., 2017). Burkhardt and Kärcher (2009) presented contrail cirrus as a new ice cloud class in the climate model using one-moment microphysics.

Other approaches represent contrail cirrus in climate models with many simplifications, like contrail may be simply treated as the source term for the ice crystal budget of the natural cirrus cloud, causes

mixing the microphysical properties of both contrail and natural cirrus and therefore, introducing biases in the contrail and natural cirrus microphysical properties. Mixing the microphysical properties of contrail and natural cirrus making it difficult to interpret the change in the natural cloud properties (Chen and Gettelman, 2013). Due to the coarser resolution in the climate model, the parameterization for contrails just as natural clouds are sub grid-scale, which means that fractional cloud coverage and its ice water content are simulated. The parameterization of Burkhardt and Kärcher (2009) considered contrail ice water content and fractional contrail coverage separately from the natural cirrus. The improved parameterization of Bock and Burkhardt (2016a) considers the following processes; horizontal and vertical spreading, deposition, precipitation and transportation of the contrail. Later, ice nucleation and ice crystal loss in the vortex phase have been added (Bier and Burkhardt, 2019).

While GCMs are well suited to simulating contrail cirrus properties and the associated radiative forcing, the low resolution of those approaches introduces uncertainties due to the fact that either contrail properties are determined from a mix of differently aged contrails (Bock und Burkhardt, 2016 a, b), from a mix of natural cirrus and contrail cirrus (Gettelman and Chen, 2013) or from the fact that contrails are not integrated into the GCM consistent with the natural cirrus (Schumann, 2013).

### 2.6.3 Contrails in NWP model

In one study, for the very first time, a numerical weather prediction model has been used to study contrail life cycles within realistic atmospheric variability (Gruber et al., 2017). A regional atmospheric model, COSMO-ART, with a spatial resolution of 2.8 km has been used for the study; this has comparably higher spatial and temporal resolution than the GCM model. In order to study the development and lifecycle of the contrails, 5 minutes old contrail (after vortex phase) properties, i.e. ice crystal number and ice water content, have been initialized in the model. The contrail ice crystals are prescribed as a separate ice class in the model since ice crystals in 5 minutes old contrails are relatively smaller than the cirrus ice crystals and, therefore, require more special treatment than the cirrus ice crystals in the model.

The development of young contrails to contrail cirrus has been studied in ice supersaturated areas and their effect on upper tropospheric cloudiness has been evaluated. The study revealed that the incoming shortwave radiation reaching the ground decreases by 5 to 10% during the eight hours of daylight due to persistent contrail clusters.

## 2.7 Summary

Contrails have been studied in detail in recent years through observations and models. All these studies have their own strengths and limitations. Observation studies are important for understanding of contrail properties at different synoptic situations and for validating model simulated contrails. In-situ measurements provide in-depth information of an individual contrail for a given atmospheric condition but are limited to only a few data samples. On the other hand, satellite remote sensing offers a large coverage of contrail cirrus but is limited to a particular optical depth and can capture only those contrails where the contrast in brightness temperature is large. This means that many hours old optically thin contrails and those contrails embedded within natural cirrus or form below the natural cirrus cannot be counted. Model studies allow us to understand processes and evaluate the life cycles of the contrails. LES studies of contrails provide in-depth knowledge of the processes in individual contrails, starting from the nucleation of ice crystals in

contrail to their loss in the vortex phase. But these studies are limited to fixed atmospheric conditions and only sample a few contrails due to high computational cost. On the other hand, studying contrails in a GCM is useful to estimate the radiative impact of the contrails. But a major drawback of GCM studies is that contrail properties are averaged over coarser spatial and temporal resolution, and therefore microphysical processes react to those average properties. A previous study using the NWP regional model has the advantage of higher resolution and, therefore, better microphysical treatment of contrails, but still requires the parameterization of ice nucleation and ice crystal loss in the vortex phase.

The studies mentioned above from different model groups focus on contrails formed in ice supersaturated regions. But recent satellite observations show evidence of natural cirrus perturbation due to contrail formation within cirrus. Therefore, a detailed study of these effects is needed in order to assess aviation-induced climate effects. In this doctoral thesis, I study for the first-time contrail-induced perturbations of natural cirrus clouds using an LES version of the ICON in high spatial and temporal resolutions. The ICON model and parameterization for contrail formation are described in chapter 3.

## Chapter 3

# Simulating contrails within ICON-LEM and definition of case studies

*This chapter partially has been published in Verma and Burkhardt (2021)*

Contrails have been studied so far only in ice supersaturated areas. There are no detailed studies currently for contrail formation within cirrus. Recent satellite observations show that contrail formation within cirrus alters the optical properties of the cirrus cloud (Tesche et al., 2016 and section 2.5.2). Therefore, a detailed study of microphysical and optical properties of contrail embedded cirrus needs to be carried out to reduce uncertainty while estimating climate impact. In the past couple of years, cirrus and contrails have been simulated as Large Eddy Simulations (LES) with a high spatial resolution (~100 meters); this provides a more realistic representation of the contrails and natural clouds (chapter 2, section 2.5). But, due to high computational power and storage requirements, past LES simulations of contrails are restricted to idealized atmospheric conditions, time periods, a limited number of case studies. With increasing computational power, the Large Eddy Simulations version of the ICOSahedral Non-hydrostatic model (ICON-LEM) allows much longer simulation (more than a day) in finer grid spacing (up to 156 meters) with realistic atmospheric conditions. Improved representation of the ice phase and microphysical processes are able to provide realistic shape, structure, distribution of the clouds and realistic representation of the precipitation (Stevens et al., 2021). The model is able to produce heterogeneity in the cloud field, thus in the optical depth, which can better estimate the radiative forcing in contrast to radiative forcing estimation in a coarser resolution model. A vast variability in model simulated cloud properties and non-idealized atmospheric conditions opens up the opportunity to study contrail within natural cirrus in the computationally inexpensive model and understand processes that affect the lifecycle, microphysical and optical properties of the contrail embedded cirrus. In order to simulate contrails within cirrus clouds, state-of-the-art ICON-LEM and implemented contrail parameterization are described in this chapter.

This chapter starts with a general discussion of the ICON-LEM based on cloud scheme and advection scheme (section 3.1). And then, a parameterization for contrail formation consisting of contrail ice crystal nucleation (section 3.2.1) and ice crystal loss in the vortex phase (section 3.2.3) is explained. Parameterization has been implemented for contrail formation in ice supersaturated areas as well as contrail formation within pre-existing cirrus. Within the nucleation parameterization, the effect of cirrus ice crystal sublimation during combustion and sublimation of cirrus ice crystals during mixing have been included for the case when aircraft fly through pre-existing cirrus (section 3.2.2). The vortex parameterization consists of the fact that entrained cirrus ice crystals in the plume sublimate together with contrail ice crystals when contrails form within cirrus clouds. Estimation of ice water mass sublimation from cirrus ice crystal during vortex descent has been explained in section 3.2.3.1. Model setup plus initial and boundary data are described in sections 3.4 and 3.3. Two different days are used for the simulation, with different synoptic conditions and cloud properties. Synoptic conditions and cloud properties are explained in section 3.5 and section 3.6, respectively. The model simulated number of nucleated ice crystals has been described in section 3.7. The effect of considering different shapes and size distributions of ice crystals on the estimation of optical depth has been explained in section 3.9.

### 3.1 ICOSahedral Non-hydrostatic model (ICON-LEM):

ICON is a unified modelling framework which is based on a non-hydrostatic system and suitable for three different physics packages e.g. climate modelling, numerical weather prediction (NWP) and large eddy simulation (LES). The main goals of ICON framework are to provide a) a better conservation property than the other global models specifically the local conservation of mass and consistency in mass transportation b) scalability of model with the parallel high-performance computation architecture c) availability of static mesh refinement, which can provide capability of combining one way nested and two-way nested grids within a single model framework (Zängl et al., 2015).

Large-eddy simulation ICON (ICON-LEM) configuration is a limited area model developed by the German Weather Service (DWD) and the Max-Planck Institute for Meteorology (Zängl et al., 2015; Dipankar et al., 2015). ICON-LEM can be refined to the spatial scales (upto O (100m)) needed to resolve convection while interacting with the large-scale atmosphere (Heinze et al. 2017, Dipankar et al. 2015). ICON solves a set of equations on an unstructured triangular grid based on the successive refinement of a spherical icosahedron (Wan et al., 2013, Zängl et al., 2015). Time stepping is performed using a predictor-corrector scheme. A summary of the model configuration and a description of the physics package is given in Heinze et al. (2017).

Due to high computational requirements, ICON-LEM usually runs in a limited area at 625m resolution and a time step of 3 seconds with an option for 2 one-way nested domains (Dipankar et al., 2015). The model uses realistic topography and periodically changes boundary conditions. The model's high horizontal resolution combined with a vertical resolution of around 150m in the upper troposphere allows resolving cloud processes, such as convection, while cloud microphysics, turbulence and radiation remain parameterized. Resolved cloud-scale dynamics leads to improvements in the structure and distribution of clouds and precipitation (Stevens et al., 2021). The heterogeneity in the cloud field and thus in the optical depth is largely resolved, enabling a more realistic estimation of the radiative forcing relative to coarser resolution models. The model is initialized at 00 UTC from operational COSMO-DE analysis data (Baldauf et al., 2011) and relaxed at the lateral boundaries within a 20km nudging zone towards COSMO-DE analysis, which is updated hourly.

An evaluation of the model simulations has been presented by Heinze et al. (2017) and Stevens et al. (2021). Finer resolution in the ICON-LEM or ICON-SRM (Storm Resolving Model) relative to lower-resolution simulations was shown to lead to improvements in precipitation patterns, their location, propagation, diurnal cycle and cloud properties, in particular the vertical structure and diurnal cycle (Stevens et al., 2021). However, processes in hectometer scale are resolved in the model but other processes which occur at different scales are unresolved; for example, cloud microphysics, radiative transfer, small scale turbulence and land surface processes are parameterized in the model (Heinze et al., 2017). The model's two-moment microphysics and advection scheme are described in the following sections.

#### 3.1.1 Two moment cloud microphysics

The cloud microphysical scheme of ICON-LEM is based on the Seifert and Beheng (2006) (SB2006 henceforth) two-moment cloud microphysical scheme and includes microphysical processes in liquid ( $\geq 273.15\text{K}$ ), mixed-phase ( $238.15 \leq T \leq 273.15 \text{K}$ ) and ice phase ( $T < 238.15\text{K}$ ) clouds. The microphysical two-moment scheme predicts mass mixing ratios and number concentrations for six

hydrometeors types, namely, cloud droplets, rain, ice, hail, snow and graupel. The cloud cover scheme considers an all-or-nothing scheme disregarding sub-grid variability of total water. This two-moment microphysical scheme includes the formation of the hydrometeors mentioned above through nucleation mechanism and conversion processes. The other microphysical functions are also parameterized i.e. condensational growth of cloud droplets, depositional growth of ice crystals, evaporation, sublimation, homogeneous freezing of cloud droplets, as well as precipitation and sedimentation of ice crystals. The conversion processes of these hydrometeors are shown in figure 3.1. In liquid phase clouds, the formation and growth of cloud droplets happen by nucleation, condensation, collection and coalescence processes while raindrops form by autoconversion (coagulation of cloud droplets) and grow by accretion (raindrops collecting cloud droplets). Since only ice phase cloud processes are important in this work, the explanation is therefore limited to the ice phase processes. In ice phase clouds, ice crystals form by homogeneous and heterogeneous nucleation mechanisms (homogeneous and heterogeneous nucleation mechanisms are explained in chapter 2). The parameterization for homogeneous and heterogeneous ice nucleation is based on Kärcher et al. 2006. The parameterization considers the competition between different ice processes i.e. homogeneous, heterogeneous nucleation and the growth of pre-existing ice crystals simultaneously for given ice supersaturation. The parameterization considers both homogeneous freezing of cloud water and aqueous solution; however homogeneous freezing of the aqueous solution is the dominating mode in cirrus cloud formation below  $-38^{\circ}\text{C}$ . Heterogeneous nucleation is induced by INPs (Ice nucleating particles) (chapter 2 section 2.2.2). Heterogeneous nucleation is based on prescribed mineral dust concentrations described in Hande et al. (2015). Activation of INPs for heterogeneous nucleation is parameterized based on the simulation of the aerosol conditions with the COSMO MultiScale Chemistry Aerosol Transport (COSMO-MUSCAT) model (Wolke et al., 2004, 2012). The number concentration of INPs is parameterized as a function of atmospheric pressure and vertical velocity (Hande et al., 2015). The nucleation events are triggered depending on their threshold ice supersaturation expressed as critical supersaturation. The ice supersaturation increases with increasing cooling rate (updraft velocity). This increased ice supersaturation is reduced in the presence of pre-existing ice crystals through the depositional growth process by taking away the available water vapor. After this adjustment in the updraft velocity, if the updraft velocity is large enough and ice supersaturation reaches the nucleation threshold for heterogeneous or homogeneous nucleation, then nucleation will take place. The heterogeneous nucleation triggered in the low ice supersaturation depends on the INPs and heterogeneous nucleation mode, while very high ice supersaturation is needed ( $\sim 1.5$ ) for the homogeneous nucleation (chapter 2 section 2.2.1). Additionally, a tracer is used to track the number of ice nuclei that have formed ice crystals and therefore, is no longer available for ice nucleation (Köhler and Seifert 2013).

The growths of single ice, snow and graupel are calculated by the depositional growth equation from Pruppacher and Klett, 1996. Various collection processes and interactions between the hydrometeors, e.g. collection and rimming, are also considered in the scheme. For example, rimming of ice and cloud droplets form ice and further conversion to graupel, rimming of ice and rain form graupel, aggregation of ice to ice form snow, rimming of snow and cloud droplets form ice, rimming of snow and rain form graupel, aggregation of ice and snow form snow and rimming of graupel with cloud droplets or rain or snow form graupel (figure 3.1). The sedimentation of the ice, snow and graupel is based on the power-law relationship of velocity and mass. In the presence of contrail ice crystals, microphysical processes are affected. For example, the growth rate of the natural cirrus ice particles will be restricted in the presence of many small contrail ice crystals because available water vapor for deposition will distribute among all ice particles (contrail +

cirrus) (competition between contrail ice and cirrus ice particles for deposition of available water vapor). Therefore, other microphysical processes e.g. sedimentation rate, which is dependent on mean mass and diameter, collection processes between hydrometeors and contact freezing of cloud droplets in the mixed-phase cloud due to sedimentation of ice crystals from the upper layer will be affected. The change in sedimentation rate in the ice cloud due to the formation of contrail ice crystals has been studied in chapter 5.

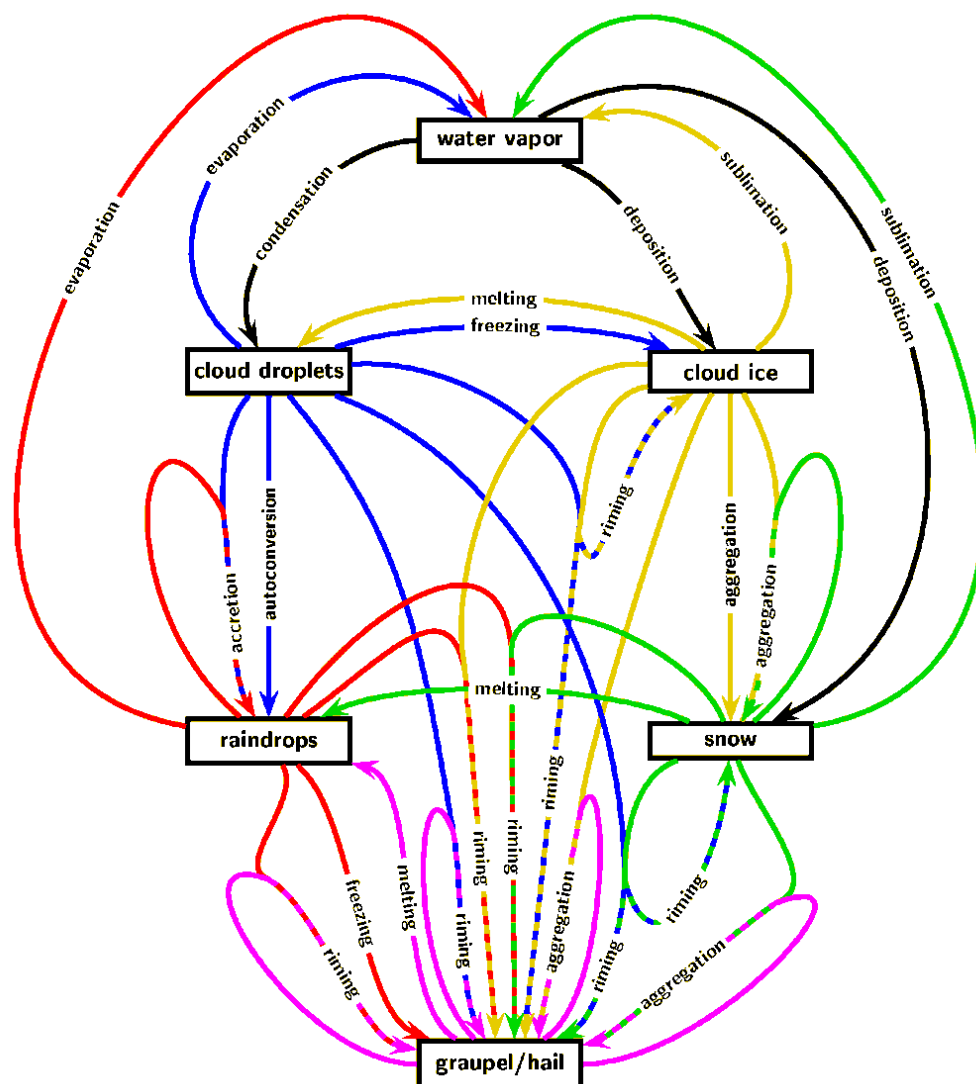


Figure 3.1: Schematic diagram of different collection processes, accretion, autoconversion, aggregation, freezing, melting, riming between six hydrometeors, cloud droplet, rain, ice, snow, hail and graupel (Seifert and Beheng 2006). Figure courtesy of Axel Seifert.

### 3.1.2 Tracer advection

Advective terms in the prognostic equations are second-order accurate except for vertical advection of tracers which is third-order accurate. Whereas the advection of momentum uses centered differences, the tracer variables, including all water species, are advected using the second-order

upwind-biased scheme of Miura (2007) and vertical advection terms are calculated by the third-order piecewise parabolic method of Colella and Woodward (1984).

Flux limiters are used in order to avoid spurious oscillations that occur e.g. in the presence of steep gradients. In ICON, two flux limiters are available, the positive definite and the monotonic flux limiter. By default, the positive definite flux limiter is used for all tracers due to the lower computational cost. The positive-definite flux limiter prevents the occurrence of negative mixing ratios and the monotonic flux limiter prohibits overshoots and undershoots during advection (Thuburn, 1996). Cloud variables often display strong gradients and differences in the gradients of, i.e. ice mass mixing ratio and ice crystal number concentration, can lead to inconsistencies between the variables during advection. Ice crystal numbers, which often display stronger gradients than ice water mass at the cloud edge, may be set to zero to avoid negative concentrations using the positive definite flux limiter. In contrast, the ice mass mixing ratio may remain non-zero. This problem is exacerbated when implementing contrail ice nucleation within the model. Contrail formation creates strong gradients in ice crystal number but only small changes and gradients in ice water content which may lead to zero ice crystal number concentration on the edge of the contrail after the flux correction using the positive definite flux limiter. Therefore, we use in our simulations the monotonic flux limiter for all the tracers in the model (e.g., water vapor, number concentration, water content of all six hydrometeors ice, snow, graupel, hail, rain and water droplet).

## 3.2 Contrail formation parameterization for ICON-LEM

A contrail formation parameterization has been implemented within the ICON-LEM. The contrail formation parameterization consists of ice nucleation within the jet phase and ice crystal loss and vertical spreading of contrail ice crystals during the vortex phase. The further development within the contrail's dissipation and diffusion phase is accounted for by the model's cloud and advection scheme.

Contrail formation can take place within cirrus cloud and cloud-free areas. The cloud-free areas and clouds have been distinguished using a minimum ice water content threshold of  $10^{-11}$  kg-m<sup>-3</sup>. The effect of pre-existing cirrus on contrail formation has been included in the parameterization. In this section, firstly, the contrail ice formation threshold temperature is explained, followed by a description of the parameterization for ice crystal nucleation. In the case of contrail formation within cirrus, the nucleation parameterization considers the effect of sublimation of ice crystals sucked into the combustor and sublimation of cirrus ice crystals entrained during the mixing. The estimation of sublimated cirrus ice crystals is explained in sections 3.2.2 and 3.2.3. After nucleation, the vortex phase parameterization is clarified in section 3.2.4. During the vortex descent, the cirrus ice crystals that are mixed in the plume will be sublimated together with contrail ice crystals. The sublimated ice water mass increases the water vapor in the plume and therefore increases the survival fraction of the contrail ice crystals. The effect of pre-existing clouds that are mixed into the plume is explained in section 3.2.4.1.

In order to keep additional I/O and computational costs low, the contrail scheme uses accumulated air traffic for 5 minutes to calculate the contrail ice crystal nucleation and ice crystal loss in the vortex phase. After that, contrail ice crystals are distributed vertically over a few hundred meters depending on the calculated contrail depth after the vortex phase. Finally, the contrail ice crystals are fed into the model's cloud scheme. The cloud variables, i.e., ice number concentration and ice water content, are then adjusted accordingly (figure 3.2).

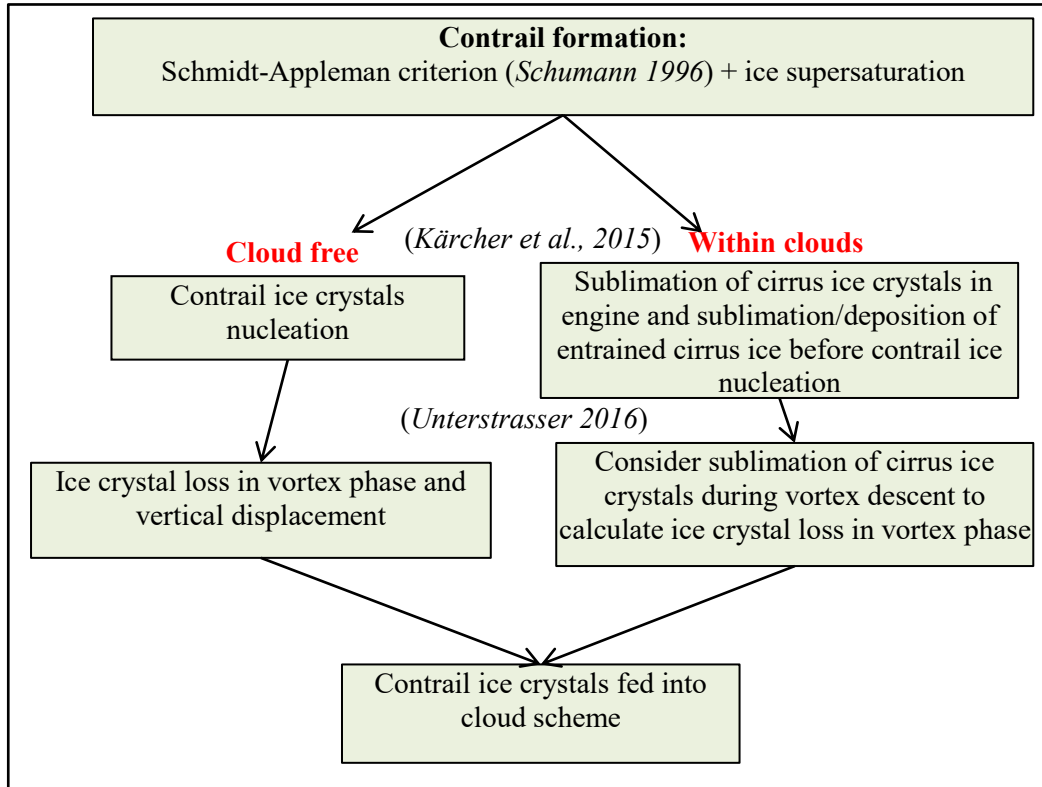


Figure 3.2: Flow chart to show difference in implemented parameterization for contrail formation in cloud free area and within cloud.

### 3.2.1 Contrail ice crystal nucleation

This section explains the contrail ice crystals formation criterion and a parameterization for contrail ice nucleation implemented in ICON-LEM. Firstly, a thermodynamic theory for contrail formation given by Schmidt (1941) and Appleman (1953) is explained; a parameterization for contrail ice nucleation has then been described. The parameterization for contrail ice crystal nucleation is based on Kärcher et al., 2015 which estimates the number of ice crystals nucleated in a contrail. In the case of contrail formation within pre-existing cirrus, the effect of pre-existing cirrus on contrail ice crystal nucleation has been considered. The estimation of sublimated ice water mass from cirrus sublimation in combustion and during mixing is explained in section 3.2.1.3.

#### 3.2.1.1 Thermodynamic criterion for contrail formation

The thermodynamic criterion for contrail formation was first given by Schmidt (1941) and Appleman (1953) (Schmidt-Appleman criterion), later extended by Schumann (1996). The thermodynamic criterion is used to decide whether contrail ice will form or not in the given atmospheric conditions. The necessary condition for ice crystal nucleation in a contrail is that plume air should reach water saturation during mixing. The Schmidt-Appleman criterion shows that water saturation occurs locally in the plume if the ambient air is colder than the contrail formation threshold temperature.

The thermodynamic criterion for contrail formation considers the mixing process between two independent air masses with different temperatures and relative humidity (mixing between hot and moist but initially subsaturated exhaust jet plume plus cold and dry ambient air). The atmospheric parameters (i.e. pressure, temperature and relative humidity), fuel, and aircraft parameters (i.e. water vapor emission and heat from the aircraft engine, propulsion efficiency) determine the contrail formation threshold condition. Figure 3.3 shows thermodynamic conditions for contrail formation during mixing. The mixing process starts somewhere far away from the top-right corner of figure 3.3; the starting point of the mixing line is characterized by the water vapor partial pressure and temperature within the plume at the beginning of the mixing. Hot and moist exhaust plume air gradually mixes with the cold and dry ambient air and rapidly cools down. The mixing line first crosses the ice saturation vapor pressure curve. Contrail ice crystal nucleate if the mixing line crosses the water saturation pressure curve. Between saturation vapor pressure with respect to ice and saturation vapor pressure with respect to water, ice nuclei may form ice crystals depending on their nucleation efficiency. Since ambient air and exhaust plumes typically contain very few ice nuclei, therefore, the number of nucleated ice crystals will be low and the contrail will not be visible at this point. When the mixing line reaches the water saturation vapor pressure curve, droplets start to form mainly on emitted soot particles and ambient aerosols and subsequently freeze. If the ambient air is subsaturated with respect to ice (figure 3.3b), then nucleated ice crystals in contrail will sublimate immediately. If the mixing line ends above the ice saturation vapor pressure curve, persistent contrails will form. Contrail ice crystals do not form if the mixing line does not touch the water saturation pressure curve at all (figure 3.3). Note that the second mixing line in figure 3.3b is unrealistic since highly ice supersaturated or even water supersaturated air cannot persist because natural cirrus would have formed already at high ice supersaturation and below water saturation.

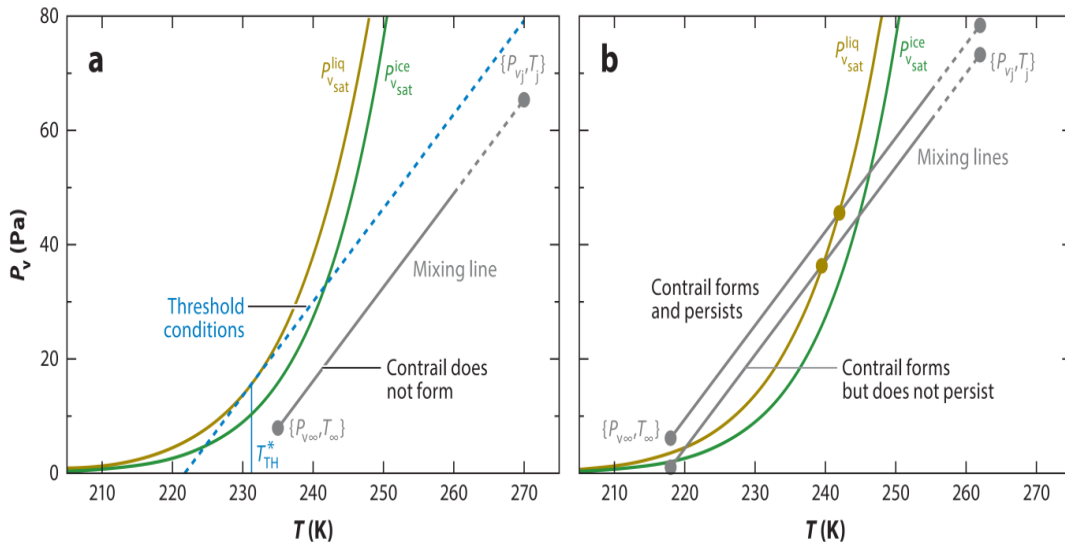


Figure 3.3: Schematic diagram for contrail formation conditions. The water saturation vapor curve and ice saturation curve are represented. Gray lines show three different mixing lines following the path from exhaust conditions to ambient conditions. Contrails do not form if the mixing line does not touch the water saturation pressure curve. Contrails form if mixing line crosses the water saturation curve. Source: (Paoli and Shariff 2016).

The point of contact between the mixing line and the water saturation vapor pressure is the threshold temperature  $\theta_{100}$  for contrail formation in the water-saturated atmosphere (relative humidity with respect to water ( $RH_w$ ) is 100%); therefore,  $\theta_{100}$  is the highest ambient temperature at which

contrails can form in water-saturated air. In a water sub-saturated atmosphere ( $RH_w < 100\%$ ), the contrail formation threshold temperature  $T_{sa}(RH_w)$  is lower than the  $\theta_{100}$  and can be estimated using the iterative method (Schumann, 1996). The endpoint of the mixing line denotes the temperature and relative humidity (with respect to water) of the ambient atmosphere. The lower the relative humidity of the ambient air the lower is  $T_{sa}(RH_w)$ . Therefore, the thermodynamic criterion for contrail formation is defined as:

$$T_a \leq T_{sa}(RH_w) \quad (3.1)$$

The contrail formation threshold temperature  $T_{sa}$  depends on the slope of the mixing line defined by  $G$ . The slope of the mixing line depends on atmospheric conditions and aircraft parameters.

$$G = \frac{M_w c_p P_a}{0.622Q(1 - \eta)} \quad (3.2)$$

where  $M_w$ ,  $c_p$ ,  $P_a$ ,  $Q$ , and  $\eta$  are aircraft emitted water vapor, specific heat capacity, atmospheric pressure, combustion heat and propulsion efficiency, respectively.

The mass emission of water vapor is set to  $1.25 \text{ kg (kg-fuel)}^{-1}$ , specific combustion heat to  $43.2 \text{ MJ (kg-fuel)}^{-1}$  and propulsion efficiency to 0.3 (Bock and Burkhardt, 2019). The temperature threshold of contrail formation,  $T_{sa}$ , is the ambient temperature for which the slope of the water saturation curve is equal to  $G$ , the slope of the plume mixing line. At ambient temperatures below that threshold, contrails will form if the ambient humidity is high enough. Contrails will only persist if the ambient humidity is at least saturated relative to ice. At a given pressure level and for a given propulsion efficiency, the slope of the mixing line depends on the ratio of emitted water vapor and combustion heat. An increase in water vapor emissions at constant combustion heat therefore leads to an increase in the slope of the mixing line and therefore to a higher temperature threshold of contrail formation. When neglecting droplets of ice crystal formation, maximum supersaturation within the plume will increase for decreasing ambient temperature (Schumann, 1996; Kärcher et al., 2015; Bier and Burkhardt, 2019).

The threshold temperature  $\theta_{100}$  for contrail formation in the water-saturated atmosphere is approximated as follows, as given in Schumann (1996).

$$\theta_{100} = 226.69 + (9.43 \times \text{LOG}(G - 0.053)) + (0.720 \times (\text{LOG}(G - 0.053))^2) \quad (3.3)$$

### 3.2.1.2 Parameterization for contrail ice crystal nucleation:

The Schmidt-Appleman (SA) criterion (Schumann, 1996) (section 3.2.1.1) explains under which atmospheric conditions a contrail can form but does not give information about the number and sizes of contrail ice crystals. Kärcher et al. (2015) describe the microphysical pathway of contrail formation, explaining the underlying processes i.e. activation of aerosols, relaxation towards saturation, freezing of droplets and growth of ice crystals. Figure 3.4 illustrates the pathway of contrail formation through the water and ice saturation vapor pressure curve and mixing line of the aircraft exhaust plume. Figure 3.4(a) shows mixing in the plume without considering droplet and

ice crystal formation. Figure 3.4(b) shows the mixing line, including contrail microphysics. The hot and moist air of the plume gradually starts to mix with the cold ambient air. During mixing, supersaturation with respect to water occurs once the mixing line crosses the water saturation vapor pressure curve. Supersaturation with respect to water is important for the formation and growth of the water droplets. Once supersaturation with respect to water occurs (cross mark in figure 3.4), the condensational growth of aircraft emitted soot particles and entrained ambient aerosol particles start and activate into water droplets ("Activation and relaxation" circle mark in figure 3.4). The time for the condensational growth depends on the atmospheric temperature. That means the time for condensational growth decreases with increasing atmospheric temperature. Therefore, condensational growth is zero and no droplet may form when the ambient temperature is equal to the formation threshold temperature at  $T_{sa}(RH_w)$  ( $T_a = T_{sa}$ ). In this situation, available water vapor is zero, and to form droplets, at least a slight water supersaturation is needed.

Close to the formation threshold  $T_{sa}(RH_w)$  with ( $T_{sa} - T_a < 2K$ ), only a small fraction of total available aerosol particles will activate into water. The reason is that in low water supersaturation, only the largest and most hydrophilic particles will activate. The number of droplets that form within the contrail is dependent on the water supersaturation, size distribution and hygroscopicity of the aerosols. At current soot number emissions, volatile plume particles are generally too small to activate. Once the droplets form, within a few milliseconds (star mark), water droplets freeze into ice crystals by homogeneous freezing once plume temperature reaches the freezing temperature ("Freezing and Relaxation") (Kärcher and Yu, 2009).

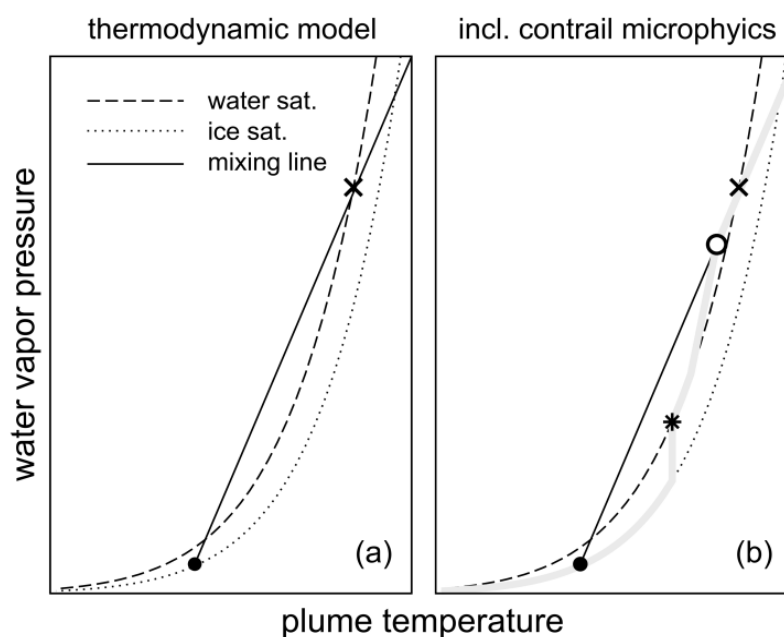


Figure 3.4: Thermodynamic model for ice nucleation in contrail same as figure 2 but showing mixing line (a) without (b) and with contrail microphysics. During the mixing, plume first reaches water saturation (cross mark), water droplets then form (open circle) and start to deplete the water supersaturation in the plume. Start mark shows the stage when frozen droplets start to quench ice supersaturation; filled circle shows ambient condition. Source: (Kärcher et al., 2015)

Parameterization makes the basic assumption that all water droplets form at the same time  $t_0$  "activation-relaxation time" during the mixing in the plume and deplete the plume supersaturation instantly. This is justified since the ambient aerosol particles and the emitted soot particles have

similar sizes. The two different contributions of soot and entrained aerosol particles are calculated from the total number concentration of activated water droplets (equation 3.4).

$$n_o = \phi_s EI_s \frac{\rho_o D_o}{N_o} + \phi_a \frac{T_a}{T_o} (1 - D_o) n_a \quad (3.4)$$

In equation 3.4,  $n_o$  is the total number concentration of droplets formed within the contrail; subscript 's' and 'a' denote emitted soot and entrained aerosol particles in the plume;  $EI_s$  denotes the soot number emission index;  $\rho_o, D_o$  and  $N_o$  are air mass density, dilution factor during the mixing and the air-to-fuel ratio at the engine outlet;  $T_a, T_o$  and  $n_a$  are ambient temperature, plume's temperature at  $t_o$ , and number concentration of entrained background aerosol particle;  $\phi_s$  and  $\phi_a$  are a factor of soot and entrained aerosol particles which are activated into water droplets. The dilution factor is used to measure the temporal evolution of the mixing process of the jet plume and ambient air; it is defined as:

$$D = \frac{T - T_a}{T_o - T_a} \quad (3.5)$$

where  $T$  is plume temperature,  $T_o$  is plume temperature at the beginning of the mixing process and  $T_a$  is ambient temperature. As in Bier and Burkhardt (2019), Kappa-Koheler theory (Petters and Kreidenweis, 2007) has been used to find the dry core radii  $r_{act}$  of particle type  $l$  ('s' soot and 'a' background aerosol) that can activate into water droplets during certain plume supersaturation  $s_w$ :

$$r_{act, l} = r_k \sqrt[3]{\frac{4}{27 \ln^2(s_w) \kappa_l}} \quad (3.6)$$

where  $r_k$  is the fixed kelvin radius with a value  $\sim 1$  nm; hygroscopic parameter  $\kappa_l$  defines the activation behavior of the particle type  $l$  and their water uptake characteristic which is dependent on the chemical composition of the particle. The effective  $\kappa_s = 0.005$  has been used for soot particles and effective  $\kappa_a = 0.5$  for fully soluble upper tropospheric ambient aerosol particles. Soot and background aerosol particle sizes are defined by log normal distributions; the activation fractions  $\phi_s$  and  $\phi_a$  are calculated by integrating over all radii larger than  $r_{act, s}$  and  $r_{act, a}$  respectively. Water droplets freeze subsequently into ice crystals by homogeneous freezing after the activation. Therefore, the number of ice crystals in a contrail is given by  $n_o$  and radius of ice crystals  $r_o$  is estimated using equation 52 given in Kärcher et al. (2015).

### 3.2.1.3 Impact of pre-existing cirrus cloud on contrail ice nucleation

This section describes the method used to estimate the sublimation of pre-existing cirrus ice crystals during a jet phase. Initially, the surrounding ice crystals that get sucked into the aircraft engine will sublimate during the combustion process. The amount of ice water mass sublimated from ice crystals has been estimated dependent on the ice water content in the pre-existing cirrus and the air-to-fuel mixing ratio of the aircraft. After exhaust emission, ice crystals from the surroundings mix with the exhaust plume air and sublimate at the beginning and later deposit available water vapor during the mixing process. The amount of water mass sublimated and deposited on cirrus ice crystals during the mixing is roughly estimated.

### 1. Impact of cirrus ice crystals sublimation in combustion

Contrail formation within pre-existing cirrus is very similar to formation in cloud-free air. The endpoint of the plume mixing line is given by the ambient temperature and the in-cloud water vapor partial pressure. The slope of the mixing line (equation 3.2) is modified by the presence of the cirrus ice crystals that are sucked into the aircraft engine together with the ambient air and sublimate. Although the number of ice crystals sublimating along the aircraft path is low, this effect could potentially impact cases where the contrail formation criterion is only slightly exceeded. Assuming a mass-based air to fuel mixing factor at engine outlet,  $N_0$  of  $70 \text{ kg-air (kg-fuel)}^{-1}$  (Kärcher et al., 2015), the change in the plume's water vapor content  $M_{eng}$  per kg-fuel due to sublimation of cirrus ice crystals in combustion has been calculated as follows:

$$M_{eng} = iwc_{ci} * N_0 \quad (3.7)$$

where  $iwc_{ci}$  is the ice water content of cirrus cloud ( $\text{kg (kg-air)}^{-1}$ ) and  $N_0$  is air to fuel mixing ratio at the engine outlet. The modified equation for the slope of the mixing line 'G' due to the change in water vapor mixing ratio in the plume is given in section 3.2.1.4 and equation 3.9.

### 2. Impact of cirrus ice sublimation and deposition during plume mixing

After exhaust emission, hot and subsaturated air of the exhaust plume starts to mix with the surrounding cold air. In the case of contrail formation within pre-existing cirrus, surrounding cirrus ice crystals entrained into the exhaust plume. At the beginning of plume mixing, plume air is hot and subsaturated. Therefore, the entrained ice crystals in the plume start to sublimate, and continuing to do so until the plume's relative humidity reaches ice saturation. The rate of sublimation of cirrus ice crystals in the plume depends mainly on the plume's relative humidity, temperature and size of the ice crystals. At the beginning of the mixing, the sublimation rate of entrained ice crystals is large since the plume's temperature is high. With the rapid mixing, the plume's temperature goes down and relative humidity goes up, causing a low sublimation rate. Once the plume's relative humidity reaches ice saturation, the sublimation of ice crystals stops. During this sublimation process, small ice crystals may sublimate completely depending on their sizes, plume relative humidity and temperature. At the same time, the surrounding ice crystals keep mixing in the plume, increasing the number concentration of cirrus ice crystals in the plume. Once plume air exceeds the ice saturation, the excess water vapor starts to deposit on entrained ice crystals and reduces the ice supersaturation in the plume. But at the same time, rapid mixing in the plume causes cooling and increases the ice supersaturation. The dominating process between the ice supersaturation depletion rate due to deposition and the ice supersaturation production rate due to mixing can be determined by the time scale of both processes. The time scale of ice supersaturation production in the plume due to rapid mixing is faster than the time needed to deplete the ice supersaturation through deposition on entrained ice crystals; therefore, nucleation of contrail ice crystals will not be significantly affected due to the deposition process during the mixing in most cases (Gierens 2012). But in some cases, it has been noted that if the number concentration of entrained ice crystals is large, then deposition can reduce the ice supersaturation in the plume and therefore reduce the number of nucleated ice crystals in contrail (chapter 4). The time-integrated change in the plume's water vapor content per kg-fuel  $M_{mix}$  due to sublimation and deposition of entrained cirrus ice crystals (with a mean mass 'm') that are mixed into the plume after emission ( $t_0$ ) and before aerosol activation ( $t_{act}$ ), is estimated as follows:

$$M_{mix} = \int_{t_0}^{t_{act}} \left( \left( \frac{dm}{dt} \right)_{sub} - \left( \frac{dm}{dt} \right)_{dep} \right) n_{ent} dt \quad (3.8)$$

where,  $n_{ent}$  is the apparent number emission index for cirrus ice crystals entrained into the plume from the surrounding air [ $\text{kg-fuel}^{-1}$ ] which increases with plume dilution:  $n_{ent}$  and the dilution are calculated using Equations 18 and 12 of Kärcher et al. (2015). The sublimated water mass per cirrus ice crystal,  $\left( \frac{dm}{dt} \right)_{sub}$ , the deposited water mass on a cirrus ice crystal,  $\left( \frac{dm}{dt} \right)_{dep}$  and their time integrated values are estimated as explained below. The change in the activation time of aerosol due to the presence of cirrus ice crystals has been neglected.  $M_{mix}$  can be positive or negative. If the total sublimated water vapor from the entrained ice crystals is larger than the total ice water mass deposited on the entrained ice crystals during mixing, then  $M_{mix}$  will be positive; otherwise it will be negative (equation 3.8). The estimated value for change in the plume's water vapor mixing ratio due to sublimation and deposition of cirrus ice crystals  $M_{mix}$  has been added to the mass emission index of water vapor  $M_w$  when calculating the slope of the new mixing line  $G_{ci}$  (equation 3.9)

### 3.2.1.3.1 Estimation of total ice water mass sublimate and deposit during mixing

The total ice water mass sublimate from entrained cirrus ice crystals has been estimated for the time period between engine exit to ice saturation in the plume during the mixing. The total sublimated ice water mass during mixing depends on the sublimation rate of the ice crystals for the given plume condition and the number of entrained ice crystals at that time. Estimating the sublimated ice water mass in every millisecond during the mixing is computationally expensive; therefore, an average value of sublimated ice water mass has been approximated using the average plume condition. As an example, the total ice water mass sublimated from entrained cirrus ice crystals in the subsaturated plume and the water vapor-deposited on the cirrus ice crystals once the plume is supersaturated, using equation 3.24 and an equation for plume dilution (Kärcher et al., 2015 (equation 12), has been shown for two contrail formation cases, one far from the contrail formation threshold temperature and one close to the contrail formation threshold temperature for the two sets of ambient conditions and aircraft parameters as in Bier et al. (2021, table 1; table 3.1); cirrus properties are specified (table 3.1). High plume temperatures immediately after emission cause a large sublimation rate of entrained ice crystals, while the number of entrained cirrus ice crystals is low. Close to ice saturation, the sublimation rate is low, while the number of entrained cirrus ice crystals is large. The resulting time-integrated sublimated ice water mass and the ice water mass deposited on the mixed-in cirrus ice crystals are given in table 3.1.

The temporal evolution of sublimation and deposition of cirrus ice crystals is calculated assuming a mean size which is given by the grid box ice water content and ice crystal number concentration. This means that the fact that when resolving the ice crystal size distribution is neglected, the smallest ice crystals ( $< \sim 1.5\mu\text{m}$ ) may completely sublimate when mixed into the plume at a time  $t_{cs} = \frac{1}{2}(t_{sat} - t_0)$  with  $t_0$  the time of emission and  $t_{sat}$  the time at which ice saturation is reached. Assuming the smallest mean cirrus ice crystal sizes within our model simulations ( $\sim 5\mu\text{m}$ ) and a generalized gamma ice crystal size distribution of Seifert and Beheng (2006),  $\sim 10\%$  of the cirrus ice crystals have a size below  $\sim 1.5\mu\text{m}$  and that may sublimate when mixed at time  $t_{cs}$  into the aircraft plume. The loss of cirrus ice crystals is likely to have a larger impact on estimated deposition than

of the sublimation and may accordingly lead to a conservative estimate for the plume water vapor increase due entrained cirrus ice crystals. Furthermore, spherical particle's shapes are assumed for this work, since there is no information on the habit of the ice crystals in our model, which can lead to an underestimation of the growth/decay of ice crystals. For young contrail ice crystals or newly nucleated cirrus ice crystals (including newly frozen water droplets) sphericity should be a good assumption while for larger cirrus ice crystals this assumption is often not good.

To approximate the sublimated ice water mass from the cirrus ice crystals depending on their volume, mean sizes have been calculated using the diffusional growth equation (section 3.2.4) for plume condition i.e. plume's temperature, relative humidity, entrained cirrus ice crystals at  $t_{as} = \frac{2}{3}(t_{sat} - t_0)$  with  $t_0$  the time of emission and  $t_{sat}$  the time at which ice saturation is reached. For both examples shown in table 3.1, the time integrated sublimated ice water mass from entrained cirrus ice crystals is very close to the estimate when using plume conditions at time  $t_{as}$  with deviations lower than 1% (table 3.1). The deposition of water vapor on cirrus ice crystals in the supersaturated plume has been estimated from the plume atmospheric variables midway between ice saturation ( $t_{sat}$ ) and aerosol activation ( $t_{act}$ ) at  $t_{ad} = \frac{1}{2}(t_{act} - t_{sat})$ . Since the ICON model doesn't provide any information on the size distribution of the cirrus ice crystals, the number of ice crystals lost during sublimation within the subsaturated plume cannot be estimated. Therefore, it has been assumed in this work that 20% of cirrus ice crystals were lost until the plume reached ice saturation. Table 3.1 shows that the time-integrated deposition and the estimates midway between ice saturation and aerosol activation agree reasonably well.

In order to estimate the range of errors that can be made if the deposition and sublimation have been estimated in the above way, the time-integrated and approximated deposition and sublimation have been estimated for the different background relative humidity, cirrus ice crystal numbers and ice water content - one far from the contrail formation threshold and one close to contrail formation threshold. It has been found that the errors in estimating sublimation are mostly below 3% and in estimating deposition, around 2%. Larger errors in sublimation and deposition are up to 4-5% only for combinations of atmospheric variables that are unlikely to occur, such as high relative humidity combined with many cirrus ice crystals and a large ice water content, or for many very small ice crystals with small ice water content and low supersaturation. Therefore, when estimating contrail formation within the ICON model, sublimation of cirrus ice crystals and water vapor deposition on cirrus ice crystals before aerosol activation have been estimated by approximating them based on the sublimation and deposition rates at  $t_{as}$  and  $t_{ad}$ , respectively. In order to calculate the deposition on cirrus ice crystals before aerosol activation,  $t_{act}$  has been determined by using the contrail ice nucleation parameterization of Kärcher et al. (2015), assuming  $t_{act}$  is unchanged by the sublimation and deposition.

**Table 3.1: Estimation for sublimation and deposition of cirrus ice crystals within the plume before contrail formation**

Engine exit condition				
Temperature at the engine exit	580 K			
Air to fuel ratio 'N <sub>0</sub> '	75			
Cirrus property				
Ice water content	1.0x10 <sup>-5</sup> kg/m <sup>3</sup>			
Number concentration of ice crystal	2x10 <sup>4</sup> m <sup>-3</sup>			
Ambient conditions				
	Far away from contrail formation threshold		Close to formation threshold condition	
Contrail formation threshold temperature	226.2 K		226.2 K	
Temperature	220 K		225 K	
RH <sub>i</sub>	120%		120%	
Pressure	240 hPa		240 hPa	
Sublimation of entrained cirrus ice crystals before contrail ice nucleation AEI (kg/kg-fuel) $\left(\frac{dm}{dt}\right)_{sub}$				
Time of reaching ice saturation 't <sub>sat</sub> '	0.19 s		0.271 s	
	Temporal evolution	based on sublimation rate at t <sub>as</sub>	Temporal evolution	based on sublimation rate at t <sub>as</sub>
Total sublimated ice water mass	8.81x10 <sup>-5</sup>	8.88x10 <sup>-5</sup> (+0.866%)	3.72x10 <sup>-4</sup>	3.75x10 <sup>-4</sup> (0.92%)
Deposition on entrained cirrus ice crystals before contrail ice nucleation (kg/kg-fuel) $\left(\frac{dm}{dt}\right)_{dep}$				
Time at aerosol activation 't <sub>act</sub> '	0.45 s		1.1 s	
	Temporal evolution	based on sublimation rate at t <sub>ad</sub>	Temporal evolution	based on sublimation rate at t <sub>ad</sub>
Total deposited ice water mass	8.08x10 <sup>-5</sup>	8.28x10 <sup>-5</sup> (2.498%)	3.04x10 <sup>-4</sup>	3.1x10 <sup>-4</sup> (1.82%)

### 3.2.1.4 Modification in the slope of the mixing line after including the effect of pre-existing cirrus

The ice water mass sublimated in combustion  $M_{eng}$  (equation 3.7) and sublimated and deposited during mixing  $M_{mix}$  (equation 3.8) changes the water vapor mixing ratio in the plume. Sublimation and deposition on cirrus ice crystals lead to a deviation of the plume's water partial pressure away from the mixing line approximation, with variations largest shortly after emissions due to the

plume's large subsaturation and high temperature. The evolution of the plume properties has been approximated by a new mixing line, treating the change in the plume's water vapor content from the sublimation and deposition as a change in the water vapor emission. The change in water vapor mixing ratio due to  $M_{eng}$  and  $M_{mix}$  is added to the mass emission index of water vapor,  $M_w$ , to calculate the new slope of the mixing line. The mass emission index of water vapor ( $M_w + M_{eng} + M_{mix}$ ) is hereafter referred to as 'aviation induced increase in water vapor'. The new slope  $G_{ci}$  for the mixing line (equation (3.2)) is modified in the following way:

$$G_{ci} = \frac{(M_w + M_{eng} + M_{mix})c_p P_a}{0.622Q(1 - \eta)} \quad (3.9)$$

The slope of the mixing line  $G_{ci}$  increases slightly due to the sublimation of the background cirrus ice crystals; the change depends on the cirrus cloud properties, in particular the ice water content (equations (3.7 and 3.8)). When calculating the slope of the time series of water partial pressure at the time of contrail ice nucleation, we find deviations from the simple mixing line approximation (equation 3.9) of a few tenths of a percent. Only when assuming a very large cirrus ice crystal number concentration of  $5 \cdot 10^6 \text{ m}^{-3}$ , can deviation from the mixing line slope at the time of aerosol activation reach values of up to 1%. This agrees with Gierens (2012), who found that for a plume age of 1 second, at typical cirrus ice crystal concentrations and typical atmospheric conditions, the deposition time scale is 2 to 3 orders of magnitude smaller than the dynamic jet timescale. This indicates that cirrus ice crystals grow too slowly to effectively reduce plume supersaturation production due to cooling.

This increase in the slope of the mixing line leads to an increase in the temperature threshold for contrail formation. This means that plume supersaturation can occur earlier and the maximum attainable relative humidity, which is reached within the plume when neglecting the decrease in supersaturation due to droplet formation, can be larger. Therefore, ice nucleation can be increased. The aviation-induced increase in water vapor mixing ratio in the plume ( $M_w + M_{eng} + M_{mix}$ ) due to sublimation of cirrus ice crystals along the aircraft path has been calculated for air traffic over Germany for two different synoptic situations (section 3.5). Figure 3.5 shows the percentage change in water vapor emission due to sublimation of cirrus ice crystals during combustion and sublimation/deposition of cirrus ice crystals during mixing. The change in water vapor emission has been calculated for the two different cloud fields. One cloud field consists of very thin cirrus with low ice water content and low ice crystal number concentrations; the other is a thick cirrus connected with a frontal system that has a high ice water content and high ice crystal number concentrations. These two synoptic situations are presented in detail in section 3.5.

The percentage change in water vapor emission (figure 3.5) is calculated as follows:

$$\Delta q_v(\%) = \frac{((M_w + M_{eng} + M_{mix}) - M_w)}{M_w} * 100 \quad (3.10)$$

The fixed water vapor emission index  $M_w = 1.25$  kg/kg-fuel for kerosene has been used (Schumann 1996) for the study. The probability of the ratio of cirrus ice crystal sublimation and the aviation-induced increase in water vapor is generally minimal. The sublimation of cirrus ice crystals usually contributes a few thousands to a few hundreds of a percent to the aviation-induced increase in water vapor (figure 3.5). Maximum contributions reach values of half a percent on the 24<sup>th</sup> April at 6 am (probability of  $10^{-4}$ ) and 10% on the 26<sup>th</sup> April at 5 pm (probability of  $5 \cdot 10^{-2}$ ). On the 26<sup>th</sup> of April, contributions reach values of about 20% with a probability of  $10^{-2}$ . The PDF of the changes only due to sublimation of cirrus ice crystals in the combustor is simply shifted towards lower values. The large change in water vapor content shows very low probability but these are those gridboxes where effect of background cirrus is significant large. This is despite the fact that the change in the plume water vapor concentration due to the sublimation of and deposition on cirrus ice crystals that were mixed into the plume can also be negative. This is roughly in agreement with the cirrus ice water content reaching values of  $0.5 \text{ gm}^{-3}$  at 220K (figure 3.10b). Assuming a pressure of 230 hPa, the ice water mass mixing ratio can be estimated. Prescribing an air to fuel mixing factor of 70 kg-air/kg-fuel, the cirrus ice water mass sublimated in the engine per mass of fuel burned is shown to agree with the ratio of sublimated cirrus ice water mass and aviation induced increase in water vapor (figure 3.5).

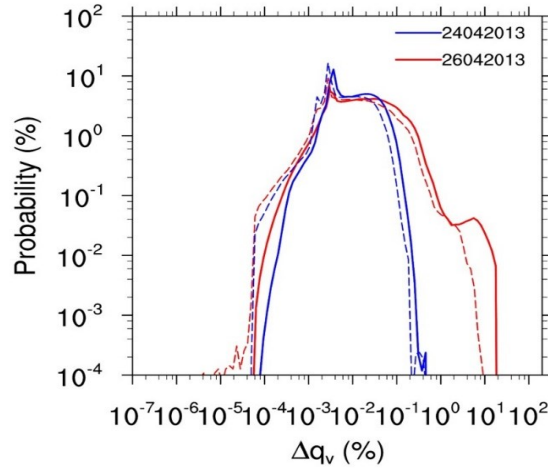


Figure 3.5: Probability of percentage change in water vapor ‘emission’ ( $\Delta q_v$  (%)) due to sublimation of background cirrus ice crystals in the aircraft’s engine (dashed line) and due to sublimation of cirrus ice crystals in engine ( $M_{eng}$ ) + during mixing ( $M_{mix}$ ) (solid line).  $\Delta q_v$  due to sublimation of a thin cirrus cloud field on 24<sup>th</sup> April 2013, 6 am (blue curve) a thick cirrus cloud field on 26<sup>th</sup> April 2013, 5 pm (red curve) for areas with temperatures lower than 233.15K, ice saturation ratio larger than 1 and IWC larger than  $10^{-11} \text{ kgm}^{-3}$ .

After including the effect of the cirrus ice crystal sublimation, the slope of the mixing line increases slightly, directly affecting the contrail formation threshold temperature. The change in threshold temperature for both case studies is presented in chapter 4. The change in contrail formation threshold condition is large; this leads to a significant increase in the number of nucleated contrail ice crystals (see chapter 4).

### 3.2.2 Parameterization for the ice crystal loss during vortex descent

This section consists of the parameterization of contrail ice crystals loss during vortex descent for cloud-free areas based on Unterstrasser (2016) (3.2.2.1) followed by the impact of pre-existing

cirrus on the survival of contrail ice crystals. The presence of cirrus ice crystals in the plume can affect the growth of the contrail ice crystals after nucleation and subsequently can affect the sublimation of contrail ice crystals during descent. The estimation of the distribution of available water vapor in the plume after nucleation among nucleated contrail ice crystals and entrained cirrus ice crystals followed by an estimation for the impact of entrained cirrus ice sublimation during vortex descent on contrail ice crystals survival are explained in section 3.2.2.2.

### 3.2.2.1 Parameterization for ice crystal loss during vortex descent

After contrail ice nucleation the plume ice water mass grows and approximately ten seconds after the emission, the exhaust plume, including the newly formed contrail ice crystals, trapped by a pair of counter-rotating vortices (primary wake). The vortices are created when the vorticity sheet originating from the pressure differences at the aircraft wings rolls up (Paoli and Sharif, 2016). The counter-rotating vortices propagate downward with a vertical displacement depending on atmospheric stability and aircraft properties. The density contrast between the air in the vortex and the immediate surroundings creates vorticity that is shed upwards (secondary wave) with part of the exhaust, including some ice crystals, detrained into the secondary wake (approx. 30%). The secondary wake stays close to the flight level at colder temperatures and in higher relative humidity air therefore, the probability of ice crystal survival in the secondary vortex is much higher. Many ice crystals within the primary downward propagating vortices sublime due to adiabatic heating. Survival of the ice crystals during the vortex descent depends on atmospheric temperature, humidity, the number of nucleated ice crystals and the final descent of the vortices. The vortex phase and important results from the LES simulation have been explained in chapter 2, section 2.3 and section 2.6.1, respectively. Here, the parameterization for ice crystal loss and contrail depth after the vortex phase is explained.

The implemented parameterization for ice crystal loss during vortex phase in ICON-LEM is based on the work of Unterstrasser (2016). The parameterization estimates (1) the final descent of the vortices in the atmosphere (2) the vertical depth of the contrail, given by the final descent of the vortices if ice crystals survive at the location of maximum descent and smaller otherwise and (3) the fraction of contrail ice crystals surviving due to the change in the relative humidity connected with adiabatic warming of air due to vortex descent. The aircraft properties of a medium-size aircraft (Aircraft type A350 and B767) have been assumed in the parameterization to estimate the survival fraction of ice crystals and the cross-sectional area of the contrail after the vortex descent.

The vertical depth of the contrail and ice crystal loss during vortex descent are dependent on three-length scales. The first is the final descent of the vortices ' $z_{desc}$ ' represents the displacement of the vortices in the atmosphere due to aircraft properties and atmospheric stability. The second length scale is ' $z_{atm}$ ' that shows the effect of atmospheric ice supersaturation on contrail ice crystals trapped within downward propagating vortices. The third length scale is ' $z_{emit}$ ' shows the impact of aircraft emitted water vapor on contrail ice crystals. These three length scales are explained in Unterstrasser (2016). Note that, in the case of contrail formation within cirrus, sublimation of pre-existing cirrus will modify the aircraft emitted water vapor concentration which will lead to a change in  $z_{emit}$  length scale. The modification in the  $z_{emit}$  length scale is described in the next section.

The contrail depth, final descent of vortices and the number of surviving ice crystals after the vortex phase are important because later, surviving ice crystals and sublimated ice mass are distributed into the lower altitudes. Surviving ice crystals are distributed over the contrail vertical extent after the vortex phase assuming that total plume water is distributed vertically evenly. The surviving ice

crystals are distributed vertically assuming that at flight level, no ice crystals sublimate and assuming a linear increase in ice crystal numbers.

### 3.2.2.2 Impact of cirrus ice crystals on the growth of contrail ice crystals after nucleation and on sublimation of contrail ice crystals during vortex descent

When contrails form within cirrus the cirrus ice crystals entrained into the plume do not only have an impact on ice nucleation but can also have an impact on the growth of contrail ice crystals after nucleation and on the subsequent loss of contrail ice crystals during the contrail's vortex descent. After nucleation cirrus and contrail ice crystals together act to relax the plume's supersaturation towards the ice saturation value. The diffusional growth equation (e.g. Pruppacher and Klett, 1997, Paoli and Shariff, 2016, section 3.8) is used in order to estimate the temporal evolution of water vapor deposition on the contrail and cirrus ice crystals over 9s after nucleation and before vortices start to descend. The deposition rate for ice crystals has been determined for every millisecond by adjusting the available water vapor after deposition in the previous time step, the temperature of the plume due to dilution, causing an increase in ice supersaturation and entrainment of cirrus ice crystals due to dilution in the plume. Once the plume's relative humidity approaches ice saturation, the smaller contrail ice crystals may sublimate while larger cirrus ice crystals may still grow due to the dependence of the saturation vapor pressure on the curvature of the ice crystals (Kelvin effect). In this situation, the difference in ice crystal sizes between cirrus and contrail ice crystals increases. This behavior may be often found in contrails (Lewellen, 2012) and is most frequent in areas of low background relative humidity and large cirrus ice crystals. This means that the presence of cirrus ice crystals limits the deposition on the contrail ice crystals, due to the competition for water vapor. This competition during the growth phase before vortex descent acts to increase contrail ice crystal loss during vortex descent since the ice mass of contrail ice crystals is lower than it would have been in the absence of cirrus ice crystals.

The cirrus ice crystals entrained during the jet phase coexist with the contrail ice crystals in the plume and during the vortex descent, adiabatic heating causes sub-saturation in the plume; therefore, contrail and cirrus ice crystals start to sublimate. The sublimation of cirrus ice crystals reduces the sublimation rate of the contrail ice crystals by weakening the decrease in relative humidity within the vortex. This may lead to a reduction in the number of contrail ice crystals that sublimate within the vortex phase. Instead of calculating the temporal evolution of contrail and cirrus ice crystal sublimation during the vortex descent, the amount of cirrus ice water mass that sublimates in the time period of complete sublimation of contrail ice crystals has been estimated using the diffusional growth equation (section 3.8), assuming spherical particles and ice sub-saturation value 0.98 in the plume. The used ice sub-saturation value in the plume is a typical ice sub-saturation found in LES-simulated descending vortices (personal communication Simon Unterstrasser; Naiman et al., 2011). The time period for cirrus ice sublimation is either given by the length of time the vortices descend or by the time it takes to sublimate all contrail ice crystals during vortex descent. The estimation for the ratio of sublimated cirrus water mass,  $M_{\text{cirrus}}$ , and sublimated contrail water mass,  $M_{\text{contrail}}$ , is made by dividing the diffusional growth equation for cirrus ice crystals by that for contrail ice crystals and multiplying by the ratio of the number of ice crystals within the air volume:

$$\frac{dM_{\text{cirrus}}}{dM_{\text{contrail}}} = \frac{dm_{\text{cirrus}}/dt}{dm_{\text{contrail}}/dt} * \left( \frac{N_{\text{cirrus}}}{N_{\text{contrail}}} \right) \quad (3.11)$$

This equation allows to roughly estimate the amount of cirrus ice water that can sublimate while the contrail ice crystals sublimate. Maximally  $dM_{cirrus}$  is the cirrus ice water mass sublimating in the time  $dt_{desc}$ , the vortex descent time scale. The vortex descent time scale we estimate from the vortex descent length scale,  $z_{desc}$ , and the vortex descent speed,  $w_0$ , given by the parameterization and in table 1 of Unterstrasser (2016), respectively. The sum of the cirrus ice water sublimation calculated in this way and the deposition on cirrus ice crystals, that was happening before vortex descent, is a measure of the impact of cirrus ice crystals on the water vapor content of the plume. If the background cirrus has the same ice crystal size distribution as the newly formed contrail, then the cirrus ice crystals would sublimate completely in the same time interval as contrail ice crystals. Usually, in natural cirrus, ice crystal densities are much lower than in young contrails, with ice crystal sizes being larger. Assuming that the ice water mass in natural cirrus and contrail is the same, the smaller number of ice crystals in natural cirrus leads to the sublimation of less ice water mass of the natural cirrus than of the young contrail within the same time period. This is because a decrease in the number of ice crystals at fixed cirrus ice water mass leads to an increase in ice crystal mass by the same amount, while the increase in the ice crystal radius is proportional to the third root of the volume. This means that given a fixed cirrus ice water mass, the impact of cirrus ice crystal sublimation on the survival rate of contrail ice crystals is largest when the cirrus consists of a large number of small ice crystals. An increase in cirrus ice crystal numbers always leads to an increase in the contrail's ice crystal survival fraction.

Finally, the parameterization of Unterstrasser (2016) is used, which does not include the impact of cirrus ice crystals on the survival fraction of contrail ice crystals, adjusting the water vapor 'emissions' of the air plane, which is an input in the parameterization. While the water vapor emission is usually given by the  $M_w$  coming from fuel combustion, in the context of contrail formation within cirrus, we use the 'aviation induced increase in water vapor ( $M_{cir}$ )' and add the sum of the sublimation of and deposition on cirrus ice crystals within the first 9s after ice nucleation and during vortex descent ( $M_{vort}$ ). This sum of sublimation and deposition on cirrus ice crystals ( $M_{vort}$ ) describes the impact of the cirrus ice crystals on the plume water vapor content integrated over the vortex phase which is together with  $M_{cir}$  a measure for the modification of the plume's water vapor content that is seen by the contrail ice crystals. Then the parameterization of Unterstrasser (2016) is used to estimate the contrail ice crystal loss.

The steps to calculate impact of pre-existing cirrus on survival of contrail ice crystals are as follows: a. Estimate diffusional growth on contrail and entrained cirrus ice crystals before vortex descent. b. Estimate the cirrus ice water mass that sublimates within the time that contrail ice crystals sublimate which is either given by the time the vortex descends or by the time it takes to sublimate all contrail ice crystals. c. Adjust the water vapor emission in the parameterization of Unterstrasser (2016) as explained above the net effect of water vapor uptake of and ice mass release from cirrus crystals during the respective phases is calculated and added this negative or positive contribution to the sum of water vapor emission originating from combustion and  $M_{cir}$ . d. Recalculate the number of contrail ice crystals that sublimate and the fraction that survives the vortex descent based on Unterstrasser (2016) with the modified water vapor emission. This approach should give a very rough estimate of the impact of cirrus ice crystals on the survival of contrail ice crystals within the vortex phase. In a sensitivity simulation the growth time period before vortex descent ( $t_{grow} = 19s$  instead of 9s) has been varied since, on the one hand, the time until vortex descent is not well defined and, on the other hand, during the first few seconds of vortex descent relative humidity may be such that cirrus ice crystals could grow at the cost of contrail ice

crystals. It has been found that increasing the growth time period hardly change the survival fraction.

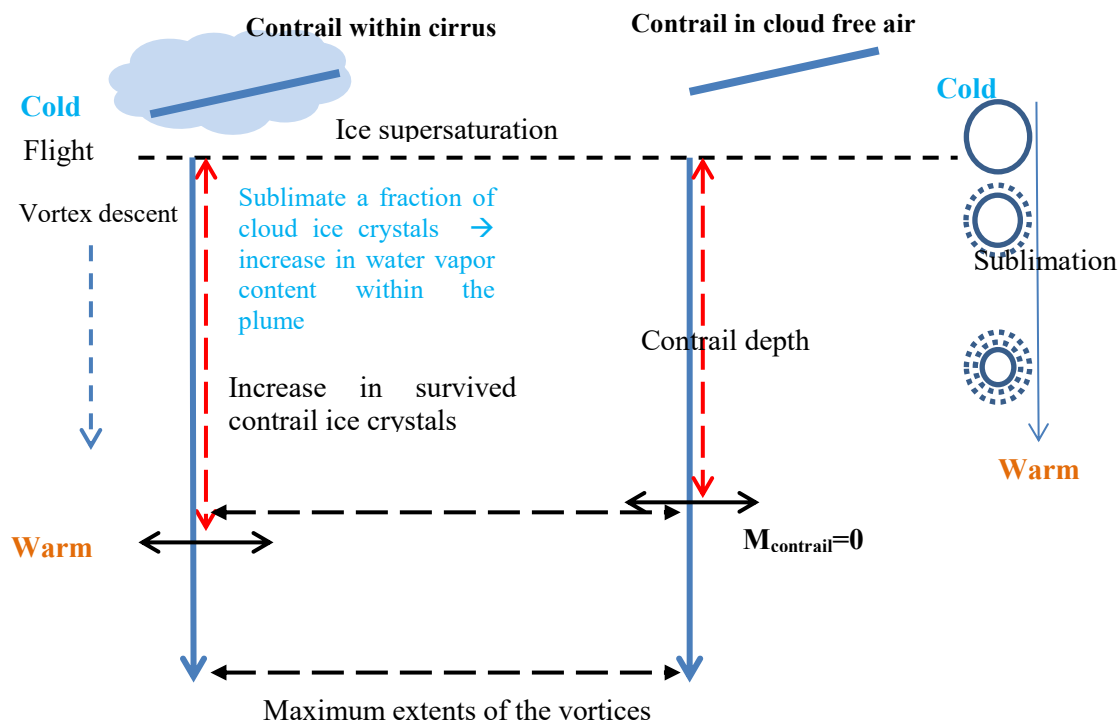


Figure 3.6: Schematic diagram to show effect of entrained cirrus ice crystals sublimation on the survival of contrail ice crystals during vortex descent.

### 3.3 Data

#### 3.3.1 Initial and boundary data

The model is initialized at 00 UTC from operational COSMO-DE analysis data (Baldauf et al., 2011). The reason for initializing the ICON model at midnight is that boundary layer turbulence develops in the morning so that the model is spun up during daytime. The initial and boundary condition data are interpolated to the domain grids by using a radial basis function (RBF) interpolation algorithm (Ruppert, 2007) with 3D variables interpolated vertically during initialization. COSMO-DE analysis data is used to prescribe lateral boundary data for the domain and is updated every hour. Soil moisture simulated by soil model Terra is used for initialization. Soil moisture is not interpolated vertically as both model COSMO-DE and ICON are using the same soil model. The time-invariant high-resolution observational dataset is used for topography, land use and soil-type specification at the lateral boundary. The datasets are gridded into the icosahedral grid using a pre-processor (Smiatek et al., 2008) and read in during the initialization of the model.

#### 3.3.2 Flight inventory

A four-dimensional (latitude, longitude, altitude and time) air traffic inventory for the year 2006 has been used for the simulation. The air traffic inventory was developed at the Volpe National Transportation Center using the U.S. Federal Aviation Administration Aviation Environmental

Design Tool (AEDT) (Wilkerson et al., 2010). AEDT inventory provides flight waypoints using real data from all global commercial flights at high temporal resolution (seconds, minutes and hourly) and predicts fuel burn and emission from the aircraft. The real aircraft data is collected from numerous sources, including Terminal Radar Approach Control Facilities (TRACON), individual airlines, Automated Radar Tracking Systems (ARTS) and Air Route Traffic Control Centers (ARTCC). The 2006 inventory included data collected by EUROCONTROL's Enhanced Tactical Flow Management System (ETFMS) which expanded flight data coverage over Europe. In AEDT emission flight inventory, each flight is divided into multiple linear segments; each segment consists of the spatial information of the flight - flight identification information e.g. speed, engine and aircraft type) and emissions e.g. black carbon, NO<sub>x</sub>, water vapor, fuel burn, CO<sub>2</sub> etc. The flight inventory (distance traveled within a grid box and fuel consumption to travel this distance) has been aggregated into 5-minute temporal resolution and horizontally into the 625 meters resolution icosahedral grid and vertically interpolated into 40 levels between 7 km altitude to 13 km altitude with 150 meters fixed spacing. The data consists of all aircraft (long distance aircraft and short distance aircraft) that fly over Germany and their emissions between 7 km to 13 km altitude. The flight inventory has been re-gridded into an icosahedral grid structure in two steps (figure 3.7). In the first step, the flight's waypoint data has been transformed into a regular grid and in the second step, the flight inventory has been transformed from regular grid structure to icosahedral grid structure using Radial Basis function (RBL). The horizontal resolution for regular as well as icosahedral grid structures is 625 meters. Vertical interpolation of flight data into the model vertical levels has been made during the initialization of the data into the model. To minimize model I/O, a temporal resolution of 5 minutes has been chosen for our gridded flight inventory, updating air traffic within the ICON-LEM every 5 minutes. Figure 3.7 shows the aggregated flight distance for 1 hour for a 150-meter thick vertical layer over Germany in regular grid structure (middle) and icosahedral grid structure (right). The horizontal area in the lat-lon box is larger than in the triangle box so that the aggregated flight distance within a grid box in the icosahedral grid structure is slightly lower than the aggregated flight distance in the regular grid box; however, the overall distance traveled remains the same. In the same way, a flight's waypoint data is gridded for all levels.

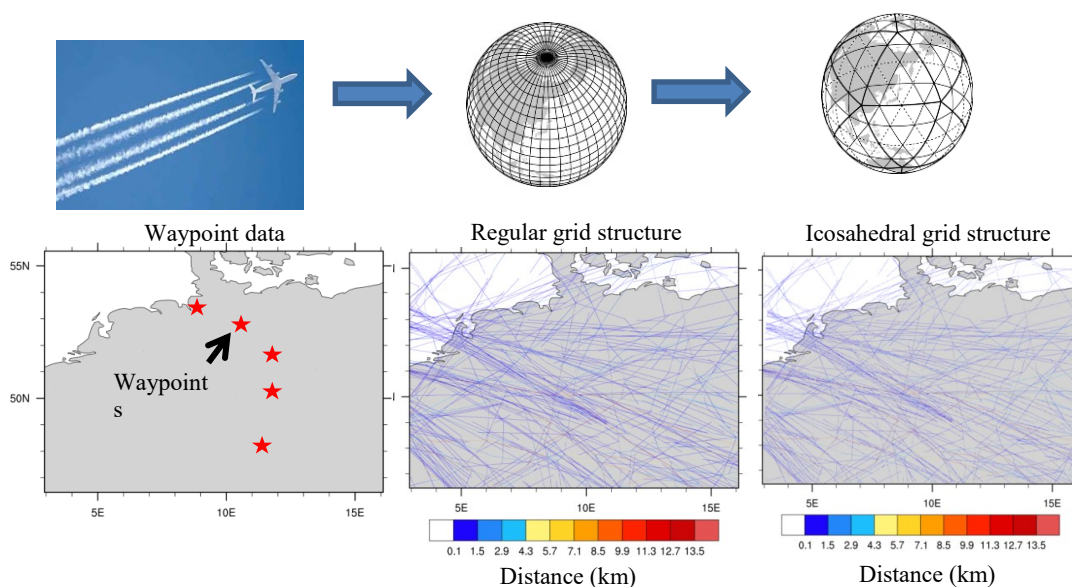


Figure 3.7: Gridding of flight's waypoint data into icosahedral grid structure: (left) schematic diagram for waypoint data; (middle) one-hour flight inventory for 150 meters thick vertical layer in lat-lon grid structure; (right) interpolated flight inventory in icosahedra grid structure.

### 3.4 Model setup

LES simulation with high resolution over a big domain like Germany is a huge computational challenge. Therefore, the ICON-LES has been set up only for the outer domain of 625 m resolution to perform high-resolution simulations over Germany. Here the resolution means the square root of the mean cell area in the icosahedral grid, equivalent to  $\sim 1.5$  times the regular grid. The 150 vertical levels are used from surface to 21 km altitude. The thickness of each layer varies with minimal thickness in the atmospheric boundary layer close to the surface and coarser at the top. A fast physics time-step for the outer domain is set to 3s. The fast physics time-step for inner domains is halved for each nest. An eight-grid element wide zone at the outer boundary of the domain is used for nudging of the prognostic variable to the COSMO-DE simulations. The initial and lateral boundary data is taken from operational COSMO-DE and gridded on the ICON grid separately beforehand with a pre-processor and read-in by ICON from the input files during the model initialization. The model is spun up for 6 hours starting from midnight.

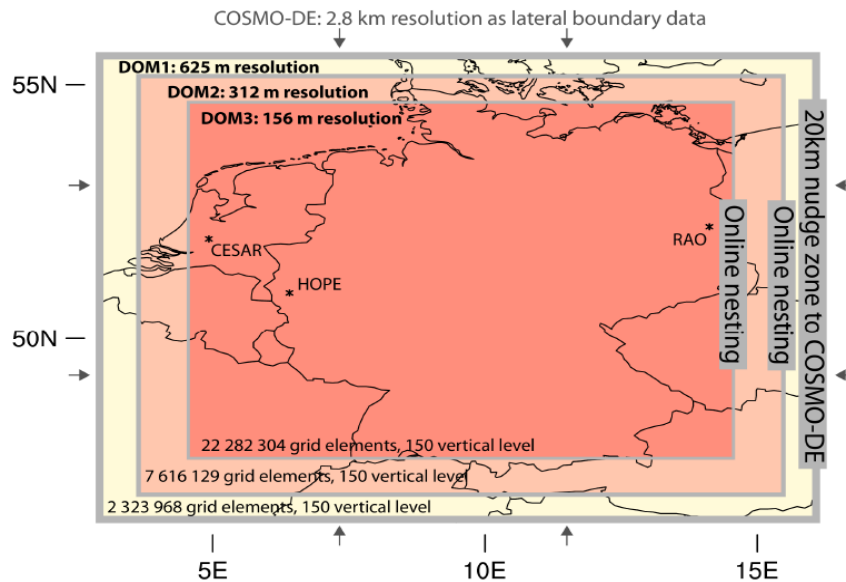


Figure 3.8: Simulation setup, domain set up over Germany with two nests with refinement 312 m and 156 m (figure taken from Heinze et al. (2017)). Only the outer domain of 625 meters resolution has been used in this doctoral thesis.

### 3.5 Synoptic conditions for the case studies

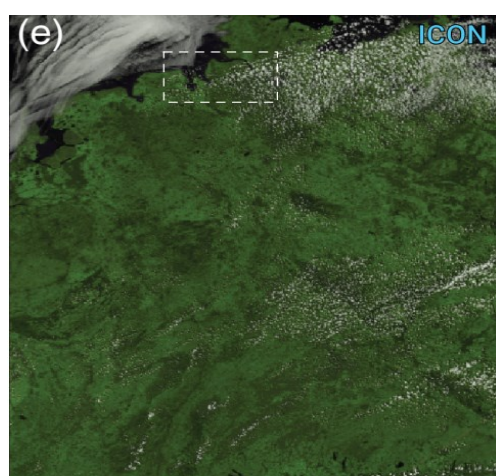
The two different synoptic conditions have been used for the simulations, 24<sup>th</sup> April 2013 and 26<sup>th</sup> April 2013. The days were part of the HD(CP)<sup>2</sup> HOPE measurement campaign (Macke et al., 2017) that had the goal of evaluating the performance of the high-resolution ICON simulations. The synoptic conditions on those two days were very different; this allows studying contrail formation within pre-existing cirrus in strongly varying synoptic settings leading to distinct cloud microphysical properties. On the 24<sup>th</sup> of April, a high-pressure system dominated over Germany with close to clear sky conditions in many areas and some thin cirrus in the morning; from noon onwards, the sky was more or less clear (Figure 3.9(a)). The situation stayed the same till the next

day. The simulation, including air traffic, began at 06:00 am starting from a state simulated by ICON-LES, not including air traffic effects (Heinze et al., 2017).

Another synoptic condition on 26<sup>th</sup> April 2013 has been used for the analysis. On this day, a frontal system was passing over Germany, moving towards the southeast, connected with a conveyor belt supplying the upper troposphere with moist air. A thick cirrus cloud field was formed and extended along the frontal passage. The front separated the cold and dry air coming from the north, with warm and moist air from the south. The cold front was connected with a low-pressure system and extended from southern Scandinavia to northern Germany and France. The low-level northerly flow advected the colder air from the north towards the warmer air. In the cold front system, dense cold air flows under the warm air and lifts it, forming clouds and precipitation. At higher levels, on the leading edge of a trough upstream, mid and upper-tropospheric winds were southwesterly, so that clouds were advected to the northeast. The frontal system approached the simulation domain throughout the day and caused vertically deep and optically thick clouds connected with the intense lifting. The cirrus cloud is extended from southwest to northeast along with the cold front system (figure 3.9).

The simulations for those days were part of the model evaluation performed by Heinze et al. (2017) and Stevens et al. (2020). Heinze et al., (2017) showed that the synoptic systems on those days were simulated well by ICON. The high resolution of the ICON-LEM simulations led to improvements e.g. in the vertical cloud structure and the diurnal cycle of clouds (Stevens et al., 2020). On the 24<sup>th</sup> of April, cloudiness, in general, may be overestimated in comparison with MODIS images over central Germany, while cirrus clouds, for instance in the northwest of Germany, are largely missed or are too thin in the simulations. Over the middle of Germany, a large thin cirrus cloud field with low ice water content and ice crystal number concentration is simulated in an ice saturated environment and persists for several hours. The cirrus field is spatially very homogeneous. On the 26<sup>th</sup> of April, ICON simulates the frontal passage realistically and shows a slight underestimation of cloud fraction, with good agreement regarding the cloud water path (CWP) (Heinze et al., 2017). The cirrus is scattered and the microphysical properties of the cirrus vary significantly. Lifting within the frontal zone ensures a continuous water vapor supply in the upper troposphere and provides ice supersaturated conditions within the relatively thick cirrus layer. The conditions are therefore favorable for contrail formation and ice crystal growth.

24 April 2013 at 12:35UTC (Thin cirrus or clear sky)



26 April 2013 at 12:20UTC (Frontal cloud)

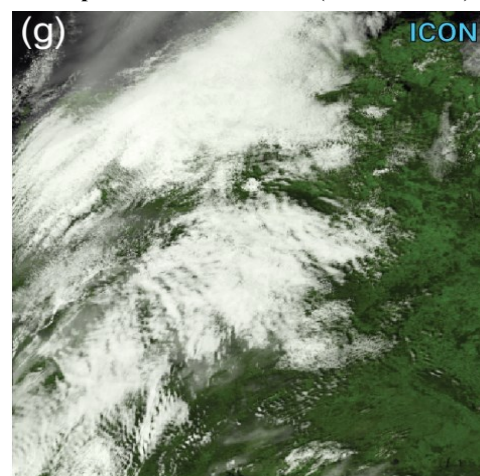


Figure 3.9: Synthetic image simulated by ICON model for 24<sup>th</sup> April 2013 at 12:35 UTC (left) and for 26<sup>th</sup> April 2013 at 12:20 UTC (right). Source: (Heinze et al., 2017)

### 3.6 Cloud frequency altitude diagram for control experiments

The cloud properties of cirrus on selected synoptic conditions have been analyzed using a cloud frequency altitude diagram (CFAD). CFAD shows the frequency of occurrence (probability density) of cloud properties, in particular, ice water content, number concentration of ice crystals and volume mean diameter of ice crystals at different temperatures.

Figure 3.10 shows the frequency of occurrence of ice crystal number concentration (figure 3.10 b, e), the mean diameter of ice crystals (figure 3.10 c, f), and ice water content IWC (figure 3.10 a, d) at different temperatures in the cirrus cloud field over Germany for the 24<sup>th</sup> and 26<sup>th</sup> April 2013 at 6-7 am and 5-6 pm, respectively. On the morning of the 24<sup>th</sup> of April, the cirrus cloud over Germany is relatively homogeneous. The probability of cloudy areas reaching ice crystal number concentrations of roughly  $10^5 \text{ m}^{-3}$  at about 220K, a typical cruise level, is 0.01%. At the same time, IWC is low and only in 0.01% of the cirrus at 220K values of  $3 \cdot 10^{-3} \text{ gm}^{-3}$  are reached. On the evening of the 26<sup>th</sup> of April, the distributions of ice crystal number concentration and IWC are much wider, with 0.01% of cloudy areas reaching values of up to  $10^8 \text{ m}^{-3}$  and  $0.5 \text{ gm}^{-3}$  at 220K. Describing the width of the distribution by the values occurring with a probability of 0.01%, the diameter of the ice crystals varies strongly with temperature, ranging between 20 $\mu\text{m}$  and 200 $\mu\text{m}$  at a temperature of 210K and between 20 $\mu\text{m}$  and 400 $\mu\text{m}$  at a temperature of 230K on the 24<sup>th</sup> April 2013. On the evening of the 26<sup>th</sup> April 2013, the range is between less than 10 $\mu\text{m}$  and 200 $\mu\text{m}$  and between 15  $\mu\text{m}$  and 600 $\mu\text{m}$  at temperatures of 210K and 230K, respectively. The most striking difference between the cirrus properties on the two days is the large differences in ice number concentrations with extrema in ice number concentrations at 220K, about 3 orders of magnitude higher on the 26<sup>th</sup> of April than on the 24<sup>th</sup> of April. At the same time, extrema in IWC are approximately 1 order of magnitude larger on the 26<sup>th</sup> of April, with the probability of small ice crystal sizes increased. Those high concentrations of small ice crystals on the 26<sup>th</sup> of April are probably connected with homogeneous freezing events happening in the areas of high ice supersaturation caused by lifting in the conveyor belts and with the freezing of droplets lifted within convective systems along the front. The vertical line in the diameter diagram (figure 3.10 c and f) is an artifact coming from the lateral boundary conditions supplied by COSMO, which is run using a 1-moment microphysical scheme. When using COSMO data for the forcing fields, a diameter of 100 $\mu\text{m}$  and associated ice crystal numbers are assumed (personal communication Axel Seifert, DWD), leading to an increased probability of ice crystal sizes of 100 $\mu\text{m}$ , particularly in areas close to the model edge.

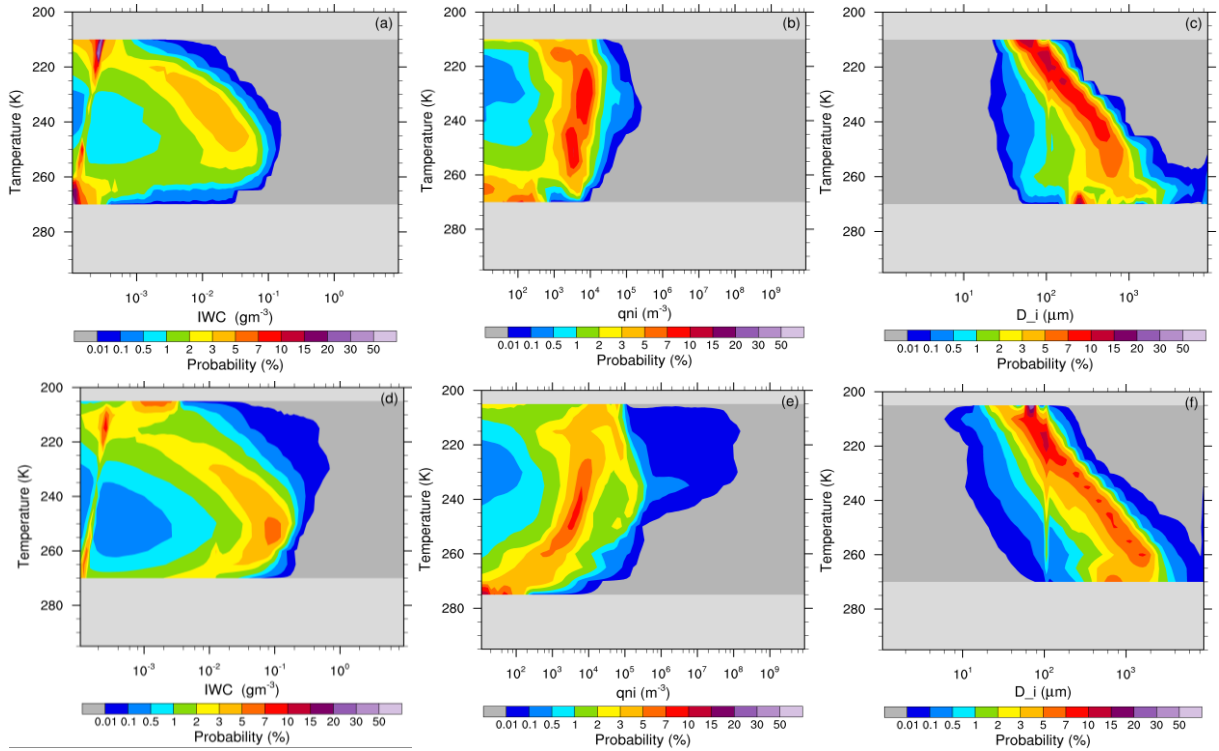


Figure 3.10: Frequency of occurrence of IWC (a, d), ice crystal number concentration (b, e), and mean volume diameter of ice crystals (c, f) on the (a,b,c) 24<sup>th</sup> April 2013 at 06 - 07 am and (d,e,f) 26<sup>th</sup> April at 5 – 6 pm. The frequencies of occurrence refer to individual temperature bins.

### 3.7 Apparent ice emission index of contrail ice crystal

In this section, the model simulated apparent emission index of the contrail ice crystals  $AEI_i$  using parameterization for contrail ice nucleation based on Kärcher et al. (2015), is shown. The apparent emission index of contrail ice crystals has been calculated by prescribing soot emission index ( $EI_s$ ), assuming current day soot rich emission  $2.5 \times 10^{15}$  soot particles per kg-fuel (Bräuer et al., 2021), on model levels between 7 km to 13 km altitudes. Figure 3.11 shows the dependency of  $AEI_i$  on the difference between the ambient and the contrail formation threshold temperature in the altitude range between 9.6 to 10.8 km for varying atmospheric conditions. Close to the formation threshold ( $T_{sa} - T_a < 3K$ ),  $AEI_i$  rapidly increases with an increasing difference between ambient temperature and the contrail formation threshold temperature. Since the mixing time scale of the plume with ambient air will be small, and thus the plume supersaturation will be low, this causes activation of only a few soot particles into the water droplets to form ice crystals. Ambient temperature close to the formation threshold condition very often occurs in low altitudes where the air is relatively warm. At ambient temperature far below the temperature threshold, a large percentage of the soot particles activate and form contrail ice crystals so that  $AEI_i$  approaches  $EI_s$ . The apparent emission index of ice varies for the fixed difference between ambient and Schmidt-Appleman temperature since atmospheric conditions, i.e. pressure, water vapor mixing ratio, and the Schmidt-Appleman temperature are not constant. The model simulated  $AEI_i$  shows a similar kind of tendency as  $AEI_i$  in Kärcher et al. (2015); however, their  $AEI_i$  is shown for fixed atmospheric conditions.

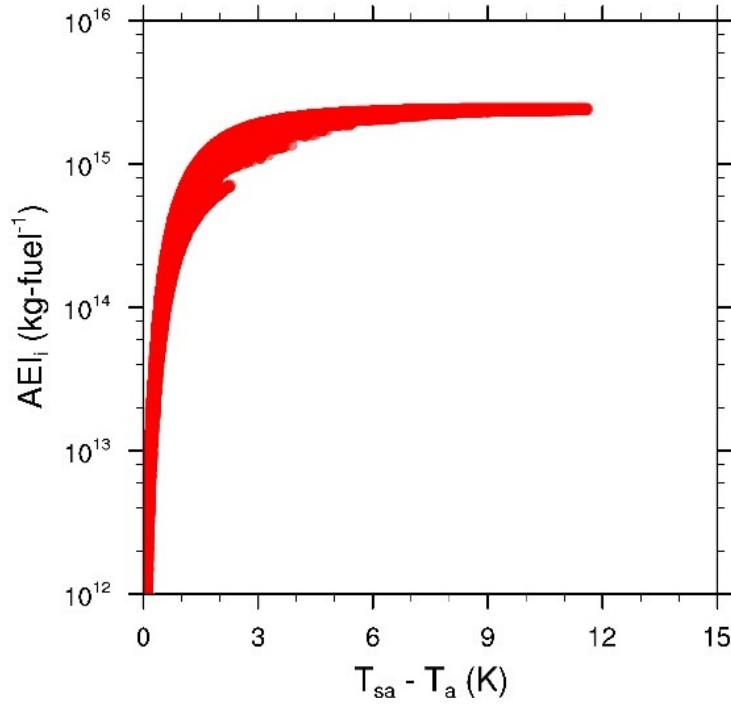


Figure 3.11: Apparent emission index ( $AEI_i$ ) for contrail ice crystals after nucleation simulated by ICON-LEM. The X-axis shows the offset between the formation threshold and ambient temperature,  $T_{sa}$ , for the 26<sup>th</sup> April 2013 at altitudes between 9.6km to 10.8km for varying atmospheric pressure and ice saturation ratio when including the impact of cirrus ice crystal sublimation during combustion.

### 3.8 Diffusional growth equation to calculate sublimation and deposition rate of an ice crystal

This section describes the diffusional growth equation to calculate sublimation and deposition rate of an ice crystal during temporal evolution of aircraft plume i.e., sublimation and deposition of entrained cirrus ice crystals during plume mixing in jet phase (section 3.2.1.3), deposition on cirrus and contrail ice crystal after nucleation (section 3.2.2.2) and sublimation of ice crystals during vortex descent (section 3.2.2.2). The sublimation rate (deposition rate) of an ice crystal in an ice subsaturated (ice supersaturated) environment has been calculated using the diffusional growth equation given in Pruppacher and Klett, (1997, page 547) and Lewellen (2012) (equation 5). The curvature effect in diffusional growth due to the different sizes of the ice crystals has been taken into account. The curvature term ' $a_k$ ' in the depositional growth equation is set to  $2 \times 10^{-9}$  as given in Lewellen 2012. The diffusivity of water vapor and thermal conductivity of air is calculated using modified equations with curvature effect given in Pruppacher and Klett, (1996, page 506,509, equation 13-14,13-20). Coefficients used in the depositional growth equation, diffusivity and thermal conductivity are given in table 3.2.

$$\frac{dm}{dt} = \frac{4\pi r(S - e^{a_k/r})}{L_S^2 K / R_v T^2 + R_v T / e_i(T) D} \quad (3.24)$$

where  $r$  is the radius of the ice crystal,  $S$  is the ice saturation ratio,  $D$  is the diffusivity of water vapor,  $K$  is the thermal conductivity of air and  $e_i(T)$  is saturation vapor pressure at temperature  $T$ .

**Table 3.2: Coefficient used in the diffusional growth equation**

kelvin term ' $a_k$ '	$2.0 \times 10^{-9}$
Thermal accommodation coefficient ' $\alpha_t$ '	0.7
Mass accommodation coefficient ' $\alpha_d$ '	0.5 Kärcher (2003)

### 3.9 Optical depth calculation of the contrail perturbed cirrus

This section explains the optical depth of the cirrus cloud when considering different shapes and size distributions of ice crystals. Cloud optical depth is an important parameter to represent the optical properties of the cloud and to estimate the cloud radiative forcing. Cloud particles reflect solar radiation and absorb terrestrial radiation, affecting the radiation budget of the earth. The optical properties of the cloud are dependent on the microphysical properties of the cloud i.e. ice water content, number concentration, sizes and shapes of the cloud particles. The shape of the ice crystal depends on the nucleation process and later the growth in the presence of ice supersaturation. For example, ice crystals formed from homogeneous freezing of liquid droplets initially have a spherical shape and later, if they grow at low temperatures ( $-40^\circ$  to  $-70^\circ\text{C}$ ) by depositional growth in the presence of ice supersaturation, then can form the columnar shape. Later ice crystals can also have a mix of different habits and form irregular shapes if two or more ice crystals stick together depending on the aggregation and rimming processes. It has been shown that large ice crystals have a greater number of habits mixed than smaller ice crystals (Schumann et al., 2010).

The optical depth of the cloud is dependent on the mean effective radius of the ice crystals and ice water content over the cloud depth (ice water path IWP). The optical depth can be calculated by vertically integrate extinction of the ice crystals (Schumann et al., 2010; Kärcher et al., 2009; Voigt et al., 2011). The extinction of the ice crystals is determined by the effective radius of the ice crystals (equation 20 and 21 in Kärcher et al., 2009), where, the effective radius of the ice crystals is dependent on the shape and size of the ice crystals (Schumann et al., 2010 and Kärcher et al., 2009). The effective radius for spherical and non-spherical particles can be expressed as:

$$r_e = \text{volume of the ice crystal/cross sectional area} = \frac{\int \pi r^3 n(r) dr}{\int \pi r^2 n(r) dr} \quad (3.12)$$

where ' $r$ ' is the radius of the ice crystal and  $n(r)$  is the number of ice particles of radius  $r$ . Calculating effective radius becomes more complicated for non-spherical particles as they don't have a well-defined radius, but their particle size distribution is defined from the maximum dimension or length of ice crystals. Therefore, for model studies, it is important to understand the relationship between volume mean radius ' $r_{vol}$ ' and the effective radius for different ice crystal shapes and their impact on the estimation of optical depth. Schumann et al. (2010) defined a parameter ( $C=r_{vol}/r_e$ ) to represent the relationship between mean volume radius and effective radius. In order to understand the relationship between volume mean radius and effective radius, different shapes and particle size distribution suggested in previous literature and observations have been considered. The considered shape and particle size distributions are (1) monodisperse spherical particles (2) irregular shapes and log-normal distribution of ice crystals (as considered in the ICON model) (3) habit mix ice

crystals and monodisperse (Schumann et al., 2010) and (4) habit mix ice crystals and log-normal particle size distribution (Schumann et al., 2010).

To simplify the calculation, firstly, all the ice crystals are assumed to be spherical and monodisperse; this makes effective radius ' $r_e$ ' equivalent to volume mean radius, and therefore, parameter C is 1. If ice crystals are irregular in shape, then C is less than 1 because the effective radius is larger than the volume mean radius for irregular shape ice crystals (figure 3.13). An assumption is made that habit mix gives parameter C larger than 1 because an increase in habit mix increases the volume mean radius; therefore, effective radius decreases as described in equation (3.12). While considering habit mix and particle size distribution, parameter C is larger than 1 but lower than parameter C calculated for habit mix monodisperse particles. The reason for this is that the effective radius decreases with increasing mean volume radius, but due to particle size distribution, the mean effective radius moves towards a large value (figure 3.13).

The optical depth of the cirrus cloud has been calculated using all four assumptions. The optical depth of the cirrus cloud on 24<sup>th</sup> April 2013 has been calculated along the vertical cut shown in figure 5.3 in chapter 5. Figure 3.13 shows the optical depth of the cloud along the vertical cut for both contrail perturbed cirrus and without perturbation of cirrus. Contrail ice crystal formation within cirrus introduces many small spherical and droxtal shape ice crystals in the cirrus cloud; these change the effective radius and particle size distribution in the cirrus and, therefore, change the optical depth of the cloud. Contrail formation within cirrus increases the number of ice crystals in the cloud but doesn't make a significant change in the ice water content; this means that the mean volume radius of the ice crystal population moves towards the small sizes, increasing the extinction of radiation. The previous study by Zhang et al. (1999) also explained that small ice crystals reflect more shortwave radiation than big ice crystals while keeping the ice water content unchanged. Contrail ice crystals also have the same effect on the reflectivity of shortwave radiation because contrail formation increases the number of small ice crystals within the cloud but ice water content remains more or less the same.

The optical depth has been calculated for a single wavelength of 550 nm for shortwave radiation by integrating extinction over the cloud length, where extinction of ice crystal is dependent on the mean effective radius. The extinction for short-wavelength has been calculated using the equation described in Schumann et al. (2010).

Optical depth calculated by assuming irregular shape is overall larger than the optical depth calculated from other shapes and particle size distribution. The reason is that the extinction is large for irregular shaped particles, with resultant large optical depth. Optical depth is fairly large in the area of contrail formation for all four cases because the number concentration of ice crystals is relatively high in contrail and causes an increase in the extinction and optical depth in those areas.

Assuming a habit mix and monodisperse particle is showing the smallest optical depth because the effective radius is smaller than the mean volume radius ( $C > 1$ ), the result is low extinction and low optical depth. On the other hand, optical depth is calculated by assuming spherical monodisperse particle is larger than the optical depth calculated by assuming habit mix monodisperse because effective radius for monodisperse spherical particles is equivalent to volume mean radius ( $C = 1$ ).

Optical depth calculated assuming habit mix and particle size distribution is more realistic since it has the effect of habit mix and particle size distribution. The assumption is that irregular shape particles reduce the effect of contrail ice crystals because newly formed contrail ice crystals are

more spherical and that irregular shape leads to a large effective radius for the small ice crystals. Irregular shape may be useful for calculating optical depth for cirrus clouds that have large ice crystals but in this special case, where contrail and cirrus ice crystals are mixed, considering irregular shape leads to high optical depth. Assuming that spherical and monodisperse particles will show the effect of the spherical particle e.g. contrail, but in the natural cloud, ice crystal's habits depend on their nucleation processes and growth processes. Therefore, assuming spherical monodisperse particles reduce the effect of shape and sizes is usually found in the cirrus cloud.

Assuming a habit mix and monodisperse particle will show the effect of habit mix but reduces the effect of different particle sizes in the cirrus. Therefore, to account for the effect of contrail ice crystal and cirrus ice crystal properties on the optical depth of the cloud, it is important to consider habit mix and particle size distribution. For further optical depth analysis, the habit mix and particle size distribution have been considered (chapter 5, section 5.4).

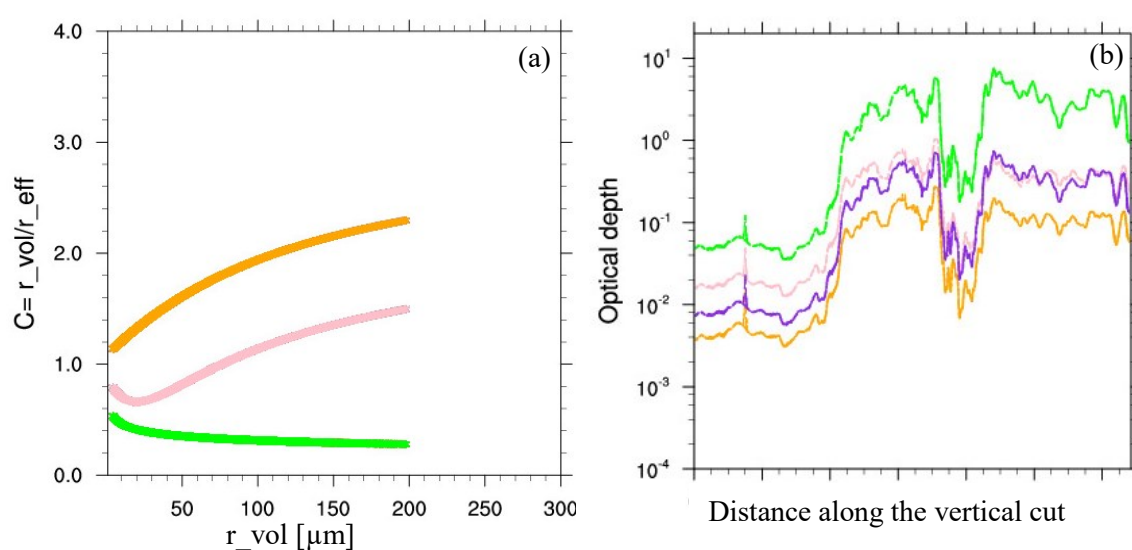


Figure 3.12: Volume mean radius,  $r_{vol}$  vs ratio between volume mean radius and effective radius, 'C' (left figure) and optical depth (right figure) have been calculated along the black line shown in figure 5.3. The optical depth and effective radius have been calculated for four different assumptions (1) assuming spherical and monodisperse ice crystals (purple line) (2) assuming the irregular shape of ice crystal and log-normal particle size distribution (green line) (3) assuming habit mix and monodisperse ice particles (orange line) and (4) habit mix and log-normal particle size distribution (pink line).



## Chapter 4

# Impact of the background cirrus on contrail formation

*The results of this chapter have been published in Verma and Burkhardt (2021)*

The previous chapter describes parameterization for contrail ice formation in a high-resolution model ICON-LEM. The contrail parameterization includes the effect of the pre-existing cirrus on contrail formation within cirrus, i.e. change in contrail formation threshold temperature, the number of nucleated ice crystals in contrail, and ice crystal loss in the vortex phase.

This chapter explains the effect of pre-existing cirrus ice on contrail ice crystals formation. The sublimation of cirrus ice crystals during combustion and after exhaust emission the sublimation and the deposition of the entrained cirrus ice crystals may cause a change in the water vapor mixing ratio in the plume (Chapter 3 section 3.2.1.3). It may lead to a change in the contrail formation threshold temperature and ice nucleation rate in contrail. Therefore, the first section explains the pre-existing cirrus's effect on contrail formation threshold temperature (section 4.1.1). Following the change in formation threshold temperature, section 4.1.2 shows the effect of change in formation threshold on the number of nucleated ice crystals in a contrail. It has been shown how significant the impact of pre-existing cirrus on contrail ice nucleation can be, what kind of atmospheric and cirrus properties can significantly affect ice nucleation rate, and how often those situations can be found within the cloud.

Later in this chapter, the effect of the cirrus ice sublimation on the survival fraction of contrail ice crystals during vortex descent has been explained (section 4.2). The contrail ice crystal's survival fraction depends on the atmospheric and aircraft properties but strongly depends on relative humidity. The survival fraction of the contrail ice crystals increases with increasing saturation ratio with respect to ice (chapter 3, section 3.2.2). In case of contrail formation within cirrus, pre-existing cirrus ice crystals that are mixed in the plume air can have an impact on the survival of the contrail ice crystals by affecting contrail ice crystals growth before vortex descent and by increasing the relative humidity in the vortex due to sublimation of ice crystals during vortex descent and therefore, can cause a change in survival of the contrail ice crystals (section 4.2).

Two synoptic conditions on 24<sup>th</sup> and 26<sup>th</sup> April 2013 have been used to analyze simulated contrails within cirrus. A detailed introduction of chosen synoptic conditions has been described in chapter 3 (section 3.5). The selected cirrus clouds covered a large range of cloud properties that are suitable for the study. Instead of prescribing a flight inventory, air traffic and their emission have been prescribed everywhere in the upper troposphere, where persistent contrails can form to analyze the impact of natural cirrus on contrail formation. A fixed aircraft emission within each grid box at altitudes between 7km to 13km, assuming distance traveled within a grid box is 600 meters, and fuel burn per kilometer is 6 kg-fuel/km, which is typical for cruise condition over Germany according to the Aviation Environmental Design Tool AEDT air traffic inventory (Wilkerson et al., 2010). Soot number emissions are set to  $2.5 \times 10^{15}$  kg-fuel<sup>-1</sup> in line with Bräuer et al., (2021). The aircraft emission has been prescribed only for one timestep at 6 am and 5 pm on 24<sup>th</sup> and 26<sup>th</sup> April 2013, respectively. The number of cloudy grid boxes (where ice water content >  $10^{-11}$  kg m<sup>-3</sup>)

between altitudes from 7km to 13km are approximately 6 million on 24<sup>th</sup> April at 6 am and approximately 5.5 million on 26<sup>th</sup> April at 5 pm.

## 4.1 Effect of pre-existing cirrus ice crystals on contrail ice nucleation

The effect of the cirrus ice crystals sublimation on the contrail ice crystal nucleation has been analyzed in this section. When aircraft fly through the cirrus, then cirrus ice crystals get sucked in together with air and sublimate in the combustion chamber, which causes an increase in the total water vapor content in the aircraft exhaust plume. The total sublimated ice water mass from cirrus ice crystals during combustion is estimated by the number of ice crystals that are sucked into the aircraft and their associated total ice water mass (chapter 3 and section 3.2.1.3). Furthermore, after exhaust emission, the surrounding cirrus ice crystals start to mix with the plume's air and sublimate during initial mixing due to high subsaturation and high temperature of the exhaust air, which causes a further increase in the water vapor content in the plume. Ice crystals sublimate until plume air reaches ice saturation; after that, available water vapor starts to deposit on the entrained cirrus ice crystals and causes a decrease in the water vapor mixing ratio in the plume (chapter 3 and section 3.2.1.3). This adjustment in the plume's water vapor content slightly changes the slope of the average mixing line (Chapter 3 section 3.2.1.4) and, therefore, the contrail formation threshold temperature. In the following sections, the effect of the adjustment in plume water vapor content due to pre-existing cirrus on contrail formation threshold temperature has been described (section 4.1.1), and then effect on contrail ice nucleation rate due to change in formation threshold has been described (section 4.1.2).

### 4.1.1 Effect of pre-existing cirrus on contrail formation threshold temperature

In order to nucleate ice crystals in contrail, the Schmidt-Appleman criterion should be fulfilled (Schumann, 1996). This criterion quantifies the warmest threshold ambient temperature beyond which contrails can form. This threshold temperature is calculated from given ambient conditions and aircraft parameters (chapter 3, section 3.2.1.1) and depends on the slope of the mixing line. In the case of contrail formation within pre-existing cirrus, cirrus ice crystals cause a change in the plume's water vapor mixing ratio. This aviation-induced change in the plume's water vapor mixing ratio changes the slope of the mixing line and, therefore, contrail formation threshold temperature (chapter 3). It has been seen that the maximum change in water vapor in the plume is 0.5% in the case of thin cirrus (24<sup>th</sup> April 2013) and 20% in the case of thick cirrus (26<sup>th</sup> April 2013) (chapter 3 section 3.2.2 and figure 3.5). The maximum change in aviation-induced increase in plume's water vapor is associated with the large ice water content in the pre-existing cirrus. However, the probability of these maximum changes in the aviation-induced increase in plume's water vapor mixing ratio is very low (below 10<sup>-2</sup>%). Since low altitudes have more ice water content than high altitudes, a large increase in plume's water vapor due to sublimation of cirrus ice crystals and thus change in the contrail formation threshold can be seen in the low altitudes. Although, the change in the plume's water vapor content due to sublimation and deposition of cirrus ice crystals has a small impact on aviation-induced water vapor increase but shows a significant change in the contrail formation threshold temperature.

In high altitudes, above 11 km, the difference between formation threshold temperature and ambient temperature is always more than 5K (figure 4.1(a), &(b)), and due to low ice water content in cirrus in those altitudes, changes in the contrail formation threshold temperature are negligible. Therefore,

to analyze the effect of sublimated ice water mass on the contrail formation threshold temperature ( $T_{sa}$ ), two different altitudes ranges between  $\sim 9.6$  km to  $\sim 9.8$  km and  $\sim 10.3$  km to  $\sim 10.8$  km, have been selected.

At main air traffic altitudes between 10.3 km to 10.8 km, the difference between contrail formation threshold temperature and ambient temperatures are between 4K and 10K on the date 26<sup>th</sup> April 2013, and in the case of thin cirrus on 24<sup>th</sup> April 2013, the temperature difference is between the range 1.5K to 7K. At altitudes between 9.6 km to 9.8 km, ambient temperature is close to the formation threshold (difference below 5 K).

The change in  $T_{sa}$  on the date 24<sup>th</sup> April 2013 is very insignificant, specifically for high altitudes above 10 km. For the altitudes between 9.6 km to 9.8 km, the change in the contrail formation threshold temperature ranges only between -0.01K to 0.04K connected with the small impact of cirrus ice sublimation on the aviation-induced increase in water vapor. On this synoptic day, cirrus cloud has very low ice water content and ice number concentration; therefore, the contribution of water mass from ice crystals sublimation to the plume's relative humidity is very low (figure 3.4 in chapter 3) and the resultant change in the contrail formation threshold temperature is low (figure 4.1). On the 26<sup>th</sup> of April, the change in the threshold temperature  $\Delta T_{sa}$  is relatively large and can reach values up to 1.6 K in the lower and relatively warmer atmospheric levels (between 9.6 km and 9.8 km at ambient temperatures between 223K and 227K) and values of up to 2 K in the higher altitudes (between 10.3 km and 10.8 km at ambient temperatures between 215K and 221K).

On the 26<sup>th</sup> of April, large changes in the contrail formation threshold temperature are associated with low ambient relative humidity (figure 4.1 (c) & (d)). An ice saturation ratio close to 1 within a cloud indicates the presence of a high ice crystal number concentration that reduces the available water vapor due to diffusional growth of the ice crystals and leads to an efficient relaxation of supersaturation to the saturation value. The high saturation ratios, i.e., at ice saturation ratios of 1.4 and 1.5, on the other hand, indicate low ice crystal concentrations and ice water content and are likely to be the areas in which homogeneous and/or heterogeneous nucleation may occur within the next few time steps. In areas with a high ice saturation ratio ( $\sim 1.4$ ), the change in  $T_{sa}$  is negligible.

As will be shown in the next subsection, the areas of large ice crystal number concentration are on the 26<sup>th</sup> April connected with ice saturation and large ice water content and ice number concentration in cirrus, which causes the large changes in  $T_{sa}$ . Sublimation of cirrus ice crystals strongly affects the number of nucleated ice crystals in those areas where contrail formation threshold temperature is close to the ambient temperature 'Close to formation threshold condition' ( $T_{sa} \rightarrow T_a$ ) because the number of nucleated ice crystals close to the formation threshold is highly sensitive to the amount of water vapor in the plume for condensation and to the difference between contrail formation threshold temperature and ambient temperature. Since, a very small amount of water vapor is available for the condensation when contrail forms under 'close to formation threshold condition', therefore only a few droplets form (Kärcher et al., 2015 and chapter 3).

The close to the threshold condition often occurs in lower altitudes where the ambient temperature is relatively warm. In higher altitudes, where the ambient temperature is quite cold, and far away from contrail formation threshold temperature, the number of nucleated ice crystals in the contrail is limited by the number of emitted soot particles (Kärcher et al., 2015 and chapter 3).

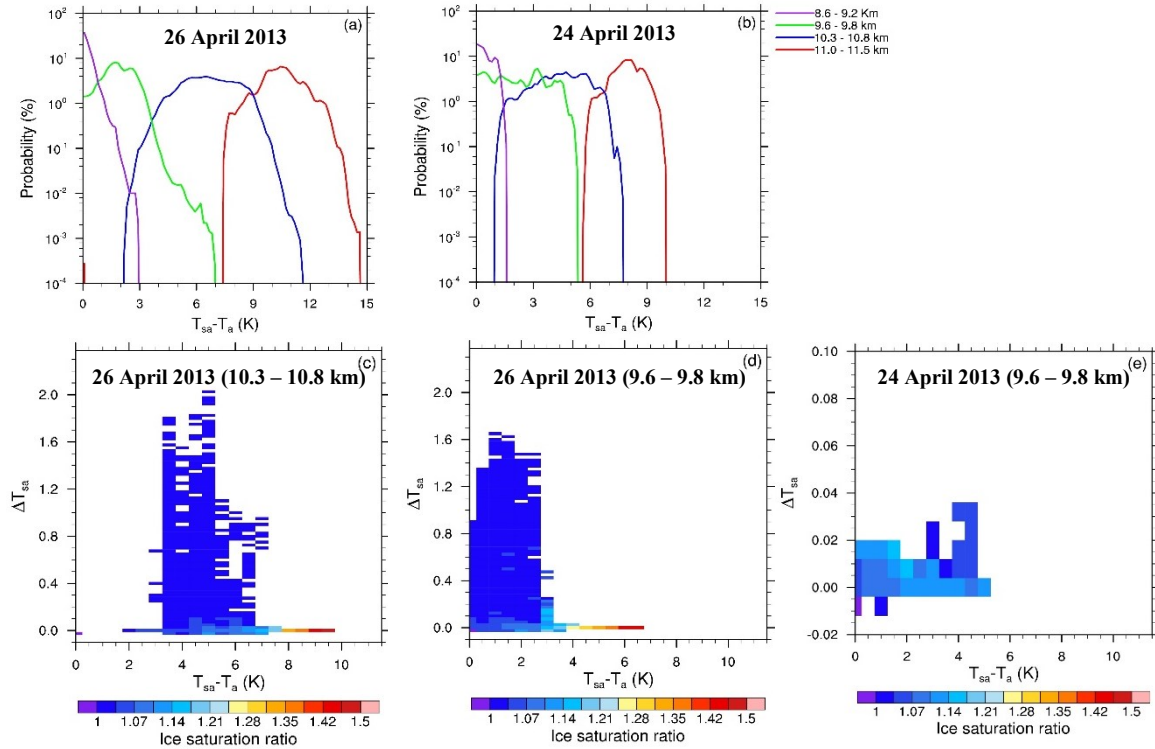


Figure 4.1: Probability distribution of the difference between the Schmidt-Appleman temperature threshold of contrail formation ( $T_{sa}$ ) and the ambient temperature ( $T_a$ ) at 11 – 11.5 km (red), 10.3 – 10.8 km (blue), 9.6 – 9.8 km (green) and 8.6 – 9.2 km (purple) on the 26<sup>th</sup> April (a) and 24<sup>th</sup> April (b). Difference between the Schmidt-Appleman temperature threshold ( $T_{sa}$ ) and the ambient temperature and change in  $T_{sa}$  due to impact of cirrus ice crystals on the 26<sup>th</sup> April 2013 5pm at altitudes of 10.3 (~250 hPa) to 10.8km (~225 hPa) (c) and at 9.6 (~280 hPa) to 9.8km (~270 hPa) (d) and on 24<sup>th</sup> April 2013 6am at altitudes of 9.6 (~280 hPa) to 9.8km (~270 hPa) (e). In all figures the difference of ambient air temperature and  $T_{sa}$  refers to the  $T_{sa}$  that is not modified due to the sublimation of pre-existing cirrus ice.

#### 4.1.2 Effect of pre-existing cirrus ice crystals on number of nucleated contrail ice crystals

The sublimation and deposition of pre-existing cirrus ice crystals before contrail ice nucleation changes the water vapor content in the exhaust plume, which causes a change in the contrail formation threshold temperature and, therefore, the number of nucleated contrail ice crystals. Although the change in the  $T_{sa}$  due to the sublimation of cirrus ice crystals is not very large, but it significantly affects the number of nucleated contrail ice crystals, specifically in lower altitudes where the ambient temperature is relatively warm, and formation threshold temperature is close to the ambient temperature. Close to the formation threshold condition, rapidly increasing fewer ice crystals form as formation threshold temperature moves away from the ambient temperature. A slight increase in the  $T_{sa}$  rapidly increases the number of nucleated ice crystals; therefore, a significant change in the number of nucleated contrail ice crystals can be expected when contrail ice forms close to the ambient temperature (figure 12 in Kärcher et al., 2015 and chapter 3 sections 3.2 & 3.7).

When contrail ice crystals form far away from the ambient temperature, a sufficient large supersaturation with respect to the water is produced during plume mixing causes activation of all the soot particles and entrained aerosol particles into the water droplets (figure 12 in Kärcher et al., 2015 and chapter 3 sections 3.2 & 3.7). Usually, high altitudes have much colder temperatures than the lower altitudes; therefore, offset between contrail formation threshold temperature and ambient temperature most likely are more than 5 K in higher altitudes.

In order to understand the impact of pre-existing cirrus ice on the number of nucleated contrail ice crystals, two different altitudes range 10.3 km to 10.8 km (typical flight levels), and 9.6 km to 9.8 km (low altitudes) similar as shown in section 4.1.1 have been analyzed for both synoptic conditions on 24<sup>th</sup> and 26<sup>th</sup> April 2013 (chapter 3, section 3.5).

The change in the contrail formation threshold shows a significant impact on contrail ice nucleation depending on the distance of the ambient temperature from the temperature threshold for contrail formation and on the amount of sublimated cirrus ice water. In the case of large difference ( $>2\text{K}$ ) between contrail formation threshold temperature and ambient temperature, if all the soot particles are activated into the ice, then the number concentration of contrail ice crystals within a model grid box (approx. volume of the model grid box is  $625 \times 625 \times 150 \text{ m}^3$ ) would reach around  $1.5 \times 10^8 \text{ m}^{-3}$ . At altitudes between 10.3 to 10.8 km, the number concentration of contrail ice crystals is  $1.2 \times 10^8$  and  $1.3 \times 10^8 \text{ m}^{-3}$  on 24<sup>th</sup> and 26<sup>th</sup> April 2013, respectively. The nucleated number of contrail ice crystals within pre-existing cirrus is significantly larger than the ice number concentration in the background cirrus. Therefore, contrail formation leads to significant perturbation in ice crystal number concentration in cirrus. At altitudes between 9.6 km to 9.8 km, the ambient temperature is often close to the formation threshold temperature, which leads to lower contrail ice concentration lie typically between  $4.0 \times 10^7 \text{ m}^{-3}$  and  $1.1 \times 10^8 \text{ m}^{-3}$  on the 26<sup>th</sup> of April (figure 4.3) and between  $1.0 \times 10^7 \text{ m}^{-3}$  and  $1.3 \times 10^8 \text{ m}^{-3}$  on the 24<sup>th</sup> of April (figure 4.5).

24<sup>th</sup> April 2013 case has cloud field with low ice water content and low ice number concentration ( $> 5 \times 10^5 \text{ per m}^3$ ); therefore, change in the number concentration of contrail ice crystal is not very large, specially in main flight levels where ice water content is not very large (figures 4.4). The ice number concentration has increased up to  $\sim 4 \times 10^5 \text{ m}^{-3}$  at main flight levels and has up to  $10^6 \text{ m}^{-3}$  in lower altitudes where the offset between formation threshold temperature and ambient temperature is below 2K (figure 4.5). The percentage change in the number concentration of ice crystal decreases with increasing distance between formation threshold temperature and ambient temperature and has low as  $\sim 0.008\%$  change in the number concentration of contrail ice crystal when the temperature difference between formation threshold and ambient is more than 7 kelvins (figures 4.4 & 4.5).

26<sup>th</sup> April 2013 case has cloud field with high ice water content and high ice number concentration of ice crystal; therefore, change in the number concentration of contrail ice crystal is significant in this particular case. Change in ice number concentration has increased with an increase in the ice water content and ice number concentration in cirrus. On the main flight levels around 10.5 km, a change in contrail formation threshold leads to a change in contrail ice number concentrations between  $10^1$  to  $10^7 \text{ m}^{-3}$ . The maximum change in the number concentration of contrail ice crystal is up to  $\sim 10\%$  with low probability. The largest probability of change in contrail ice number concentration is for the change in contrail ice number concentration around  $10^{-4} \text{ m}^{-3}$ .

The maximum changes in the number concentration of contrail ice crystals are visible in those cloudy areas where ice water content and ice number concentration are very high (figures 4.2 (b),

(c) & 4.3 (b), (c)) and well connected with the low ice saturation ratio (figures 4.2 (e) & 4.3 (e)). Large-scale lifting appears to lead to the freezing of water droplets and homogeneous nucleation events. The resulting large ice crystal number concentrations lead to an efficient relaxation of ice supersaturation to saturation values. In areas of lower ice crystal number concentrations, ice supersaturation can be large (figures 4.2 (c), (e) & 4.3 (c), (e)). The larger ice saturation ratio in those areas leads to high contrail ice nucleation rates and low corrections of this nucleation rate due to the sublimation and deposition of cirrus ice crystals during mixing. On the 24th of April 2013, ice nucleation was lower due to the higher temperatures (figures 4.4 (d)), and the change in ice nucleation was lower due to the cirrus clouds containing less ice water (figure 4.4 (b)).

The change in the nucleation rate can also be negative if the total deposition of water vapor on entrained cirrus ice crystals is larger than the total water vapor sublimated (in combustion + during mixing) from the entrained cirrus ice crystals. The maximum reduction in contrail ice crystal number concentration is only up to  $10^4 \text{ m}^{-3}$  which is several orders of magnitude smaller than the maximum possible increase in the contrail ice crystals number concentration, and around 22% and 14% of the total cloudy grid boxes has a reduction in nucleation rate on the 26<sup>th</sup> and 24<sup>th</sup> April cases respectively. Therefore, in this section, mainly the positive change in contrail ice nucleation rate has been discussed.

At lower altitudes, between 9.6 km and 9.8 km, the ambient temperature lies mostly within 5K of the contrail formation threshold (figures 4.1 (c) & 4.2 (c)). At those altitudes, changes in contrail ice nucleation due to sublimation of cirrus ice crystals within the engine are significantly large (figures 4.3 & 4.5) because the atmosphere is generally closer to the contrail formation threshold, and IWC is on average slightly higher in the lower altitudes. The change in the number concentration of contrail ice crystals is well connected with the ice water content and ice number concentration in the cloud. The maximum change in the number concentration of contrail ice crystal is visible where the formation threshold temperature is less than 5K, close to the ambient temperature (figure 4.3). The maximum changes are approximately one order of magnitude and by a factor of 3 larger than on the cruise level on 26<sup>th</sup> and 24<sup>th</sup> April, respectively. This means that on the 26<sup>th</sup> of April, the change in ice nucleation has the same order of magnitude as the ice nucleation when neglecting the impact of sublimating cirrus ice crystals, while on the 24<sup>th</sup> of April, the change due to the sublimation of cirrus ice crystals remains significantly lower. The negative change in the contrail ice number concentration in lower altitudes is comparably low. Around 7% of the total cloudy grid boxes have a negative impact of pre-existing cirrus on contrail ice nucleation rate in both synoptic conditions.

When compared to higher flight levels around 10.5 km, the maximum change in the nucleation of ice crystal number is at altitudes between 9.6 km to 9.8 km, a factor of 2 larger on both 26<sup>th</sup> of April and 24<sup>th</sup> of April cases (figures 4.2, 4.3, 4.4 & 4.5). In the case of 24<sup>th</sup> April 2013, change in number concentration of nucleated contrail ice crystal is maximally possible up to  $\sim 5 \times 10^5 \text{ m}^{-3}$  at altitudes between 10.3 km to 10.8 km (figure 4.4) and up to  $\sim 10^6 \text{ m}^{-3}$  for the altitudes between 9.6 km to 9.8 km (figure 4.5). For the 26<sup>th</sup> April 2013 case, the change in the number concentration of nucleated contrail ice crystal is maximum around  $5 \times 10^7 \text{ m}^{-3}$  for the altitude range 9.6 km to 9.8 km (figure 4.3) and around  $10^7 \text{ m}^{-3}$  for altitude range 10.3 km to 10.4 km (figure 4.2). Relative changes in ice nucleation are much larger in the lower levels because contrail forms close to the formation threshold. In the upper levels, relative changes in ice crystal numbers on 26<sup>th</sup> April case are approximately 10% (figure 4.2), while in the lower levels at around 9.7 km, the relative change can amount to 400% of the ice nucleation when neglecting the impact of cirrus ice crystals (figure 4.3). At both altitude ranges, maximum absolute changes in ice nucleation are between 1 and 2 orders of

magnitude smaller on the 24<sup>th</sup> April than on the 26<sup>th</sup> of April 2013, connecting to the lower IWC (figures 4.5 (b), 4.6 (b)), and ice saturation ratio (figures 4.5 (e), 4.6 (e)). The probability of maximum changes is very low, only 0.05% of grid boxes have a large change in the number concentration of nucleated contrail ice crystals at altitude levels 10.3 km to 10.4 km, and 0.0005% of grid boxes has maximum changes in the number concentration of nucleated contrail ice crystals at altitude levels 9.6 km to 9.8 km on 26<sup>th</sup> April 2013. Moreover, on 24<sup>th</sup> April 2013, maximum changes in the number concentration of nucleated contrail ice crystals at both altitude levels 10.3 km to 10.4 km and 9.6 km to 9.8 km are only 0.05% out of total cloudy grid boxes.

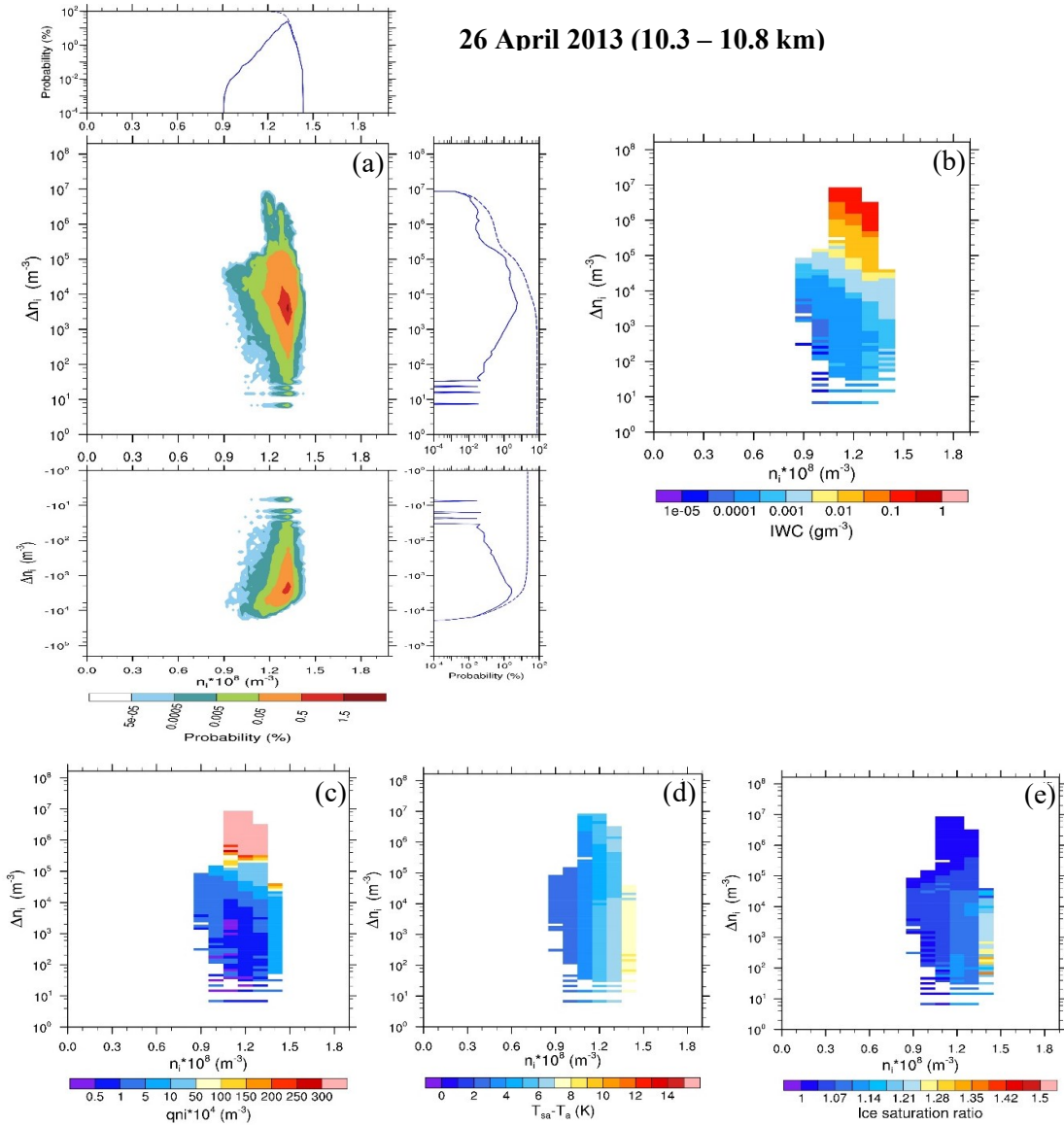


Figure 4.2: Joint probability distribution of ice crystal number concentration due to contrail ice nucleation,  $n_i$ , and its change due to the sublimation of cirrus ice crystals within the aircraft engine,  $\Delta n_i$ , for current soot number emissions,  $2.5 \cdot 10^{15} \text{ kg-fuel}^{-1}$ , for altitudes from 10.3 km to 10.8 km (230 hPa to 225 hPa) on the (a) 26<sup>th</sup> April 2013 5 pm. Additionally, the PDF of ice nucleation (solid) and the associated cumulative PDF (dashed), when neglecting the impact of natural cirrus ice crystals (top) and its change due to the presence of cirrus ice crystals (right), is shown. Mean ice cloud properties for the combination of  $n_i$  and  $\Delta n_i$  (b) IWC, (c)  $qni$ , (d) difference between temperature formation threshold and ambient temperature, and (e) ice saturation ratio. If all emitted soot particles would form an ice crystal, then the ice crystal number concentration within the grid box,  $n_i$ , would reach approximately  $1.5 \cdot 10^8 \text{ m}^{-3}$ .

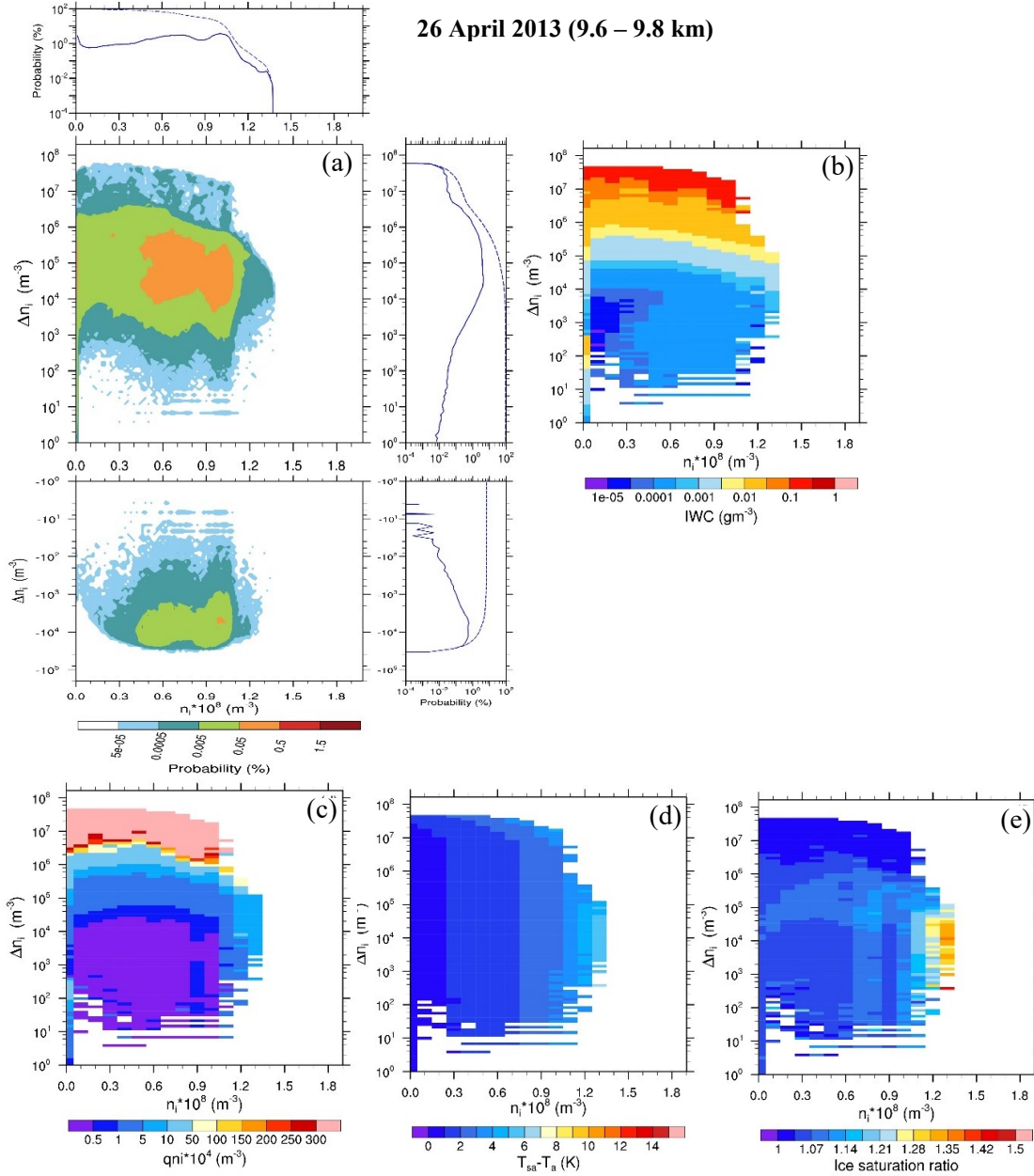


Figure 4.3: Joint probability distribution of ice crystal number concentration due to contrail ice nucleation,  $n_i$ , and its change due to the sublimation of cirrus ice crystals within the aircraft engine,  $\Delta n_i$ , for current soot number emissions,  $2.5 \cdot 10^{15} \text{ kg-fuel}^{-1}$ , for altitudes from 9.6 km to 9.8 km (280 hPa to 270 hPa) on the (a) 26<sup>th</sup> April 2013 5 pm. Additionally, the PDF of ice nucleation (solid) and the associated cumulative PDF (dashed), when neglecting the impact of natural cirrus ice crystals (top) and its change due to the presence of cirrus ice crystals (right), is shown. Mean ice cloud properties for the combination of  $n_i$  and  $\Delta n_i$  (b) IWC, (c)  $q_{ni}$ , (d) difference between temperature formation threshold and ambient temperature, and (e) ice saturation ratio. If all emitted soot particles would form an ice crystal, then the ice crystal number concentration within the grid box,  $n_i$ , would reach approximately  $1.5 \cdot 10^8 \text{ m}^{-3}$ .

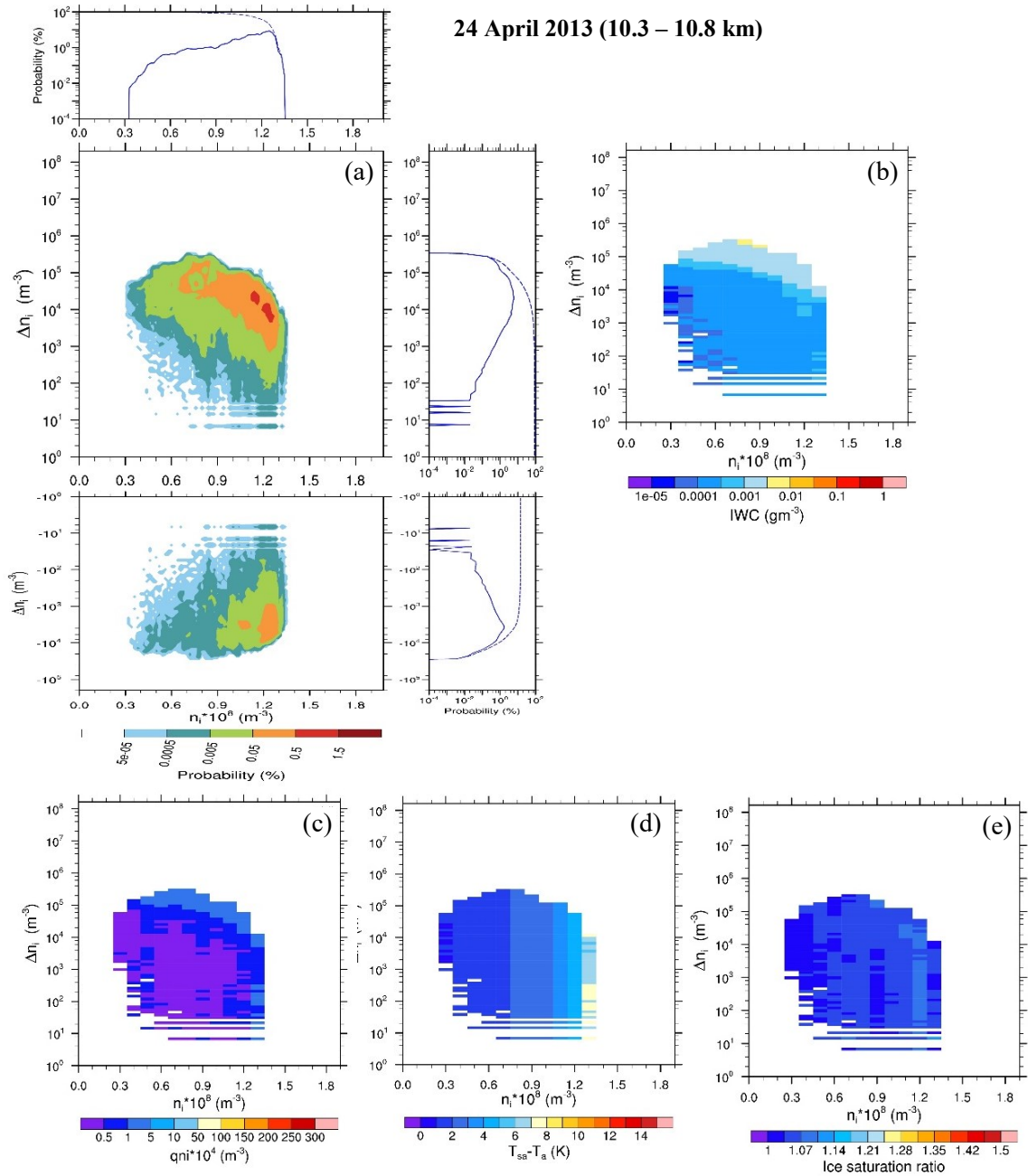


Figure 4.4: Joint probability distribution of ice crystal number concentration due to contrail ice nucleation,  $n_i$ , and its change due to the sublimation of cirrus ice crystals within the aircraft engine,  $\Delta n_i$ , for current soot number emissions,  $2.5 \times 10^{15} \text{ kg-fuel}^{-1}$ , for altitudes from 10.3 km to 10.4 km (230 hPa to 225 hPa) on the (a) 24<sup>th</sup> April 2013 6 am. Additionally, the PDF of ice nucleation (solid) and the associated cumulative PDF (dashed), when neglecting the impact of natural cirrus ice crystals (top) and its change due to the presence of cirrus ice crystals (right), is shown. Mean ice cloud properties for the combination of  $n_i$  and  $\Delta n_i$ : (b) IWC, (c)  $q n_i$ , (d) difference between temperature formation threshold and ambient temperature, and (e) ice saturation ratio. If all emitted soot particles would form an ice crystal, then the ice crystal number concentration within the grid box,  $n_i$ , would reach approximately  $1.5 \times 10^8 \text{ m}^{-3}$ .

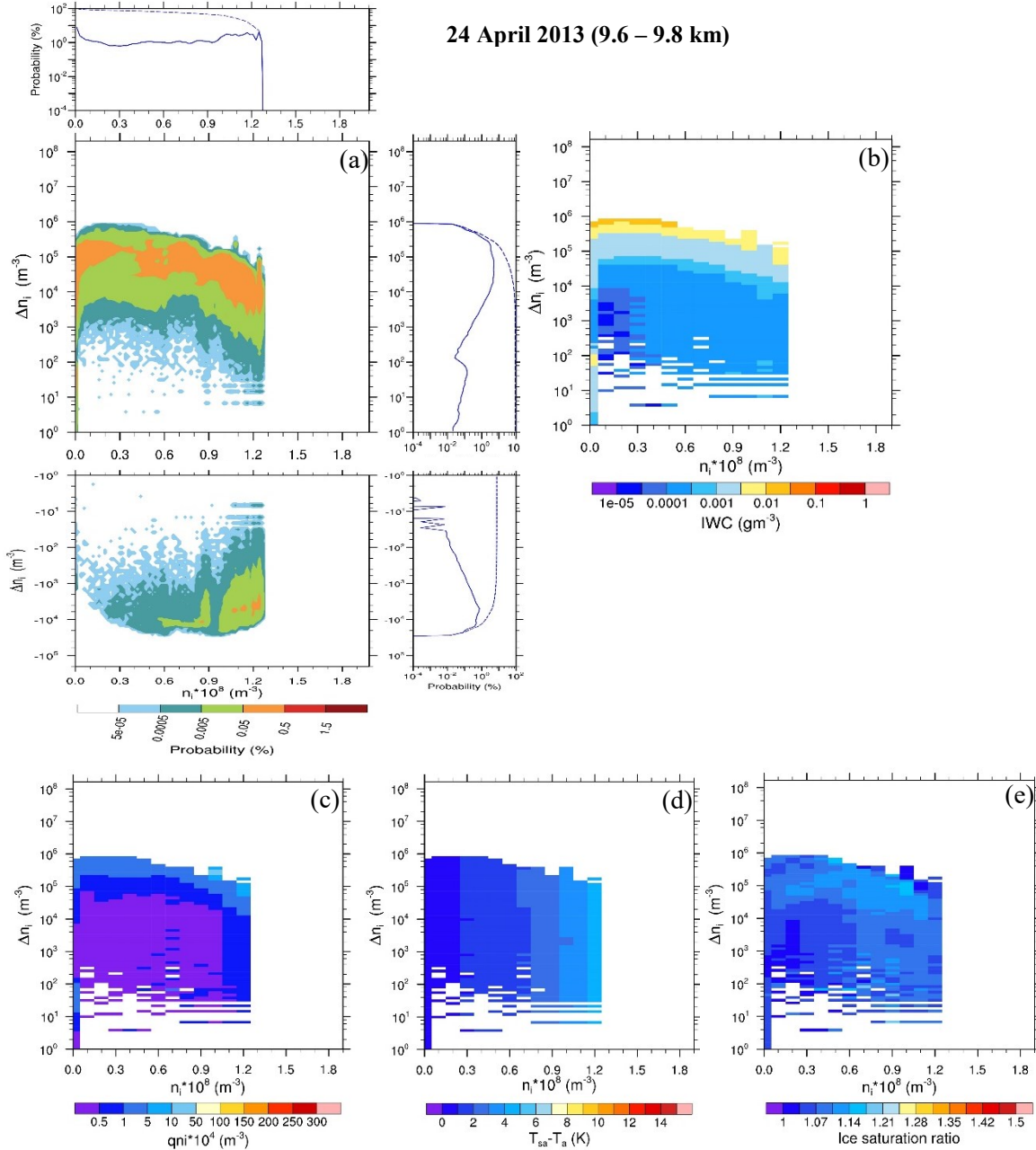


Figure 4.5: Joint probability distribution of ice crystal number concentration due to contrail ice nucleation,  $n_i$ , and its change due to the sublimation of cirrus ice crystals within the aircraft engine,  $\Delta n_i$ , for current soot number emissions,  $2.5 \cdot 10^{15} \text{ kg-fuel}^{-1}$ , for altitudes from 9.6 km to 9.8 km (280 hPa to 270 hPa) on the (a) 24<sup>th</sup> April 2013 6 am. Additionally, the PDF of ice nucleation (solid) and the associated cumulative PDF (dashed), when neglecting the impact of natural cirrus ice crystals (top) and its change due to the presence of cirrus ice crystals (right), is shown. Mean ice cloud properties for the combination of  $n_i$  and  $\Delta n_i$  (b) IWC, (c)  $q_{ni}$ , (d) difference between temperature formation threshold and ambient temperature, and (e) ice saturation ratio. If all emitted soot particles would form an ice crystal, then the ice crystal number concentration within the grid box,  $n_i$ , would reach approximately  $1.5 \cdot 10^8 \text{ m}^{-3}$ .

**Summary:** Section 4.1 concisely describes the impact of pre-existing cirrus ice crystals on the contrail formation threshold temperature and, subsequently, the number of nucleated contrail ice crystals. The sublimation of cirrus ice crystals during the combustion and subsequently sublimation of

/deposition on mixed in cirrus ice crystals in the plume causes a change in the contrail formation threshold temperature. The change in the contrail formation threshold temperature can be positive and negative. The positive change in the contrail formation threshold temperature can occasionally reach up to 2K when the ice water content is large in the pre-existing cirrus. The negative change in contrail formation threshold is very small ( $<0.1$  K). The change in the contrail formation threshold on the 24<sup>th</sup> April cloud is negligible since the ice water content of the cloud is very low. The change in contrail formation threshold temperature is relatively large on 26<sup>th</sup> April cloud because ice water content and ice number concentration are large in background cirrus. The change in the contrail formation threshold leads to a change in the number of nucleated contrail ice crystals. The positive change in the number of nucleated contrail ice crystals is large for large cirrus ice water content and cirrus ice number concentration. The relative change in the contrail ice number concentration is maximally reached up to 10% when contrails form far away from the contrail formation threshold temperature on the 26<sup>th</sup> April case. The relative change in contrail formation threshold can reach up to 400% in lower altitudes where contrails form under close to formation threshold conditions. On 24<sup>th</sup> April 2013, the change in contrail ice crystal number concentration is comparably lower than the change in contrail ice crystal number on 26<sup>th</sup> April connecting with low ice water content. The probability of a large change in the nucleated contrail ice is seldom.

## **4.2 Impact of pre-existing cirrus ice crystals on contrail ice crystals loss during vortex descent**

In this section, the effect of the pre-existing cirrus on the survival fraction of the contrail ice crystal is analyzed for both synoptic conditions. During the jet phase, the surrounding natural cirrus ice crystals entrained into the exhaust plume and affected the growth of the freshly nucleated contrail ice crystals (Chapter 3, section 3.2.1.3) because, in the presence of cirrus ice crystals, the available water vapor in the plume distributes among contrail and entrained cirrus ice crystals and causes a reduction in the contrail ice crystal sizes. The lower the water vapor mass deposited on contrail ice crystals, the faster the contrail ice crystals may sublime completely during vortex descent. Furthermore, contrail ice crystals and entrained cirrus ice crystals start to sublime during vortex descent due to adiabatic heating. Sublimation of cirrus ice crystal increases the water vapor slightly in the plume, which increases the surviving fraction of the contrail ice crystals (chapter 3, section 3.2.1.3).

In order to analyze the effect of entrained cirrus ice crystals on the survival fraction of the contrail ice crystals, the simulation results have been analyzed separately for the condition where contrail formation threshold temperature is more than 5K from the ambient temperature and for the condition where the difference between contrail formation threshold temperature and ambient temperature is less than 5K. For contrails forming more than 5K below the contrail formation threshold temperature, the number of nucleated ice crystals can be approximated by the emitted soot numbers (Kärcher et al., 2015). For contrails forming closer than 5K below the contrail formation threshold, ice crystal nucleation has been calculated according to the parameterization of Kärcher et al., (2015) and then calculated the survival fraction, which is additionally dependent on the number of nucleated ice crystals in the contrail. A reduced soot emission increases the probability of high survival fraction (section 4.2.1.1); therefore, a soot number emission with an 80% reduction in current soot emission index ( $2.5 \times 10^{15} - (0.8 \times 2.5 \times 10^{15}) = 5 \times 10^{14}$  kg-fuel<sup>-1</sup>) has been prescribed for this analysis. That means the apparent emission index of contrail ice crystals  $AEI_i = \text{soot emission index } EI_s$ , that is  $5 \times 10^{14}$  kg-fuel<sup>-1</sup> in the case of contrail forming more than 5K

below the contrail formation threshold temperature. Moreover, a fixed Brünt-Vaisala frequency of  $0.012 \text{ s}^{-1}$  has been used while calculating the vortex displacement. Assuming a fixed Brunt-Väisälä frequency and varying it reduces the degrees of freedom in calculations, making it easier to analyze the dependency on ice cloud properties.

In the case of far away from formation threshold condition (more than 5K difference), analysis has shown for both the synoptic systems (24<sup>th</sup> and 26<sup>th</sup> April 2013), and in the case of close to the formation threshold condition (less than 5K difference), analysis has shown only for synoptic system on 26<sup>th</sup> April 2013 and not for 24<sup>th</sup> April 2013, because the change in the survival fraction of contrail ice crystal is not significant in this synoptic system.

Survival fraction values equal to one mean all nucleated contrail ice crystals survived during the vortex descent, and zero means all nucleated contrail ice crystals sublimated. The survival fraction is calculated as follow:

$$\text{Survival fraction} = \frac{\text{survived number of contrail ice crystal during vortex descent}}{\text{total number of nucleated contrail ice crystal}}$$

Change in survival fraction ‘ $\Delta$  survival fraction’ is calculated by subtracting old survival fraction (survival fraction without considering cirrus ice) from new survival fraction (survival fraction after including the effect of surrounding cirrus ice):

$$\Delta \text{ survival fraction} = \text{new survival fraction} - \text{old survival fraction}$$

For calculating the new survival fraction, an estimation for sublimated from and deposited total water vapor on the entrained cirrus ice crystal during the vortex descent has been explained in chapter 3 (section 3.2.2).

### 4.2.1 Far away from contrail formation threshold condition

At altitudes above 10km, the ambient temperature is often below more than 5K from contrail formation threshold temperature. On 24<sup>th</sup> April 2013, at altitudes more than 11km, the difference between contrail formation threshold temperature and ambient temperature is always more than 5 K, which means at those altitudes, the apparent emission index of nucleated contrail ice crystals  $AEI_i \sim EI_s$  (soot emission index) because almost all the soot particles are activated. Since, at those levels, the ice saturation ratio is very low; therefore, the survival fraction of the contrail ice crystals during the vortex phase is very small (figure 4.6). Only about 1% of the total grid boxes have survival fractions of more than 20%. The pre-existing cirrus cloud has very low ice water content, which causes very small changes in the survival fraction due to the sublimation of cirrus ice crystals during vortex descent (section 3.6).

On the 26<sup>th</sup> of April, at altitudes above 10 km, the difference between threshold temperature and ambient temperature is more than 5K (figure 4.1(a)). At those levels, ice supersaturation and cirrus ice water content (section 3.6) are significantly larger than on the 24<sup>th</sup> April 2013 cirrus due to the large-scale rising motion connected with the frontal system. Therefore, ice crystal survival fractions and, in particular, their change due to the impact of cirrus ice crystals are large (figure 4.6 (b)). The survival fraction reaches almost 0.8 in some cases, but the survival fraction up to 0.1 has the highest probability. About 1% of the total grid boxes have a survival fraction of more than 0.4. The change

in the survival fraction due to the sublimation of cirrus ice crystals is very low. The maximum changes in survival fraction are found in those areas where survival fractions are low, and cirrus ice water content and ice number concentrations are large. The negative change in the survival fraction due to the presence of cirrus ice crystals in the plume is also found. However, the negative impact is even smaller than the survival fraction's positive impact. The following section discusses the dependency of the survival fraction and its change due to the sublimation of natural cirrus ice crystals on the various parameters (discussed in chapter 3, section 3.2.3).

#### **4.2.1.1 Impact of soot reduction and atmospheric stability on the survival fraction of contrail ice crystals**

Reducing the soot number emission reduces the number of nucleated contrail ice crystals in contrail (Kärcher et al., 2015). However, lowering the ice crystal number with unchanged aircraft emitted water vapor leads to relatively large contrail (cirrus) ice crystals, leading to a higher survival fraction during the vortex descent (Unterstrasser 2016). In order to analyze the effect of the soot reduction on contrail's ice crystals survival fraction, the current soot emission index ( $EI_s=2.5 \times 10^{15}$  kg-fuel<sup>-1</sup>) has been reduced by 80% (figure 4.6 (c)). The reduction in soot emission increased the probability of high survival fractions, decreased the probability of low survival fractions, and increased the maximum survival fraction slightly. Due to the reduction in the soot emission, the survival fractions exceed 65% in 1% of total grid boxes and exceed 25%-30% in 10% of total grid boxes. Furthermore, the decrease in the soot number emissions affects the change in the survival fraction due to the sublimation of natural cirrus ice crystals. The decrease in soot number emissions leads to an increase in the contrail ice crystal sizes, with the relative increase in sizes smaller than the relative decrease in numbers. Therefore, a relatively larger part of the ice water content of the natural cirrus can sublimate in the time it takes the contrail ice crystals to sublimate completely during vortex descent (section 3.2.3.1). This increases the water vapor within the descending vortices and consequently increases the contrail ice crystal survival fraction. The change in the survival fraction due to cirrus ice crystals is very low (not more than 0.5%), even for 80% soot reduction. Only for survival fraction close to zero the change in survival fraction is slightly large, reaching up to 1% but only in around 0.08% of the total number of cloudy grid boxes. The change in survival fraction on the 24<sup>th</sup> April cirrus is almost negligible even for 80% of soot emission reduction due to low ice water content in the cirrus (figure 4.6 (a)).

The Atmospheric stability plays a crucial role to limit the vertical extent of the contrail, a strongly stable atmosphere restricts the vortices from going far lower down into the atmosphere, and on the other hand, a weakly stable atmosphere allows the vortices to move further down into the atmosphere; therefore, the vertical extent of the contrail plume will be large in a weakly stable atmosphere and will be small in a strongly stable atmosphere. Due to the large vertical extent in weak stability case, a large fraction of the total number of nucleated contrail ice crystals will sublimate due to adiabatic heating; therefore, the survival fraction of the total number of nucleated contrail ice crystals will be small in weak stability case. In the strongly stable atmosphere, a large fraction of the total nucleated contrail ice crystals will stay in cold and ice supersaturated air; therefore, survival fraction will be large. The analysis shows (not shown here) the probability of large changes in the survival fraction at survival fractions close to zero is significantly reduced in a weakly stable atmosphere. Overall the impact of cirrus ice crystals on the survival of contrail ice crystals in the vortex phase is minimal.

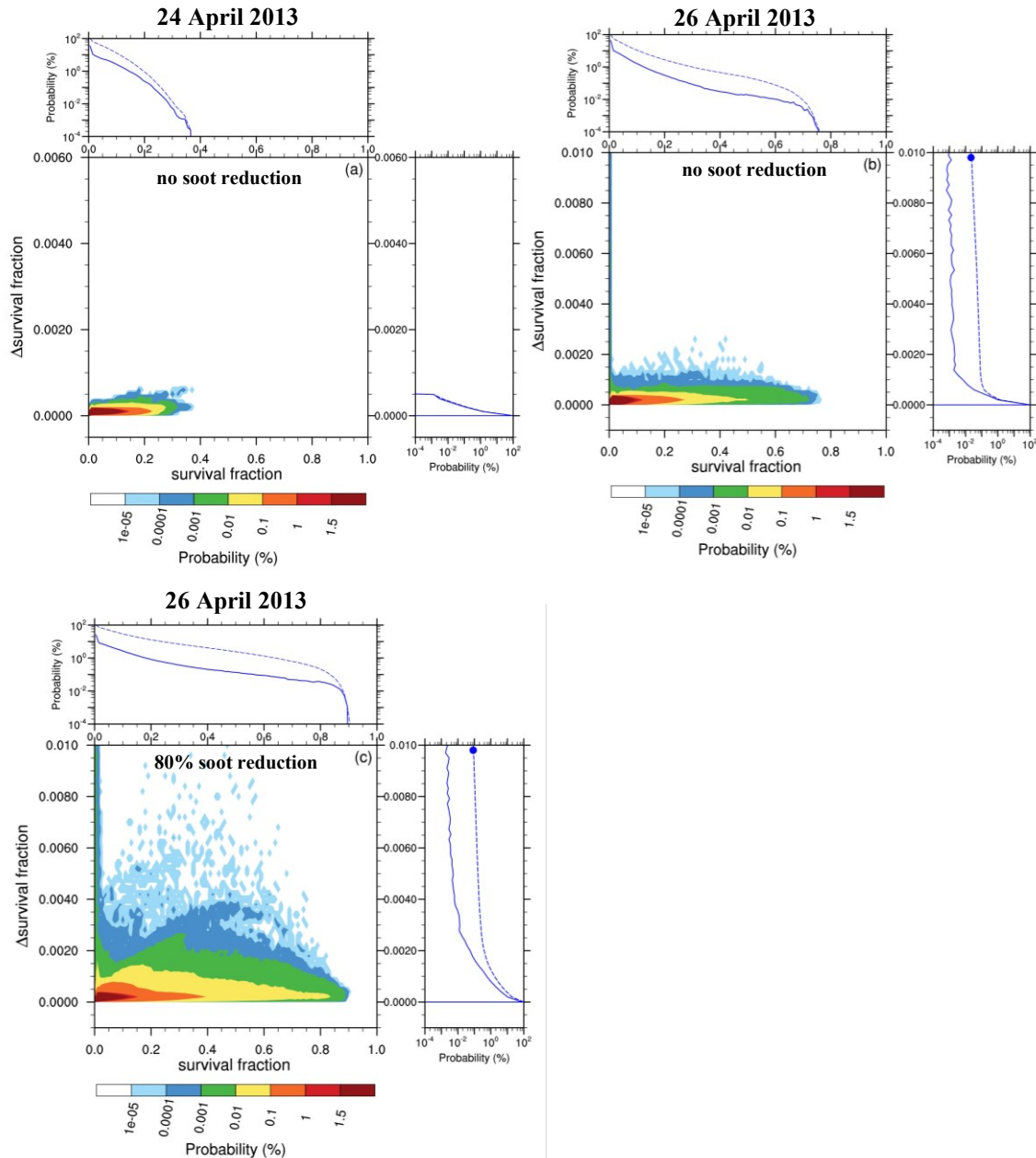


Figure 4.6: Joint probability distribution of contrail ice crystal survival fraction during the vortex phase when neglecting the impact of cirrus ice crystals and its change due to the sublimation of cirrus ice crystals for current soot number emissions,  $2.5 \cdot 10^{15} \text{ kg-fuel}^{-1}$ , for (a) the 24<sup>th</sup> April and (b) the 26<sup>th</sup> April 2013 and for the 26<sup>th</sup> April for (c) 80% reduced soot number emissions. Additionally, the PDF of the fraction of surviving ice crystals (solid) and the associated cumulative PDF (dashed) when neglecting the impact of natural cirrus ice crystals (top) and its change due to the presence of cirrus ice crystals (right) is shown. A Brunt-Väisälä frequency of  $0.012 \text{ s}^{-1}$  (strong stability) has been assumed for all cases. In (a), the y-axis is changed compared to the other figures. Ice crystal survival fractions were calculated whenever the ambient temperature was 5K below the temperature threshold for contrail formation. The dots in the probability distribution of the change in survival rate (right) indicate the probability of changes in the survival fraction that are larger than 1%.

### **4.2.1.2 Effect of pre-existing cirrus ice crystals on survival fraction of contrail ice crystals**

The impact of the natural cirrus on the survival fraction on the contrail ice crystals during vortex descent is dependent on the cirrus properties, i.e. IWC, ice crystal number concentration, and in-cloud ice supersaturation. The survival fraction of the contrail ice crystals increases with the increasing number concentration of the cirrus ice crystals and the size of the ice crystals since sublimated mass from cirrus ice crystals increases which causes an increase in the plume's relative humidity. In this section, the effect of cirrus properties on the survival of contrail ice crystals is only shown for cirrus on 26<sup>th</sup> April 2013 because, on 24<sup>th</sup> April 2013, the effect of pre-existing cirrus on the survival of the contrail ice crystals is insignificant.

Figure 4.7 shows the cirrus properties, IWC, ice crystal number concentration, and in-cloud ice supersaturation for each set of survival fractions of contrail ice crystals and its change due to the presence of natural cirrus ice crystals in the plume for the 26<sup>th</sup> of April. A soot number emission of  $0.5 \cdot 10^{15} \text{ kg-fuel}^{-1}$  and a Brunt Väisälä frequency of  $0.012 \text{ s}^{-1}$  have been prescribed. In-cloud relative humidity directly affects the survival fraction of contrail ice crystals in descending vortices. High ice supersaturation is associated with the large survival fraction, and low ice supersaturation is associated with the low survival fraction (figure 4.7(c)). If the in-cloud ice supersaturation is high (e.g., ice saturation ratio is 1.4 or 1.5), then most contrail ice crystals survive since ice crystals experience only a slight sub saturation during the vortex descent. If the ice saturation ratio is close to 1.0, then ice water mass in a contrail is low, and sublimation due to adiabatic heating will lead to a low survival fraction. In that case, the ice crystals in the secondary wake will survive only.

The impact of pre-existing cirrus on the survival fraction of the contrail ice crystals is large when ice water content and ice crystal number are large in the background cirrus. Cirrus ice crystals are small, so the difference between cirrus and contrail ice crystals is small, resulting in smaller differences in the diffusional growth of the ice crystals. As a result, contrail ice crystals become larger so that the sublimation of cirrus ice crystals during descending vortices can have an increased impact on contrail ice crystal survival. Furthermore, the large number of cirrus ice crystals associated with a large amount of ice water in the cirrus cloud can effectively increase the water vapor in the descending vortex and reduce contrail ice loss.

High numbers of ice crystals and high ice water content in the clouds are related to a low in-cloud ice saturation ratio. Therefore, high cirrus ice crystal number concentrations are often found in areas where the contrail ice crystal survival fraction is low (figure 4.7 (b)), and when the high ice number concentration in cirrus are associated with relatively high ice water content (figure 4.7(a) & (b)) then pre-existing cirrus induced a relatively large impact on the contrail ice crystal survival fraction. Survival fraction is more than 50%, when neglecting the impact of cirrus ice, is usually connected with ice saturation ratios above around 1.2. However, having a high ice crystal number concentration in those altitudes are relatively uncommon and hint at recent ice nucleation events presumably connected with the fast lifting of moist environmental air within the frontal system. Where the survival fraction is greater than 50%, the combination of high ice concentrations and ice water content in cirrus rarely affects the survival fraction by more than 0.2%-0.4%. High cirrus ice crystal number concentrations and ice water content can lead to large absolute and relative changes in the contrail ice crystal survival fractions where survival fraction is low.

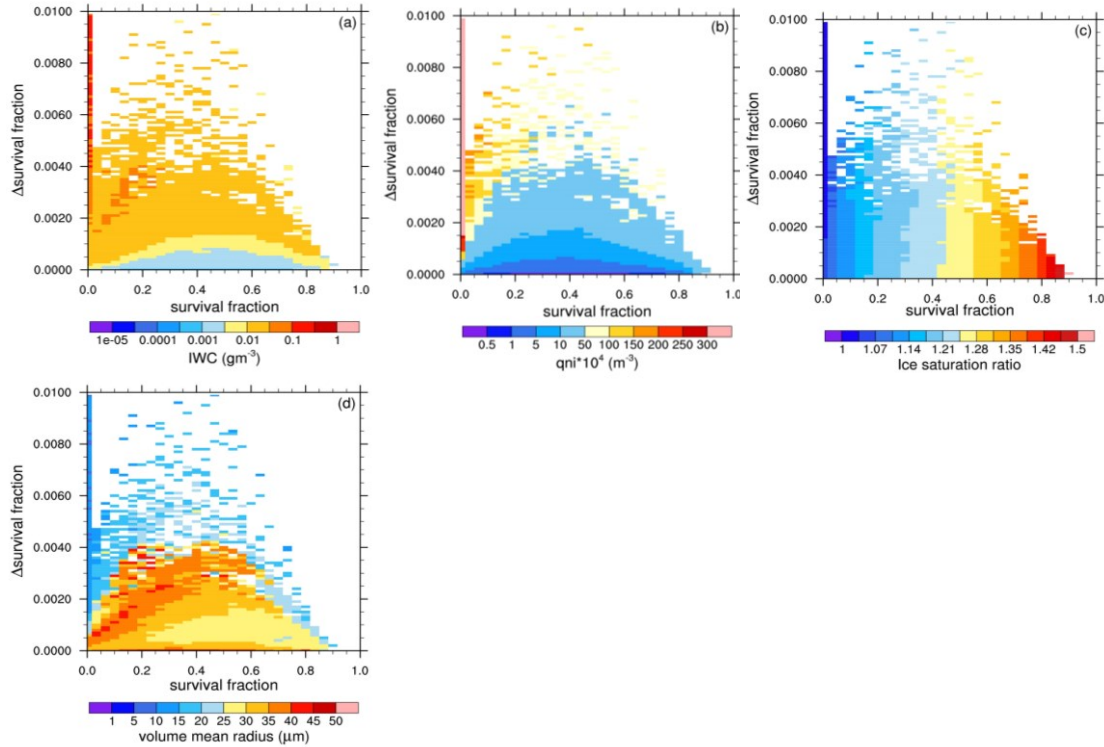


Figure 4.7: Ice cloud properties for combinations of contrail ice crystal survival fraction during the vortex phase when neglecting the impact of cirrus ice crystals and its change due to the impact of cirrus ice crystals,  $\Delta$ survival fraction, for the 26th April for cases of contrail formation more than 5K below the contrail formation threshold. Color coded are the cloud properties of the pre-existing cirrus, IWC (a), cirrus ice crystal number concentration (b), in-cloud ice saturation ratio (c) and cirrus ice crystal radius (d). A Brunt-Väisälä frequency of  $0.012s^{-1}$  and soot number emissions of  $0.5 \cdot 10^{15} kg-fuel^{-1}$  are assumed.

#### 4.2.2 Close to contrail formation threshold condition

The effect of the pre-existing cirrus ice crystal on the survival fraction of contrail ice crystal for contrail formation 'close to formation threshold condition' has been analyzed separately because the change in the survival fraction additionally depends on the number of nucleated ice crystals in a contrail. Assuming fixed soot number emissions and ambient aerosols and their properties, the ambient atmospheric state controls contrail ice nucleation while the survival of the ice crystals during the vortex phase is dependent on atmospheric variables and the contrail ice nucleation. The number of nucleated ice crystals in contrail increases with the difference between formation threshold and ambient temperature.

High survival fractions have been found in areas where either in-cloud ice saturation ratio is high or where contrail formation occurs close to the formation threshold. The probability of changes in the survival fraction due to the sublimation of pre-existing cirrus ice crystals larger than 1% is significantly smaller in the close to formation threshold cases. However, the maximum changes in the survival fraction can be significantly larger when contrails form close to the contrail formation threshold. In 0.1% of the cases, the change in the survival fraction exceeds 2-3%, but changes can also occasionally reach values of 5-10% and higher (figure 4.8).

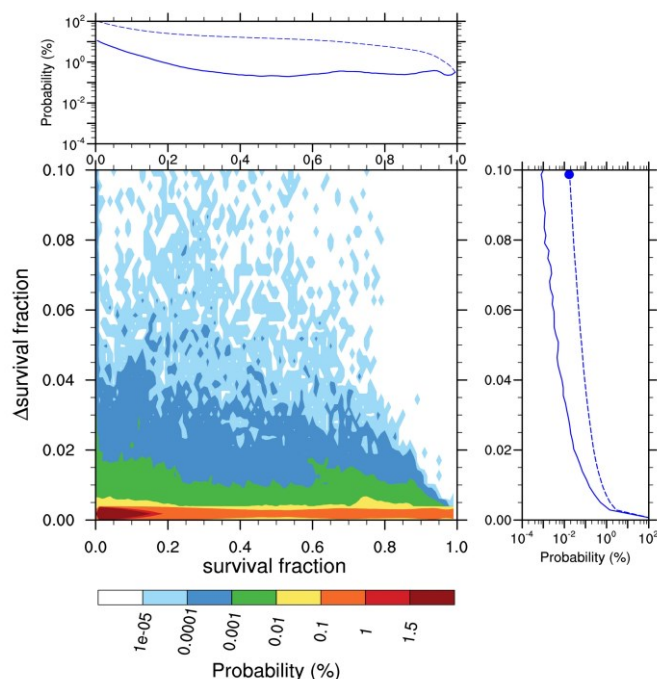


Figure 4.8: Joint probability distribution of contrail ice crystal survival fraction during the vortex phase when neglecting the impact of cirrus ice crystals and its change due to the impact of cirrus ice crystals for the 26th April 2013 when contrails form closer than 5K from the contrail formation threshold. Additionally, the PDF of the fraction of surviving ice crystals (solid) and the associated cumulative PDF (dashed) when neglecting the impact of natural cirrus ice crystals (top) and its change due to the presence of cirrus ice crystals (right) is shown. A Brunt-Väisälä frequency of  $0.012 \text{ s}^{-1}$  (strong stability) and soot number emissions of  $0.5 \cdot 10^{15} \text{ kg-fuel}^{-1}$  have been prescribed. The dot in the cumulative probability distribution of the change in survival fraction (right) indicates the probability of a change in the survival fraction that is larger than 10%.

The survival of the contrail ice crystals is large for large ice supersaturation in general and large when only a few ice crystals are nucleated (figure 4.9 (c) & (d)). Due to the low number of contrail ice crystal nucleation close to the formation threshold, the size of the ice crystals is comparably large and leads to a large survival fraction, similar to the increased survival fractions when reducing soot number emissions. The change in the survival fraction primarily depends on the difference between formation threshold temperature and ambient temperature, therefore the  $\text{AEI}_i$  of contrail ice crystals. The closer contrail formation happens to the threshold, the fewer ice crystals are formed so that the impact of the pre-existing cirrus on the survival fraction can be large (figure 4.9 (d), (e)). Large changes are also found for high  $\text{AEI}_i$  when cirrus IWC and ice crystal number concentrations are particularly large (figure 4.9 (a), (b)). In the case of a few contrail ice crystals, the change in survival fraction is large because contrail ice crystals are comparably bigger. When the survival fraction is close to zero, then many small cirrus ice crystals in the plume can lead to a large change in the survival fraction. The increase in the number concentration of survived contrail ice crystals in the case of close to the formation threshold may not be significant (maybe a fainted contrail) compared to the number concentration of ice usually found in contrails but can perturb cirrus ice number concentration significantly.

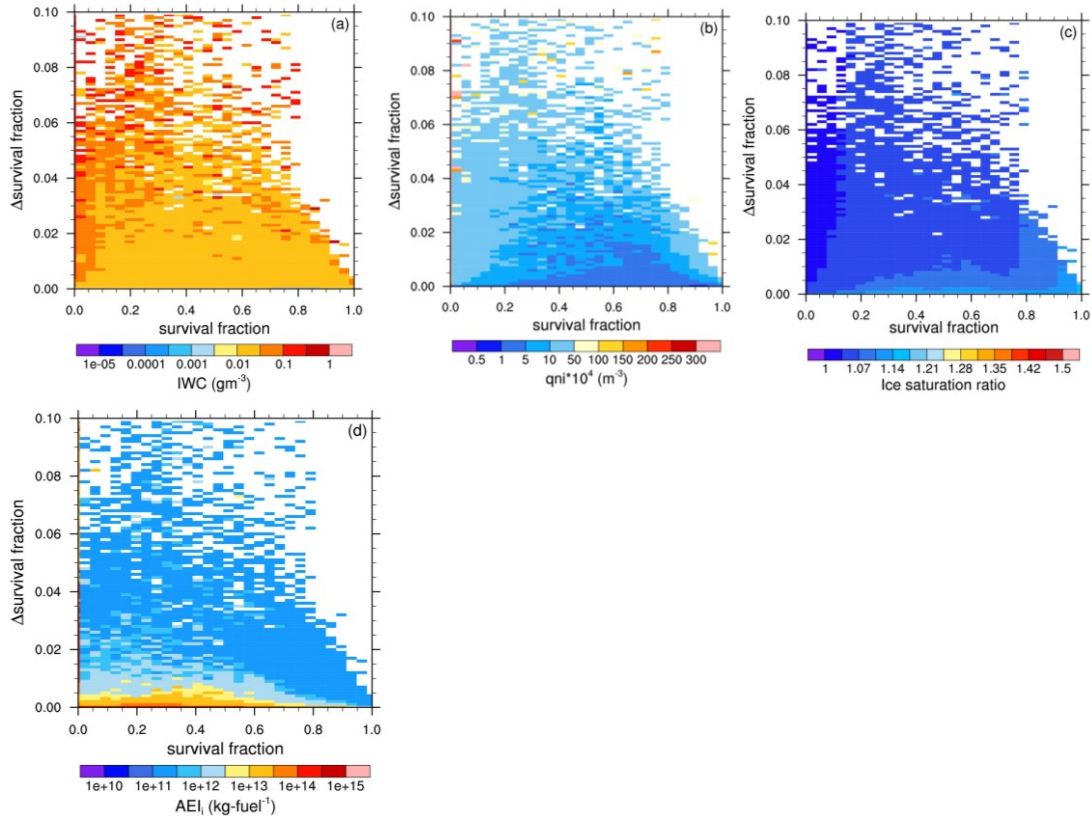


Figure 4.9: Ice cloud properties for combinations of contrail ice crystal survival fraction during the vortex phase when neglecting the impact of cirrus ice crystals and its change due to the impact of cirrus ice crystals,  $\Delta$ survival fraction, for the 26<sup>th</sup> April for contrail formation at temperatures closer than 5K from the contrail formation threshold. Color coded are the cloud properties of the pre-existing cirrus, IWC (a), cirrus ice crystal number concentration (b), in-cloud ice saturation ratio (c) and ‘new’ apparent emission index of contrail ice crystals (d) with ‘new’ indicating that changes in the nucleation due to the presence of cirrus ice crystals have been considered. A Brunt-Väisälä frequency of  $0.012s^{-1}$  and soot number emissions of  $0.5 \cdot 10^{15} \text{ kg-fuel}^{-1}$  are assumed.  $AEI_i$  of  $5 \cdot 10^{14}$  translates into  $q_{n_i} = 3 \cdot 10^7 m^{-3}$ .

**Summary:** The impact of the pre-existing cirrus on the survival fraction of contrail ice crystals during vortex descent has been discussed in section 4.2. The presence of cirrus ice crystals affects the survival of the contrail ice crystals slightly. The cirrus ice crystals entrained into the plume during mixing compete for the available water during the growth phase before vortex descent and sublimate together with the contrail ice crystals during vortex descent, leading to a change in the survival of contrail ice crystals. On the one hand, the presence of cirrus ice crystals in the plume during the growth phase affects the size of the contrail ice crystals will cause a low survival rate during vortex descent. On the other hand, sublimation of cirrus ice crystals in the descending vortices moistens the plume and increases the survival rate. Together, both effects show a positive change in the survival fraction of the contrail ice crystals. However, the change in the survival fraction is extremely low. Specially when contrails form far away from the formation threshold temperature. The relative change in survival fraction can be large for contrails form close to the formation threshold where a nucleated number of contrail ice crystals are low.

### 4.3 Impact of contrail formation on ice crystal number concentrations

Previous sections have shown the impact of the pre-existing cirrus on contrail formation, and now the question arises that how large can be the perturbation of cirrus microphysical properties. Because the change in the microphysical properties of the cirrus has a further impact on the development of the cirrus, its lifetime and optical properties, and its impact on climate, therefore, this section explains the change in ice crystal numbers of the cirrus on 26<sup>th</sup> April 2013 for altitudes at around 10.5km and around 9.7km only to show how large can be the change in the cirrus ice number concentration after contrail formation. However, the effect of contrail formation due to real air traffic on cirrus microphysical and optical properties has been described in detail in the next chapter (chapter 5).

Figure 4.10 shows the change in ice crystal numbers of the cirrus cloud field in cases when contrail formation conditions are met, which is in both altitude ranges in about 60% of around  $10^6$  grid boxes in which contrail formation conditions are met. Approximately 90% and 83% of cases at altitudes around 10.5 km and 9.7 km, respectively, where the ice number concentration has been increased in the cirrus. Changes in ice crystal number concentrations approximately 5 minutes after emission are most likely to range between  $10^6\text{m}^{-3}$  and  $10^7\text{m}^{-3}$  irrespective of the cirrus ice crystal number concentration (figure 4.10). In lower levels, changes are slightly lower than in upper levels. Some areas within the cloud show a large change in ice number concentration for large cirrus ice number concentration, which is likely those areas where the impact of pre-existing cirrus on contrail ice nucleation is large. Cirrus ice crystal number concentrations range between  $10^2\text{m}^{-3}$  and  $10^5\text{m}^{-3}$  before air traffic, and the formation of contrails within cirrus is most likely to change ice crystal number concentrations by 2 - 4 orders of magnitude. The negative changes in ice crystal number concentrations are not estimated mainly for two reasons. First, the impact of air traffic on cirrus properties when no contrails can form is not simulated in this thesis work and, second, negative changes in ice crystal number caused by contrails forming but nearly all ice crystals sublimating within the vortex phase are connected with a high uncertainty that may be of a similar order of magnitude as estimated, which indicate decreases of maximally  $10^3\text{m}^{-3}$  at a cirrus ice crystal number concentration of  $10^4\text{m}^{-3}$ .

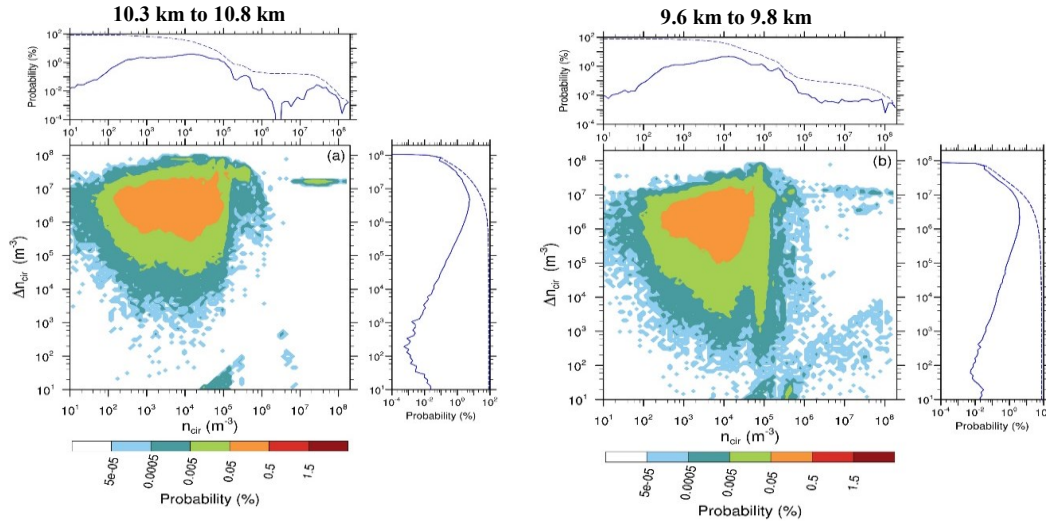


Figure 4.10: Joint probability of cirrus ice crystal number concentrations,  $n_{cir}$ , and the aviation induced change in ice crystal numbers,  $\Delta n_{cir}$ , for the cirrus cloud field on the 26<sup>th</sup> April 2013 for current soot number emissions,  $2.5 \cdot 10^{15} \text{ kg-fuel}^{-1}$ , and (a) for altitudes from 10.3km to 10.8km ( $\sim 250 \text{ hPa}$  to  $\sim 225 \text{ hPa}$ ) and (b) for 9.6km to 9.8km ( $\sim 280 \text{ hPa}$  to  $270 \text{ hPa}$ ). Only 60% of cloudy grid boxes at the two altitude ranges are analysed in which the contrail formation conditions are met. Grid mean concentrations and their changes are displayed. Cumulative probabilities of  $\Delta n_{cir}$  reach values below 100% because negative changes are not shown here as they are lower and uncertainty in those simulated changes is high.

#### 4.4 Conclusion

This chapter concludes the effect of pre-existing cirrus on the contrail ice formation within cirrus. It has been found that an increase in aviation-induced water vapor due to sublimation of and deposition on the cirrus ice crystals before contrail ice nucleation leads to the change in the contrail formation threshold temperature. In the case of thick cirrus on 26<sup>th</sup> April 2013, the maximum change in the contrail formation threshold is up to 2 K connected with large sublimated ice water mass from the pre-existing cirrus. In the case of thin cirrus on 24<sup>th</sup> April 2013, the change in the contrail formation threshold temperature is not very large because cirrus has low ice water content and low ice number concentration. There is also the negative impact of the pre-existing cirrus on the contrail formation threshold temperature, but the negative change is very small compared to the positive change in the contrail formation threshold temperature. Change in the contrail formation threshold temperature due to pre-existing cirrus has shown a significant impact on the number of nucleated ice crystals in contrail. The change in the number of nucleated ice crystals is large due to pre-existing cirrus when cirrus has high ice water content and high ice number concentration. The relative change in the number of nucleated ice crystals is up to 10% when contrail ice nucleation happens far away from the threshold temperature. At temperatures where contrail ice crystals form close to the formation threshold, the number of nucleated contrail ice crystals are often low, and relative change in the number of nucleated ice crystals due to pre-existing cirrus are large. Overall, the sublimation of pre-existing cirrus in the engine and the impact of cirrus ice crystals sublimation/deposition during mixing significantly impact the number of nucleated ice crystals in contrail.

Furthermore, the impact of the pre-existing cirrus on the survival of the contrail ice crystals has been analyzed. The presence of cirrus ice crystals in the plume affects the survival of the contrail

ice crystals by affecting the growth of the freshly nucleated ice crystals after nucleation and sublimation of contrail ice crystals in the descending vortices. The survival fraction of the contrail ice crystals is large for the large in-cloud ice supersaturation. It has been found that the survival fraction of contrail ice crystals is large in thick cirrus as compared to the thin cirrus because in-cloud ice supersaturation is relatively large in thick cirrus. The change in the survival fraction of contrail ice crystals due to cirrus ice crystals is not significantly large. The largest impact of pre-existing cirrus on survival fraction is when cirrus has a large number of small ice crystals or when the number of nucleated contrail ice crystals is low. Additionally, reducing the soot number emission causes a slight increase in the survival fraction and change in the survival fraction due to pre-existing cirrus but still not larger than 1%. The change in survival fraction of the ice crystals can be larger when contrail formation happens close to the formation threshold temperature. However, the probability of those changes is very low.

The contrail formation within cirrus introduces a large change in cirrus's ice crystal number concentration. When comparing cirrus ice crystal number concentrations before air traffic and the impact of air traffic approximately 5 minutes after emission, ice crystal number concentrations commonly increase by 2 to 4 orders of magnitude.



## Chapter 5

# Impact of contrail formation within pre-existing cirrus on cirrus properties

The previous chapter discusses the effects of the cirrus cloud on the contrail formation when contrail ice crystals form within the pre-existing cirrus cloud. In this chapter, the effect of contrail formation within cirrus on cirrus cloud properties is explained.

As shown in chapter 4, contrail formation within cirrus is a large perturbation to the cirrus ice crystal number concentration. How long those perturbations exist and what kind of effect they have on average cirrus microphysical and optical properties is not clear. Therefore, in this chapter, the perturbation of microphysical and optical properties of the contrail perturbed cirrus cloud has been examined. The statistical distributions of cloud properties, i.e. ice water content, number concentration of ice crystals and their sizes, are analyzed at different altitudes in section 5.1. The spatial pattern of cloud perturbations has been studied in sections 5.2 and 5.3, revealing that a large area of the cloud has been perturbed due to continuous air traffic. Contrail induced perturbations in cirrus microphysical properties may cause changes in optical properties of the cirrus. Those changes in the optical depth of the cloud are discussed in section 5.4.

The temporal evolution of the contrail-induced modification in the cirrus is studied in section 5.5. The life cycle of the contrail perturbed cirrus has been analyzed in terms of changes in for example, the number concentration of ice crystal, mean volume diameter of the ice crystals and ice crystal fall velocity; the direct impact of these on the ice crystal sizes is described in section 5.5.3.

In order to analyze the impact of contrail ice formation on cloud fields, simulations have been analyzed over 2 hours with prescribed air traffic emission. The 5 minutes aggregated air traffic emission for the year 2006 (Wilkerson et al., 2010) has been prescribed between altitudes from 7 km to 13 km and updated every 5 minutes. The analysis has been done for both thin (24th April 2013) and thick cirrus (26th April 2013) with simulation results explained in the following sections.

### 5.1 Perturbation of cirrus cloud properties

The effect of contrail formation due to two hours of continuous air traffic on the cirrus cloud properties can be seen when comparing figures 5.1 (a, c, e), figure 5.2 (a, c, e)) with figures 5.1 (b, d, f), figure 5.2 (b, d, f)). The cirrus ice number concentration, ice water content and mean volume diameter of ice crystals is shown after contrail formation within cirrus for both synoptic conditions on 24<sup>th</sup> and 26<sup>th</sup> April 2013. The equivalent analysis of cirrus properties unperturbed by air traffic was described in chapter 3 section 3.5 for both days. The Cloud Frequency Altitude Diagram (CFAD) shows the probability of the cloud variables for different temperature bins (figures 5.1 and 5.2) with numbers from the unperturbed simulations.

#### Impact of air traffic on ice crystal number concentrations

In the case of the thin cirrus within the high-pressure system on 24<sup>th</sup> April 2013, the number concentration of ice crystals in the cirrus is low, only up to  $1 \times 10^5 \text{ m}^{-3}$  at flight levels, representing

the properties of in-situ origin clouds (chapter 2, table 2.1). Due to contrail formation, the ice number concentration has been increased at colder temperatures (below  $-40^{\circ}\text{C}$ ). The number concentration of ice crystals has been increased up to 3 orders of magnitude at the flight levels (ambient temperature below 233.15 K in figure 5.1) in the case of thin cirrus. Due to contrail ice formation within cirrus, almost 0.5% of the total cloudy grid boxes have a high number concentration of ice crystals ( $> 10^5 \text{ m}^{-3}$ ) at flight levels. On 26<sup>th</sup> April 2013, synoptic conditions show a medium to thick cloud connected with a frontal system with high ice water content and high number concentration of ice crystals within the cloud. Most of the cirrus clouds on this day had properties typical for average thick in-situ formed cirrus with a small fraction of the cirrus having properties that are typical for liquid origin cirrus (Krämer et al., 2020). The number concentration of ice crystals is high, up to  $2 \times 10^8 \text{ m}^{-3}$ , in some areas of the cloud. These high number concentrations of ice crystals within the cloud likely indicate the homogeneous nucleation events in those areas (chapter 3, section 3.5). Since this cloud already has a high ice number concentration, after contrail formation, the probability of the high ice number concentration has increased in the cirrus. After contrail formation, the probability of a high number concentration of ice crystals has increased at flight levels reaching 0.5 % while within the unperturbed cirrus, those ice number concentrations are found with a probability of only  $\sim 0.1\%$  (figure 5.2 a and b). This means the number of grid boxes with a high number concentration of ice crystals has been increased by a factor of 5 due to the formation of contrail ice crystals.

### Impact of air traffic on ice crystal sizes

Due to low water vapor emission from fuel burn and the large number of nucleated ice crystals, initially, the mean volume diameter of the contrail ice crystals is very small (less than 2 micrometers), much smaller than the ice crystals usually found in cirrus clouds. The sizes of freshly nucleated cirrus ice crystals can also be small when they were formed via the homogeneous nucleation process (ice crystal radius  $\sim 2 \mu\text{m}$ , (chapter 2, section 2.3). Due to small sizes of the contrail ice crystals, contrail introduces the perturbation towards the small ice crystals in the cirrus clouds which causes a change in the size distribution in the cloud and therefore, microphysical processes and optical properties of the cloud. The mean volume diameter of ice crystals at flight level in the undisturbed cirrus cloud are larger than  $20 \mu\text{m}$  on the 24<sup>th</sup> April 2013 study. However, after contrail ice formation, small ice crystals ( $\sim 1 \mu\text{m}$ ) could appear at flight levels in the thin cirrus on 24<sup>th</sup> April 2013 with a low probability of around 0.5% (figure 5.1, f, g and h). On the other hand, the mean diameter of the ice crystals in unperturbed thick cloud on 26<sup>th</sup> April 2013 can be as small as  $\sim 1 \mu\text{m}$ . After contrail ice formation, the probability of small diameters has been increased slightly in the case of thick cirrus (figure 2, e and f).

The aircraft emitted water vapor does not change ice water content significantly because aircraft emitted water vapor mass is very low compared to the ice water in cirrus and water vapor content in the upper troposphere. However, ice water content may change in the contrail perturbed regions due to diffusional growth of the contrail ice crystals in the presence of in-cloud ice supersaturation. Since change in ice water content is not as significantly large as change in the ice number concentration due to contrail formation, the ice water content of the cloud looks approximately unchanged in the cirrus cloud fields on both days due to the formation of the contrails.

**Summary:** Contrail formation within cirrus shows a large increase of small ice crystals. The number of ice crystals increased at flight levels after contrail formation. In the case of thin cloud on 24<sup>th</sup> April, the ice number concentration has increased up to 3 to 4 order of magnitude where ice number concentration was maximally  $10^5 \text{ m}^{-3}$  in unperturbed cirrus. Contrail formation within

cirrus introduced small ice crystals below 5 micrometers at flight levels in thin cirrus. In the case of thick cirrus on 26<sup>th</sup> April, the probability of many small ice crystals at flight levels has increased up to ~0.5% instead of 0.1% after contrail formation.

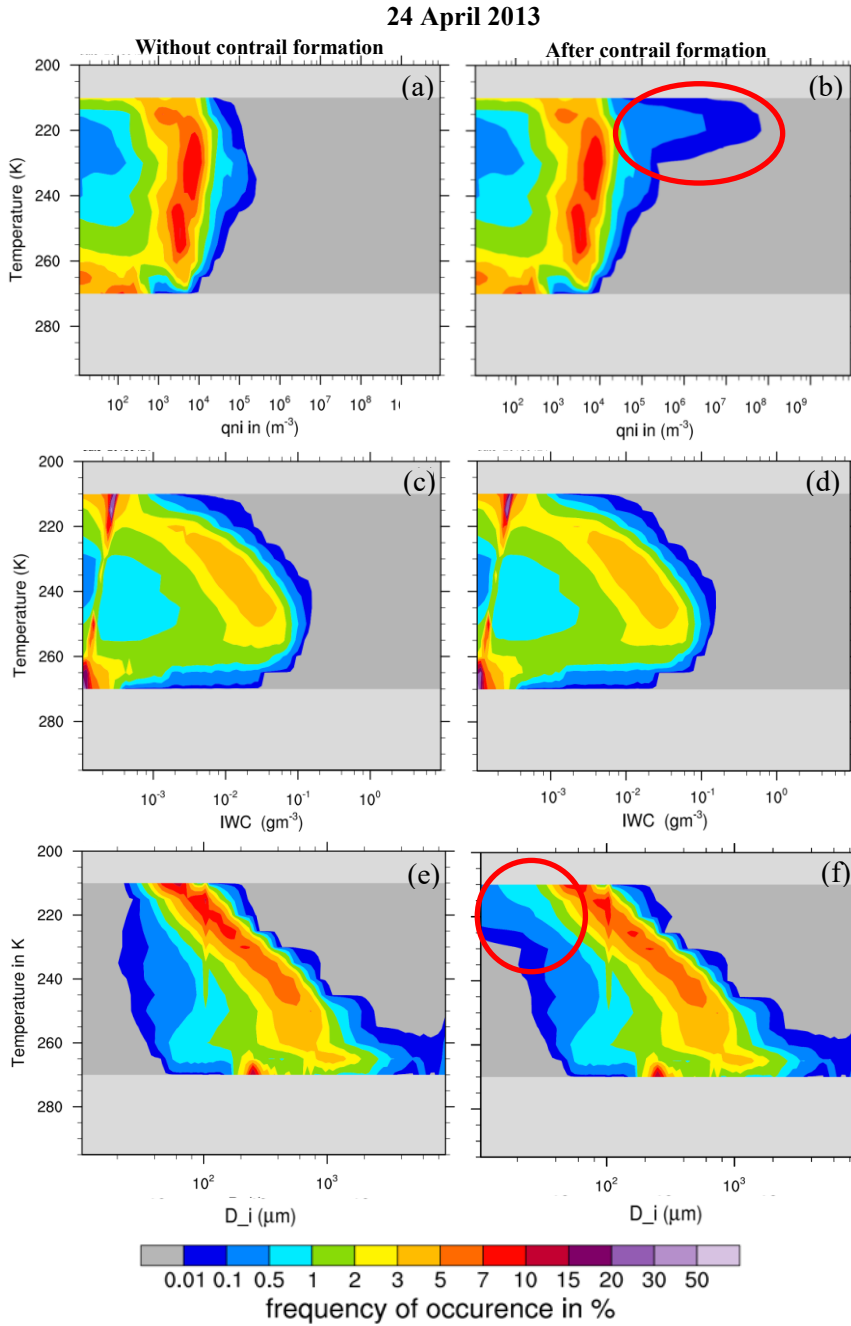


Figure 5.1: Frequency of occurrence of grid mean ice number concentration 'qni' (m<sup>-3</sup>) (a, b), ice water content 'IWC' (gm<sup>-3</sup>) (c, d) and mean volume diameter 'D<sub>i</sub>' (μm) (e, f) in cloud on 24<sup>th</sup> April 2013 at 06 - 07 am. The first column shows properties of the undisturbed cloud. The last column shows the cloud properties including contrail induced disturbances after two hours of air traffic. The vertical line in the mean volume diameter is an artifact caused by the lateral boundary condition in the model. Lateral boundary conditions do not include information on ice crystal sizes because they come from a model using single-moment microphysics. Therefore, for the boundary data, a diameter of 100 micrometers is simply assumed when calculating the number concentration from boundary data (personal communication Axel Seifert (DWD)).

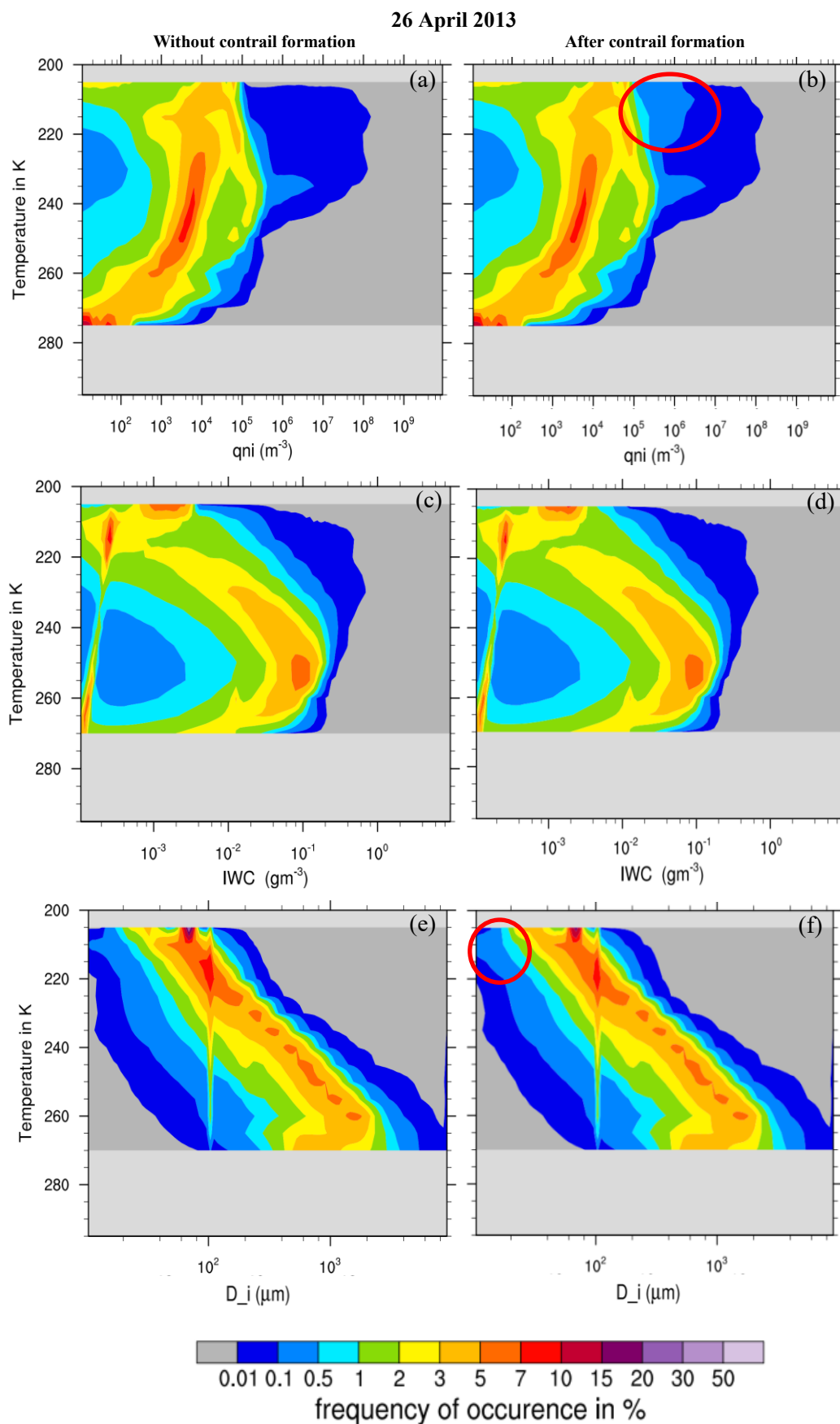


Figure 5.2: Similar to figure 5.1 but for cirrus on 26<sup>th</sup> April 2013 at 17-18 pm.

## 5.2 Spatial distribution of the cirrus and its contrail induced perturbation

Contrail formation within cirrus introduces large differences in ice number concentration of the cirrus cloud. Therefore, in this section, the spatial distribution of number concentration of ice crystals in the unperturbed cirrus (without contrail formation) and perturbed cirrus (after contrail formation) have been shown in order to analyze the modification. Since ice water content in the cirrus is not changed significantly due to aircraft emitted water vapor, variability in ice water content has been shown only for thin cirrus in section 5.3.

### 5.2.1 24<sup>th</sup> April 2013 case

A high-pressure system originated cirrus is covering a large area of the simulation domain. The cirrus has a low ice number concentration and ice water content (section 5.1 CFAD). As previously seen, most areas of the cirrus have a number concentration of ice crystals of up to  $1 \times 10^4 \text{ m}^{-3}$  but some parts have a slightly high ice number concentration up to  $5 \times 10^4 \text{ m}^{-3}$ . The cloudiness due to cirrus is very similar in all three atmospheric levels as shown in figure 5.3 (a) & figure 5.4 (a, c) and covers a large area of the domain. The cloudiness does not change much over time in these atmospheric altitudes. When prescribing air traffic, only a few contrails are formed within the first-time step and newly formed contrails are visible as thin lines with a high number concentration of ice crystals (figure 5.3b). The ice number concentration in newly formed contrails shown here is ice number concentration in 5 minutes old contrail because contrail scheme in the model provides a contrail ice crystal number that survived during vortex descent and was distributed over a few hundred meters at lower altitudes depending on the contrail depth (chapter 3, section 3.2.2). The ice number concentration in contrails is as high as  $1.5 \times 10^6 \text{ m}^{-3}$ , which is around 2 orders of magnitude higher than the surrounding cirrus ice number concentration. Depending on the atmospheric flow and cloud microphysical processes, contrail ice crystals mix slowly and gradually with the surrounding air and spread to cover a relatively large area.

One hour after the start of the simulation (figure 5.4), more contrails have been formed and a large area of the cloud is showing a high number concentration of ice crystals. In the meantime, old contrails widen up and are visible as comparably thick lines with slightly lower number concentrations of ice crystal. The number concentration of ice crystals reaches  $3 \times 10^5 \text{ m}^{-3}$  in one-hour old contrails which is again higher than the number concentration of ice crystals in surrounding cirrus. The ice crystal number concentration in one-hour old contrails are often about 1 order of magnitude lower than the number concentration of ice crystals in the newly formed contrails and 1 order of magnitude higher than the ice number concentration in the surrounding cirrus cloud.

After two hours of continuous air traffic, a large area of the cloud is modified due to contrail ice formation, showing high number concentration of the ice crystals in large parts of the cloud compared to the ice number concentration in cirrus without contrail disturbance (figure 5.4). Old contrails spread, covering large areas of the cloud. Additionally, many new contrails have been formed within the cloud. Even in two hours old contrails, the ice number concentration is on average  $2 \times 10^5 \text{ m}^{-3}$  that is one order of magnitude higher than the ice number concentration in the surrounding cirrus cloud and one order of magnitude lower than the freshly formed contrail.

Since, most parts of the cloud are polluted due to contrail ice nucleation, some contrails may form within old contrails. Some contrails with relatively high ice number concentration can be seen as thin lines within old contrails (figure 5.4 f) which indicates the formation of contrail ice crystals

within aged contrail. A new contrail forming within an old contrail is affected by the properties of the old contrails similar to contrail formation within pre-existing cirrus. The number of nucleated contrail ice crystals and their survival fraction may increase in the new contrail due to the sublimation of old contrail ice crystals in the jet and vortex phase. The effect of the old contrail ice crystals on the formation of new contrail ice nucleation can be larger than the effect of pre-existing cirrus because the size of ice crystals in a contrail is comparably smaller than the size of ice crystals in cirrus. Also, the number concentration of contrail ice crystal can still be large even in one-hour old contrails which can provide a large sublimated ice water mass during combustion and during mixing in the plume. However, the presence of a high number concentration of ice crystals in a plume before contrail ice nucleation can reduce the water vapor concentration in the plume by deposition of the available water vapor. Nevertheless, it has been seen in the previous chapter that high ice water content and high ice crystal number in the background field cause an increase in contrail ice nucleation rate in most cases. After nucleation, the presence of aged contrail ice crystals in the plume affects the growth of freshly nucleated ice crystals. Furthermore, the high number concentration in aged contrails can provide a large ice water mass during vortex descent which may increase the survival rate of the freshly nucleated contrail ice crystals. Contrails that were formed in warm conveyor belt outflow regions may cause a large change in new contrail ice formation because the ice water content in those aged contrails can be large since a continuous supply of moisture in these regions allows ice crystals to grow large. Moreover, newly formed contrail ice crystals in this synoptic condition can persist for a long period of time. Apart from that, the previous chapter has shown that the probability of a large change in contrail ice formation is less because very few areas have cloud fields with high ice water content and high ice number concentration. But due to continuous air traffic, a large part of the cirrus may have a large ice number concentration after some time; this will increase the probability of a large change in the contrail ice formation.

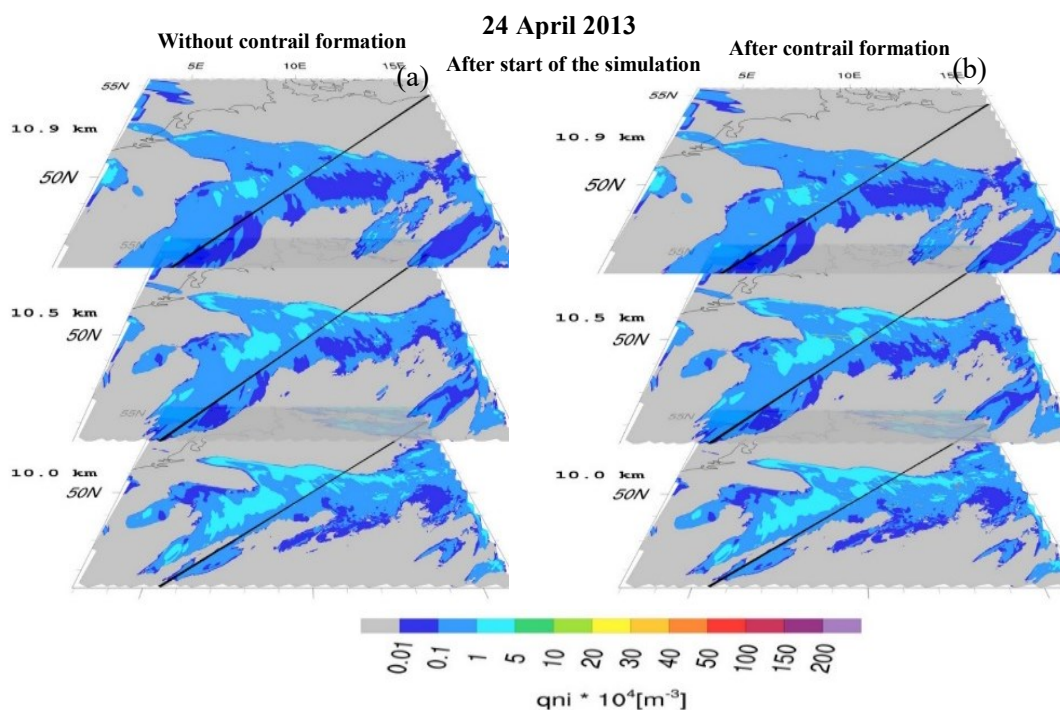


Figure 5.3: Ice number concentration 'qni' in the cirrus cloud field on the 24<sup>th</sup> April 2013 at start of the simulation for three different altitudes 10.0, 10.5 and 10.9 km over the Germany domain (48.5°N - 55.5°N; 2.0°E - 17°E) simulated by ICON-LEM without contrail induced perturbations (left) and including contrail perturbations (right). Each altitude level has a thickness of approximately 150m

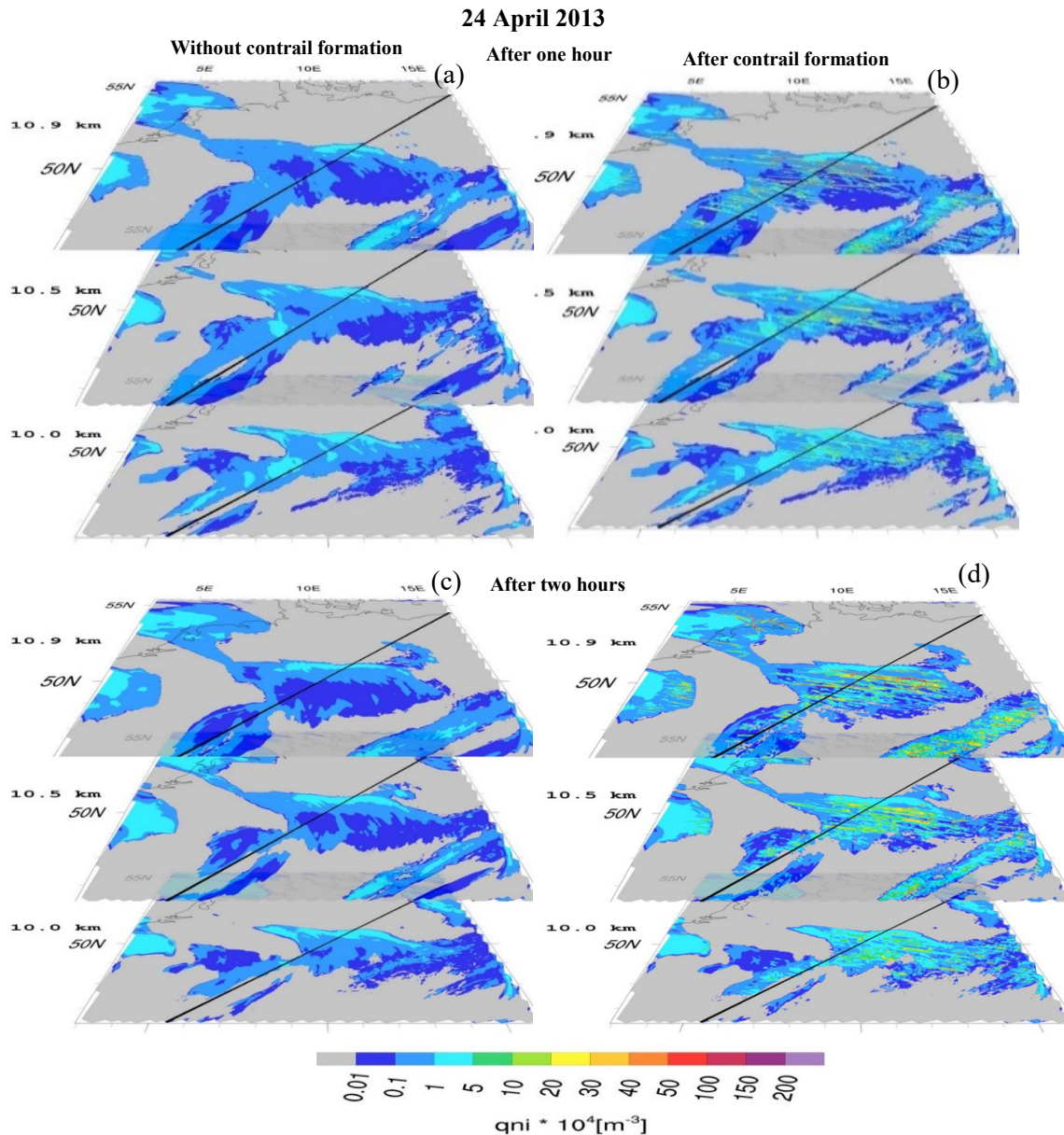


Figure 5.4: Similar to figure 5.3 but a snapshot of the cloud after one (first row) and two hours (second row) of continuous air traffic.

### 5.2.2 26<sup>th</sup> April 2013 case

As described before, the cirrus clouds on the 26<sup>th</sup> April are connected with a frontal system. The passage of a cold front over Germany moving towards the southeast connected with a conveyor belt that was supplying the upper troposphere with moist air. Therefore, cloudiness is rapidly increasing and strong frontal convection, geometrically thick clouds and precipitation could be found along the front. The cirrus cloud covers a large part of the simulated domain specifically in the altitudes 9.5 km and 10.5 km (figure 5.5). At 11.5 km altitude, only a small area in the southeastern part of the domain is cloudy. Most parts of the cloud at all altitudes has comparably higher number concentrations of ice crystals than the ice number concentration in the thin cirrus on 24<sup>th</sup> April 2013. A large area of the cloud has an ice number concentration between  $1 \times 10^4 \text{ m}^{-3}$  to  $2 \times 10^6 \text{ m}^{-3}$  which is around 2 orders of magnitude higher than the ice number concentration range in thin cirrus on 24<sup>th</sup>

April 2013. Occasionally, ice number concentration reaches more than  $2 \times 10^6 \text{ m}^{-3}$  in some small areas, indicating homogeneous nucleation events in those areas as discussed in section 5.1. The sizes and the number concentrations of ice crystals are similar to the sizes and number concentrations that are usually formed in contrails (CFAD section 5.1).

Figure 5.5 shows a horizontal section through the cloud field with and without contrail disturbance. After the start of air traffic, cirrus has been perturbed due to the formation of contrail ice crystals and is visible as thin lines specifically in the center part of the cloud at 10.5 km altitude. Some contrails are difficult to see in figure 5.5 because they are very thin and the background ice number concentration is already relatively high. The number concentration of contrail ice crystal in this newly formed contrail is slightly higher than surrounding cirrus ice crystal number concentration; it reaches more than  $2 \times 10^6 \text{ m}^{-3}$  which is 2 orders of magnitude higher than the surrounding cirrus ice crystal number concentration.

After an hour from the start of air traffic, a large part of the cloud field is perturbed due to contrail formation. The contrail induced perturbation is visible mainly at altitudes above 10.5 km because low temperatures at these altitudes and background cirrus properties e.g. large ice water content, high number concentration and large in-cloud ice supersaturation, provide favorable conditions for contrail ice nucleation and for their survival (chapter 4). Furthermore, a high supersaturation in those altitudes due to the supply of water vapor through warm conveyor belts allows ice crystals to grow further and persist for a longer time. Therefore, a high number of ice crystals can be seen in contrail formed under this synoptic condition. Even a high ice number concentration up to  $1 \times 10^6 \text{ m}^{-3}$  can be seen in aged contrails, a factor of 2 lower than the number concentration of ice crystals in young contrails and 1 order of magnitude higher than the number of ice crystals in the one-hour old contrails in the case of thin cirrus on 24<sup>th</sup> April 2013. The contrail perturbation of cirrus field at altitude 9.5 km after an hour of air traffic is not large as the perturbation of cirrus field above 10.5 km altitude, in only a few places, shows an increase in ice number concentration after contrail formation. However, the change in ice number concentration is not as large as the change in ice number concentration at upper altitudes. Due to relatively warm ambient temperature at low altitudes, contrail ice crystals mainly nucleate close to ambient temperature (chapter 4, section 4.1) and therefore, only a few ice crystals form, depending on the atmospheric variability.

Two hours of continuing air traffic shows a further increase in the contrail perturbed regions. Most parts of the cloud show a relatively high ice number concentration compared to the cirrus without contrail formation. The ice number concentration is almost double in areas where contrails have formed. Since most parts of the cloud are perturbed, young line shaped contrails with relatively higher ice number concentration than surrounding areas can be seen mostly within regions that are already polluted. Some parts of the cloud field at 9.5 km altitude show an increase in the ice number concentration after two hours of simulation. The increase in ice number concentration at low altitude is mainly visible just below the perturbed cloud field in upper altitude, indicating the distribution of contrail ice crystals at lower altitudes. The contrail ice crystals can reach lower altitudes due to different processes e.g. dilution of contrail plume, growth of contrail ice crystals and then their sedimentation, leading to aggregation of cirrus and contrail ice crystals. These processes are explained in detail in section 5.5. A part of the cirrus around 50°N and 5°E at altitude 10.5 km shows dissolution of the cirrus after contrail perturbation (figure 5.5).

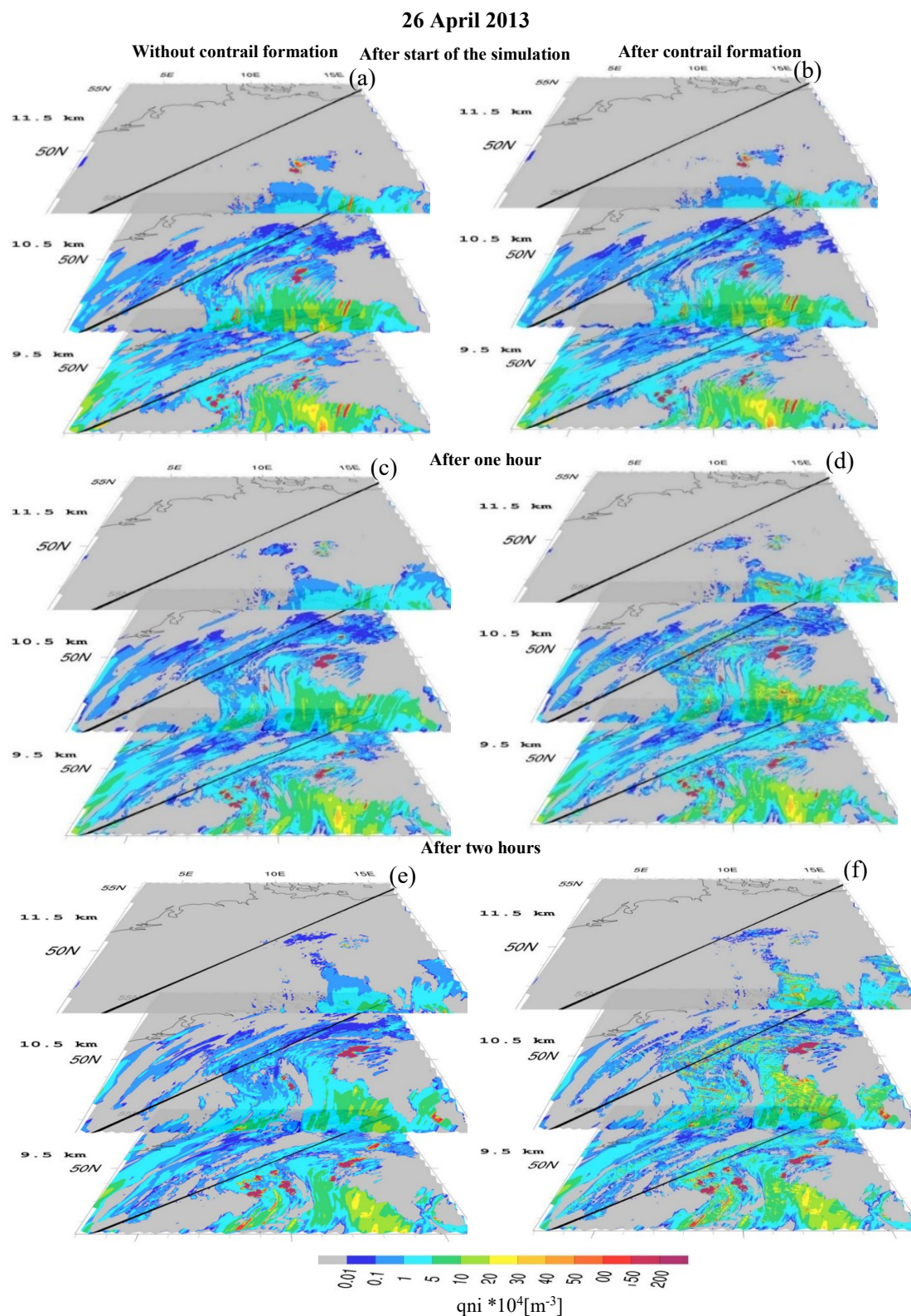


Figure 5.5: Ice number concentration ‘ $q_{ni}$ ’ in the cirrus cloud field on the 26<sup>th</sup> April 2013 for three different altitudes 9.5, 10.5 and 11.5 km over the Germany domain (48.5°N - 55.5°N; 2.0°E - 17°E) simulated by ICON-LEM without contrail induced perturbations (left) and including contrail perturbations (right). At the top a snapshot of the cloud at the start of the simulation and below after one hour of continuous air traffic is shown. Each altitude level has a thickness of approximately 150m.

**Summary:** In section 5.2, the spatial distribution of contrail-induced cirrus perturbation is shown for both thick and thin clouds. The contrails can be seen as lines with a relatively large ice number concentration than the ice number concentration in the surrounding cirrus. The number concentration of ice crystals in cirrus has reached up to  $106 \text{ m}^{-3}$  at flight levels. After some time, contrails dilute and spread and cover a large area. Therefore, old contrails can be seen as relatively thick lines and slightly low ice number concentration ( $\sim 104 \text{ m}^{-3}$ ) than the newly formed contrails. In both synoptic conditions, a large part of the cirrus is perturbed due to continuous air traffic.

### 5.3 Vertical distribution of the cirrus and its contrail induced perturbations

Here the vertical distribution of contrail-induced perturbations is discussed. Initially, contrail ice crystals are distributed over a few hundred meters downwards in the atmosphere during vortex descent (chapter 3). Later, they mix with the surrounding air and may grow due to water vapor deposition or aggregation and sediment, reaching lower atmospheric levels depending on the atmospheric variability.

In order to explore the vertical development of the cloud and its perturbations, a vertical transect of the cloud along the black line (shown in Figures 5.3 and 5.4) is displayed in figure 5.6 for the thin cirrus on 24<sup>th</sup> April 2013. Similarly, figure 5.7 shows the vertical development of the cirrus and its contrail induced perturbations along the black line shown in figure 5.5 for the thick cirrus on 26<sup>th</sup> April 2013. The length of this black line (vertical cut) is around 1093 km from southwest to northeast within the domain. In this section, the cloud properties after contrail formation have been analyzed in terms of the number concentration of ice crystals and ice water content. Since aircraft emitted ice water mass is small in comparison to the grid mean water vapor and ice water mass, and therefore the emissions do not change the ice water content significantly, the ice water content has been analyzed only for thin cirrus.

#### 5.3.1 24<sup>th</sup> April 2013 case

The cloud on this synoptic condition has a geometric thickness of around 6 km starting from  $\sim 6.5$  km and stretching up to 12 km altitude. The western part of the cloud starts slightly higher, above 7.5 km altitude, and has a cloud top height of around 12 km; the eastern part of the cloud starts from a much lower altitude (below 6.5 km) and reaches only up to 10.5 km. Large parts of the cloud field have low number concentration of ice crystals up to  $1 \times 10^4$  per  $\text{m}^{-3}$  and are relatively homogeneous. During the simulation period, the cloud is advected from northwest to southeast; therefore, the vertical distribution of the ice number concentration shown in figure 5.6 is a snapshot of the different part of the cloud.

When prescribing air traffic, contrail perturbations are visible mostly above 10 km. The number concentration of ice crystals increases drastically in those areas where contrails have been formed. Initially, during vortex phase, ice crystals are distributed a few hundred meters down from the air-traffic level (figure 5.6) and are visible as thin vertical lines of high ice crystal number concentration. As seen in figure 5.2, the number concentration of ice crystals is around  $1.5 \times 10^6 \text{ m}^{-3}$  in the contrails. After some time with increases in ice crystals, number concentrations can be found lower down in the atmosphere. Different processes, e.g. turbulence mixing, sedimentation, aggregation of ice crystals and wind shear, can cause the spreading of ice crystals into lower levels. For example, atmospheric turbulence increases the mixing of contrail plume with the surrounding air and deposits ice crystals further down in the atmosphere. Depending on the sedimentation rate

of the ice crystals, ice crystals may distribute into lower levels. Also, due to aggregation of ice crystals in particular, when large ice crystals are above a small contrail, ice crystals fall on the contrail ice crystals and form bigger ice crystals. Moreover, the wind shear also controls the spreading of contrail ice crystals in horizontal and vertical directions; if wind shear is large, then contrail width will be large and contrail ice crystals will be spread into a large area. One hour after the start of air traffic, a much larger area above 9 km altitude has been perturbed, specifically the middle part of the cloud. The peak of ice number concentration in old contrails has been reduced by 1 order of magnitude, similar to the rate of reduction of ice number concentration in the horizontal direction. In the meantime, new contrails have also been formed and can be seen as areas of high number concentration of ice crystals.

Extending the simulation for one more hour (two hours after the start of the air traffic) an increase in the contrail perturbed area can be seen. The old contrails have been expanded, perturbing a large part of the cloud both horizontally and vertically; those places where ice number concentration was very low in the simulations without contrail perturbations now have a high number concentration of ice crystals.

Apart from that, some parts of the cloud have been dissolved during the simulation period (around one and a half hours from the start of air traffic) (figure 5.6). This effect is visible in the western part of the cloud where ice water content and the number concentration of the ice crystals are very low and the cloud is geometrically very thin. Furthermore, in this area, the geometric thickness, the ice number concentration and ice water content of the cloud decrease constantly. The reason for the dissolution of the thin part of the cirrus is because the air in this area is subsaturated with sublimation of the ice crystals in those areas. The sublimation rate of the ice crystals and therefore dissolution rate of the cloud depends on the size of the ice crystals and ice subsaturation in the cloud. The large ice crystals take longer to sublimate completely whereas small ice crystals disappear relatively fast. In the case of contrail perturbed cirrus, the dissolution is large because contrail formation in this thin part of the cloud replaces a few big ice crystals by many small ice crystals, leading to faster dissolution of the cloud.

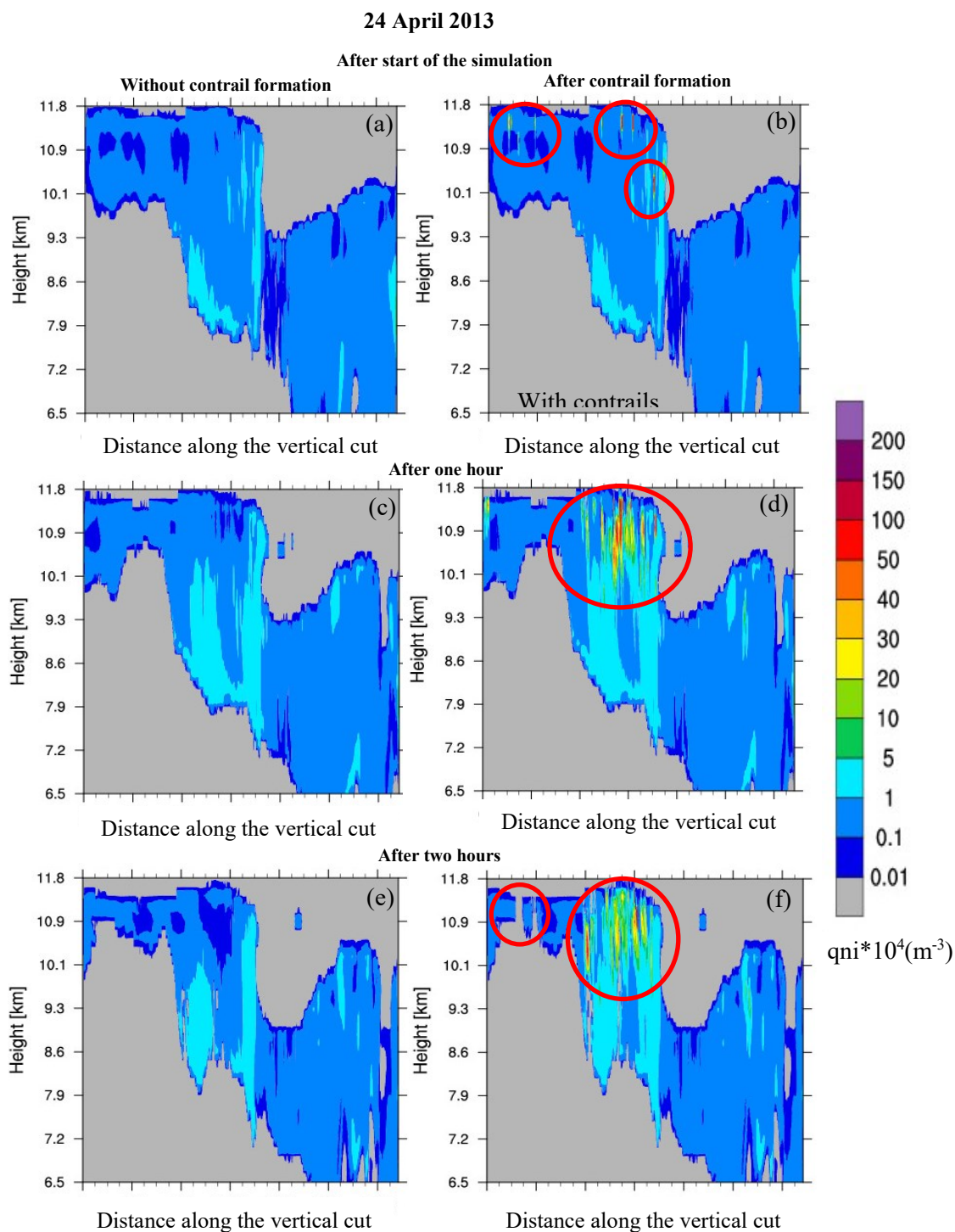


Figure 5.6: Vertical distribution of the ice crystal number concentration ‘ $q_{ni}$ ’ of the cirrus cloud field on 24<sup>th</sup> April 2013 along the black line shown in figure 5.3 simulated by ICON-LEM without contrail induced perturbation (left) and including contrail perturbations (right). The length of the vertical cut from left to right is around 1093 km. At the top a snapshot of the cloud at the start of the air traffic induced perturbations, middle after one hour of continuous air traffic and below after two hours of continuous air traffic are shown.

### 5.3.2 26<sup>th</sup> April 2013 case

The vertical transect through the cloud deck on the 26<sup>th</sup> April displays a large variability in the ice crystal number concentration. Some parts of the cloud have a very high number concentration, up to  $2 \times 10^5 \text{ m}^{-3}$ . The vertical distribution of the ice number concentration in the cloud has been shown along the black line in figure 5.5, similar to the case of thin cirrus. The cloud is scattered in a large area of the domain and has a geometrical thickness of more than 4 km in some parts. The cloud top reaches above 11 km in most of the area. The western part of the cloud has a very high number concentration in some areas and stretches over a few kilometers, from below 7 km to around 10 km. The high number concentration of ice crystals in this region indicates formation of liquid origin clouds (chapter 2, section 2.3).

At the beginning of air traffic, only a few contrails have been formed that cross the transect and display slightly increased number concentration relative to the surroundings (figure 5.7b). An hour or two after the start of air traffic, many contrails are clearly visible as vertical lines with relatively high number concentrations, more than  $1.5 \times 10^6 \text{ m}^{-3}$ . The vertical view is showing ice number concentration in old and freshly formed contrails, whereas the thin small lines with high number concentration are indicating freshly formed contrails (around 5 minutes old contrails) and the relatively thick lines with slightly lower ice number concentration are indicating older contrails. Most of the contrails are formed above 10 km, the main air-traffic level. However, there are a few contrails that have formed at lower altitudes as well. The ice number concentration in contrails formed at high altitudes are comparably higher than the ice number concentration in contrails at low altitudes. Low temperatures at high altitudes cause contrail ice formation far away from contrail formation threshold temperature with many small ice crystals formed. Whereas at low altitudes, due to relatively warm temperatures, contrail ice nucleated close to the ambient temperature and the number of nucleated contrail ice crystals are dependent on how far contrail ice crystals are forming from ambient temperature (chapter 4). Moreover, the surviving number of contrail ice crystals can be large in upper altitudes since ice crystals stay in much colder temperatures than at low altitudes. The reason for the low number concentration in some contrails may be because of dilution of old contrails. In this cloud, the perturbation of the cirrus due to contrail ice formation can be seen in cloud layers of approx. 2 km.

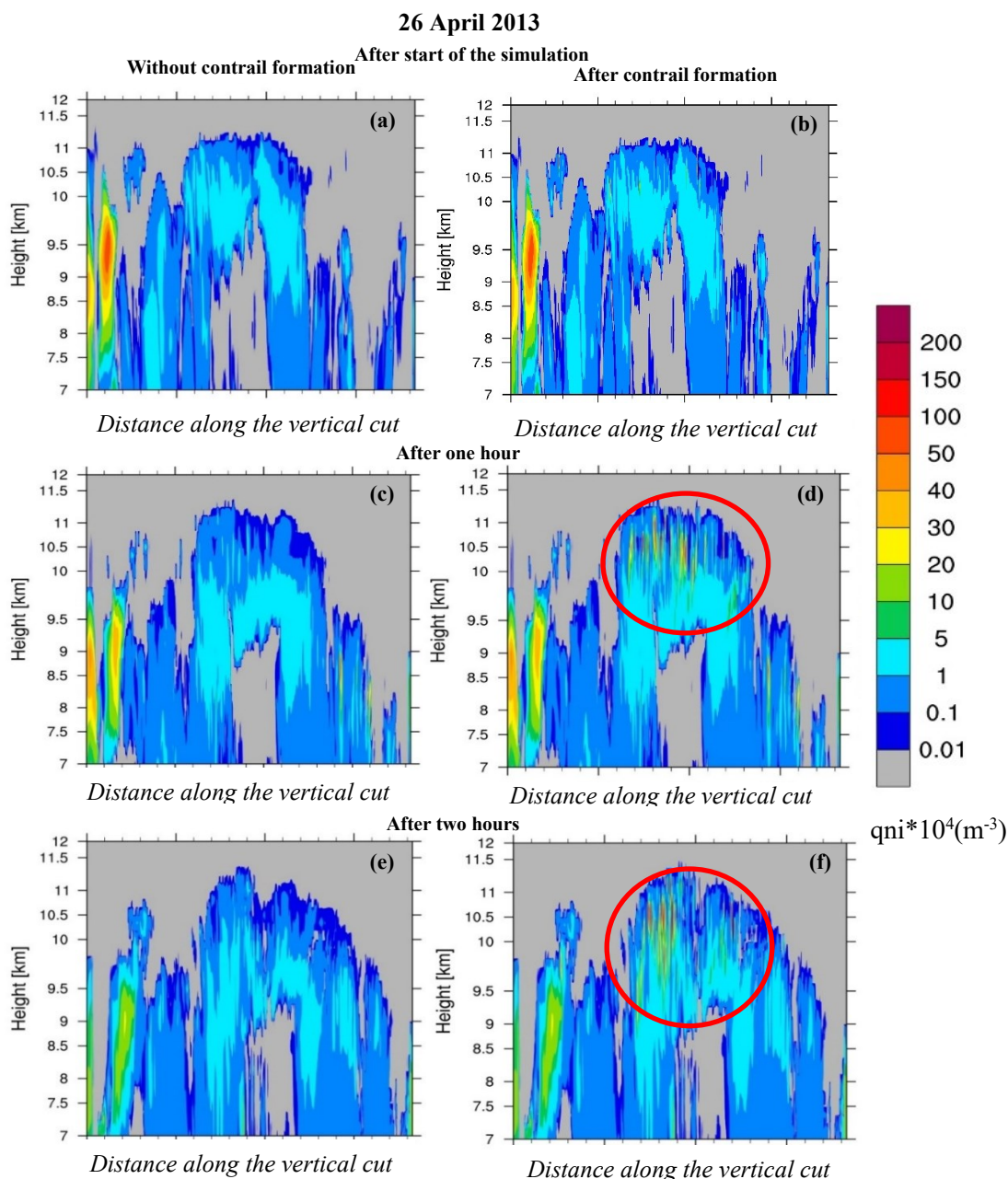


Figure 5.7: Vertical distribution of the number concentration of the ice crystals ‘ $q_{ni}$ ’ of the cirrus cloud field on 26<sup>th</sup> April 2013 along the black line shown in figure 5.5. The number concentration of the ice crystals simulated by ICON-LEM without contrail induced perturbation (left) and including contrail perturbation (right). The length of the vertical cut from left to right is around 1093 km. At the top a snapshot of the cloud at the start of the simulation, middle after one hour of continuous air traffic and below after one hour of continuous air traffic are shown.

A large area of the cloud has been modified by contrail formation at flight altitudes. Figure 5.8 shows percentiles of the distribution of ice crystal number concentration in contrail perturbed cirrus and unperturbed cirrus and gives an indication of how much of the cloudy area has been modified after two hours of continuous air traffic. The result is shown for both synoptic conditions for altitudes between 10 km to 12 km. In the case of thin cirrus, the ice number concentration in the unperturbed cirrus cloud slightly increases with time, while in the thick cloud, the number concentration of the ice crystals slightly decreases over time. After prescribing air traffic, around

0.1% of the total cloudy grid boxes between altitudes 10 km to 12 km perturbed in every timestep due to contrail ice nucleation. Initially, only 0.1% of the total cloudy area has a high ice number concentration; therefore, the 95 percentiles do not change at the beginning of the simulation (figure 5.8). That 0.1% area of the cloud shows high ice number concentration, mostly around  $10^6 \text{ m}^{-3}$  and  $5 \times 10^7 \text{ m}^{-3}$  in the case of thin and thick cirrus, respectively. Later, the spreading of previously formed contrails and the formation of new contrails in the unperturbed area increases the total perturbed area within cirrus. Therefore, a continuous increase in the contrail perturbed area can be seen over time. After an hour of the continuous air traffic, 5% of the cloudy area on the 26th has a significantly higher ice number concentration (more than  $2.5 \times 10^5 \text{ m}^{-3}$ ), and around 25% of the cloudy has an ice number concentration of  $> 5 \times 10^4 \text{ m}^{-3}$  which is larger than the ice crystal number concentrations in the cirrus without contrail perturbation (control simulation) (figure 5.8). The change in the ice number concentration in the thick cirrus is larger than the change in ice number concentration in the thin cirrus. The reason for this large change in ice number is because of the different microphysical properties of these two clouds and therefore have different effects on contrail ice nucleation and their survival fraction (chapter 4). In the case of thick cirrus, the survival fraction of the ice crystals are larger than the surviving ice crystals in thin cirrus; therefore, the contrail ice number is large in the case of thick cirrus. After around two hours of continuous air traffic, the number concentration of the ice crystals has increased further. 25% of the area of the cloud have more than  $\sim 2 \times 10^4 \text{ m}^{-3}$  number concentration of ice in the case of thin cirrus and more than  $6 \times 10^4 \text{ m}^{-3}$  in the case of thick cirrus, which is around a factor of 3 higher than the number concentration of ice crystals in the unperturbed case. Around 5% of the total area of the cloud has a number concentration of more than  $1.0 \times 10^5 \text{ m}^{-3}$  in thin cirrus and  $3.5 \times 10^5 \text{ m}^{-3}$  (3 times higher than the thin cirrus case) in thick cirrus (figure 5.8). The ice number concentration in 25% and 5% cloudy air is slightly lower than the number concentration in newly formed contrails because only  $\sim 0.1\%$  part of the cloud has air traffic at a time. However, air traffic perturbed only 0.1% of the total cloudy area at a time and cumulatively 1.2% of the total cloudy area in two hours but can perturb a large area of the cloud. Even the median properties of the cirrus have been changed due to continuous air traffic. That means contrail formation within cirrus due to continuous air traffic can change the average cirrus properties. To quantify the total cirrus area perturbed due to air traffic is not possible with this model because total cloudy area changes over time since new cloud fields come into the domain and new contrails may form within that area, and simultaneously some part of the cloud may move out from the domain area.

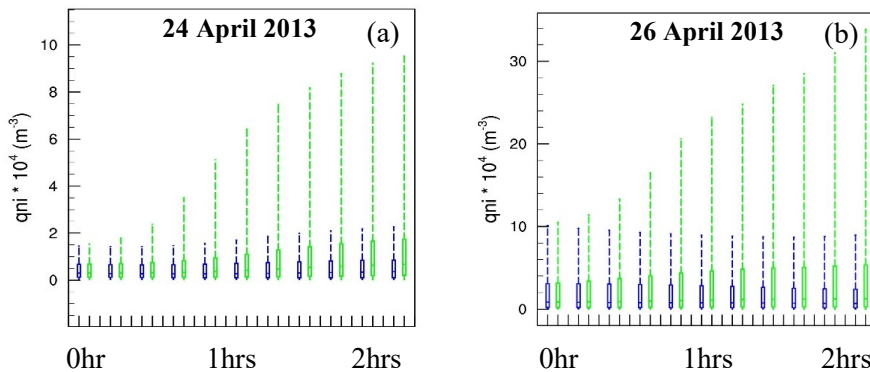


Figure 5.8: 5, 25, 50, 75, and 95 percentiles of the number concentration of ice ‘ $q_{ni}$ ’ in the cloud at 10.5 km with and without contrail perturbation. blue whisker boxes show percentiles of ‘ $q_{ni}$ ’ in the cloud without contrail perturbation ‘control’ and green whisker boxes are showing percentile with contrail perturbation ‘perturbed’ in every 10 minutes after start of simulation ‘0 hrs’, one hour after ‘1 hrs’ and two hours after ‘2 hrs’ start of the simulation. The left plot shows analysis for 24<sup>th</sup> April 2013 and the right-hand side plot shows analysis for 26<sup>th</sup> April 2013.

### 5.3.3 Change in ice water content

The formation of contrail ice crystals within cirrus can change the ice water content in cirrus. However, the change in the cirrus ice water content due to contrail formation is not as large as the change in the ice number concentration. Figure 5.9 shows the effect of the contrail formation within cirrus on the ice water content of the cloud for thin cirrus on the 24<sup>th</sup> April 2013. On that day, the change in IWC is easier to detect because the IWC of the undisturbed cloud is lower. The ice water content in this cloud is very low, only up to  $5 \times 10^{-4} \text{ gm}^{-3}$  on the main air-traffic levels, and in the lower altitudes up to  $5 \times 10^{-2} \text{ gm}^{-3}$ . The ice water content in the undisturbed cirrus has been reduced slightly in altitudes above 10 km during two hours of simulation.

Initially, the increase in ice water content is very slightly due to contrail formation since aircraft emitted water vapor is not very large (section 5.1). The emitted water vapor from aircraft fuel burn contributes only around  $7.68 \times 10^{-5} \text{ gm}^{-3}$  when an aircraft travels 600 meters within a grid box; this is 15% of the cirrus ice water content value  $5 \times 10^{-4} \text{ gm}^{-3}$  at flight levels (above 10 km).

After contrail formation, the ice water content increases slightly to values of  $\sim 5 \times 10^{-4} \text{ gm}^{-3}$  in main air traffic levels and is visible as small vertical thin lines (figure 5.9b). The formation of the many small contrail ice crystals high up in the cloud tends to increase the ice water content in high altitudes since small ice crystals will not sediment quickly. Therefore, contrail ice crystals and associated ice water content will stay in upper altitudes for relatively longer periods of time. That kind of tendency could be visible in nature. Moreover, contrail ice formation within cirrus can increase the aggregation of the ice crystals if large particles e.g. cirrus ice crystals from an upper level fall into the contrail perturbed areas. Large ice crystals that are falling meet the small ice crystals on the surface to form even bigger ice crystals, tending to increase the sedimentation.

During the contrail life cycle, contrail ice crystals mix with the surrounding air and can grow by depositional growth together with surrounding cirrus ice crystals if the air is ice supersaturated. Since ice supersaturation is not very large in this thin cirrus, reaching only up to 1.2 in some areas, the ice water content in contrails is increased slightly one and two hours after the start of the air traffic reaching up to  $5 \times 10^{-3} \text{ gm}^{-3}$  (figure 5.9d). The left section of the cloud has a very low ice water content and is dissolved when contrail ice crystals form in those areas (section 5.3.1). The dissolution of the thin part of the cloud can be speeded up in the presence of contrail ice crystals for different reasons for example, fast sublimation of small contrail ice crystals may be due to fluctuation in relative humidity or due to an increase in the aggregation of ice crystals can lead to a relatively fast sedimentation of the ice crystals.

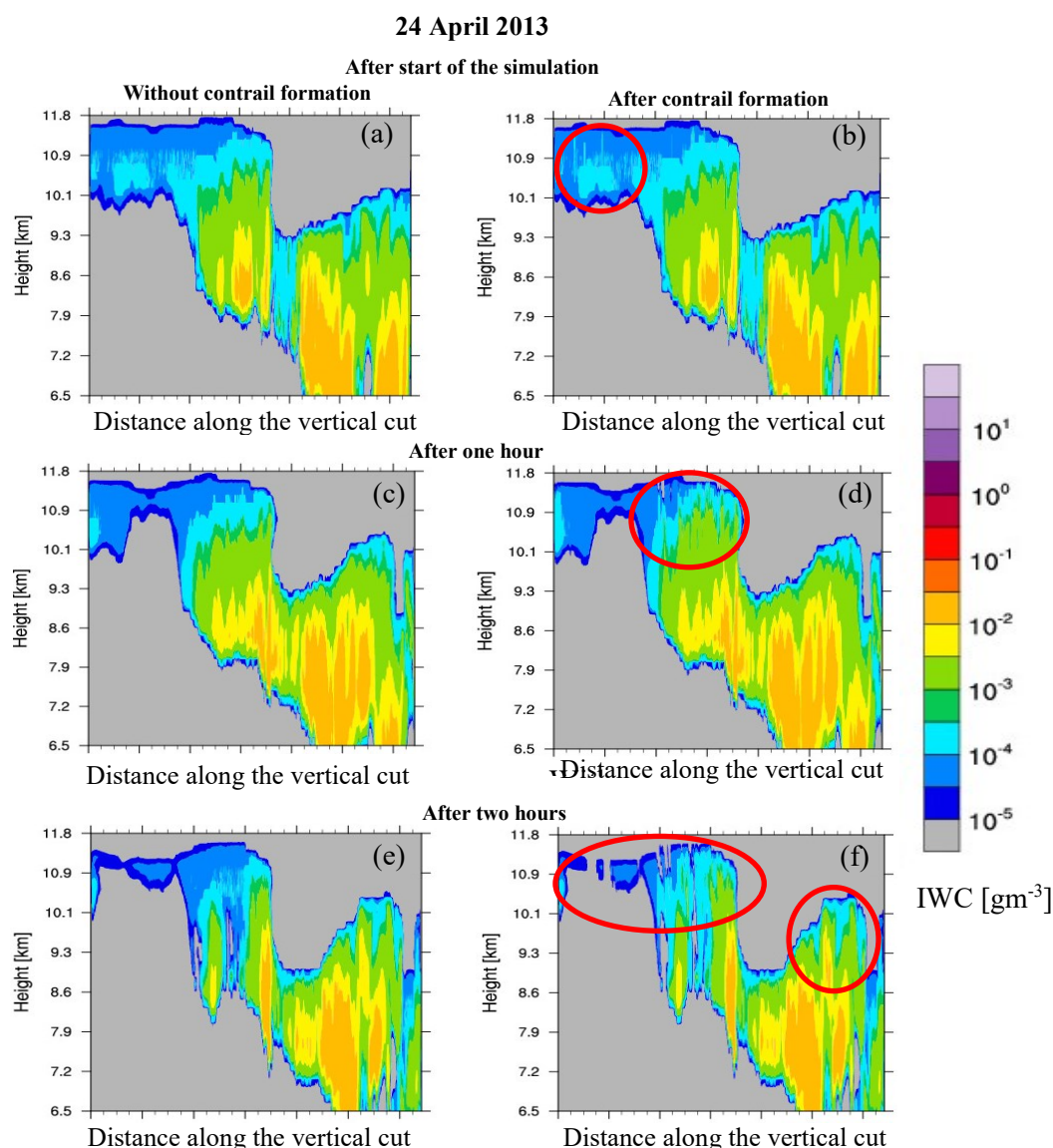


Figure 5.9: Vertical distribution of the ice water content 'IWC' in the cloud on 24<sup>th</sup> April 2013 along the black line shown in figure 5.3 and 5.4. First column shows ICON-LEM simulated cloud without contrail perturbation and second column shows cloud with contrail perturbation. Top row shows snapshot of the cloud at start of simulation, middle row shows snapshot of the cloud after one hour and bottom row shows snapshot of the cloud after two hours.

**Summary:** In the section 5.3, the vertical distribution of contrail-induced cirrus perturbation has been shown. After formation, contrail ice crystals are distributed over a few hundred meters during vortex descent. Later, they mix with the surrounding air and reach the much lower altitudes. The contrails can be seen as vertical lines with much higher ice number concentration than the surrounding undisturbed cirrus ice number concentration. One and two hours after the start of the air traffic, the contrail ice crystals have reached almost two kilometers from their formation altitudes.

Later, in this section, change in cirrus ice water content due to contrail ice formation has been discussed. Initially, ice water content does not change significantly because the emitted water vapor from the aircraft is not large compared to the ice mass available in the cirrus. Therefore, ice water

content at flight levels changes slightly due to air traffic. Later, contrail ice crystals mix with the surrounding air and grow further, increasing the ice water content within the contrails. One and two hours after air traffic, the increase in the ice water content can be seen at flight levels. Contrail ice formation in the thin part of the cloud shows the fast dissolution of the cloud.

## 5.4 Optical depth of the contrail perturbed cirrus

Cloud optical depth is an important parameter when studying the radiative impact of a cloud. Optical depth of the cloud depends on the microphysical properties of the cloud e.g. ice water content, sizes and shapes of the cloud particles (chapter 3, section 3.9). The model used in this study resolves the ice water content and ice crystal's mean radius but does not resolve the shape of the ice crystals; therefore, the shape of the ice crystals have been assumed as explained in chapter 3. Contrail formation within cirrus changes the cloud's microphysical properties and therefore affects the optical properties. Contrail ice formation introduces many small ice crystals in the cirrus; droxtals and spherical shapes result in a change in the particle size distribution in the cirrus and therefore, changes extinction. Freshly nucleated contrail ice crystals within cirrus increases the number of ice crystals in the cloud significantly but increases ice water content only slightly because aircraft emitted water vapor is not large. That means, the mean volume radius of the ice crystal population in cirrus moves towards the small sizes after contrail ice formation. The growth of the contrail ice crystals over time in the presence of ice supersaturation increases ice crystal sizes and ice water content in the contrail. A cloud consisting of many small ice crystals has larger reflectivity (extinction) of shortwave radiation than a cloud consisting of big ice crystals at constant ice water content. Therefore, contrail perturbations that cause large number concentrations of small ice crystals in the cirrus without changing ice water content strongly increase the reflectivity because small ice crystals tend to strongly reflect solar radiation than absorb terrestrial radiation (Zhang et al., 1999).

In this section, optical depth has been calculated for both days, 24<sup>th</sup> April 2013 and 26<sup>th</sup> April 2013. Firstly, optical depth has been calculated for a vertical slice of the cloud along the cloud transect shown in figures 5.3 and figure 5.5 respectively. Optical depth has then been analyzed for the whole cloud. The optical depth has been calculated by assuming ice crystal habit mix and ice particle size distribution as explained in chapter 3, section 3.9.

### 5.4.1 Optical depth of the contrail perturbed cirrus along with the vertical cut

#### 5.4.1.1 24<sup>th</sup> April 2013 case

The optical depth of the cloud is the vertically integrated extinction of the cloud (Kärcher et al., 2009; Voigt et al., 2011). The extinction of the shortwave radiation is dependent on the effective radius of the ice crystals (effective radius of the ice crystal depends on size, shape and orientation of the ice crystals) (Schumann et al., 2010). The extinction and optical depth of the cloud will be large if the ice water content and ice number concentration in the cloud is large. Therefore, the optical depth of the cloud is large in the middle part where the cloud is geometrically thick and has high ice water content (figure 5.9). Some parts of the cloud (mainly the western part of the cloud) are thin and have low optical depth (figure 5.10). Overall cloud is optically thin, optical depth reaching only up to 1. After contrail formation, many small spherical and droxtal ice crystals increase in the cirrus causing a change in the particle size distribution; this means that the mean

volume radius will move towards the small ice crystals, causing a change in extinction and thus a change in the optical depth (Zhang et al., 1999). Since small spherical and droxtal shape ice crystals interact strongly with the shortwave radiation, this will cause increase in the extinction (Schumann et al., 2010, and chapter 3, section 3.9). Initially, only a few contrails are formed along the transect (figure 5.10a). They are visible in the form of relatively high optical depth up to 1 where the optical depth of the undisturbed cloud is 0.6. Specifically, the middle part of the cloud shows the largest change in optical depth because this part of the cloud has been perturbed most. Contrails formed in thin parts of the cloud are connected with small changes in the optical depth. The reason for this is that the number of ice crystals formed in a contrail is comparably low in the thin part of the cirrus because ice water content and ice supersaturation are low in those parts of the cloud. Low ice supersaturation and low ice water content in cirrus cause low ice crystal number (after vortex phase) in contrails (chapter 4).

After some time, contrails dilute and the number concentration of ice crystals decreases (section 5.2.1 and 5.2.2); this causes a slight decrease in the peak optical depth values. Since the number of ice crystals in a contrail is relatively higher than the number in the surrounding cirrus, optical depth remains high in the contrail perturbed areas. The optical depth reaches values of up to 2 after one hour of continuous air traffic which is 2 times higher than the surrounding cirrus optical depth (figure 5.10 b, e). The formation of new contrails within old contrails increases ice crystal numbers in those areas which also causes an increase in the optical depth. Continuous air traffic for an hour introduces perturbations in a large area of the cloud resulting in large optical depth in the contrail perturbed areas. Continuing the air traffic for two hours shows an increase in optical depth in the geometrically thick part of the cloud since ice crystals grow and a decrease in optical depth of the

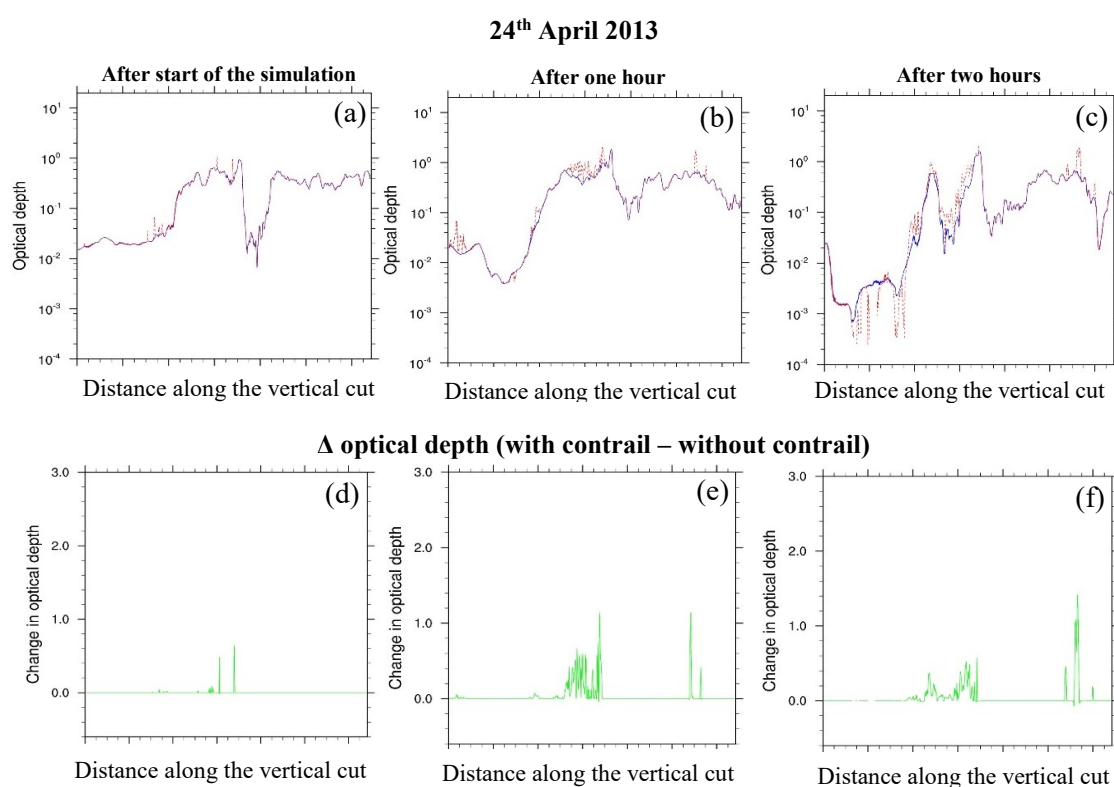


Figure 5.10: Optical depth of the cloud for 24<sup>th</sup> April 2013 along the transect (shown in figure 5.3) for the simulation without contrail formation (blue curve) and with contrail formation (red curve) (first row); The difference in the optical depth due to contrail formation (with contrail – without contrail) (second row) immediately after start of the air traffic (a, d), after one hour of continuous air-traffic (b, e) and after two hours of continuous air-traffic (c, f).

thin part of the cloud where cloud has been dissolved due to formation of contrail ice crystals (section 5.3.1). The optical depth has been decreased up to  $2 \times 10^{-4}$  in the thin part of the cirrus.

#### 5.4.1.2 26<sup>th</sup> April 2013 case

As described earlier, the cloud formed on this day has significantly different microphysical and optical properties than the thin cirrus on 24<sup>th</sup> April 2013. The cloud is connected with the frontal system and therefore, has high ice water content and ice crystal number concentration, resulting generally in large optical depth. Most of the cloud has large optical depth with a range between  $10^{-2}$  to 10.

After formation of contrails, the optical depth of the cirrus has been increased significantly. Figure 5.11 shows the cloud optical depth in contrail perturbed and unperturbed cirrus along the vertical cut shown in figure 5.5. After the start of the simulation, when only few contrails have formed and only a small part of the cirrus has been perturbed, there is a change in the optical depth in contrail perturbed cirrus to below 1.0 (figure 5.11 a). After an hour, due to formation of more contrails within cirrus, a large part of the cirrus shows the change in optical depth. The change in optical depth after an hour is larger than the change in optical depth at the beginning of the simulation (5.11 a, b) because, due to growth of the ice crystals over time, the ice water content and the optical depth have been increased. The optical depth in perturbed cirrus has reached up to 1, while the optical depth of the unperturbed cirrus is below 0.4. The contrail perturbed area within cirrus has been increased with time as new contrails have been formed and the aged contrails have been diluted and spread into the relatively large volume of the cloud. Therefore, change in the optical depth can be seen in a large part of the cirrus after two hours of air traffic (figure 5.11 c, f). The change in the optical depth is mostly below 3.0 in contrail perturbed regions but occasionally reaching more than 3.0. Those large changes in optical depth are possibly connected with contrail ice formation within aged contrails because the area along the vertical transect is mostly perturbed by the contrails in those regions (figure 5.5). Therefore, there is the possibility that new contrails will be formed within aged contrails which will introduce many small ice crystals in that area and further increase the optical depth of contrail perturbed parts of the cloud.

The area with change in optical depth in this cloud is larger than the change in the optical depth in the thin cloud (figure 5.10 d, e, f) because the number of contrails formed in this synoptic condition is large. Cloud properties, specifically in-cloud ice saturation and ice water content, are relatively larger than in clouds on other days which have provided favorable conditions for formation and persistence of contrails.

Apart from that, few places show a decrease in the optical depth of the contrail perturbed cloud. The decrease in optical depth is mainly visible after one and two hours of perturbation and mostly close to the contrail perturbed areas. The reason for decrease in optical depth has been explained in detail in section 5.4.3 because horizontal variability of change in cloud optical depth shown in that section provides a clearer view of areas where optical depth has been decreased.

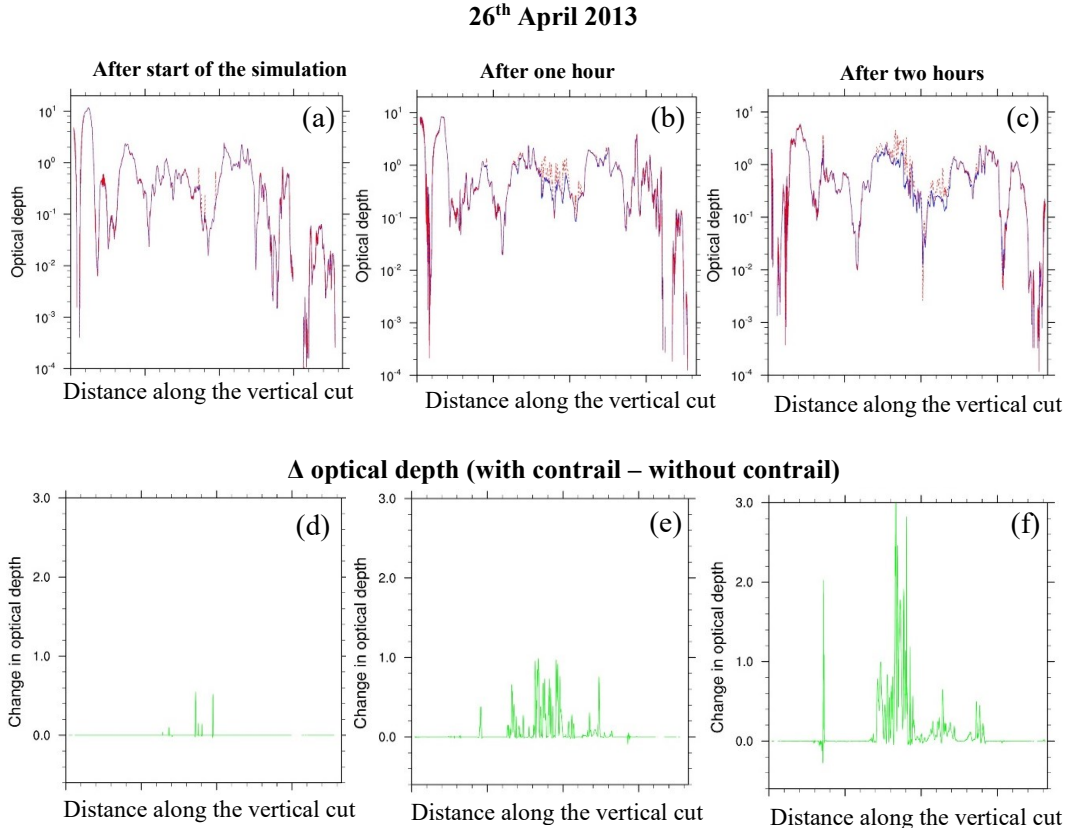


Figure 5.11: Similar as figure 5.10 but for cloud on 26<sup>th</sup> April 2013 and along the vertical cut shown in figure 5.5.

## 5.4.2 Optical depth of the whole cloud

In this section, optical depth has been calculated for the whole cloud between altitudes 7 km to 13 km (because air traffic has been initialized between these altitudes only). The probability distribution of cloud optical depth has been calculated for contrail perturbed cirrus and unperturbed cirrus (figure 5.12). At the start of the simulation when only a few contrails have been formed, a change in the optical depth is not visible because only a small part of the cloud is perturbed; therefore, the probability distribution of optical depth is unchanged. One hour after the start of the simulation, the probability of high optical depths above 1 is increased in the case of thin cirrus and the probability of lower optical depths is decreased. However, in the thick cirrus, the change in optical depth is not clearly visible (due to the logarithmic scale) because the thick cirrus already has high optical depth in most parts of the cloud. Two hours after the start of air traffic, the probability of high optical depths has increased in the contrail perturbed cirrus (figure 5.12). The probability of lower optical depth has decreased. There are two possible reasons for the decrease in the probability of low optical depth. One is that the optical depth of the cloud has been increased due to the formation of contrail ice crystals with resultant shift of probability from low optical depth to high optical depth. Another reason is that the thin part of the cloud has been dissolved due to formation of contrail ice crystals. The change in optical depth is much clearer in the horizontal variability of the cloud as explained in section 5.4.3.

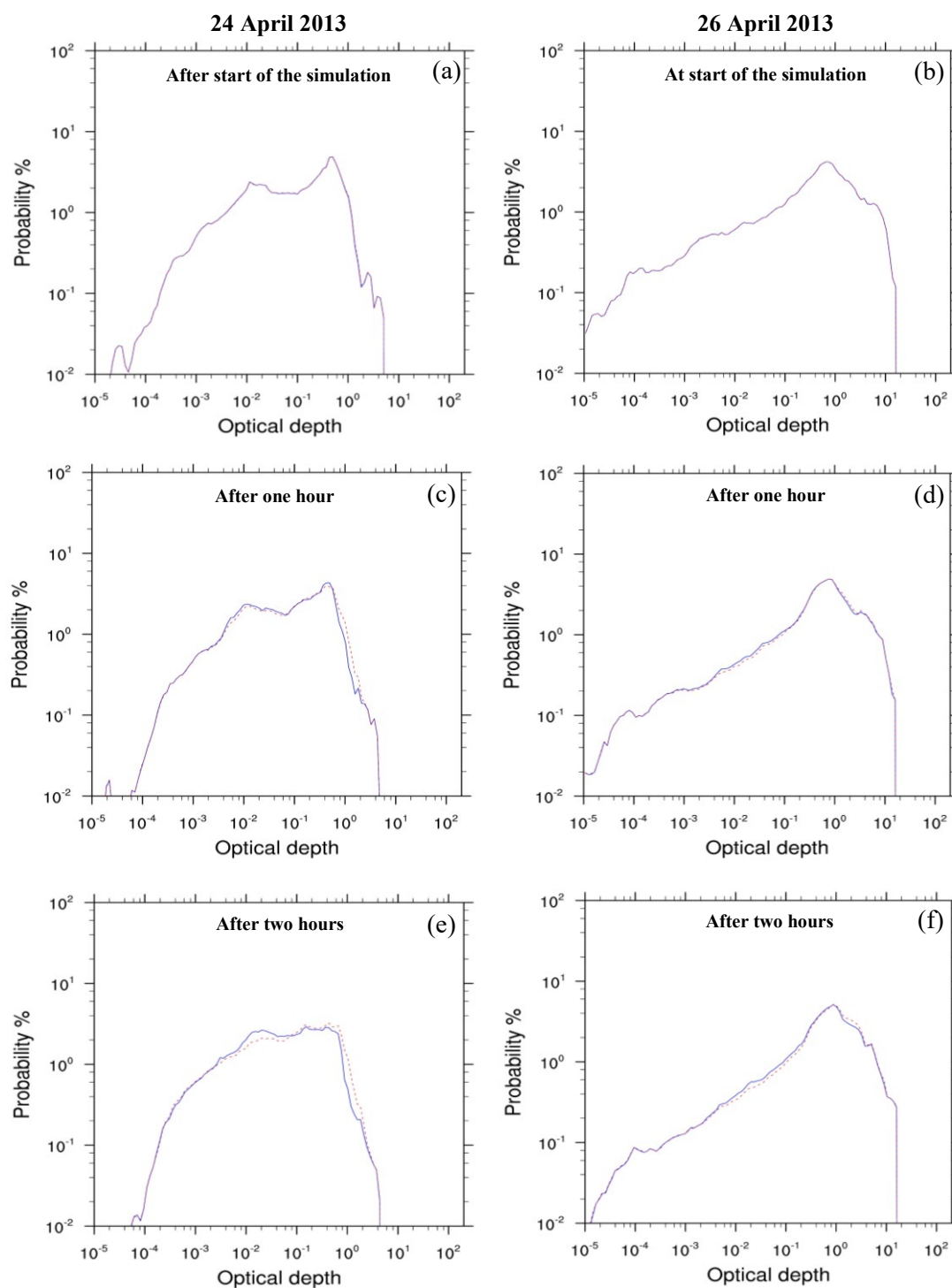


Figure 5.12: Probability distribution of optical depth of the cloud on 24<sup>th</sup> (left column) & 26<sup>th</sup> April 2013 (right column) without contrail perturbation (blue curve) and with contrail perturbation (red curve) immediately after start of the air traffic (top row), one hour after start of continuous air traffic (middle row) and two hours after start of continuous air traffic (bottom row). The probability of the cloud optical depth is calculated by using logarithmic bin size.

### 5.4.3 Horizontal variability of the optical depth in the contrail modified cirrus

The horizontal variability of the change in cloud optical depth due to the formation of the contrails has been analyzed in this section for the cirrus cloud on 24th and 26th April 2013 (figures 5.13 and 5.14). The change in cloud optical depth is associated with ice water content and ice number concentration in cirrus. The increase in the ice number concentration and ice water content increases the cloud optical depth.

After the start of the air traffic, the ice number concentration in contrail perturbed areas has been increased and is visible as thin lines. However, the ice water content in contrail perturbed areas did not change much because emitted water vapor is not large; therefore, the ice water content in the newly formed contrail is not large. The change in cloud optical depth can be seen in contrail perturbed regions. However, the change in optical depth is very small initially (figures 5.13 and 5.14) since the change in cloud optical depth in freshly nucleated contrail ice crystals is mainly due to an increase in the ice number concentration. The optical depth in contrail perturbed areas can be seen increasing over time as the ice water content in the contrail increases and the ice number concentration remain relatively higher than the ice number concentration in the surrounding cirrus air. This means the high ice number concentration in contrail alone cannot produce a large change in optical depth, but a high ice water content and a high ice number concentration together can change the optical depth significantly. The increase in the ice water content in contrail perturbed regions is due to the diffusional growth of the contrail ice crystals. The ice water path is relatively large in the contrails formed in highly ice supersaturated regions than in slightly ice supersaturated regions (figure 5.15) because the ice crystals cannot grow large when air is close to the ice saturation. Therefore, optical depth is relatively larger in the contrails formed in highly ice supersaturated regions than those formed in slightly ice supersaturated regions. In some areas where ice supersaturation within cirrus is very small (less than 110%), the ice water path does not increase significantly. For example, the area around 48 °N and 12 °E shows a slight increase in the ice water path since ice supersaturation is low in this region (figure 5.14(i) and 5.15). However, the ice number concentration and the cloud optical depth are large in this region.

After contrail ice formation, the ice supersaturation in contrail perturbed regions has been reached close to ice saturation while ice supersaturation remains large in the unperturbed cirrus (figure 5.15). The reduction in the ice supersaturation due to the presence of contrail ice crystals reduces the chance of ice nucleation events in the cirrus and the growth of the cirrus ice crystals. Therefore, cirrus air around the contrail perturbed regions shows a decrease in the ice water path, ice number concentration, and optical depth. The decrease in the optical depth can be seen where ice water path and ice number concentration decreased in the cirrus. Although, the left-most part of the cloud stretched from south-west to north-east shows a decrease in the ice water path around the contrail induced perturbed area but, a decrease in the ice number concentration is not visible because the decrease in the cirrus ice number concentration is significantly low compared to the increase in the ice number concentration due to the formation of contrail ice crystals (figure 5.14 f, i). The decrease in ice water path and ice number concentration in cirrus is possibly due to the reduction of available water vapor in those areas. The adjustment in the available water vapor can reduce the ice nucleation frequency in cirrus and the growth of the already existing cirrus ice crystals. These effects are mainly visible in the downwind of the contrail perturbed areas (figure 5.15) which indicates that the formation of contrail ice crystals reduces the available water vapor along its path and therefore affects the nucleation frequency in cirrus and the growth of the cirrus ice crystals and optical depth.

Tesche et al., (2016) showed an increase in cloud optical depth behind the aircraft 30 minutes after passing of an aircraft within natural cirrus. If contrail-induced perturbed areas were observed for a longer time, then an increase in optical depth would have been still expected in the contrail perturbed area, and a reduced optical depth might also be observed in the neighborhood regions.

During the simulation period, a large area of the cloud has been perturbed due to the formation of contrails and shows high ice number concentration and high ice water content in perturbed regions. The change in the cloud optical depth in the case of thick cloud is comparably larger than thin cloud because the number of formed ice crystals in a contrail is relatively high in thick cirrus due to relatively high in-cloud ice supersaturation, thus providing a favorable condition for the growth of ice crystals.

After one and two hours of continuous air traffic, a large area of the cloud contains contrail ice crystals and shows high optical depth. Old contrails cover a relatively large area and can be seen as thick lines. Contrails formed within old contrails are visible as lines with a relatively large change in optical depth surrounded by a slightly low change in optical depth.

After two hours of perturbation, the increase in the cloud optical depth is mostly around  $\sim 2.0$ , and the decrease in optical depth after contrail perturbation is below 0.1 in thin cirrus. In the case of a thick cloud, the change in optical depth is large in both directions (negative and positive), the optical depth reaching as high as 3.0 in some parts of the cloud after two hours of perturbation (figure 5.14, c). Some contrails that have been formed within old contrails show a significantly large change in optical depth (greater than 4.0) (figure 5.14).

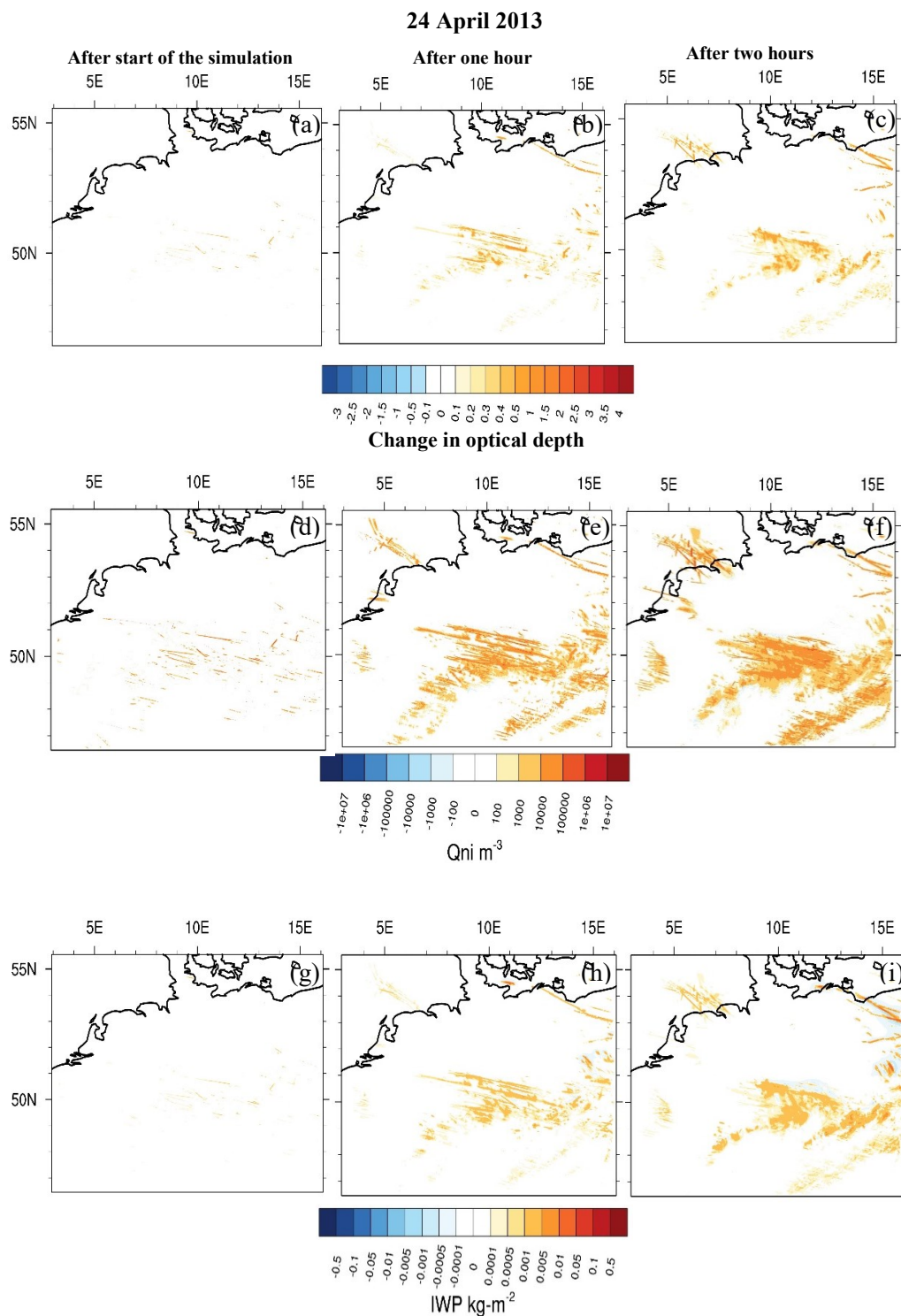


Figure 5.13: Change in cirrus optical depth (top row), number concentration of ice crystals ‘qni’ (middle row) and ice water path ‘IWP’ (bottom row) due to formation of contrail ice crystals within cirrus on 24<sup>th</sup> April 2013. Changes are shown (after contrail perturbation-without contrail perturbation) immediately after start of the air traffic (a, d, g), one hour after start of the simulation (b, e, h) and two hours after start of the simulation (c, f, i).

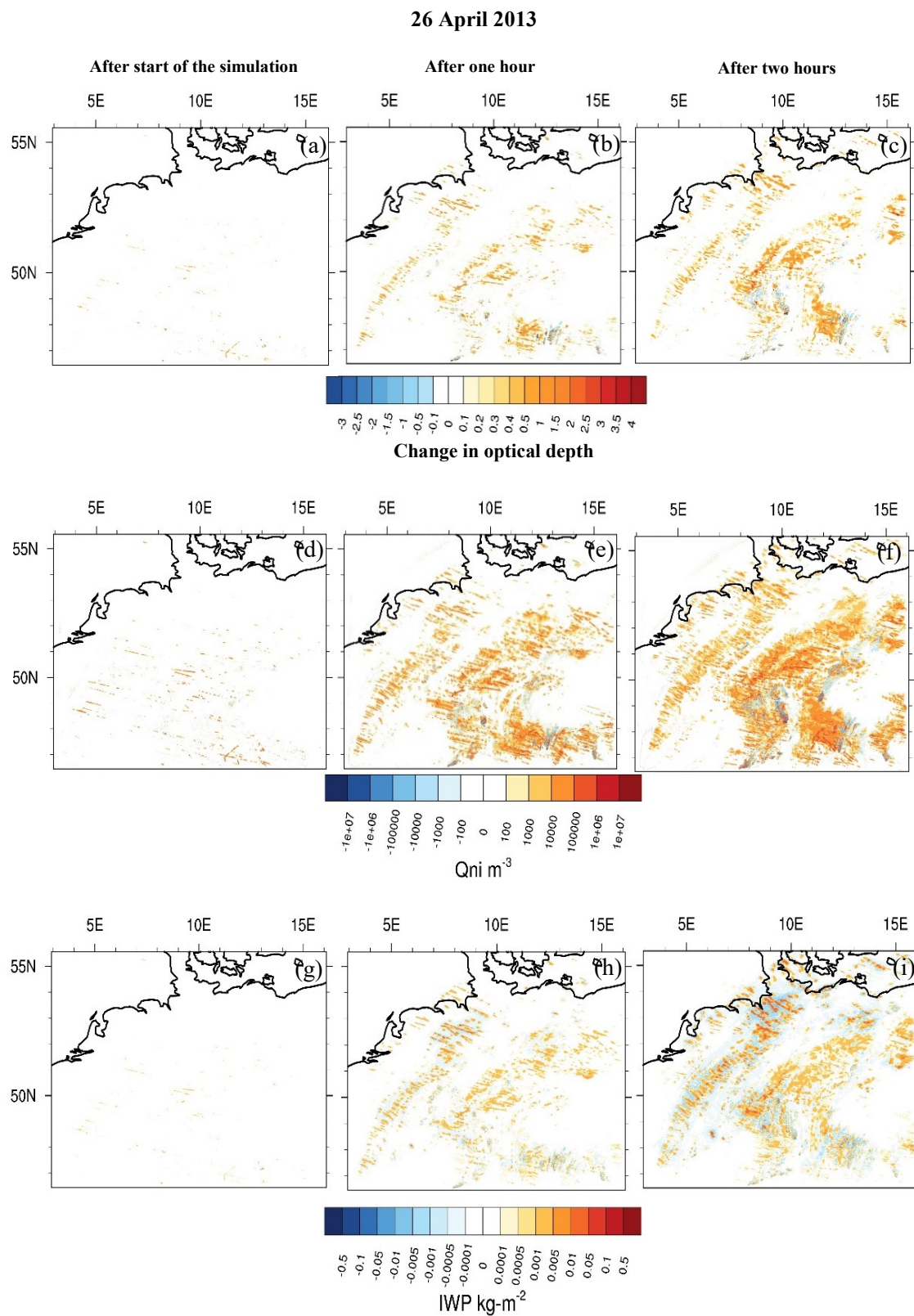


Figure 5.14: Similar to figure 5.13 but for cirrus on 26th April 2013.

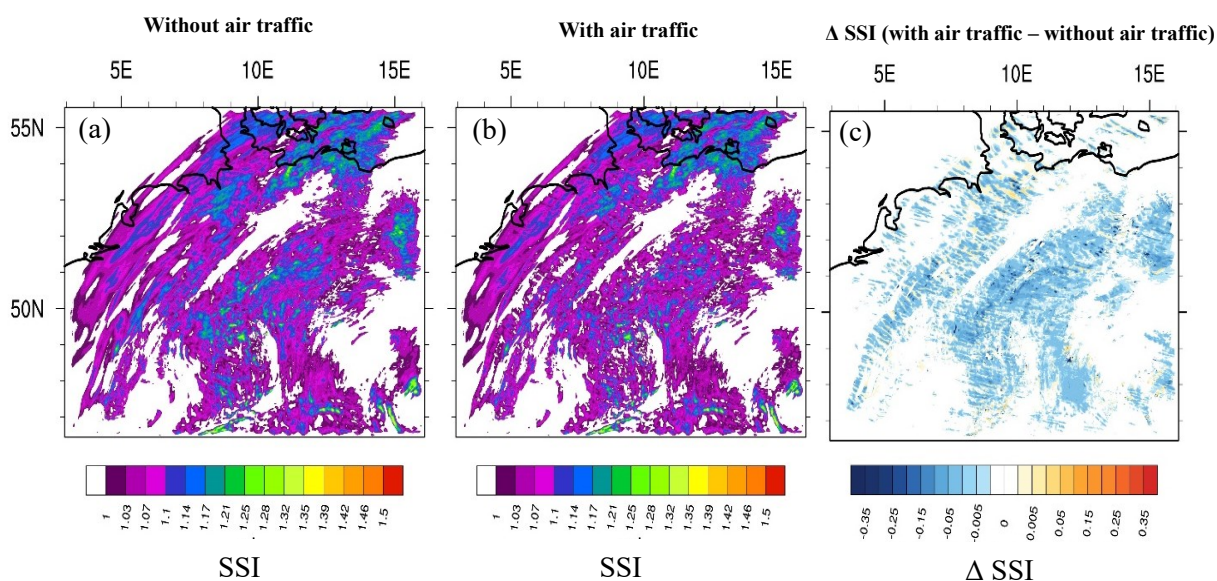


Figure 5.15: A snapshot of the average ice supersaturation ‘SSI’ in the cirrus on 26<sup>th</sup> April 2013 between 10 km to 12 km altitudes two hours after the start of the simulation (a) without air traffic and (b) with air traffic. ‘ $\Delta$  SSI’ is the change in SSI after contrail formation (with air traffic – without air traffic).

Furthermore, the probability distribution of change in cloud optical depth has been calculated (figure 5.16). The cloudy grid boxes where the change in the optical depth is more than 0.01 have been considered for the probability distribution estimation. The change in optical depth varies from -4.0 to 4.5 in thick cirrus and -0.12 to 2.2 in thin cirrus. In the case of thick cirrus, the increase in the optical depth is often well below 2.0 but occasionally reaches more than 4.0, and the decrease in the optical depth is below 1.0 mostly but can reach up to 4.0 in some places. In the case of thin cirrus, changes are mostly below 1.0 but reach more than 2.0 in some regions. The reduction in the optical depth in thin cirrus is very low reaches only up to 0.12. In both clouds, initially, the probability of an increase in the optical depth is large and reduces with time, and the probability of a decrease in the optical depth increases with time. In the thick cirrus at the start of the air traffic, around 98.7% of the total perturbed area has a positive change in the optical depth, and less than 0.3% has a reduction in the optical depth due to contrail formation. After two hours of perturbation, around 95.85% of the total perturbed area shows an increase in the optical depth, and 4.15% of the perturbed area shows a decrease in the optical depth. In the thin cirrus, almost 99.9% area of the total perturbed area of the cloud shows an increase in the optical depth at the beginning of the simulation. After two hours of continued air traffic, around 99.6% of the total perturbed area has an increase in the optical depth. Overall, the probability of an increase in cloud optical depth is larger than the probability of a reduction in optical depth due to contrail ice formation within cirrus, which means contrail formation within cirrus will cause a positive impact on the cloud optical depth in most of the cases.

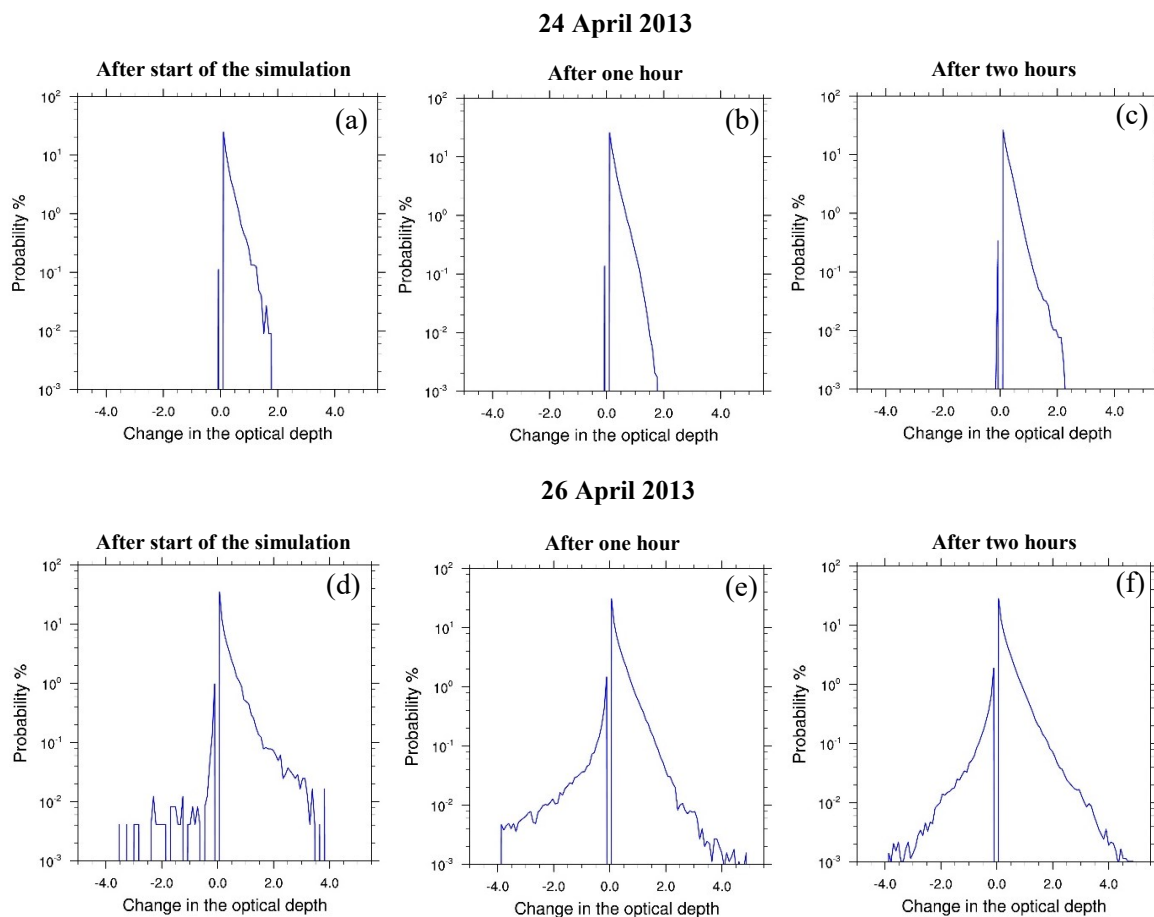


Figure 5.16: Probability distribution of the change in cloud optical depth after contrail formation within cirrus on 24<sup>th</sup> April 2013 (first row) and cirrus on 26<sup>th</sup> April 2013 (last row). Change in optical depth is shown immediate after start of air traffic (a, d), one hour after (b, e), and two hours after (c, f). the change in optical depth below 0.01 has been excluded and bin spacing is 0.01.

**Summary:** In section 5.4, the cirrus optical depth has been shown after contrail formation. The cirrus optical depth is determined from the cirrus ice water content and ice number concentration when assuming a fixed ice crystal shape. Contrail ice formation within cirrus introduces many small droplets and spherical shape ice crystals cause an increase in the cirrus optical depth. Initially, the change in contrail perturbed regions is mainly due to an increase in the ice number concentration. The formation of many ice crystals leads to a larger relaxation of in-cloud ice supersaturation and increases the ice water content, and therefore, increases the optical depth of those regions. As a result, the large change in optical depth can be seen due to aged contrail. The change in the optical depth is large as 4.0 in the case of thick clouds; however, the probability of a large change in cirrus optical depth is low. In the case of thin cirrus, the change in optical depth after contrail formation reaches up to only 2.0. Contrail ice formation can also cause a decrease in optical depth in the vicinity of contrail perturbed areas due to modification in cirrus properties. Reductions in the available water vapor can lead to a decrease in cirrus ice nucleation and to slower growth of the cirrus ice crystals. The probability of a reduction in optical depth is not large as the increase in optical depth in other areas.

## 5.5 Life cycle of the contrail induced cirrus perturbation and impact on the ice number concentration and ice crystal sizes

Contrail formation within cirrus is initially a large perturbation to the number concentration of ice crystals. But it is not clear how long the perturbation can persist. Depending on the synoptic situation, ice crystals may grow and can eventually reach sizes similar to cirrus ice crystals. In this case, contrail perturbation may change the microphysical and optical properties of the cirrus for many hours. On the other hand, they may sublimate speeding up cloud dissolution relative to the unperturbed cloud.

In this section, the life cycle of the contrail perturbed cirrus of the 24<sup>th</sup> April 2013 has been analyzed. The change in the ice number concentration in the cloud, ice crystal size distribution and ice crystal fall velocity and their temporal evolution are explored next. For this study, 10 minutes aggregated air traffic has been prescribed at one model timestep at the beginning of the simulation and then switched off for the next six hours.

Figure 5.18 shows the temporal evolution of the ice crystal number concentration, mean volume diameter and associated fall velocity in cirrus without contrail formation and after contrail formation. An increase in the number concentration of ice crystals is seen in the cirrus after contrail ice formation (figure 5.18 a). Around 0.01% area of the cloud has number concentration of ice crystals more than  $10^5 \text{ m}^{-3}$  immediately after contrail formation. The formation of contrail ice crystals within cirrus introduces small ice crystals in the cirrus causing a change in the size spectrum of the ice crystals; this leads to a change in the sedimentation rate within cirrus (figure 5.18 d) because the sedimentation velocity of an ice crystal is directly connected to the size and mass of the ice crystal. This means that the sedimentation velocity of big ice crystals is faster than small ice crystals. Dilution in contrail over time and growth of the ice crystals causes a decrease in the ice number concentration in cirrus and an increase in the mean volume diameters of the ice crystals and a resulting increase in the fall velocity.

Increased number concentrations of ice crystals in the perturbed cirrus can be seen four and six hours after contrail induced perturbation; the peak number concentrations and the probability of those changes decrease strongly. The number concentration of ice crystals is still more than 1 order of magnitude higher in the perturbed cirrus than the unperturbed cirrus after 4 hours. There is some low probability of the high number concentration after 4 hours in the undisturbed cirrus (figure 5.18 b, black curve), indicating that the nucleation event probably happened within some parts of the cirrus. Moreover, the fall velocity moved towards the large values as mean volume diameter increases with time. The slightly low fall velocity connected with a small mean volume diameter can still be seen six hours after the contrail formation. Also, a very low probability of high fall velocity connected with big ice crystals has been seen in the contrail induced perturbed cirrus. The formation of big ice crystals in perturbed cirrus can be because of an increase in the aggregation of ice crystals. Due to the different fall velocities of cirrus and contrail ice crystals, the falling cirrus ice crystals from the upper level to contrail can take small ice crystals onto its surface. Change in the sedimentation rate also affects the other microphysical processes as well, e.g. precipitation rate, collision, aggregation, multiplication of ice and conversion processes like snow to graupel. The distribution of ice water content in the cirrus is modified due to contrail formation within cirrus. This is because contrail ice crystals and associated ice water content stay at the upper levels in the cloud due to their slow sedimentation velocity. Moreover, the presence of the contrail ice crystals may affect the growth of the cirrus ice crystals due to distribution of available water vapor among contrail and cirrus ice crystals.

The change in size of the cirrus ice crystals may further cause a change in their fall velocity and therefore precipitation rate. It is thus important to study in detail the effect of contrail ice crystals on these microphysical processes. A study of the above-mentioned microphysical processes was not possible during the time frame of this work and has therefore been included in future work opportunities.

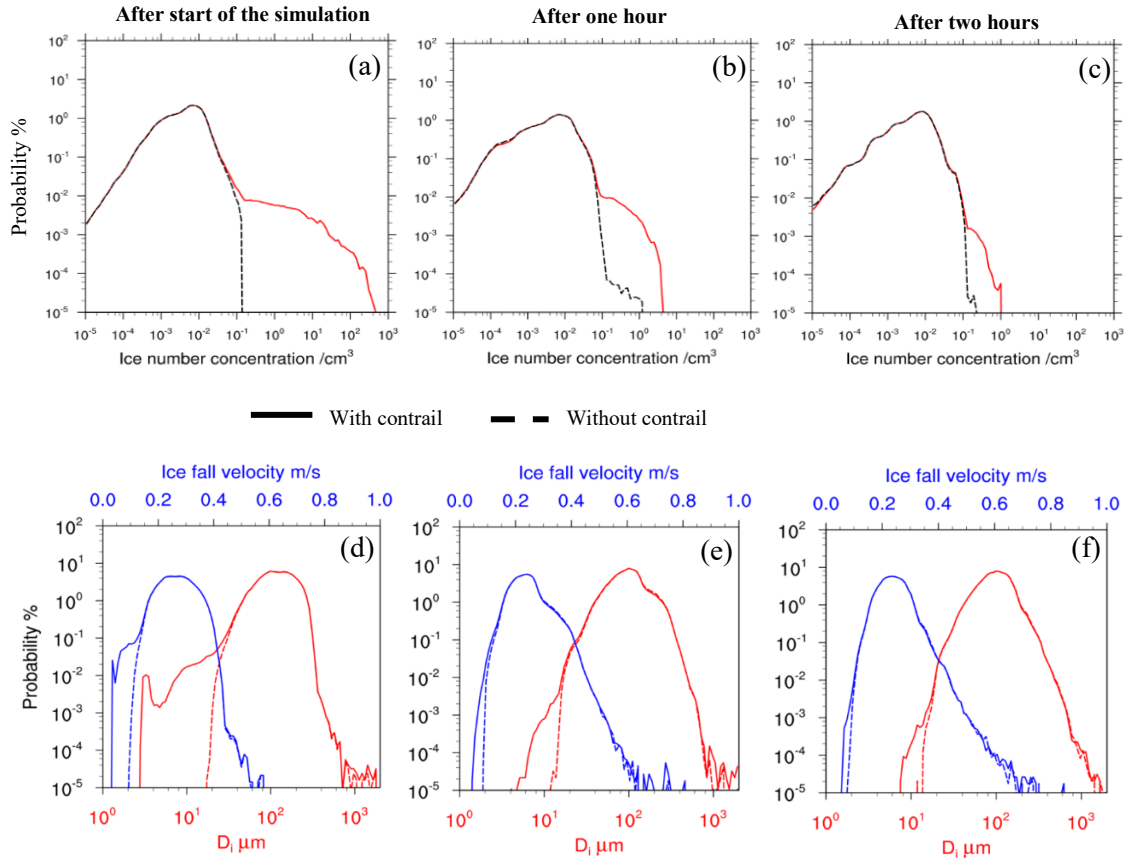


Figure 5.17: : Probability distribution of ice crystal number concentration ‘ $q_{ni}$ ’ (top row) and mean volume diameter and associated ice fall velocity (bottom row) in cirrus on 24<sup>th</sup> April 2013 without contrail formation (dashed curve) and after contrail formation (solid curve) immediately after initializing air-traffic (a, d), four hours after (b, e), and six hours after (c, f) the start of the simulation. In bottom row, red curve shows probability distribution of mean volume diameter of ice crystal and blue curve shows probability distribution ice fall velocity of ice crystal. Air traffic has been initialized for 10 minutes only at the beginning of the simulation.

### 5.5.1 Ice crystal number size distributions in contrail perturbed cirrus

In this section, the temporal evolution of the ice crystal number size distribution on contrail perturbed cirrus has been analyzed. Figure 5.18 shows the evolution of ice crystal number size distribution in the cirrus without contrail formation and after contrail formation. The mean volume diameter in the perturbed case has been calculated using the total number of ice crystals (cirrus + contrail) within a grid box. Therefore, mean volume diameter sizes can be slightly bigger than the actual mean volume diameter of the contrail ice crystal. After contrail formation, the small diameter range with high ice number concentration can be seen. The smallest diameter approx.  $\sim 2.0$  micrometers in the contrail perturbed cloud has a peak of ice number concentration  $5 \times 10^2 \text{ cm}^{-3}$ . The mean diameter of cirrus ice crystals in the unperturbed cirrus cloud is larger than 10 micrometers

and their ice number concentration is around  $1 \times 10^{-1} \text{ cm}^{-3}$ . The number concentration of small ice crystals has been decreased over time while the mean volume diameter has been increased in the contrail perturbed cirrus. Whereas, the variability in mean volume diameter in unperturbed cirrus has been more or less unchanged. The number concentration of ice crystals in the contrail perturbed cirrus has been reduced by a factor of 10 while the range of mean volume diameter has increased slightly to around 4 to 5 micrometers (figure 5.18 c and d).

Six hours after the formation of contrail ice crystals, the mean diameter of the ice crystal is slightly smaller than the mean volume diameter of ice crystals in undisturbed cirrus. The number concentration of ice crystals is also slightly higher than the number concentration in unperturbed cirrus. The effect of contrail perturbation can stay for many hours within the cloud. Contrail ice crystals grow further and can show similar properties as cirrus ice crystals. However, their nucleation processes are different.

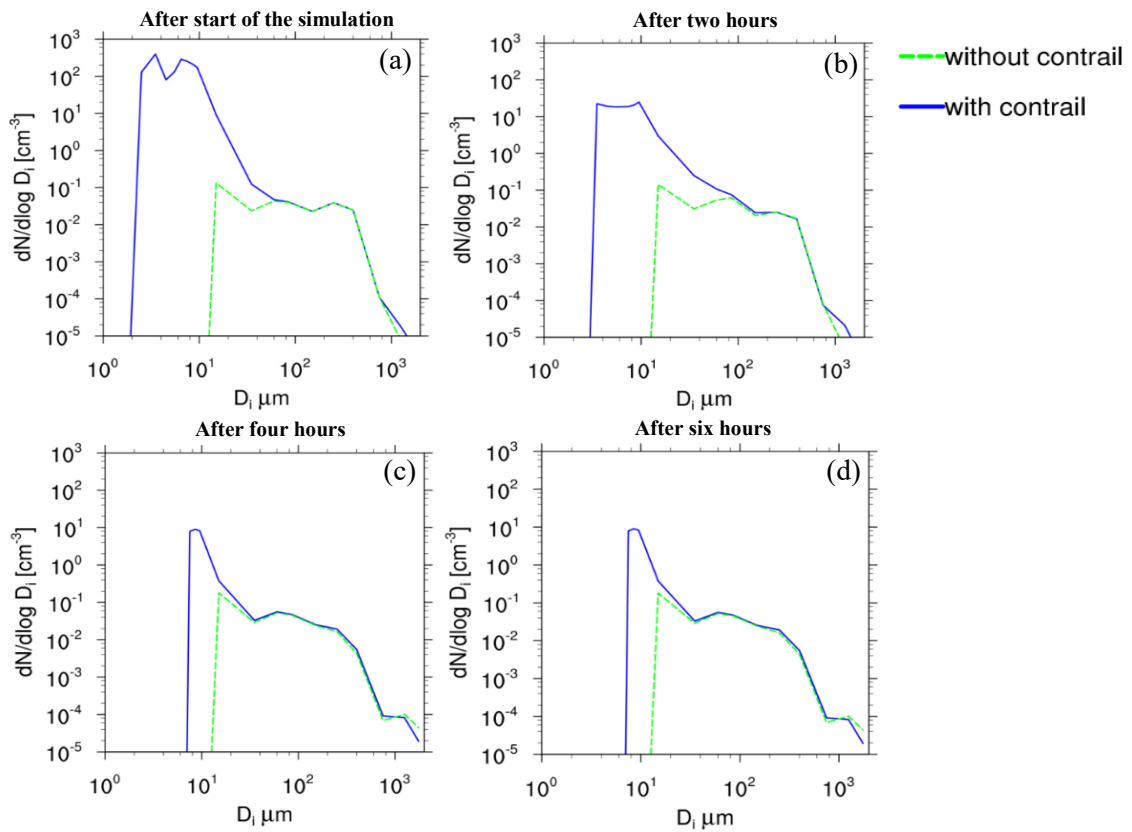


Figure 5.18: Ice crystal number size distribution in the cirrus on 24<sup>th</sup> April 2013 without contrail formation (green curve) and after contrail formation (blue curve) at (a) start of the simulation, (b) after two hours, (c) after four hours and (d) after six hours. An air traffic emission has been initialized for 10 minutes only at the beginning of the simulation and then air traffic has been switched off for the rest of the simulation time period.

### 5.5.2 Comparison with the observation

The model simulated mean volume diameter of ice crystals and their number concentrations in contrail perturbed cirrus have been compared with the observed diameters and number concentrations of ice crystals in contrails during the various flight campaigns (Schröder et al., 1999) (figure 5.19). The ice crystal number distribution range provided in the observational data is the ice

crystal sizes and their number concentration observed in the individual contrails. However, the ice crystal number distribution shown in figure 5.18 and 5.19 are mean volume diameter and ice number concentration within a grid box since the model used here doesn't provide the size distribution of ice crystals. Nevertheless, the model simulated ice crystals number distribution well represents the ice crystals number distribution observed in contrails of different ages. Since number concentration and mean volume diameters shown in the model simulation are after the vortex phase, mean volume diameters and number concentrations of contrail ice crystal are comparable to the diameters and number concentration of ice crystals in ~3 minutes of old contrails. The model simulated number concentration of ice crystals in 3 minutes old contrails are comparable with the observed ice number concentration and ice crystals diameter in 3 minutes old contrails. 30 minutes after contrail formation, the number concentration of ice crystals has been decreased slightly and the highest peak of the number concentration of ice crystal is around  $10^2$  per  $\text{cm}^3$  for the mean volume diameter 10 micrometers. The observation data also shows a similar number concentration of contrail ice crystals and diameters in the 30 minutes old contrails. Some parts of the unperturbed cirrus show similar levels of ice crystals number distribution as observed in young cirrus.

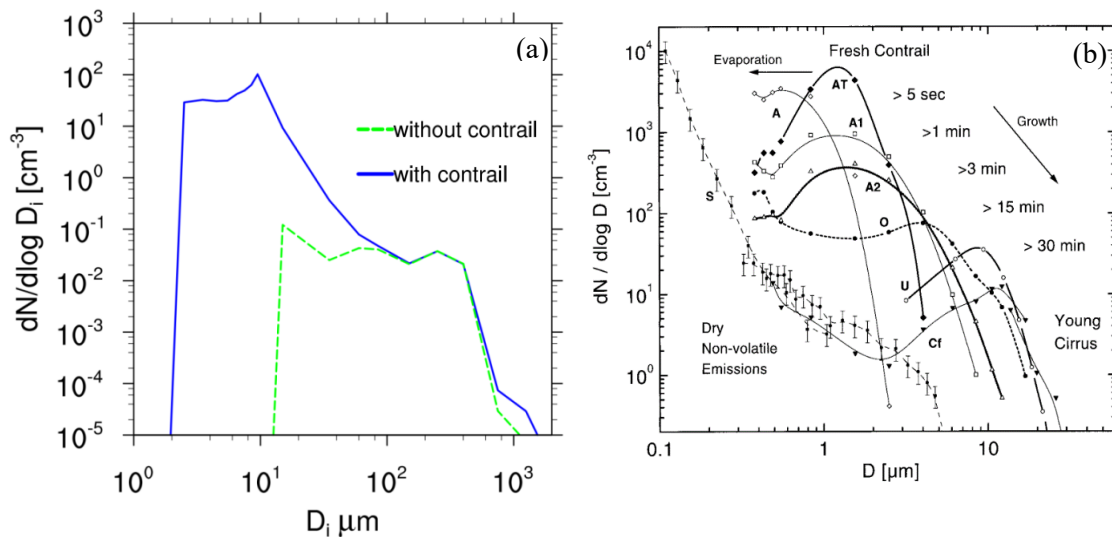


Figure 5.19: Ice crystal number size distribution in the cirrus on 24<sup>th</sup> April 2013 30 minutes after contrail formation (left figure). Ice crystal number size distribution observed in contrails during the transition from fresh contrails to young cirrus has been taken from 'Schröder et al., 1999' (right figure). The model simulated mean volume diameter and number density of ice crystals at the start of the simulation and 30 minutes after the start of the simulation are comparable with the observed mean diameter and number density of ice crystals in 3 minutes and 30 minutes old contrails respectively.

**Summary:** Section 5.5 shows the lifecycle of contrail-induced cirrus perturbation. The 10 minutes aggregated air traffic was initialized for one step and then switched off to see the temporal evolution of contrail-induced cirrus perturbation. The simulation results show that the effect of the 10 minutes of air traffic on the cirrus ice crystal number concentration can be seen for more than six hours. After contrail formation, a low probability of high ice crystal number concentration can be seen within the cloud. The probability of a high ice number decreases over time as contrails dilute and spread into a large area. After contrail formation, the mean volume radius of the ice crystals within cirrus moved towards the small values. The mean volume radius in contrail perturbed cirrus moves towards large sizes over time as ice crystals grow. The model simulated temporal evolution of the

volume mean diameter of ice crystals in contrail perturbed cirrus shows a similar tendency observed in the contrails. However, a detailed comparison with observational data is needed.

## 5.6 Conclusion

This chapter concludes the perturbation of pre-existing cirrus due to air traffic. The contrail formation within cirrus is a large perturbation towards a high number concentration of small ice crystals in cirrus. The number concentration of ice crystals has been increased significantly in the upper troposphere due to continuous air traffic. The modification in the number concentration of ice crystals within cirrus is relatively large in the frontal system originated cirrus on 26<sup>th</sup> April 2013 since the effect of pre-existing cirrus is large on contrail formation (nucleation and ice crystal loss in vortex phase). The number concentration of ice crystals in cirrus has reached up to  $10^6 \text{ m}^{-3}$  at flight levels. In both synoptic conditions, a large part of the cirrus has been perturbed due to two hours of continuous air traffic. The old contrails are visible as thick lines with high number concentration around  $\sim 10^4 \text{ m}^{-3}$  while newly formed contrails are visible as slightly thin lines with high ice number concentration around  $10^6 \text{ m}^{-3}$ . The perturbation in ice number can be seen far below from their formation altitudes in the cloud. The perturbation in ice number concentration due to contrail formation can be seen up to 2 km below from their formation altitudes. The thin part of the cirrus dissolves due to contrail ice crystal formation in those areas. The presence of small ice crystals in the thin part of cirrus has accelerated the dissolution in those areas. The contrail formation within cirrus shows the change in ice water content distribution in the cloud. An increase in the ice water content can be seen in contrail perturbed areas and a slight decrease in ice water content and ice number concentration can be seen next to the contrail perturbed areas. The perturbation due to contrail ice formation shows large optical depth in the contrail perturbed areas. The modification in optical depth is large in those areas where ice number concentration and ice water content are large. The change in optical depth in the contrail perturbed area reaches up to 4 in thick cirrus and up to 2 in thin cirrus. A decrease in optical depth can be seen next to the contrail perturbed areas due to a change in the ice water content and ice number concentration, specifically in thick cloud.

The life cycle of the contrail-induced perturbation has been analyzed. The 10 minutes aggregated air traffic has been initialized for one-time step and then air traffic has been switched off. The effect of 10 minutes of air traffic can be seen on the cirrus properties for more than 6 hours. The temporal evolution of contrail perturbed cirrus shows a low probability of high ice number concentration of ice crystal in the cirrus for a long period of time. The probability of a high number concentration of contrail ice in cirrus reduces with time. But, slightly high number concentration of ice crystals can still be seen for more than six hours after contrail ice formation within cirrus. The same tendency has been seen in the mean volume diameter of the ice crystals in contrail perturbed cirrus. Initially, the number concentration of small ice crystals (mean volume diameter  $\sim 2$  micrometers) is appeared in contrail perturbed cirrus. Two and four hours after contrail formation, the number concentration of small ice crystals has been reduced and the mean volume diameter of the ice crystals has been increased. The temporal evolution of the model simulated mean volume diameter of contrail perturbed cirrus is well-fitting with the observation data. However, further comparison of the lifecycle of contrail perturbed cirrus with more observation data is needed. The formation of contrail ice crystals within cirrus affects the microphysical processes in the cirrus cloud e.g. aggregation of ice crystals, collision, coalescence, ice multiplication, ice nucleation, sedimentation and precipitation. In this chapter, only the effect of contrail ice on the sedimentation velocity of ice crystals has been analyzed. The primary results show a low probability of small sedimentation

velocity due to contrail ice crystals. The slow sedimentation velocity of ice crystals in cirrus will affect the ice water distribution and precipitation rate in the cirrus since small ice crystals will stay in the upper altitudes for a relatively long period of time. On the other hand, the difference in sedimentation velocity due to the presence of small ice crystals increases the aggregation processes if big cirrus ice crystals fall into the contrail perturbed area. The small ice crystals in the contrail will stick onto the falling big ice crystals, changing the size of the ice crystals and therefore, sedimentation velocity. The formation of the ice crystals can potentially affect the cloud microphysical and optical properties; therefore, further detailed investigation is needed.

# Conclusion and outlook

### 6.1 Conclusion

Contrail formation in cloud-free ice supersaturated regions increases the upper tropospheric cloudiness and affects the radiation budget (Lee et al., 2021). According to current knowledge, contrail cirrus is the largest contributor to aviation-related climate change but is connected with considerable uncertainty. Close to all of the studies related to contrails and their impact on climate have so far been done for contrail formation in cloud-free ice supersaturated air. Very little is known about the effect of contrail formation within cirrus. Recently, satellite observations of contrail-induced cirrus perturbations have been made, demonstrating a significant change in optical properties of the cirrus in the wake of a passing aircraft (Tesche et al., 2016). This raised interest in contrail formation within natural cirrus and its impact on cirrus microphysical and optical properties. This thesis work strives to improve our understanding of contrail formation within cirrus and its impact on cirrus cloud properties; therefore, it may lay the foundation for estimating the climate impact of contrail-induced cirrus perturbations and thus help reduce the uncertainty in aviation-induced radiative forcing. To study the effect of contrail formation within cirrus on cirrus properties, this thesis work is divided into two major parts. The first part investigates the impact of pre-existing cirrus on contrail formation, i.e., contrail formation condition, contrail ice crystal nucleation, and ice crystals loss during vortex descent. The second part of this thesis investigates the effect of contrail formation within cirrus on cirrus microphysical and optical properties and studies the lifecycle of the contrail-induced cirrus perturbations.

For this study, ICON-LEM has been used at a grid spacing of 625 meters. The model can resolve clouds and cloud-relevant dynamics and thus is able to produce heterogeneity in the cloud field while allowing long simulations with realistic atmospheric conditions; therefore, the model is suitable for studying contrail formation within cirrus, their lifecycle, and their interaction with atmospheric variability. To study contrail formation within cirrus, a parameterization scheme for contrail formation has been implemented in the model. The contrail scheme consists of the determination of whether persistent contrails can form in given background conditions and with given emissions, the estimation of contrail ice nucleation (based on the parameterization of Kärcher et al. (2015)), and contrail ice crystal loss in the vortex phase (based on the parameterization of Unterstrasser (2016)). Both parameterizations have been modified, taking into the account the impact of pre-existing cirrus ice crystals on contrail ice nucleation and their survival during vortex descent. Cirrus ice crystals that are sucked into the engine sublimates in the engine, causing a change in ‘emitted’ water vapor (Gierens, 2012). Furthermore, after emission, surrounding cirrus ice crystals get mixed into the plume and partially sublimates initially due to subsaturation in the plume (Kärcher et al., 2015), and once the plume reaches ice saturation, the available plume water vapor starts to deposit on the entrained cirrus ice crystals. The adjustment in the plume water vapor concentration due to sublimation and deposition of the entrained cirrus ice crystals has been approximated and included in the calculation of contrail formation conditions and ice nucleation. After the nucleation of contrail ice crystals, the effect of the cirrus ice crystals on the survival of contrail ice crystals in the vortex phase has been estimated by including the impact of entrained

cirrus ice crystals on the contrail ice crystal growth before vortex descent and by including the effect of sublimation of entrained cirrus ice crystals in the descending vortices on the survival of contrail ice crystals. To study contrail formation within cirrus, two very different synoptic conditions, one thin cirrus connected with a high-pressure system and a medium to thick cirrus associated with a frontal system over Germany on 24<sup>th</sup> and 26<sup>th</sup> April 2013, have been considered (Heinze et al., 2017).

In the first part of this thesis, the effect of pre-existing cirrus on the contrail formation has been analyzed. Depending on the atmospheric conditions, the contrail formation threshold temperature and the number of nucleated ice crystals can be significantly affected by pre-existing cirrus, while ice crystal survival is hardly modified. The sublimation of cirrus ice crystals that are sucked into the aircraft engine was shown to cause an increase in the aircraft-induced water vapor content of the exhaust plume. Compared to the water vapor emissions due to fuel combustion, this increase amounts to a few percent, roughly in agreement with Gierens (2012). Furthermore, after exhaust emission, sublimation of entrained cirrus ice crystals and water vapor deposition on them further change the water vapor mixing ratio in the plume. In most cases, the sublimated ice water mass from cirrus ice crystals is larger than the deposited water vapor on the entrained ice crystals leading to a further increase in the water vapor concentration within the plume. The fraction of the aviation-induced water vapor increases within the plume (water vapor emission due to fuel combustion plus the change in the water vapor content of the plume due to pre-existing cirrus ice crystals) that is caused by the pre-existing cirrus ice crystals one second after emission (at approximately the time of ice nucleation) amounts to 10% to 20% maximally. This means that our estimate for the impact of pre-existing cirrus ice crystals on the overall aviation-induced water vapor increase is significantly larger than the order of a percent estimate given in Gierens (2012) since he did not consider the impact of cirrus ice crystals mixed into the plume. The evolution of the plume water vapor concentration, including the impact of entrained cirrus ice crystals, can be approximated by a change in the slope of the mixing line (in temperature – partial pressure coordinates), which leads to an increase in the contrail formation threshold temperature (Schmidt-Appleman criterion). The change in the plume water vapor concentration causes an increase in the contrail formation threshold temperature, which increases by 1.5K to 2K in areas where ice water content is large and ambient temperature is relatively low. However, the impact of pre-existing cirrus ice crystals on the contrail ice nucleation is minimal in large parts of the cirrus. In the case of thin cirrus, the change in the contrail formation threshold is close to zero because the ice water content and ice crystal number concentration in the cirrus are low. Therefore, the net sublimation of ice water mass is small. In some cases, pre-existing cirrus ice crystals cause a decrease in the contrail formation threshold temperature when mixed-in cirrus ice crystals cause a reduction in the water vapor concentration in the plume. However, the probability of negative effects is low (<0.22%), and associated changes in the contrail formation threshold are very low (< -0.01K).

The change in the contrail formation threshold temperature leads to significant changes in contrail ice nucleation, i.e., in the apparent ice number emission index. When the sublimation of cirrus ice crystals is larger than the deposition on them, then the contrail formation threshold temperature increases, and contrail ice nucleation increases. The change in number concentration of nucleated contrail ice crystals reaches, at typical flight levels, maximum values of around  $1 \times 10^7 \text{ m}^{-3}$  in thick cirrus on the frontal day and  $1 \times 10^6 \text{ m}^{-3}$  in thin cirrus on the day of the high-pressure system. Changes in ice nucleation are larger at lower pressure levels where the impact of pre-existing cirrus can seldomly lead to a doubling of ice nucleation. Large changes in the number of nucleated ice crystals can be seen mainly in those areas where ice water content and ice number concentration are large

in background cirrus. However, only a low percentage of total cloudy grid boxes have a large enough IWC to have a noticeable impact on contrail formation. The effect of pre-existing cirrus on contrail ice nucleation is large in the lower flight levels and would likely also be large in the tropics or subtropics because, in those areas, contrails form often in close to formation threshold conditions, and ice water content in the cirrus can be large (Bier and Burkhardt, 2019). The impact of pre-existing cirrus on the survival fraction of the nucleated ice crystals is very small. The change in the survival fraction of contrail ice crystals due to pre-existing cirrus lies mostly well below 1% in both synoptic conditions. Only at very low ice supersaturations when close to no ice crystals survive the vortex phase can the change in the survival fraction reach values of 1%. This is partly due to the fact that the moistening of the plume due to the sublimation of cirrus ice crystals during vortex descent is balanced by the faster growth of the larger cirrus ice crystals before vortex descend leading to smaller contrail ice crystals at the beginning of the vortex descend due to the presence of cirrus ice crystals.

The analysis showed that the properties of young contrails can be significantly changed due to the impact of pre-existing cirrus but that significant changes happen only in a low fraction of cloudy grid boxes. The question is whether the large changes are likely to have a large and lasting impact on the cloud field. Changes in contrail ice formation due to pre-existing cirrus were found to be particularly large in areas with large total water content on the 26<sup>th</sup> of April 2013. On that day, the areas with large ice water content were connected with strong vertical transport of moist air within warm conveyor belts associated with the frontal activity. These are areas where contrail formation in cloud-free air has a large impact due to the large moisture supply and long lifetimes (Bier et al., 2017). It may be fair to expect that contrail formation within cirrus and the resulting cirrus perturbations may also have a long lifetime in those synoptic situations and therefore have a chance to have a large radiative impact. It may be that, similar to contrail formation in ice-supersaturated cloud-free air, only a small fraction of contrails that form within cirrus explain most of the radiative impact and that those high impact contrails are those that form in connection with the frontal activity. Since it is also in those situations that the background cirrus properties have a significant impact on contrail formation, this impact should not be neglected.

In the second part of this thesis, the properties of the contrail perturbed cirrus, the contrail induced change in the cloud optical depth, and the life cycle of the contrail perturbation have been analyzed. Prescribing an air traffic inventory over Germany for the year 2006 in ICON-LEM, the simulations show large changes in the microphysical and optical properties of the natural cirrus cloud. A major change can be seen in the ice crystal number concentration of cirrus in the main air-traffic cruise altitudes, mostly above 10 km. The maximum ice crystal number concentration in the contrail perturbed cirrus can reach values of  $10^7 \text{ m}^{-3}$  which is 2 to 4 orders of magnitude larger than the ice number concentration in the unperturbed cirrus. Those maximum values are mostly connected with very young contrails shortly after the vortex phase. With time those high number concentrations are reduced while the perturbed area grows. Eventually, after a few hours of air traffic, a large part of the clouds is perturbed in terms of ice crystal number concentration due to the formation and the spreading of contrails over time. Contrail ice crystal can move far down from their formation altitudes initially during vortex descent and later due to different processes, e.g. aggregation and sedimentation, causing perturbations in much lower altitudes than the flight altitudes. In areas of thin cirrus clouds, cirrus can dissolve due to the formation of contrail ice crystals. This is because a low number of large natural cirrus ice crystals is replaced by many small contrail ice crystals that sublimate faster than the large ones as soon as the air becomes ice subsaturated. Often contrail

formation will only speed up cirrus dissolution as cirrus dissolution occurs predominantly on the edge of clouds in sinking air volumes in which cloud ice water content is decreasing with time.

Contrail formation within cirrus significantly affects the ice number concentration in the cirrus cloud but also changes the ice water content. However, the relative change in the ice water content is much lower than the relative change in ice number concentration. The change in the ice water content is mainly due to the diffusional growth of the contrail ice crystals over time in ice supersaturated regions within the cloud. Since ice supersaturation within clouds can be predominantly found in areas with low ice crystal number concentrations, changes in the in-cloud ice water content often are particularly large in those situations. The contrail-induced perturbation in the ice crystal number concentration and ice water content of cirrus affects the cirrus ice crystal size spectrum and causes a change in the microphysical processes within cirrus. The growth of the individual cirrus ice crystals is restricted due to the presence of many small contrail ice crystals competing for the available water vapor. The change in the ice crystal sizes influences the sedimentation rate within cirrus, resulting in changes in the vertical distribution of ice crystals and associated ice water content with increases in ice water content in the upper troposphere at or close to flight levels. Aggregation of ice crystals can increase due to the formation of contrail ice crystals, particularly if contrails form well below the cloud top. The reason for this is that contrail and cirrus ice crystals fall with different velocities due to their mass and shape, and if big cirrus ice crystals fall into the perturbed contrail region, then small contrail ice crystals may stick to the larger cirrus ice crystals. An increase in aggregation rate will lead to higher ice crystal fall velocities. Therefore, the presence of contrail ice crystals, on the one hand, may slow down the sedimentation by changing the ice crystal size spectrum in particular if contrails form at cloud top and, on the other hand, may increase the sedimentation rate in the cirrus by increasing ice crystal growth due to aggregation in cases when contrails form well below the cloud top.

Contrail ice crystal formation within cirrus changes cloud optical depth by altering the ice crystal size spectrum. The cloud optical depth, which is determined from the ice number concentration and the ice water content in the cirrus when assuming a fixed ice crystal shape, increases in contrail perturbed regions due to the formation of many ice crystals. Initially, the change in the optical depth is mainly due to the significant increase in the ice crystal number concentration. This leads to a larger relaxation of in-cloud ice supersaturation due to the many contrail ice crystals increasing the ice water content and therefore, increasing the optical depth of the contrail perturbed cirrus. As a result, the optical depth changed due to aged contrail perturbations can be larger than the one due to newly formed contrails. Approx. 95% of the total cloudy area shows an increase in the cloud optical depth after contrail-induced perturbation. The analyzed results show a maximum increase in the optical depth by a factor of 2 for thin cirrus and by a factor of 4 for thick cirrus. An increase in the cloud optical depth was also observed from satellite 30 minutes after passing of an aircraft within cirrus (Tesche et al., 2016). If contrail-induced perturbation were observed for a longer period of time, then an increase in the optical depth would have been still expected in the perturbed areas. Contrail ice formation can also cause a decrease in optical depth in the vicinity of contrail perturbed areas due to modification in cirrus properties. Reductions in the available water vapor can lead to a decrease in cirrus ice nucleation and to slower growth of the cirrus ice crystals. The probability of a reduction in optical depth is not large as the increase in optical depth in other areas. Less than 5% of the total cloudy area shows a decrease in the optical depth. This decrease of cirrus optical depth in the vicinity of the contrail-induced perturbations was not seen by Tesche et al. (2016). Since this decrease in optical depth is much lower than the increase in the contrail formation areas, it may not be possible to detect it in observational data. Nevertheless, if the statistics of such

observations were improved, it may become possible to detect even those smaller optical depth changes. Finally, the life cycle of the cirrus perturbed by contrail formation has been analyzed, prescribing air traffic for 10 minutes only. Initially, the cirrus has a low probability of very high ice number concentration up to 3 orders of magnitude larger than the ice number concentrations in the cirrus without contrail perturbation. Since contrail formation introduces small ice crystals; therefore, ice crystal size distribution in contrail perturbed cirrus is shifted towards the small ice crystals. The ice crystal number concentration in contrail perturbed regions decreases with time, and ice crystal sizes increase since the contrail plume dilutes and ice crystals grow over time. The temporal evolution of the ice crystal number concentration shows a steady decrease in maximum number concentrations connected with an increase in the contrail perturbed areas. The perturbation of cirrus ice number concentration due to contrails can be seen for many hours after contrail ice formation. The ice number concentration in some parts of the perturbed cloud is one order of magnitude larger than the ice number concentration in unperturbed cirrus even six hours after contrail ice formation within cirrus. The ice crystal size distribution of the contrail perturbed cirrus resembles the distribution observed in young contrails (Schröder et al., 1999). Furthermore, the temporal evolution of the ice crystal size distribution compares well with the observed development. However, a closer comparison of the size distributions is hampered by the model's two-moment microphysics that does not supply us only with the mean volume diameters of ice crystals within a grid box.

## 6.2 Outlook

The presented work shows that contrail formation within cirrus can significantly affect the natural cirrus optical properties justifying the inclusion of this effect in estimates of the aviation-induced climate impact. This work is a first step towards understanding contrail formation and its modification due to pre-existing cirrus and the impacts of contrail formation within cirrus on cirrus properties. The large dependence of the cirrus modifications on the background atmospheric conditions justifies performing similar studies for additional synoptic situations. Studies could also be performed for different seasons and also for other regions, which can provide a large statistic about cirrus properties and associated synoptic conditions where contrail formation within cirrus can have a large impact on the cirrus properties.

A detailed study of contrail-induced cirrus perturbation using LES simulations would be important to improve the knowledge of the effect that our model with its microphysical two-moment scheme cannot resolve. These are in particular the impact of considering ice crystal size distributions, plume inhomogeneities, and sequential nucleation of aerosols of different sizes and properties on contrail formation and on the impact of pre-existing cirrus on contrail formation.

Satellite and in-situ observations should be used in order to validate the simulated contrail-induced cirrus perturbations. Work is currently being performed in order to study contrail-induced cirrus perturbations in satellite observations over Europe. It remains to be seen if those observations are able to detect similar patterns in cirrus optical depth modifications as presented simulations. Furthermore, contrail formation within cirrus has shown a reduction in cloudiness and cloud optical depth in the downwind of the contrail perturbation. Is it possible to find in observational data the reduction in cloudiness and optical depth in downwind of the contrail perturbation? Furthermore, in-situ observations from measurement campaigns would be ideally suited to an evaluation of contrail formation as simulated by our model.

So far, the radiative impact of contrail formation within cirrus has not been included in the assessment of aviation-induced climate change (Lee et al., 2021) because the effect of contrail formation in cloudy air is still unknown. It is clear from the presented study that the perturbations induced by contrail formation within natural cirrus lead to large modifications in cirrus microphysical and optical properties that should be included in estimates of the aviation-induced climate impact. Therefore, building on this work, a contrail parameterization within a climate model should be modified to consider the impact of pre-existing cirrus on contrail formation, and the impact of contrail perturbations should be estimated. As for contrail formation in cloud-free air, contrail formation within cirrus has an impact on the upper tropospheric water budget and may lead to moistening of the upper troposphere in the area of the perturbation and drying in the vicinity. Any climate impact estimate of contrail formation within cirrus should also consider this feedback.

The large climate impact of contrail formation in cloud-free air led to the proposal of contrail avoidance strategies, in which aircraft routes are diverted from ice supersaturated regions. Due to that, aircraft may fly more often through clouds, which induces changes in the cirrus properties and lead to a change in the cloud radiative forcing. Therefore, it is necessary to quantify the radiative impact of contrail-induced cloud perturbations in order to perform a fair assessment of the impact of this kind of rerouting.

This work may also be important in order to improve the interpretation of observational cirrus data (e.g., flight campaign and remote sensing data) because quite often, a high number concentration of ice crystals within cirrus are observed (Urbanek et al., 2018). Often only small areas of very high ice crystal number concentrations are interpreted as contrail perturbations, but presented simulations show that contrail formation can modify the microphysical properties of large parts of the cloud.

Finally, it is still an open discussion that which nucleation pathway, heterogeneous or homogeneous nucleation, is dominant in the formation of cirrus clouds. Recent studies show that heterogeneous nucleation is the dominant nucleation pathway in the ice cloud (Cziczo et al., 2013), while other studies claim that ice clouds form predominantly by homogeneous nucleation (Sassen and Campbell, 2001), in particular in the southern hemisphere. But, contrail ice nucleation can be another nucleation method that can produce many ice crystals within cirrus. Persistent contrails can form in slight ice supersaturated regions, whereas other ice nucleation pathways need high ice supersaturation to nucleate the ice crystals. Also, the presence of contrail ice crystals within cirrus can reduce available water vapor due to diffusional growth, can cause a reduction in ice supersaturation, and, therefore, change in the nucleation frequency in the cirrus. Therefore, statistics regarding how large is the effect of contrail ice nucleation within cirrus on the nucleation frequency of the ice crystals formed through other nucleation pathways should be needed. Analysis about dominant nucleation pathway among above mentioned all three nucleation pathways could be useful for better interpretation of observed cirrus properties.

# List of Figures

Figure 2.1: Frequency of occurrence of ice supersaturation globally for pressure layer 200 to 250 hPa. This shows statistics of 7 years' data from the years 2003 to 2009 taken from Atmospheric Infrared sounder (AIRS). Lamquin et al., 2012.....	9
Figure 2.2: Schematic diagram for different ice nucleation modes. (Hoose and Möhler 2012)....	11
Figure 2.3: Schematic diagram of aircraft wake evolution into four regimes - jet, vortex, dissipation and diffusion (Paoli and Shariff, 2016).....	16
Figure 2.4: Number concentration and mean diameter of the ice crystals for different contrail ages and cirrus clouds. The data has been collected from various measurements campaign, e.g. AEROCOTRIL, from the year 1996 to 1997. (Schröder et al., 1999). ....	19
Figure 2.5: The normalized optical thickness of the cloud with a geometrical depth of 5 km for four categories (I) inside the flight track ahead of the aircraft, (II) outside the flight track, (III) inside the flight track behind the aircraft and (IV) outside the flight track behind the aircraft. Diamond (Cyan color) indicates a mean value of normalized optical thickness for all four categories. Mean optical thickness is highest for category III inside the flight track and behind the aircraft. (Tesche et al., 2016).....	22
Figure 2.6: Temporal evolution of the normalized ice crystal number is shown for the first 5 minutes after contrail formation. Relative humidity over ice (red-100%, green-110%, blue-120%, brown-130%, and purple- 140%) at a fixed temperature of 217K has been taken to simulate contrail for a B777 aircraft type (Unterstrasser, 2016). $f_N$ is a surviving ice crystal number fraction. Value 1 means all ice crystals survived, value 0 means all ice crystals sublimated. ....	24
Figure 3.1: Schematic diagram of different collection processes, accretion, autoconversion, aggregation, freezing, melting, rimming between six hydrometeors, cloud droplet, rain, ice, snow, hail and graupel. ....	30
Figure 3.2: Flow chart to show difference in implemented parameterization for contrail formation in cloud free area and within cloud.....	32
Figure 3.3: Schematic diagram for contrail formation conditions. The water saturation vapor curve and ice saturation curve are represented. Gray lines show three different mixing lines following the path from exhaust conditions to ambient conditions. Contrails do not form if the mixing line does not touch the water saturation pressure curve. Contrails form if mixing line crosses the water saturation curve (Paoli and Shariff 2016).....	33
Figure 3.4: Thermodynamic model for ice nucleation in contrail same as figure 2 but showing mixing line (a) without (b) and with contrail microphysics. During the mixing, plume first reaches water saturation (cross mark), water droplets then form (open circle) and start to deplete the water supersaturation in the plume. Start mark shows the stage when frozen droplets start to quench ice supersaturation; filled circle shows ambient condition (Kärcher et al., 2015).....	35
Figure 3.5: Probability of percentage change in water vapor 'emission' ( $\Delta q_v$ (%)) due to sublimation of background cirrus ice crystals in the aircraft's engine (dashed line) and due to sublimation of cirrus ice crystals in engine ( $M_{eng}$ ) + during mixing ( $M_{mix}$ ) (solid line). $\Delta q_v$ due to sublimation of a thin cirrus cloud field on 24 <sup>th</sup> April 2013, 6 am (blue curve) a thick cirrus cloud field on 26 <sup>th</sup> April 2013, 5 pm (red curve) for areas with temperatures lower than 233.15K, ice saturation ratio larger than 1 and IWC larger than $10^{-11}$ kgm <sup>-3</sup> . ....	42

- Figure 3.6: Schematic diagram to show effect of entrained cirrus ice crystals sublimation on the survival of contrail ice crystals during vortex descent. .... 46
- Figure 3.7: Gridding of flight's way point data into icosahedral grid structure: (left) schematic diagram for waypoint data; (middle) one-hour flight inventory for 150 meters thick vertical layer in lat-lon grid structure; (right) interpolated flight inventory in icosahedra grid structure. .... 47
- Figure 3.8: Simulation setup, domain set up over Germany with two nests with refinement 312 m and 156 m (Heinze et al., 2017). Only the outer domain of 625 meters resolution has been used in this doctoral thesis. .... 48
- Figure 3.9: Synthetic image simulated by ICON model for 24<sup>th</sup> April 2013 at 12:35 UTC (left) and for 26<sup>th</sup> April 2013 at 12:20 UTC (right). Source: (Heinze et al., 2017) ..... 49
- Figure 3.10: Frequency of occurrence of IWC (a, d), ice crystal number concentration (b, e), and mean volume diameter of ice crystals (c, f) on the (a,b,c) 24<sup>th</sup> April 2013 at 06 - 07 am and (d,e,f) 26<sup>th</sup> April at 5 - 6 pm. The frequencies of occurrence refer to individual temperature bins. .... 51
- Figure 3.11: Apparent emission index ( $AEI_i$ ) for contrail ice crystals after nucleation simulated by ICON-LEM. The X-axis shows the offset between the formation threshold and ambient temperature,  $T_{sa}$ , for the 26<sup>th</sup> April 2013 at altitudes between 9.6km to 10.8km for varying atmospheric pressure and ice saturation ratio when including the impact of cirrus ice crystal sublimation during combustion. .... 52
- Figure 3.12: Volume mean radius,  $r_{vol}$  vs ratio between volume mean radius and effective radius, 'C' (left figure) and optical depth (right figure) have been calculated along the black line shown in figure 5.3. The optical depth and effective radius have been calculated for four different assumptions (1) assuming spherical and monodisperse ice crystals (purple line) (2) assuming the irregular shape of ice crystal and log-normal particle size distribution (green line) (3) assuming habit mix and monodisperse ice particles (orange line) and (4) habit mix and log-normal particle size distribution (pink line). .... 55
- Figure 4.1: Probability distribution of the difference between the Schmidt-Appleman temperature threshold of contrail formation ( $T_{sa}$ ) and the ambient temperature ( $T_a$ ) at 11 - 11.5 km (red), 10.3 - 10.8 km (blue), 9.6 - 9.8 km (green) and 8.6 - 9.2 km (purple) on the 26<sup>th</sup> April (a) and 24<sup>th</sup> April (b). Difference between the Schmidt-Appleman temperature threshold ( $T_{sa}$ ) and the ambient temperature and change in  $T_{sa}$  due to impact of cirrus ice crystals on the 26<sup>th</sup> April 2013 5pm at altitudes of 10.3 (~250 hPa) to 10.8km (~225 hPa) (c) and at 9.6 (~280 hPa) to 9.8km (~270 hPa) (d) and on 24<sup>th</sup> April 2013 6am at altitudes of 9.6 (~280 hPa) to 9.8km (~270 hPa) (e). In all figures the difference of ambient air temperature and  $T_{sa}$  refers to the  $T_{sa}$  that is not modified due to the sublimation of pre-existing cirrus ice. .... 60
- Figure 4.2: Joint probability distribution of ice crystal number concentration due to contrail ice nucleation,  $n_i$ , and its change due to the sublimation of cirrus ice crystals within the aircraft engine,  $\Delta n_i$ , for current soot number emissions,  $2.5 \cdot 10^{15} \text{ kg-fuel}^{-1}$ , for altitudes from 10.3km to 10.4km (230 hPa to 225 hPa) on the (a) 26<sup>th</sup> April 2013 5 pm. Additionally, the PDF of ice nucleation (solid) and the associated cumulative PDF (dashed), when neglecting the impact of natural cirrus ice crystals (top) and its change due to the presence of cirrus ice crystals (right), is shown. Mean ice cloud properties for the combination of  $n_i$  and  $\Delta n_i$  (b) IWC, (c)  $q_{ni}$ , (d) difference between temperature formation threshold and ambient temperature, and (e) ice saturation ratio. If all emitted soot particles would form an ice crystal, then the ice crystal number concentration within the grid box,  $n_i$ , would reach approximately  $1.5 \cdot 10^8 \text{ m}^{-3}$ . .... 63

Figure 4.3: Joint probability distribution of ice crystal number concentration due to contrail ice nucleation,  $n_i$ , and its change due to the sublimation of cirrus ice crystals within the aircraft engine,  $\Delta n_i$ , for current soot number emissions,  $2.5 \cdot 10^{15} \text{ kg-fuel}^{-1}$ , for altitudes from 9.6km to 9.8km (280 hPa to 270 hPa) on the (a) 26<sup>th</sup> April 2013 5 pm. Additionally, the PDF of ice nucleation (solid) and the associated cumulative PDF (dashed), when neglecting the impact of natural cirrus ice crystals (top) and its change due to the presence of cirrus ice crystals (right), is shown. Mean ice cloud properties for the combination of  $n_i$  and  $\Delta n_i$  (b) IWC, (c)  $q_{ni}$ , (d) difference between temperature formation threshold and ambient temperature, and (e) ice saturation ratio. If all emitted soot particles would form an ice crystal, then the ice crystal number concentration within the grid box,  $n_i$ , would reach approximately  $1.5 \cdot 10^8 \text{ m}^{-3}$  ..... 64

Figure 4.4: Joint probability distribution of ice crystal number concentration due to contrail ice nucleation,  $n_i$ , and its change due to the sublimation of cirrus ice crystals within the aircraft engine,  $\Delta n_i$ , for current soot number emissions,  $2.5 \cdot 10^{15} \text{ kg-fuel}^{-1}$ , for altitudes from 10.3km to 10.4km (230 hPa to 225 hPa) on the (a) 24<sup>th</sup> April 2013 6 am. Additionally, the PDF of ice nucleation (solid) and the associated cumulative PDF (dashed), when neglecting the impact of natural cirrus ice crystals (top) and its change due to the presence of cirrus ice crystals (right), is shown. Mean ice cloud properties for the combination of  $n_i$  and  $\Delta n_i$  (b) IWC, (c)  $q_{ni}$ , (d) difference between temperature formation threshold and ambient temperature, and (e) ice saturation ratio. If all emitted soot particles would form an ice crystal, then the ice crystal number concentration within the grid box,  $n_i$ , would reach approximately  $1.5 \cdot 10^8 \text{ m}^{-3}$  ..... 65

Figure 4.5: Joint probability distribution of ice crystal number concentration due to contrail ice nucleation,  $n_i$ , and its change due to the sublimation of cirrus ice crystals within the aircraft engine,  $\Delta n_i$ , for current soot number emissions,  $2.5 \cdot 10^{15} \text{ kg-fuel}^{-1}$ , for altitudes from 9.6km to 9.8km (280 hPa to 270 hPa) on the (a) 24<sup>th</sup> April 2013 6 am. Additionally, the PDF of ice nucleation (solid) and the associated cumulative PDF (dashed), when neglecting the impact of natural cirrus ice crystals (top) and its change due to the presence of cirrus ice crystals (right), is shown. Mean ice cloud properties for the combination of  $n_i$  and  $\Delta n_i$  (b) IWC, (c)  $q_{ni}$ , (d) difference between temperature formation threshold and ambient temperature, and (e) ice saturation ratio. If all emitted soot particles would form an ice crystal, then the ice crystal number concentration within the grid box,  $n_i$ , would reach approximately  $1.5 \cdot 10^8 \text{ m}^{-3}$  ..... 66

Figure 4.6: Joint probability distribution of contrail ice crystal survival fraction during the vortex phase when neglecting the impact of cirrus ice crystals and its change due to the sublimation of cirrus ice crystals for current soot number emissions,  $2.5 \cdot 10^{15} \text{ kg-fuel}^{-1}$ , for (a) the 24<sup>th</sup> April and (b) the 26<sup>th</sup> April 2013 and for the 26<sup>th</sup> April for (c) 50% reduced soot number emissions and (d) 80% reduced soot number emissions. Additionally, the PDF of the fraction of surviving ice crystals (solid) and the associated cumulative PDF (dashed) when neglecting the impact of natural cirrus ice crystals (top) and its change due to the presence of cirrus ice crystals (right) is shown. A Brunt-Väisälä frequency of  $0.012 \text{ s}^{-1}$  (strong stability) has been assumed for all cases. In (c), red lines indicate the probabilities when reducing the Brunt-Väisälä frequency to  $0.005 \text{ s}^{-1}$  (weak stability). In (a), the y-axis is changed compared to the other figures. Ice crystal survival fractions were calculated whenever the ambient temperature was 5K below the temperature threshold for contrail formation. The dots in the probability distribution of the change in survival rate (right) indicate the probability of changes in the survival fraction that are larger than 1% ..... 70

Figure 4.7: Ice cloud properties for combinations of contrail ice crystal survival fraction during the vortex phase when neglecting the impact of cirrus ice crystals and its change due to the impact of cirrus ice crystals,  $\Delta$ survival fraction, for the 26th April for cases of contrail formation more

than 5K below the contrail formation threshold. Color coded are the cloud properties of the pre-existing cirrus, IWC (a), cirrus ice crystal number concentration (b), in-cloud ice saturation ratio (c) and cirrus ice crystal radius (d). A Brunt-Väisälä frequency of  $0.012s^{-1}$  and soot number emissions of  $0.5 \cdot 10^{15} \text{ kg-fuel}^{-1}$  are assumed. .... 72

Figure 4.8: Joint probability distribution of contrail ice crystal survival fraction during the vortex phase when neglecting the impact of cirrus ice crystals and its change due to the impact of cirrus ice crystals for the 26th April 2013 when contrails form closer than 5K from the contrail formation threshold. Additionally, the PDF of the fraction of surviving ice crystals (solid) and the associated cumulative PDF (dashed) when neglecting the impact of natural cirrus ice crystals (top) and its change due to the presence of cirrus ice crystals (right) is shown. A Brunt-Väisälä frequency of  $0.012 \text{ s}^{-1}$  (strong stability) and soot number emissions of  $0.5 \cdot 10^{15} \text{ kg-fuel}^{-1}$  have been prescribed. The dot in the cumulative probability distribution of the change in survival fraction (right) indicates the probability of a change in the survival fraction that is larger than 10%. .... 73

Figure 4.9: Ice cloud properties for combinations of contrail ice crystal survival fraction during the vortex phase when neglecting the impact of cirrus ice crystals and its change due to the impact of cirrus ice crystals,  $\Delta$ survival fraction, for the 26<sup>th</sup> April for contrail formation at temperatures closer than 5K from the contrail formation threshold. Color coded are the cloud properties of the pre-existing cirrus, IWC (a), cirrus ice crystal number concentration (b), in-cloud ice saturation ratio (c) and ‘new’ apparent emission index of contrail ice crystals (d) with ‘new’ indicating that changes in the nucleation due to the presence of cirrus ice crystals have been considered. A Brunt-Väisälä frequency of  $0.012s^{-1}$  and soot number emissions of  $0.5 \cdot 10^{15} \text{ kg-fuel}^{-1}$  are assumed.  $AEI_i$  of  $5 \cdot 10^{14}$  translates into  $qn_i = 3 \cdot 10^7 m^{-3}$ . .... 74

Figure 4.10: Joint probability of cirrus ice crystal number concentrations,  $n_{cir}$ , and the aviation induced change in ice crystal numbers,  $\Delta n_{cir}$ , for the cirrus cloud field on the 26<sup>th</sup> April 2013 for current soot number emissions,  $2.5 \cdot 10^{15} \text{ kg-fuel}^{-1}$ , and (a) for altitudes from 10.3km to 10.8km ( $\sim 250 \text{ hPa}$  to  $\sim 225 \text{ hPa}$ ) and (b) for 9.6km to 9.8km ( $\sim 280 \text{ hPa}$  to  $270 \text{ hPa}$ ). Only 60% of cloudy grid boxes at the two altitude ranges are analysed in which the contrail formation conditions are met. Grid mean concentrations and their changes are displayed. Cumulative probabilities of  $\Delta n_{cir}$  reach values below 100% because negative changes are not shown here as they are lower and uncertainty in those simulated changes is high. .... 76

Figure 5.1: : Frequency of occurrence of grid mean ice number concentration ‘ $q_{ni}$ ’ ( $m^{-3}$ ) (a, b), ice water content ‘IWC’ ( $gm^{-3}$ ) (c, d) and mean volume diameter ‘ $D_i$ ’ ( $\mu m$ ) (e, f) in cloud on 24<sup>th</sup> April 2013 at 06 - 07 am . The first column shows properties of the undisturbed cloud. The last column shows the cloud properties including contrail induced disturbances after two hours of air traffic. The vertical line in the mean volume diameter is an artifact caused by the lateral boundary condition in the model. Lateral boundary conditions do not include information on ice crystal sizes because they come from a model using single-moment microphysics. Therefore, for the boundary data, a diameter of 100 micrometers is simply assumed when calculating the number concentration from boundary data (personal communication Axel Seifert (DWD)). .... 81

Figure 5.2: Similar to figure 5.1 but for cirrus on 26<sup>th</sup> April 2013 at 17-18 pm. .... 82

Figure 5.3: Ice number concentration ‘ $q_{ni}$ ’ in the cirrus cloud field on the 24<sup>th</sup> April 2013 at start of the simulation for three different altitudes 10.0, 10.5 and 10.9 km over the Germany domain ( $48.5^\circ N - 55.5^\circ N$ ;  $2.0^\circ E - 17^\circ E$ ) simulated by ICON-LEM without contrail induced perturbations (left) and including contrail perturbations (right). Each altitude level has a thickness of approximately 150m. .... 84

- Figure 5.4: Similar to figure 5.3 but a snapshot of the cloud after one (first row) and two hours (second row) of continuous air traffic. .... 85
- Figure 5.5: Ice number concentration 'qni' in the cirrus cloud field on the 26<sup>th</sup> April 2013 for three different altitudes 9.5, 10.5 and 11.5 km over the Germany domain (48.5°N - 55.5°N; 2.0°E - 17°E) simulated by ICON-LEM without contrail induced perturbations (left) and including contrail perturbations (right). At the top a snapshot of the cloud at the start of the simulation and below after one hour of continuous air traffic is shown. Each altitude level has a thickness of approximately 150m. .... 87
- Figure 5.6: Vertical distribution of the ice crystal number concentration 'qni' of the cirrus cloud field on 24<sup>th</sup> April 2013 along the black line shown in figure 5.3 simulated by ICON-LEM without contrail induced perturbation (left) and including contrail perturbations (right). The length of the vertical cut from left to right is around 1093 km. At the top a snapshot of the cloud at the start of the air traffic induced perturbations, middle after one hour of continuous air traffic and below after two hours of continuous air traffic are shown. .... 90
- Figure 5.7: Vertical distribution of the number concentration of the ice crystals 'qni' of the cirrus cloud field on 26<sup>th</sup> April 2013 along the black line shown in figure 5.5. The number concentration of the ice crystals simulated by ICON-LEM without contrail induced perturbation (left) and including contrail perturbation (right). The length of the vertical cut from left to right is around 1093 km. At the top a snapshot of the cloud at the start of the simulation, middle after one hour of continuous air traffic and below after one hour of continuous air traffic are shown. .... 92
- Figure 5.8: 5, 25, 50, 75, and 95 percentiles of the number concentration of ice 'qni' in the cloud at 10.5km with and without contrail perturbation. blue whisker boxes show percentiles of 'qni' in the cloud without contrail perturbation 'control' and green whisker boxes are showing percentile with contrail perturbation 'perturbed' in every 10 minutes after start of simulation '0 hrs', one hour after '1 hrs' and two hours after '2 hrs' start of the simulation. The left plot shows analysis for 24<sup>th</sup> April 2013 and the right-hand side plot shows analysis for 26<sup>th</sup> April 2013. .... 93
- Figure 5.9: Vertical distribution of the ice water content 'IWC' in the cloud on 24<sup>th</sup> April 2013 along the black line shown in figure 5.3 and 5.4. First column shows ICON-LEM simulated cloud without contrail perturbation and second column shows cloud with contrail perturbation. Top row shows snapshot of the cloud at start of simulation, middle row shows snapshot of the cloud after one hour and bottom row shows snapshot of the cloud after two hours. .... 95
- Figure 5.10: Optical depth of the cloud for 24<sup>th</sup> April 2013 along the transect (shown in figure 5.3) for the simulation without contrail formation (blue curve) and with contrail formation (red curve) (first row); change in the optical depth due to contrail formation (second row) immediately after start of the air traffic (a, d), after one hour of continuous air-traffic (b, e) and after two hours of continuous air-traffic (c, f). .... 97
- Figure 5.11: Similar as figure 5.10 but for cloud on 26<sup>th</sup> April 2013 and along the vertical cut shown in figure 5.5. .... 99
- Figure 5.12: Probability distribution of optical depth of the cloud on 24<sup>th</sup> (left column) & 26<sup>th</sup> April 2013 (right column) without contrail perturbation (blue curve) and with contrail perturbation (red curve) immediately after start of the air traffic (top row), one hour after start of continuous air traffic (middle row) and two hours after start of continuous air traffic (bottom row). The probability of the cloud optical depth is calculated by using logarithmic bin size. .... 100

- Figure 5.13: Change in cirrus optical depth (top row), number concentration of ice crystals 'qni' (middle row) and ice water path 'IWP' (bottom row) due to formation of contrail ice crystals within cirrus on 24<sup>th</sup> April 2013. Changes are shown (after contrail perturbation-without contrail perturbation) immediately after start of the air traffic (a, d, g), one hour after start of the simulation (b, e, h) and two hours after start of the simulation (c, f, i)..... 103
- Figure 5.14: Similar to figure 5.13 but for cirrus on 26<sup>th</sup> April 2013. .... 104
- Figure 5.15: A snapshot of the average ice supersaturation 'SSI' in the cirrus on 26<sup>th</sup> April 2013 between 10 km to 12 km altitudes two hours after the start of the simulation (a) without air traffic and (b) with air traffic. ' $\Delta$  SSI' is the change in SSI after contrail formation (with air traffic – without air traffic)..... 105
- Figure 5.16: Probability distribution of the change in cloud optical depth after contrail formation within cirrus on 24<sup>th</sup> April 2013 (first row) and cirrus on 26<sup>th</sup> April 2013 (last row). Change in optical depth is shown immediate after start of air traffic (a, d), one hour after (b, e), and two hours after (c,f). the change in optical depth below 0.01 has been excluded and bin spacing is 0.01. ..106
- Figure 5.17: : Probability distribution of ice crystal number concentration 'qni' (top row) and mean volume diameter and associated ice fall velocity (bottom row) in cirrus on 24<sup>th</sup> April 2013 without contrail formation (dashed curve) and after contrail formation (solid curve) immediately after initializing air-traffic (a, d), four hours after (b, e), and six hours after (c, f) the start of the simulation. In bottom row, red curve shows probability distribution of mean volume diameter of ice crystal and blue curve shows probability distribution ice fall velocity of ice crystal. Air traffic has been initialized for 10 minutes only at the beginning of the simulation. .... 108
- Figure 5.18: Ice crystal number size distribution in the cirrus on 24<sup>th</sup> April 2013 without contrail formation (green curve) and after contrail formation (blue curve) at (a) start of the simulation, (b) after two hours, (c) after four hours and (d) after six hours. An air traffic emission has been initialized for 10 minutes only at the beginning of the simulation and then air traffic has been switched off for the rest of the simulation time period. .... 109
- Figure 5.19: Ice crystal number size distribution in the cirrus on 24<sup>th</sup> April 2013 30 minutes after contrail formation (left figure). Ice crystal number size distribution observed in contrails during the transition from fresh contrails to young cirrus has been taken from 'Schröder et al., 1999' (right figure). The model simulated mean volume diameter and number density of ice crystals at the start of the simulation and 30 minutes after the start of the simulation are comparable with the observed mean diameter and number density of ice crystals in 3 minutes and 30 minutes old contrails respectively. .... 110

# List of Tables

<i>Table 2.1: Observed cirrus cloud properties for different cirrus types (Krämer et al., 2020).....</i>	<i>14</i>
<i>Table 3.1: Estimation for sublimation and deposition of cirrus ice crystals within the plume before contrail formation.....</i>	<i>40</i>
<i>Table 3.2: Coefficient used in the diffusional growth equation .....</i>	<i>53</i>



# References

- Appleman, H. (1953). The formation of exhaust condensation trails by jet aircraft, *Bulletin of the American Meteorological Society*, 34(1), 14-20.
- Bakan, S., Betancor, M., Gayler, V., & Graßl, H. (1994). Contrail frequency over Europe from NOAA-satellite images. *Annales Geophysicae*, 12(10), 962. <https://doi.org/10.1007/s005850050118>
- Baldauf, M., & Brdar, S. (2016). 3D diffusion in terrain-following coordinates: testing and stability of horizontally explicit, vertically implicit discretizations. *Quarterly Journal of the Royal Meteorological Society*, 142(698), 2087–2101. <https://doi.org/10.1002/qj.2805>
- Bedka, S. T., Minnis, P., Duda, D. P., Chee, T. L., & Palikonda, R. (2013). Properties of linear contrails in the Northern Hemisphere derived from 2006 Aqua MODIS observations. *Geophysical Research Letters*, 40(4), 772–777. <https://doi.org/10.1029/2012gl054363>
- Bickel, M., Ponater, M., Bock, L., Burkhardt, U., & Reineke, S. (2020). Estimating the Effective Radiative Forcing of Contrail Cirrus. *Journal of Climate*, 33(5), 1991–2005. <https://doi.org/10.1175/jcli-d-19-0467.1>
- Bier, A., & Burkhardt, U. (2019). Variability in Contrail Ice Nucleation and Its Dependence on Soot Number Emissions. *Journal of Geophysical Research: Atmospheres*, 124(6), 3384–3400. <https://doi.org/10.1029/2018jd029155>
- Bier, A., Burkhardt, U., & Bock, L. (2017). Synoptic Control of Contrail Cirrus Life Cycles and Their Modification Due to Reduced Soot Number Emissions. *Journal of Geophysical Research: Atmospheres*, 122(21), 11,584–11,603. <https://doi.org/10.1002/2017jd027011>
- Bier, A., Unterstrasser, S., and Vancassel, X. (2021): Box model trajectory studies of contrail formation using a particle-based cloud microphysics scheme, *Atmos. Chem. Phys. Discuss.* [preprint], <https://doi.org/10.5194/acp-2021-361>, in review
- Bock, L., & Burkhardt, U. (2016a). Reassessing properties and radiative forcing of contrail cirrus using a climate model. *Journal of Geophysical Research: Atmospheres*, 121(16), 9717–9736. <https://doi.org/10.1002/2016jd025112>
- Bock, L., & Burkhardt, U. (2016b). The temporal evolution of a long-lived contrail cirrus cluster: Simulations with a global climate model. *Journal of Geophysical Research: Atmospheres*, 121(7), 3548–3565. <https://doi.org/10.1002/2015jd024475>
- Bock, L., & Burkhardt, U. (2019). Contrail cirrus radiative forcing for future air traffic. *Atmospheric Chemistry and Physics*, 19(12), 8163–8174. <https://doi.org/10.5194/acp-19-8163-2019>
- Bond, T. C., Doherty, S. J., Fahey, D. W., Forster, P. M., Berntsen, T., DeAngelo, B. J., Flanner, M. G., Ghan, S., Kärcher, B., Koch, D., Kinne, S., Kondo, Y., Quinn, P. K., Sarofim, M. C., Schultz, M. G., Schulz, M., Venkataraman, C., Zhang, H., Zhang, S., . . . Zender, C. S. (2013). Bounding the role of black carbon in the climate system: A scientific assessment. *Journal of Geophysical Research: Atmospheres*, 118(11), 5380–5552. <https://doi.org/10.1002/jgrd.50171>

- Boucher, O. (1999). Air traffic may increase cirrus cloudiness. *Nature*, 397(6714), 30–31. <https://doi.org/10.1038/16169>
- Boucher, O., D. Randall, P. Artaxo, C. Bretherton, G. Feingold, P. Forster, V.-M. Kerminen, Y. Kondo, H. Liao, U. Lohmann, P. Rasch, S.K. Satheesh, S. Sherwood, B. Stevens, and X.Y. Zhang, T.F. Stocker, D. Qin, G.-K. Plattner, M. Tignor, S.K. Allen, J. Doschung, A. Nauels, Y. Xia, V. Bex, and P.M. Midgley (2013). Clouds and aerosols. In *Climate Change 2013: The Physical Science Basis, Contribution of Working Group I to the Fifth Assessment Report of the Intergovernmental Panel on Climate Change*, Eds. Cambridge University Press, pp. 571-657, <https://doi:10.1017/CBO9781107415324.016>
- Bräuer, T., Voigt, C., Sauer, D., Kaufmann, S., Hahn, V., Scheibe, M., Schlager, H., Diskin, G. S., Nowak, J. B., DiGangi, J. P., Huber, F., Moore, R. H., & Anderson, B. E. (2021). Airborne Measurements of Contrail Ice Properties - Dependence on Temperature and Humidity. *Geophysical Research Letters*, 1. <https://doi.org/10.1029/2020gl092166>
- Burkhardt, U., Bock, L., & Bier, A. (2018). Mitigating the contrail cirrus climate impact by reducing aircraft soot number emissions. *Npj Climate and Atmospheric Science*, 1(1), 37. <https://doi.org/10.1038/s41612-018-0046-4>
- Burkhardt, U., & Kärcher, B. (2009). Process-based simulation of contrail cirrus in a global climate model. *Journal of Geophysical Research*, 114(D16). <https://doi.org/10.1029/2008jd011491>
- Burkhardt, U., & Kärcher, B. (2011). Global radiative forcing from contrail cirrus. *Nature Climate Change*, 1(1), 54–58. <https://doi.org/10.1038/nclimate1068>
- Burkhardt, U., Kärcher, B., & Schumann, U. (2010). Global Modeling of the Contrail and Contrail Cirrus Climate Impact. *Bulletin of the American Meteorological Society*, 91(4), 479–484. <https://doi.org/10.1175/2009bams2656.1>
- Carleton, A. M., Travis, D. J., Master, K., & Vezhapparambu, S. (2008). Composite Atmospheric Environments of Jet Contrail Outbreaks for the United States. *Journal of Applied Meteorology and Climatology*, 47(2), 641–667. <https://doi.org/10.1175/2007jamc1481.1>
- Carlson, T. N. (1993). Mid-latitude weather systems by T. N. Carlson. *Weather*, 48(2), 46. <https://doi.org/10.1002/j.1477-8696.1993.tb07226.x>
- Chen, C. C., Gettelman, A., Craig, C., Minnis, P., & Duda, D. P. (2012). Global contrail coverage simulated by CAM5 with the inventory of 2006 global aircraft emissions. *Journal of Advances in Modeling Earth Systems*, 4(2), n/a. <https://doi.org/10.1029/2011ms000105>
- Chen, C.-C., & Gettelman, A. (2013). Simulated radiative forcing from contrails and contrail cirrus. *Atmospheric Chemistry and Physics*, 13(24), 12525–12536. <https://doi.org/10.5194/acp-13-12525-2013>
- Colella, P., & Woodward, P. R. (1984). The Piecewise Parabolic Method (PPM) for gas-dynamical simulations. *Journal of Computational Physics*, 54(1), 174–201. [https://doi.org/10.1016/0021-9991\(84\)90143-8](https://doi.org/10.1016/0021-9991(84)90143-8)
- Corfidi, S., & Brandli, H. (1986). GOES views aircraft distrails. *National Weather Digest*, 11, 37–39. <http://nwafiles.nwas.org/digest/papers/1986/Vol11-Issue2-May1986/Pg37-Corfidi.pdf>

- Cziczo, D. J., Froyd, K. D., Hoose, C., Jensen, E. J., Diao, M., Zondlo, M. A., Smith, J. B., Twohy, C. H., & Murphy, D. M. (2013). Clarifying the Dominant Sources and Mechanisms of Cirrus Cloud Formation. *Science*, *340*(6138), 1320–1324. <https://doi.org/10.1126/science.1234145>
- DeMott, P. J., Chen, Y., Kreidenweis, S. M., Rogers, D. C., & Sherman, D. E. (1999). Ice formation by black carbon particles. *Geophysical Research Letters*, *26*(16), 2429–2432. <https://doi.org/10.1029/1999gl900580>
- DeMott, P. J., Sassen, K., Poellot, M. R., Baumgardner, D., Rogers, D. C., Brooks, S. D., Prenni, A. J., & Kreidenweis, S. M. (2003). African dust aerosols as atmospheric ice nuclei. *Geophysical Research Letters*, *30*(14). <https://doi.org/10.1029/2003gl017410>
- Dickson, N. C., Gierens, K. M., Rogers, H. L., & Jones, R. L. (2010). Probabilistic description of ice-supersaturated layers in low resolution profiles of relative humidity. *Atmospheric Chemistry and Physics*, *10*(14), 6749–6763. <https://doi.org/10.5194/acp-10-6749-2010>
- Dipankar, A., Stevens, B., Heinze, R., Moseley, C., Zängl, G., Giorgetta, M., & Brdar, S. (2015). Large eddy simulation using the general circulation model ICON. *Journal of Advances in Modeling Earth Systems*, *7*(3), 963–986. <https://doi.org/10.1002/2015ms000431>
- Duda, D. P., Minnis, P., Khlopenkov, K., Chee, T. L., & Boeke, R. (2013). Estimation of 2006 Northern Hemisphere contrail coverage using MODIS data. *Geophysical Research Letters*, *40*(3), 612–617. <https://doi.org/10.1002/grl.50097>
- Eyers, C., P. Norman, J. Middel, M. Plohr, S. Michot, K. Atkinson and R. Christou (2004). AERO2K global aviation emissions inventories for 2002 and 2025, Tech. Rep., QINETIC/04/01113, QinetiQ, Farnborough, U. K.
- Febvre, G., Gayet, J. F., Minikin, A., Schlager, H., Shcherbakov, V., Jourdan, O., Busen, R., Fiebig, M., Kärcher, B., & Schumann, U. (2009). On optical and microphysical characteristics of contrails and cirrus. *Journal of Geophysical Research*, *114*(D2). <https://doi.org/10.1029/2008jd010184>
- Fichter, C., Marquart, S., Sausen, R., & Lee, D. S. (2005). The impact of cruise altitude on contrails and related radiative forcing. *Meteorologische Zeitschrift*, *14*(4), 563–572. <https://doi.org/10.1127/0941-2948/2005/0048>
- Field, P. R., Cotton, R. J., Johnson, D., Noone, K., Glantz, P., Kaye, P. H., Hirst, E., Greenaway, R. S., Jost, C., Gabriel, R., Reiner, T., Andreae, M., Saunders, C. P. R., Archer, A., Choularton, T., Smith, M., Brooks, B., Hoell, C., Bandy, B., & Heymsfield, A. (2001). Ice nucleation in orographic wave clouds: Measurements made during INTACC. *Quarterly Journal of the Royal Meteorological Society*, *127*(575), 1493–1512. <https://doi.org/10.1002/qj.49712757502>
- Frömming, C., Ponater, M., Burkhardt, U., Stenke, A., Pechtl, S., & Sausen, R. (2011). Sensitivity of contrail coverage and contrail radiative forcing to selected key parameters. *Atmospheric Environment*, *45*(7), 1483–1490. <https://doi.org/10.1016/j.atmosenv.2010.11.033>

- Gayet, J.-F., Febvre, G., Brogniez, G., Chepfer, H., Renger, W., & Wendling, P. (1996). Microphysical and Optical Properties of Cirrus and Contrails: Cloud Field Study on 13 October 1989. *Journal of the Atmospheric Sciences*, 53(1), 126–138. [https://journals.ametsoc.org/view/journals/atsc/53/1/1520-0469\\_1996\\_053\\_0126\\_maopoc\\_2\\_0\\_co\\_2.xml](https://journals.ametsoc.org/view/journals/atsc/53/1/1520-0469_1996_053_0126_maopoc_2_0_co_2.xml)
- Gerz, T., Dürbeck, T., & Konopka, P. (1998). Transport and effective diffusion of aircraft emissions. *Journal of Geophysical Research: Atmospheres*, 103(D20), 25905–25913. <https://doi.org/10.1029/98jd02282>
- Gettelman, A., & Chen, C. (2013). The climate impact of aviation aerosols. *Geophysical Research Letters*, 40(11), 2785–2789. <https://doi.org/10.1002/grl.50520>
- Gierens, K. (2003). On the transition between heterogeneous and homogeneous freezing. *Atmospheric Chemistry and Physics*, 3(2), 437–446. <https://doi.org/10.5194/acp-3-437-2003>
- Gierens, K. (2012). Selected topics on the interaction between cirrus clouds and embedded contrails. *Atmospheric Chemistry and Physics*, 12(24), 11943–11949. <https://doi.org/10.5194/acp-12-11943-2012>
- Gierens, K., & Brinkop, S. (2012). Dynamical characteristics of ice supersaturated regions. *Atmospheric Chemistry and Physics*, 12(24), 11933–11942. <https://doi.org/10.5194/acp-12-11933-2012>
- Gierens, K., Sausen, R., & Schumann, U. (1999). A Diagnostic Study of the Global Distribution of Contrails Part II: Future Air Traffic Scenarios. *Theoretical and Applied Climatology*, 63(1–2), 1–9. <https://doi.org/10.1007/s007040050087>
- Gierens, K., & Spichtinger, P. (2000). On the size distribution of ice-supersaturated regions in the upper troposphere and lowermost stratosphere. *Annales Geophysicae*, 18(4), 499–504. <https://doi.org/10.1007/s00585-000-0499-7>
- Gounou, A., & Hogan, R. J. (2007). A Sensitivity Study of the Effect of Horizontal Photon Transport on the Radiative Forcing of Contrails. *Journal of the Atmospheric Sciences*, 64(5), 1706–1716. <https://doi.org/10.1175/jas3915.1>
- Gruber, S., Unterstrasser, S., Bechtold, J., Vogel, H., Jung, M., Pak, H., & Vogel, B. (2018). Contrails and their impact on shortwave radiation and photovoltaic power production – a regional model study. *Atmospheric Chemistry and Physics*, 18(9), 6393–6411. <https://doi.org/10.5194/acp-18-6393-2018>
- Gu, Y., & Liou, K. N. (2000). Interactions of Radiation, Microphysics, and Turbulence in the Evolution of Cirrus Clouds. *Journal of the Atmospheric Sciences*, 57(15), 2463–2479.
- Hande, L. B., Engler, C., Hoose, C., & Tegen, I. (2016). Parameterizing cloud condensation nuclei concentrations during HOPE. *Atmospheric Chemistry and Physics*, 16(18), 12059–12079. <https://doi.org/10.5194/acp-16-12059-2016>
- Heinze, R., Dipankar, A., Henken, C. C., Moseley, C., Sourdeval, O., Trömel, S., Xie, X., Adamidis, P., Ament, F., Baars, H., Barthlott, C., Behrendt, A., Blahak, U., Bley, S., Brdar, S., Brueck,

- M., Crewell, S., Deneke, H., di Girolamo, P., . . . Quaas, J. (2017). Large-eddy simulations over Germany using ICON: a comprehensive evaluation. *Quarterly Journal of the Royal Meteorological Society*, 143(702), 69–100. <https://doi.org/10.1002/qj.2947>
- Hendricks, J., Kärcher, B., Lohmann, U., & Ponater, M. (2005). Do aircraft black carbon emissions affect cirrus clouds on the global scale? *Geophysical Research Letters*, 32(12), n/a. <https://doi.org/10.1029/2005gl022740>
- Heymsfield, A., Baumgardner, D., DeMott, P., Forster, P., Gierens, K., & Kärcher, B. (2010). Contrail Microphysics. *Bulletin of the American Meteorological Society*, 91(4), 465–472. <https://doi.org/10.1175/2009bams2839.1>
- Heymsfield, A. J., Lawson, R. P., & Sachse, G. W. (1998). Growth of ice crystals in a precipitating contrail. *Geophysical Research Letters*, 25(9), 1335–1338. <https://doi.org/10.1029/98gl00189>
- Heymsfield, A. J., & Sabin, R. M. (1989). Cirrus Crystal Nucleation by Homogeneous Freezing of Solution Droplets. *Journal of the Atmospheric Sciences*, 46(14), 2252–2264. [https://doi.org/10.1175/1520-0469\(1989\)046<2252:CCNBHF>2.0.CO;2](https://doi.org/10.1175/1520-0469(1989)046<2252:CCNBHF>2.0.CO;2)
- Hoose, C., Kristjánsson, J. E., Chen, J. P., & Hazra, A. (2010). A Classical-Theory-Based Parameterization of Heterogeneous Ice Nucleation by Mineral Dust, Soot, and Biological Particles in a Global Climate Model. *Journal of the Atmospheric Sciences*, 67(8), 2483–2503. <https://doi.org/10.1175/2010jas3425.1>
- Hoose, C., & Möhler, O. (2012). Heterogeneous ice nucleation on atmospheric aerosols: a review of results from laboratory experiments. *Atmospheric Chemistry and Physics*, 12(20), 9817–9854. <https://doi.org/10.5194/acp-12-9817-2012>
- Huebsch WW, Lewellen DC. (2006). *Sensitivity study on contrail evolution*. Presented at AIAA Fluid Dyn. Conf. Exhib., 36th, San Francisco, AIAA Pap. 2006-3749
- International Civil Aviation Organization (ICAO), Environmental Report 2013, Chap. 1: Aviation and Environment.
- Immler, F., & Schrems, O. (2002). LIDAR measurements of cirrus clouds in the northern and southern midlatitudes during INCA (55°N, 53°S): A comparative study. *Geophysical Research Letters*, 29(16), 56–1. <https://doi.org/10.1029/2002gl015077>
- International Panel on Climate Change (IPCC), Aviation and the Global Atmosphere (1999), ed. by J. E. Penner, D. H. Lister, D. J. Griggs, D. J. Dokken and M. McFarland.
- Jensen, E. J., Ackerman, A. S., Stevens, D. E., Toon, O. B., & Minnis, P. (1998). Spreading and growth of contrails in a sheared environment. *Journal of Geophysical Research: Atmospheres*, 103(D24), 31557–31567. <https://doi.org/10.1029/98jd02594>
- Jensen, E. J., & Toon, O. B. (1997). The potential impact of soot particles from aircraft exhaust on cirrus clouds. *Geophysical Research Letters*, 24(3), 249–252. <https://doi.org/10.1029/96gl03235>
- Jiang, J. H., Su, H., Zhai, C., Perun, V. S., del Genio, A., Nazarenko, L. S., Donner, L. J., Horowitz, L., Seman, C., Cole, J., Gettelman, A., Ringer, M. A., Rotstayn, L., Jeffrey, S., Wu, T.,

- Brient, F., Dufresne, J. L., Kawai, H., Koshiro, T., . . . Stephens, G. L. (2012). Evaluation of cloud and water vapor simulations in CMIP5 climate models using NASA “A-Train” satellite observations. *Journal of Geophysical Research: Atmospheres*, *117*(D14), n/a. <https://doi.org/10.1029/2011jd017237>
- Joseph, J. H., Levin, Z., Mekler, Y., Ohring, G., & Otterman, J. (1975). Study of contrails observed from the ERTS 1 satellite imagery. *Journal of Geophysical Research*, *80*(3), 366–372. <https://doi.org/10.1029/JC080i003p00366>
- Kapadia, Z. Z., Spracklen, D. V., Arnold, S. R., Borman, D. J., Mann, G. W., Pringle, K. J., Monks, S. A., Reddington, C. L., Benduhn, F., Rap, A., Scott, C. E., Butt, E. W., & Yoshioka, M. (2016). Impacts of aviation fuel sulfur content on climate and human health. *Atmospheric Chemistry and Physics*, *16*(16), 10521–10541. <https://doi.org/10.5194/acp-16-10521-2016>
- Kärcher, B. (1998). Physicochemistry of aircraft-generated liquid aerosols, soot, and ice particles: 1. Model description. *Journal of Geophysical Research: Atmospheres*, *103*(D14), 17111–17128. <https://doi.org/10.1029/98jd01044>
- Kärcher, B. (2018). Formation and radiative forcing of contrail cirrus. *Nature Communications*, *9*(1). <https://doi.org/10.1038/s41467-018-04068-0>
- Kärcher, B., Burkhardt, U., Bier, A., Bock, L., & Ford, I. J. (2015). The microphysical pathway to contrail formation. *Journal of Geophysical Research: Atmospheres*, *120*(15), 7893–7927. <https://doi.org/10.1002/2015jd023491>
- Kärcher, B., Burkhardt, U., Unterstrasser, S., & Minnis, P. (2009). Factors controlling contrail cirrus optical depth. *Atmospheric Chemistry and Physics*, *9*(16), 6229–6254. <https://doi.org/10.5194/acp-9-6229-2009>
- Kärcher, B., Busen, R., Petzold, A., Schröder, F. P., Schumann, U., & Jensen, E. J. (1998). Physicochemistry of aircraft-generated liquid aerosols, soot, and ice particles: 2. Comparison with observations and sensitivity studies. *Journal of Geophysical Research: Atmospheres*, *103*(D14), 17129–17147. <https://doi.org/10.1029/98jd01045>
- Kärcher, B., Hendricks, J., & Lohmann, U. (2006). Physically based parameterization of cirrus cloud formation for use in global atmospheric models. *Journal of Geophysical Research*, *111*(D1), 1. <https://doi.org/10.1029/2005jd006219>
- Kärcher, B., & Lohmann, U. (2002). A parameterization of cirrus cloud formation: Homogeneous freezing of supercooled aerosols. *Journal of Aerosol Science*, *32*, 919–920. [https://doi.org/10.1016/s0021-8502\(01\)00132-x](https://doi.org/10.1016/s0021-8502(01)00132-x)
- Kärcher, B., Mayer, B., Gierens, K., Burkhardt, U., Mannstein, H., & Chatterjee, R. (2009). Aerodynamic Contrails: Microphysics and Optical Properties. *Journal of the Atmospheric Sciences*, *66*(2), 227–243. <https://doi.org/10.1175/2008jas2768.1>
- Kärcher, B., Möhler, O., DeMott, P. J., Pechtl, S., & Yu, F. (2007). Insights into the role of soot aerosols in cirrus cloud formation. *Atmospheric Chemistry and Physics*, *7*(16), 4203–4227. <https://doi.org/10.5194/acp-7-4203-2007>

- Kärcher, B., Peter, T., Biermann, U. M., & Schumann, U. (1996). The Initial Composition of Jet Condensation Trails. *Journal of the Atmospheric Sciences*, 53(21), 3066–3083. [https://doi.org/10.1175/1520-0469\(1996\)053<3066:TICOJC>2.0.CO;2](https://doi.org/10.1175/1520-0469(1996)053<3066:TICOJC>2.0.CO;2)
- Kärcher, B., Turco, R. P., Yu, F., Danilin, M. Y., Weisenstein, D. K., Miake-Lye, R. C., & Busen, R. (2000). A unified model for ultrafine aircraft particle emissions. *Journal of Geophysical Research: Atmospheres*, 105(D24), 29379–29386. <https://doi.org/10.1029/2000jd900531>
- Kärcher, B., & Yu, F. (2009). Role of aircraft soot emissions in contrail formation. *Geophysical Research Letters*, 36(1), 1. <https://doi.org/10.1029/2008gl036649>
- Koehler, K. A., DeMott, P. J., Kreidenweis, S. M., Popovicheva, O. B., Petters, M. D., Carrico, C. M., Kireeva, E. D., Khokhlova, T. D., & Shonija, N. K. (2009). Cloud condensation nuclei and ice nucleation activity of hydrophobic and hydrophilic soot particles. *Physical Chemistry Chemical Physics*, 11(36), 7906. <https://doi.org/10.1039/b905334b>
- Köhler, C. G., & Seifert, A. (2014). Identifying sensitivities for cirrus modelling using a two-moment two-mode bulk microphysics scheme. *Tellus B: Chemical and Physical Meteorology*, 67(1), 24494. <https://doi.org/10.3402/tellusb.v67.24494>
- Koop, T. (2004). Homogeneous Ice Nucleation in Water and Aqueous Solutions. *Zeitschrift Für Physikalische Chemie*, 218(11), 1231–1258. <https://doi.org/10.1524/zpch.218.11.1231.50812>
- Koop, T., Luo, B., Tsias, A., & Peter, T. (2000). Water activity as the determinant for homogeneous ice nucleation in aqueous solutions. *Nature*, 406(6796), 611–614. <https://doi.org/10.1038/35020537>
- Korolev, A. V., & Mazin, I. P. (2003). Supersaturation of Water Vapor in Clouds. *Journal of the Atmospheric Sciences*, 60(24), 2957–2974.
- Krämer, M., Rolf, C., Luebke, A., Afchine, A., Spelten, N., Costa, A., Meyer, J., Zöger, M., Smith, J., Herman, R. L., Buchholz, B., Ebert, V., Baumgardner, D., Borrmann, S., Klingebiel, M., & Avallone, L. (2016). A microphysics guide to cirrus clouds – Part 1: Cirrus types. *Atmospheric Chemistry and Physics*, 16(5), 3463–3483. <https://doi.org/10.5194/acp-16-3463-2016>
- Krämer, M., Rolf, C., Spelten, N., Afchine, A., Fahey, D., Jensen, E., Khaykin, S., Kuhn, T., Lawson, P., Lykov, A., Pan, L. L., Riese, M., Rollins, A., Stroh, F., Thornberry, T., Wolf, V., Woods, S., Spichtinger, P., Quaas, J., & Sourdeval, O. (2020). A microphysics guide to cirrus – Part 2: Climatologies of clouds and humidity from observations. *Atmospheric Chemistry and Physics*, 20(21), 12569–12608. <https://doi.org/10.5194/acp-20-12569-2020>
- Krämer, M., Schiller, C., Afchine, A., Bauer, R., Gensch, I., Mangold, A., Schlicht, S., Spelten, N., Sitnikov, N., Borrmann, S., de Reus, M., & Spichtinger, P. (2009). Ice supersaturations and cirrus cloud crystal numbers. *Atmospheric Chemistry and Physics*, 9(11), 3505–3522. <https://doi.org/10.5194/acp-9-3505-2009>
- Lamquin, N., Stubenrauch, C. J., Gierens, K., Burkhardt, U., & Smit, H. (2012). A global climatology of upper-tropospheric ice supersaturation occurrence inferred from the

- Atmospheric Infrared Sounder calibrated by MOZAIC. *Atmospheric Chemistry and Physics*, 12(1), 381–405. <https://doi.org/10.5194/acp-12-381-2012>
- Lee, D. S., Fahey, D. W., Forster, P. M., Newton, P. J., Wit, R. C. N., Lim, L. L., Owen, B., & Sausen, R. (2009). Aviation and global climate change in the 21st century. *Atmospheric Environment*, 43(22–23), 3520–3537. <https://doi.org/10.1016/j.atmosenv.2009.04.024>
- Lee, D. S., Fahey, D. W., Skowron, A., Allen, M. R., Burkhardt, U., Chen, Q., Doherty, S. J., Freeman, S., Forster, P. M., Fuglestedt, J., Gettelman, A., de León, R. R., Lim, L. L., Lund, M. T., Millar, R. J., Owen, B., Penner, J. E., Pitari, G., Prather, M. J., . . . Wilcox, L. J. (2021). The contribution of global aviation to anthropogenic climate forcing for 2000 to 2018. *Atmospheric Environment*, 244, 117834. <https://doi.org/10.1016/j.atmosenv.2020.117834>
- Lewellen, D. C. (2012). Analytic Solutions for Evolving Size Distributions of Spherical Crystals or Droplets Undergoing Diffusional Growth in Different Regimes. *Journal of the Atmospheric Sciences*, 69(2), 417–434. <https://doi.org/10.1175/jas-d-11-029.1>
- Lewellen, D. C. (2020). A Large-Eddy Simulation Study of Contrail Ice Number Formation. *Journal of the Atmospheric Sciences*, 77(7), 2585–2604. <https://doi.org/10.1175/jas-d-19-0322.1>
- Lewellen, D. C., & Lewellen, W. S. (2001). The Effects of Aircraft Wake Dynamics on Contrail Development. *Journal of the Atmospheric Sciences*, 58(4), 390–406.
- Lewellen, D. C., Meza, O., & Huebsch, W. W. (2014). Persistent Contrails and Contrail Cirrus. Part I: Large-Eddy Simulations from Inception to Demise. *Journal of the Atmospheric Sciences*, 71(12), 4399–4419. <https://doi.org/10.1175/jas-d-13-0316.1>
- Liou, K. N. (1986). Influence of Cirrus Clouds on Weather and Climate Processes: A Global Perspective. *Monthly Weather Review*, 114(6), 1167–1199. [https://doi.org/10.1175/1520-0493\(1986\)114<1167:IOCCOW>2.0.CO;2](https://doi.org/10.1175/1520-0493(1986)114<1167:IOCCOW>2.0.CO;2)
- Liou, K. N., Takano, Y., Yue, Q., & Yang, P. (2013). On the radiative forcing of contrail cirrus contaminated by black carbon. *Geophysical Research Letters*, 40(4), 778–784. <https://doi.org/10.1002/grl.50110>
- Lohmann, U., Spichtinger, P., Jess, S., Peter, T., & Smit, H. (2008). Cirrus cloud formation and ice supersaturated regions in a global climate model. *Environmental Research Letters*, 3(4), 045022. <https://doi.org/10.1088/1748-9326/3/4/045022>
- Luo, Z., & Rossow, W. B. (2004). Characterizing Tropical Cirrus Life Cycle, Evolution, and Interaction with Upper-Tropospheric Water Vapor Using Lagrangian Trajectory Analysis of Satellite Observations. *Journal of Climate*, 17(23), 4541–4563. <https://doi.org/10.1175/3222.1>
- Macke, A., Seifert, P., Baars, H., Beekmans, C., Behrendt, A., Bohn, B., Bühl, J., Crewell, S., Damian, T., Deneke, H., Düsing, S., Foth, A., di Girolamo, P., Hammann, E., Heinze, R., Hirsikko, A., Kalisch, J., Kalthoff, N., Kinne, S., . . . Xie, X. (2016). The HD(CP)2 Observational Prototype Experiment HOPE – An Overview. *Atmospheric Chemistry and Physics*, 1. <https://doi.org/10.5194/acp-2016-990>

- Mannstein, H., Meyer, R., & Wendling, P. (1999). Operational detection of contrails from NOAA-AVHRR-data. *International Journal of Remote Sensing*, 20(8), 1641–1660. <https://doi.org/10.1080/014311699212650>
- Markowicz, K. M., & Witek, M. L. (2011). Simulations of Contrail Optical Properties and Radiative Forcing for Various Crystal Shapes. *Journal of Applied Meteorology and Climatology*, 50(8), 1740–1755. <https://doi.org/10.1175/2011jamc2618.1>
- Marquart, S., Ponater, M., Mager, F., & Sausen, R. (2003). Future Development of Contrail Cover, Optical Depth, and Radiative Forcing: Impacts of Increasing Air Traffic and Climate Change. *Journal of Climate*, 16(17), 2890–2904. [https://doi.org/10.1175/1520-0442\(2003\)016<2890:FDOCCO>2.0.CO;2](https://doi.org/10.1175/1520-0442(2003)016<2890:FDOCCO>2.0.CO;2)
- Matthes, S., Lim, L., Burkhardt, U., Dahlmann, K., Dietmüller, S., Grewe, V., Haslerud, A. S., Hendricks, J., Owen, B., Pitari, G., Righi, M., & Skowron, A. (2021). Mitigation of Non-CO<sub>2</sub> Aviation's Climate Impact by Changing Cruise Altitudes. *Aerospace*, 8(2), 36. <https://doi.org/10.3390/aerospace8020036>
- Meerkötter, R., Schumann, U., Doelling, D. R., Minnis, P., Nakajima, T., & Tsushima, Y. (1999). Radiative forcing by contrails. *Annales Geophysicae*, 17(8), 1080–1094. <https://doi.org/10.1007/s00585-999-1080-7>
- Meyer, R., Mannstein, H., Meerkötter, R., Schumann, U., & Wendling, P. (2002a). Regional radiative forcing by line-shaped contrails derived from satellite data. *Journal of Geophysical Research: Atmospheres*, 107(D10), ACL 17–1. <https://doi.org/10.1029/2001jd000426>
- Meyer, R., Mannstein, H., Meerkötter, R., Schumann, U., & Wendling, P. (2002b). Regional radiative forcing by line-shaped contrails derived from satellite data. *Journal of Geophysical Research: Atmospheres*, 107(D10), ACL 17–1. <https://doi.org/10.1029/2001jd000426>
- Minnis, P., Bedka, S. T., Duda, D. P., Bedka, K. M., Chee, T., Ayers, J. K., Palikonda, R., Spangenberg, D. A., Khlopenkov, K. V., & Boeke, R. (2013). Linear contrail and contrail cirrus properties determined from satellite data. *Geophysical Research Letters*, 40(12), 3220–3226. <https://doi.org/10.1002/grl.50569>
- Minnis, P., Palikonda, R., Walter, B. J., Ayers, J. K., & Mannstein, H. (2005). Contrail properties over the eastern North Pacific from AVHRR data. *Meteorologische Zeitschrift*, 14(4), 515–523. <https://doi.org/10.1127/0941-2948/2005/0056>
- Minnis, P., Schumann, U., Doelling, D. R., Gierens, K. M., & Fahey, D. W. (1999). Global distribution of contrail radiative forcing. *Geophysical Research Letters*, 26(13), 1853–1856. <https://doi.org/10.1029/1999gl900358>
- Miura, H., Satoh, M., Nasuno, T., Noda, A. T., & Oouchi, K. (2007). A Madden-Julian Oscillation Event Realistically Simulated by a Global Cloud-Resolving Model. *Science*, 318(5857), 1763–1765. <https://doi.org/10.1126/science.1148443>

- Möhler, O. (2005). Effect of sulfuric acid coating on heterogeneous ice nucleation by soot aerosol particles. *Journal of Geophysical Research*, 110(D11). <https://doi.org/10.1029/2004jd005169>
- Moore, R. H., Thornhill, K. L., Weinzierl, B., Sauer, D., D'Ascoli, E., Kim, J., Lichtenstern, M., Scheibe, M., Beaton, B., Beyersdorf, A. J., Barrick, J., Bulzan, D., Corr, C. A., Crosbie, E., Jurkat, T., Martin, R., Riddick, D., Shook, M., Slover, G., . . . Anderson, B. E. (2017). Biofuel blending reduces particle emissions from aircraft engines at cruise conditions. *Nature*, 543(7645), 411–415. <https://doi.org/10.1038/nature21420>
- Murphy, D. M., Thomson, D. S., & Mahoney, M. J. (1998). In Situ Measurements of Organics, Meteoritic Material, Mercury, and Other Elements in Aerosols at 5 to 19 Kilometers. *Science*, 282(5394), 1664–1669. <https://doi.org/10.1126/science.282.5394.1664>
- Myhre, G., Kvalevåg, M., Rädcl, G., Cook, J., Shine, K. P., Clark, H., Karcher, F., Markowicz, K., Kardas, A., Wolkenberg, P., Balkanski, Y., Ponater, M., Forster, P., Rap, A., Leon, R., & Rodriguez. (2009). Intercomparison of radiative forcing calculations of stratospheric water vapour and contrails. *Meteorologische Zeitschrift*, 18(6), 585–596. <https://doi.org/10.1127/0941-2948/2009/0411>
- Myhre, G., & Stordal, F. (2001). On the tradeoff of the solar and thermal infrared radiative impact of contrails. *Geophysical Research Letters*, 28(16), 3119–3122. <https://doi.org/10.1029/2001gl013193>
- Naiman, A. D., Lele, S. K., & Jacobson, M. Z. (2011). Large eddy simulations of contrail development: Sensitivity to initial and ambient conditions over first twenty minutes. *Journal of Geophysical Research: Atmospheres*, 116(D21), <https://doi.org/10.1029/2011jd015806>
- Palikonda, R., Minnis, P., Duda, D. P., & Mannstein, H. (2005). Contrail coverage derived from 2001 AVHRR data over the continental United States of America and surrounding areas. *Meteorologische Zeitschrift*, 14(4), 525–536. <https://doi.org/10.1127/0941-2948/2005/0051>
- Paoli, R., & Shariff, K. (2016). Contrail Modeling and Simulation. *Annual Review of Fluid Mechanics*, 48(1), 393–427. <https://doi.org/10.1146/annurev-fluid-010814-013619>
- Penner, J. E., Zhou, C., Garnier, A., & Mitchell, D. L. (2018). Anthropogenic Aerosol Indirect Effects in Cirrus Clouds. *Journal of Geophysical Research: Atmospheres*, 123(20). <https://doi.org/10.1029/2018jd029204>
- Petters, M. D., & Kreidenweis, S. M. (2007). A single parameter representation of hygroscopic growth and cloud condensation nucleus activity. *Atmospheric Chemistry and Physics*, 7(8), 1961–1971. <https://doi.org/10.5194/acp-7-1961-2007>
- Petzold, A., Busen, R., Schröder, F. P., Baumann, R., Kuhn, M., Ström, J., Hagen, D. E., Whitefield, P. D., Baumgardner, D., Arnold, F., Borrmann, S., & Schumann, U. (1997). Near-field measurements on contrail properties from fuels with different sulfur content. *Journal of Geophysical Research: Atmospheres*, 102(D25), 29867–29880. <https://doi.org/10.1029/97jd02209>

- Petzold, A., Gysel, M., Vancassel, X., Hitzenberger, R., Puxbaum, H., Vrochticky, S., Weingartner, E., Baltensperger, U., & Mirabel, P. (2005). On the effects of organic matter and sulphur-containing compounds on the CCN activation of combustion particles. *Atmospheric Chemistry and Physics*, 5(12), 3187–3203. <https://doi.org/10.5194/acp-5-3187-2005>
- Petzold, A., Ström, J., Ohlsson, S., & Schröder, F. (1998). Elemental composition and morphology of ice-crystal residual particles in cirrus clouds and contrails. *Atmospheric Research*, 49(1), 21–34. [https://doi.org/10.1016/s0169-8095\(97\)00083-5](https://doi.org/10.1016/s0169-8095(97)00083-5)
- Poellot, M. R., Arnott, W. P., & Hallett, J. (1999). In situ observations of contrail microphysics and implications for their radiative impact. *Journal of Geophysical Research: Atmospheres*, 104(D10), 12077–12084. <https://doi.org/10.1029/1999jd900109>
- Ponater, M., Marquart, S., & Sausen, R. (2002). Contrails in a comprehensive global climate model: Parameterization and radiative forcing results. *Journal of Geophysical Research*, 107(D13). <https://doi.org/10.1029/2001jd000429>
- Popovicheva, O. B., Persiantseva, N. M., Lukhovitskaya, E. E., Shonija, N. K., Zubareva, N. A., Demirdjian, B., Ferry, D., & Suzanne, J. (2004). Aircraft engine soot as contrail nuclei. *Geophysical Research Letters*, 31(11), n/a. <https://doi.org/10.1029/2003gl018888>
- Pruppacher, H. R., & Klett, J. D. (1978). *Microphysics of Clouds and Precipitation*. D. Reidel Publishing Company. <https://doi.org/10.1007/978-94-009-9905-3>
- Pruppacher, H. R., & Klett, J. D. (1996). *Microphysics of Clouds and Precipitation (Atmospheric and Oceanographic Sciences Library (18))* (2nd ed. 2010 ed.). Springer.
- Ramanathan, V., Cess, R. D., Harrison, E. F., Minnis, P., Barkstrom, B. R., Ahmad, E., & Hartmann, D. (1989). Cloud-Radiative Forcing and Climate: Results from the Earth Radiation Budget Experiment. *Science*, 243(4887), 57–63. <https://doi.org/10.1126/science.243.4887.57>
- Rap, A., Forster, P. M., Jones, A., Boucher, O., Haywood, J. M., Bellouin, N., & de Leon, R. R. (2010). Parameterization of contrails in the UK Met Office Climate Model. *Journal of Geophysical Research*, 115(D10). <https://doi.org/10.1029/2009jd012443>
- Righi, M., Hendricks, J., & Sausen, R. (2013). The global impact of the transport sectors on atmospheric aerosol: simulations for year 2000 emissions. *Atmospheric Chemistry and Physics*, 13(19), 9939–9970. <https://doi.org/10.5194/acp-13-9939-2013>
- Rojo, C., Vancassel, X., Mirabel, P., Ponche, J. L., & Garnier, F. (2015). Impact of alternative jet fuels on aircraft-induced aerosols. *Fuel*, 144, 335–341. <https://doi.org/10.1016/j.fuel.2014.12.021>
- Rybka, H., Burkhardt, U., Köhler, M., Arka, I., Bugliaro, L., Görsdorf, U., Horváth, K., Meyer, C. I., Reichardt, J., Seifert, A., & Strandgren, J. (2021). The behavior of high-CAPE (convective available potential energy) summer convection in large-domain large-eddy simulations with ICON. *Atmospheric Chemistry and Physics*, 21(6), 4285–4318. <https://doi.org/10.5194/acp-21-4285-2021>

- Sassen, K., & Campbell, J. R. (2001). A Midlatitude Cirrus Cloud Climatology from the Facility for Atmospheric Remote Sensing. Part I: Macrophysical and Synoptic Properties. *Journal of the Atmospheric Sciences*, 58(5), 481–496.
- Sassen, K., Wang, Z., & Liu, D. (2008). Global distribution of cirrus clouds from CloudSat/Cloud-Aerosol Lidar and Infrared Pathfinder Satellite Observations (CALIPSO) measurements. *Journal of Geophysical Research*, 113. <https://doi.org/10.1029/2008jd009972>
- Sausen, R., Gierens, K., Ponater, M., & Schumann, U. (1998). A Diagnostic Study of the Global Distribution of Contrails Part I: Present Day Climate ast; *Theoretical and Applied Climatology*, 61(3–4), 127–141. <https://doi.org/10.1007/s007040050058>
- Schmidt, E. (1941). Die Entstehung von Eisnebel aus den Auspuffgasen von Flugmotoren. *Schriften der Deutschen Akademie der Luftfahrtforschung*, 44, 1-15, 1941
- Schröder, F., Kärcher, B., Duroure, C., Ström, J., Petzold, A., Gayet, J.-F., Strauss, B., Wendling, P., & Borrmann, S. (1999). On the Transition of Contrails into Cirrus Clouds. *Journal of the Atmospheric Sciences*, 57(4), 464–480. [http://www.pa.op.dlr.de/~BerndKaercher/JAS57\\_464-480\\_2000.pdf](http://www.pa.op.dlr.de/~BerndKaercher/JAS57_464-480_2000.pdf)
- Schröder, F., Kärcher, B., Fiebig, M., & Petzold, A. (2002). Aerosol states in the free troposphere at northern midlatitudes. *Journal of Geophysical Research: Atmospheres*, 107(D21), LAC 8–1. <https://doi.org/10.1029/2000jd000194>
- Schröder, F. P., Kärcher, B., Petzold, A., Baumann, R., Busen, R., Hoell, C., & Schumann, U. (1998). Ultrafine aerosol particles in aircraft plumes: In situ observations. *Geophysical Research Letters*, 25(15), 2789–2792. <https://doi.org/10.1029/98gl02078>
- Schumann, U. (1996). On conditions for contrail formation from aircraft exhausts. *Meteorologische Zeitschrift*, 5(1), 4–23. <https://doi.org/10.1127/metz/5/1996/4>
- Schumann, U. (2002). Contrail cirrus, in *Cirrus*, edited by D. K. Lynch et al., 231-255, Oxford Univ. Press, New York.
- Schumann, U. (2005). Formation, properties and climatic effects of contrails. *Comptes Rendus Physique*, 6(4–5), 549–565. <https://doi.org/10.1016/j.crhy.2005.05.002>
- Schumann, U. (2012). A contrail cirrus prediction model. *Geoscientific Model Development*, 5(3), 543–580. <https://doi.org/10.5194/gmd-5-543-2012>
- Schumann, U., & Graf, K. (2013). Aviation-induced cirrus and radiation changes at diurnal timescales. *Journal of Geophysical Research: Atmospheres*, 118(5), 2404–2421. <https://doi.org/10.1002/jgrd.50184>
- Schumann, U., & Heymsfield, A. J. (2017). On the Life Cycle of Individual Contrails and Contrail Cirrus. *Meteorological Monographs*, 58, 3.1-3.24. <https://doi.org/10.1175/amsmonographs-d-16-0005.1>
- Schumann, U., Mayer, B., Gierens, K., Unterstrasser, S., Jessberger, P., Petzold, A., Voigt, C., & Gayet, J. F. (2010). Effective Radius of Ice Particles in Cirrus and Contrails. *Journal of the Atmospheric Sciences*, 68(2), 300–321. <https://doi.org/10.1175/2010jas3562.1>

- Schumann, U., Penner, J. E., Chen, Y., Zhou, C., & Graf, K. (2015). Dehydration effects from contrails in a coupled contrail–climate model. *Atmospheric Chemistry and Physics*, 15(19), 11179–11199. <https://doi.org/10.5194/acp-15-11179-2015>
- Schumann, U., Schlager, H., Arnold, F., Baumann, R., Haschberger, P., & Klemm, O. (1998). Dilution of aircraft exhaust plumes at cruise altitudes. *Atmospheric Environment*, 32(18), 3097–3103. [https://doi.org/10.1016/s1352-2310\(97\)00455-x](https://doi.org/10.1016/s1352-2310(97)00455-x)
- Seifert, A., & Beheng, K. D. (2006). A two-moment cloud microphysics parameterization for mixed-phase clouds. Part 1: Model description. *Meteorology and Atmospheric Physics*, 92(1–2), 45–66. <https://doi.org/10.1007/s00703-005-0112-4>
- Smiatek, G., Rockel, B., & Schättler, U. (2008). Time invariant data preprocessor for the climate version of the COSMO model (COSMO-CLM). *Meteorologische Zeitschrift*, 17(4), 395–405. <https://doi.org/10.1127/0941-2948/2008/0302>
- Stevens, B., Acquistapace, C., Hansen, A., Heinze, R., Klinger, C., Klocke, D., Rybka, H., Schubotz, W., Windmiller, J., Adamidis, P., Arka, I., Barlakas, V., Biercamp, J., Brueck, M., Brune, S., Buehler, S. A., Burkhardt, U., Cioni, G., Costa-Suros, M., . . . Zängl, G. (2020). The Added Value of Large-eddy and Storm-resolving Models for Simulating Clouds and Precipitation. *Journal of the Meteorological Society of Japan. Ser. II*, 98(2), 395–435. <https://doi.org/10.2151/jmsj.2020-021>
- Stevens, B., & Bony, S. (2013). What Are Climate Models Missing? *Science*, 340(6136), 1053–1054. <https://doi.org/10.1126/science.1237554>
- Sussmann, R., & Gierens, K. M. (1999). Lidar and numerical studies on the different evolution of vortex pair and secondary wake in young contrails. *Journal of Geophysical Research: Atmospheres*, 104(D2), 2131–2142. <https://doi.org/10.1029/1998jd200034>
- Tesche, M., Achtert, P., Glantz, P., & Noone, K. J. (2016). Aviation effects on already-existing cirrus clouds. *Nature Communications*, 7(1), 1. <https://doi.org/10.1038/ncomms12016>
- Thuburn, J. (1996). Multidimensional Flux-Limited Advection Schemes. *Journal of Computational Physics*, 123(1), 74–83. <https://doi.org/10.1006/jcph.1996.0006>
- Unterstrasser, S. (2014). Large-eddy simulation study of contrail microphysics and geometry during the vortex phase and consequences on contrail-to-cirrus transition. *Journal of Geophysical Research: Atmospheres*, 119(12), 7537–7555. <https://doi.org/10.1002/2013jd021418>
- Unterstrasser, S. (2016). Properties of young contrails – a parametrisation based on large-eddy simulations. *Atmospheric Chemistry and Physics*, 16(4), 2059–2082. <https://doi.org/10.5194/acp-16-2059-2016>
- Unterstrasser, S., & Gierens, K. (2010). Numerical simulations of contrail-to-cirrus transition – Part 1: An extensive parametric study. *Atmospheric Chemistry and Physics*, 10(4), 2017–2036. <https://doi.org/10.5194/acp-10-2017-2010>
- Unterstrasser, S., Gierens, K., & Spichtinger, P. (2008). The evolution of contrail microphysics in the vortex phase. *Meteorologische Zeitschrift*, 17(2), 145–156. <https://doi.org/10.1127/0941-2948/2008/0273>

- Unterstrasser, S., & Sölch, I. (2010). Study of contrail microphysics in the vortex phase with a Lagrangian particle tracking model. *Atmospheric Chemistry and Physics*, *10*(20), 10003–10015. <https://doi.org/10.5194/acp-10-10003-2010>
- Urbanek, B., Groß, S., Wirth, M., Rolf, C., Krämer, M., & Voigt, C. (2018). High Depolarization Ratios of Naturally Occurring Cirrus Clouds Near Air Traffic Regions Over Europe. *Geophysical Research Letters*, *45*(23). <https://doi.org/10.1029/2018gl079345>
- Vázquez-Navarro, M., Mannstein, H., & Kox, S. (2015). Contrail life cycle and properties from 1 year of MSG/SEVIRI rapid-scan images. *Atmospheric Chemistry and Physics*, *15*(15), 8739–8749. <https://doi.org/10.5194/acp-15-8739-2015>
- Vázquez-Navarro, M., Mannstein, H., & Mayer, B. (2010). An automatic contrail tracking algorithm. *Atmospheric Measurement Techniques*, *3*(4), 1089–1101. <https://doi.org/10.5194/amt-3-1089-2010>
- Voigt, C., Schumann, U., Jurkat, T., Schäuble, D., Schlager, H., Petzold, A., Gayet, J. F., Krämer, M., Schneider, J., Borrmann, S., Schmale, J., Jessberger, P., Hamburger, T., Lichtenstern, M., Scheibe, M., Goubeyre, C., Meyer, J., Kübbeler, M., Frey, W., . . . Dörnbrack, A. (2010). In-situ observations of young contrails – overview and selected results from the CONCERT campaign. *Atmospheric Chemistry and Physics*, *10*(18), 9039–9056. <https://doi.org/10.5194/acp-10-9039-2010>
- Voigt, C., Schumann, U., Minikin, A., Abdelmonem, A., Afchine, A., Borrmann, S., Boettcher, M., Buchholz, B., Bugliaro, L., Costa, A., Curtius, J., Dollner, M., Dörnbrack, A., Dreiling, V., Ebert, V., Ehrlich, A., Fix, A., Forster, L., Frank, F., . . . Zöger, M. (2017). ML-CIRRUS: The Airborne Experiment on Natural Cirrus and Contrail Cirrus with the High-Altitude Long-Range Research Aircraft HALO. *Bulletin of the American Meteorological Society*, *98*(2), 271–288. <https://doi.org/10.1175/bams-d-15-00213.1>
- Waliser, D. E., Li, J. L. F., Woods, C. P., Austin, R. T., Bacmeister, J., Chern, J., del Genio, A., Jiang, J. H., Kuang, Z., Meng, H., Minnis, P., Platnick, S., Rossow, W. B., Stephens, G. L., Sun-Mack, S., Tao, W. K., Tompkins, A. M., Vane, D. G., Walker, C., & Wu, D. (2009). Cloud ice: A climate model challenge with signs and expectations of progress. *Journal of Geophysical Research*, *114*. <https://doi.org/10.1029/2008jd010015>
- Wan, H., Giorgetta, M. A., Zängl, G., Restelli, M., Majewski, D., Bonaventura, L., Fröhlich, K., Reinert, D., Rípodas, P., Kornbluh, L., & Förstner, J. (2013). The ICON-1.2 hydrostatic atmospheric dynamical core on triangular grids – Part 1: Formulation and performance of the baseline version. *Geoscientific Model Development*, *6*(3), 735–763. <https://doi.org/10.5194/gmd-6-735-2013>
- Wilkerson, J. T., Jacobson, M. Z., Malwitz, A., Balasubramanian, S., Wayson, R., Fleming, G., Naiman, A. D., & Lele, S. K. (2010). Analysis of emission data from global commercial aviation: 2004 and 2006. *Atmospheric Chemistry and Physics*, *10*(13), 6391–6408. <https://doi.org/10.5194/acp-10-6391-2010>
- Wolke, R., Knoth, O., Hellmuth, O., Schröder, W., & Renner, E. (2004). The parallel model system LM-MUSCAT for chemistry-transport simulations: Coupling scheme, parallelization and

- applications. *Advances in Parallel Computing*, 363–369. [https://doi.org/10.1016/s0927-5452\(04\)80048-0](https://doi.org/10.1016/s0927-5452(04)80048-0)
- Wolke, R., Schröder, W., Schrödner, R., & Renner, E. (2012). Influence of grid resolution and meteorological forcing on simulated European air quality: A sensitivity study with the modeling system COSMO–MUSCAT. *Atmospheric Environment*, 53, 110–130. <https://doi.org/10.1016/j.atmosenv.2012.02.085>
- Wong, H. W., Beyersdorf, A. J., Heath, C. M., Ziemba, L. D., Winstead, E. L., Thornhill, K. L., Tacina, K. M., Ross, R. C., Albo, S. E., Bulzan, D. L., Anderson, B. E., & Miake-Lye, R. C. (2013). Laboratory and modeling studies on the effects of water and soot emissions and ambient conditions on the properties of contrail ice particles in the jet regime. *Atmospheric Chemistry and Physics*, 13(19), 10049–10060. <https://doi.org/10.5194/acp-13-10049-2013>
- Zängl, G., Reinert, D., Rípodas, P., & Baldauf, M. (2015). The ICON (ICOsahedral Non-hydrostatic) modelling framework of DWD and MPI-M: Description of the non-hydrostatic dynamical core. *Quarterly Journal of the Royal Meteorological Society*, 141(687), 563–579. <https://doi.org/10.1002/qj.2378>
- Zhang, Y., Macke, A., & Albers, F. (1999). Effect of crystal size spectrum and crystal shape on stratiform cirrus radiative forcing. *Atmospheric Research*, 52(1–2), 59–75. [https://doi.org/10.1016/s0169-8095\(99\)00026-5](https://doi.org/10.1016/s0169-8095(99)00026-5)
- Zhou, C., & Penner, J. E. (2014). Aircraft soot indirect effect on large-scale cirrus clouds: Is the indirect forcing by aircraft soot positive or negative? *Journal of Geophysical Research: Atmospheres*, 119(19), 11,303–11,320. <https://doi.org/10.1002/2014jd021914>



# Acknowledgements

First of all, I would like to express my deep and sincere gratitude to Dr. Ulrike Burkhardt for the opportunity to pursue my Ph.D. under her guidance. Thank you very much for your valuable guidance, effort, constant encouragement, and inspiration in each step of my Ph.D. research work throughout the last years. Thank you for giving me professional and personal support during this journey and for providing me a homely environment in Germany.

I want to thank Prof. Dr. Markus Rapp, my first examiner, and Prof. Dr. George Craig, my second examiner, for their initial review of my work and providing useful suggestions. I am very thankful to both of you for their extensive support and great interest in my work. Thank you very much for providing me with valuable suggestions during thesis committee meetings.

Further, I would like to thank my Ph.D. mentor Dr. Andreas Schäfler for his support and suggestions. I would like to thank him for attending all committee meetings and guidance throughout last year.

I am grateful to the head of the institute, Prof. Dr. Markus Rapp, and the head of the department Prof. Dr. Robert Sausen, for giving me the opportunity to work at the “Institute für Physik der Atmosphäre”. I am also thankful to the whole Earth System Modelling (ESM) group for always being helpful and supportive throughout this journey.

I am thankful to the High Definition Cloud and Precipitation HD(CP)<sup>2</sup> project that performed the ICON-LEM simulations on which our study is based. I would like to thank BMBF (German Federal Ministry of Education and Research) for providing funding for this research work.

I am thankful to Simon Unterstraßer and Klaus Gierens for their input on this work. I am deeply thankful to Winfried Beer and Bastian Kern for always being available to solve technical issues.

I express my heartiest thanks to all Ph.D. students, colleagues, and friends, especially Marius Bickel, Christof Gerhard Beer at DLR and Dr. Nidhi Yadav (India), Prof. Dr. Surabhi Jaiswal (USA), and Dr. Evan Aguirre (USA) for their valuable time for helping me during writing the thesis.

I would like to thank all my friends for their support and love during the hard time, especially Surabhi and Nidhi, who were always available to support me emotionally and professionally during a hard time.

Last but not the least, I owe a great deal of love to my parents and family for their blessings and consistent moral support throughout my life. I specially want to thank my younger brother Vipul Verma for always being there to help me and providing emotional support, specifically during the last weeks and months.